Two-Phase Flow Structure at Header-Channel Junctions:

PIV Experiments and Modeling

Wael Fairouz Saleh

A Thesis

in

The Department

of

Mechanical and Industrial Engineering

Presented in Partial Fulfillment of the Requirements
For the Degree of Doctor of Philosophy
Concordia University
Montreal, Quebec, Canada

October 2008

ABSTRACT

Two-Phase Flow Structure at Header-Channel Junctions:

PIV Experiments and Modeling

Wael Fairouz Saleh, Ph.D.

Concordia University, 2008

The discharge of a two-phase flow from a stratified region through single or multiple branches is an important process in many industrial applications including the pumping of fluid from storage tanks, shell-and-tube heat exchangers, and the fluid flow through small breaks in cooling channels of nuclear reactors. Knowledge of the flow phenomena and flow structure involved during the onset of gas entrainments (OGE) in branches is essential for the design and/or performance prediction of such thermal systems.

In the present investigation, extensive data were generated for the two-phase flow structure at the onset of gas entrainment from an air-water stratified region through small branches (d = 6.35 mm) over a wide range of Froude numbers (0 to 100). The test sections were in close dimensional resemblance with that of a CANDU header-feeder system, with branches mounted at orientation angles of 0, 45 and 90 degrees from the horizontal. Three groups of new data were generated for single discharge, dual discharge and triple discharge configurations. The Particle Image Velocimetry (PIV) was used to provide detailed measurements of the two-phase flow field. In each of these measurements, the critical height at the onset of entrainment was first achieved, and the volume of interest close to the branch-header junctions was then determined and divided

by a number of horizontal image planes. Each image plane required a separate spatial and temporal calibration for PIV measurements. The vorticity profile, stream lines, flow field development and coherent structure, were presented over a wide range of operating conditions.

A theoretical analysis for the onset of gas entrainment in a single downward discharge, from a stratified gas-liquid region, was developed. The discharge was modeled as a point-sink and Kelvin-Laplace's equation was used to incorporate surface tension effects. The dip geometry was experimentally investigated and a correlation was developed relating the dip radius of curvature to the discharge Froude number. The correlation was used in conjunction with the theoretical model. It was found that the predicted critical height demonstrated a good agreement with experimental data. The inclusion of surface tension improved the model's capability to predict the critical height, particularly at discharge Froude numbers below one. The single-discharge model was then extended to dual and triple discharge cases, with considering the branches as point sinks and two-dimensional slots. The results of dual and triple discharges were found to be a function of mass flow rate through the branches, and the position of the secondary branch (maintaining liquid phase flow only) with respect to the primary branch position (at which OGE occurs) and the angle between the branches. The present analysis applies to any two immiscible fluids with the term "gas entrainment" referring to the appearance of the lighter fluid through the upper branch.

ACKNOWLEDGEMENTS

Praise be to GOD, who gave me the success to finish my thesis.

Achieving the work presented in this thesis would not have been possible without the help and support of a number of people. My deepest appreciation and grateful to Professor Ibrahim Hassan, my supervisor and mentor who has been my source of guidance support and encourage in every step of my degree. I would like also to thank my supervisor Dr. Kadem for his direct guidance in the last year of work. I would like to thank the research colleagues I have had the pleasure of working with. Many have graduated now including Roland, Chad, Patricia Minmin Tariq A., and Minh. As well, the present research group members, Mohamed G., Dino, Ayman, Tarek E., Mohamed R., Fan, and Dr. Kim. The love of family and friends brings meaning to life, and my sincerest gratitude to all. Thanks to my family members especially my parents for their moral support. My wife deserves a heartfelt thank for being by my side through all the ups and downs in this endeavour.

TABLE OF CONTENTS

List of Figures

LIST OF TABLES

NOMENCLATURE

A	Branch at horizontal axis
A_1, A_2	Constants
a	Vertical acceleration imposed on the liquid, (m/s^2)
a_o, a_n	Constants
b_1, b_2, b_n	Constants
B	Branch located at 45° from horizontal axis
Bo	Bond number, $\left(Bo = \dfrac{d}{\sqrt{g\Delta\rho/\sigma}} \right)$
C	Bottom branch
C_1, C_2	Constants
D_1, D_2	Constants
D	Header cross-section diameter
d	Branch diameter, (m)
Fr	Froude number, $\left(Fr = \dfrac{4\dot{m}}{\pi\sqrt{(gd^5\rho\Delta\rho)}} \right)$
g	Gravitational acceleration, (m/s^2)
H	Critical height at onset of liquid or gas entrainment, measured from the center of the primary branch to the air-water interface, (m)
h	Onset point height, (m)
h^*	Dimensionless distance, $(2h/d)$
I_1	Integral function

L	Center-to-center distance between branches, (m)
L_3, L_5	Vertical and horizontal Center-to-center distance between branches, (m)
l_1	Width of the slot, (m)
$\dot{m}$	Mass flow rate of fluid entering branch, (kg/s)
N	Number of images
N_μ	Viscosity number, $\left(N_\mu = \mu_l \left(\dfrac{g \Delta \rho}{\sigma^3 \rho_l^2} \right)^{0.25} \right)$
n	Number of vectors located inside the lateral or vertical elemental surface
P	Absolute pressure, (Pa)
P_o	Absolute system pressure, (Pa)
Q	Flow rate, (m^3/s)
R	Radius of curvature, (m)
St	Strain-rate tensor, (s^{-1})
S	Flow field surface area, (m^2)
s	Downward distance of the moving surface, (m)
U	Velocity in x direction, (m/s)
V	Velocity in y direction, (m/s)
V_N	Time averaged velocity, (m/s)
v	Average velocity of fluid at the branch inlet, (m/s)
W	Velocity in z direction, (m/s)
We	Weber number
x	Quality

Greek Letters

α_o	Constant
α_n	Constant
β_c	Angle between branches *A* and *C*, degree
β_n	Constant
δ	Half of the branch angle, degree
Φ	Potential function, (m^2/s)
$\Gamma 1$	Scalar function to characterize the location of the center of the large-scale vortex
η	Disturbance, (m)
η_o	Initial disturbance, (m)
λ	The disturbance wavelength, (m)
λ_2	Scalar function for measuring the vortical structure, (s^{-2})
v	Velocity at different flow field locations, (m/s)
θ	Position angle of any point in the flow field measured from the horizontal line.
$\theta`$	Differential parameter
$\Delta\rho$	Difference between densities of heavier and lighter fluids, (kg/m^3)
ρ_1	Density of heavier fluid at the branch inlet, (kg/m^3)
ρ_2	Density of lighter fluid at the branch inlet, (kg/m^3)
σ	Surface tension, (N/m)
Ω	Spin tensor, (s^{-1})
ω	Vorticity, (s^{-1})

Subscripts

1, 2	Upper and lower orifices
A, B, C	Side, inclined, and bottom branches
a, b	Points located at the air-water interface
acc	Accumulated
f	Free surface
G	Gas
L	Liquid
m	Including meniscus effect
ri	Element radial
T	Total
TP	Two-phase
t	Tangential
z	Vertical
z^*	$\left(z^* = \dfrac{4R^2}{h^2 - z^2} \right)$
∞	Free stream

Acronyms

CANDU	Canada Deuterium and Uranium
CCD	Charge Coupled Devices
CDE	Continuous Depression Entrainment
CVE	Continuous Vortex Entrainment
IDE	Initial Depression Entrainment

IMF   Image Model Fit

IVE   Initial Vortex Entrainment

LIF   Laser Induced Fluorescence

LOCA   Loss-Of-Coolant Accident

OGE   Onset of Gas Entrainment

OLE   Onset of Liquid Entrainment

PIV   Particle Image Velocimetry

ROC   Radius of Curvature

Chapter 1

Introduction

In recent years, two-phase flows are encountered in a wide range of industrial applications, such as chemical plants, nuclear reactors, oil wells and pipe lines, and evaporators and condensers. The most important factors in designing industrial systems operating at high pressures and temperatures are performance and safety. The CANDU (Canada Deuterium and Uranium) nuclear reactor is one of these systems. The cooling cycle for the fuel element, shown in Figure 1.1, starts from a large cylindrical reservoir (32.5 cm inner diameter, and 6 m long) called the inlet header in which the coolant is distributed through a network of pipes, called feeders (5.08 cm), to the cooling channels of the reactor. Under normal operating conditions an amount of heavy water enters the header through the turrets, and the same amount of coolant enters the fuel elements through the feeders. In some instances, it is possible for a break to occur in the header causing coolant to rapidly escape the header. As a result, the pressure may be reduced inside the header allowing the coolant to evaporate, creating a two phase stratified region. And the level of coolant inside the header will begin to decrease until an instant when two-phase flow occurs in the feeder tubes, known as the onset of gas entrainment.

The occurrence of two-phase flow inside a branch may be achieved even if the water level is higher than the discharge branch at the onset of gas entrainment. If the level of coolant inside the header continues to decrease, an instant will occur where the fluid flowing in the feeder branch will be single phase gas only. This point is called the onset of liquid entrainment. In this case, the core of the reactor is being cooled in the

1

particular feeder branch by gas only, causing a reduction in cooling capability. Consequently, the loss of cooling accident (LOCA) scenario can lead to a partial or total meltdown of the reactor core. As such, the prediction of the onset of gas entrainment (OGE) and onset of liquid entrainment (OLE) phenomena have received significant attention. Furthermore the determination of flow rates, and flow quality, from inlet headers to reactor coolant channels through feeders is very important for the safety of the reactor. These flow rates are influenced by geometry, configuration of connecting feeders, system pressure and vortex formation.
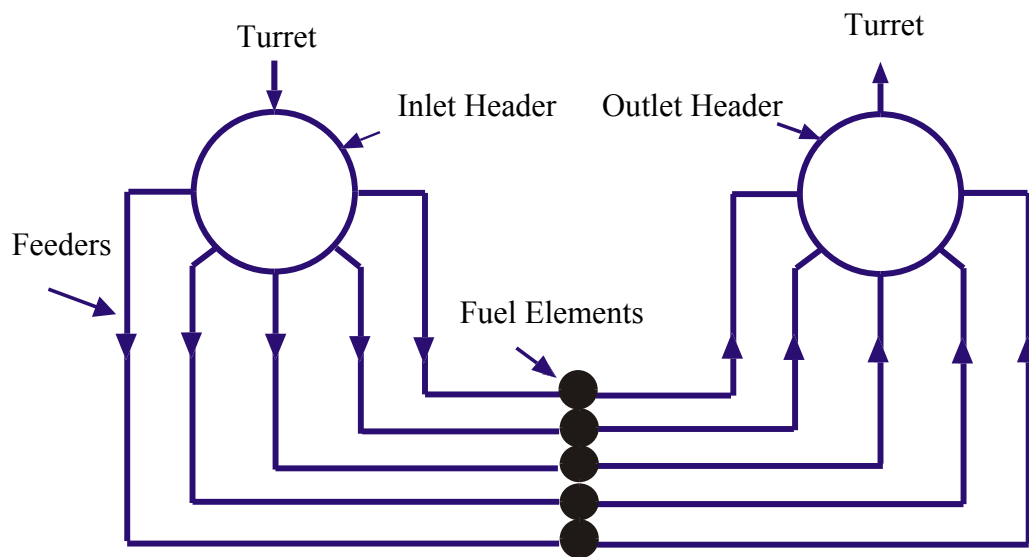
Figure 1.1 A CANDU-Type Header Feeder System.

Chapter 2

Literature Review

The research and development of experimental correlations and theoretical models of the onset of gas and liquid entrainments during discharge from a stratified, two-phase region through branches of finite diameter have gained great importance in recent literature due to their relevance to several industrial applications. This includes nuclear reactor safety during postulated loss-of-coolant accidents and two-phase distribution systems, where a certain incoming stream is fed into a larger header, as found in a shell-and-tube heat exchanger. Knowledge of the flow phenomena involved, the mass flow rate, and the quality of all discharging streams is essential for the design and performance prediction of such systems.

2.1 Single Discharge Investigations

For single discharge from a stratified flow region, Zuber (1980) reviewed past literature concerning the onset of gas and liquid entrainment and completed a description of the onset phenomena that may occur during the two-phase flow through small breaks found in horizontal pipes (LOCA). Zuber concluded that two individual phenomena may occur depending on the location of the gas liquid interface relative to the break. If the horizontal gas liquid interface is located above the break, the gas may be entrained by a vortex or vortex-free motion through the break into the predominantly liquid flow (onset of gas entrainment, OGE). Similarly, if the break is located below the gas-liquid interface, the liquid may be entrained in the primarily gas flow through the break (onset of liquid entrainment, OLE). Zuber then developed a correlation for the onset of gas and

liquid entrainments relating the vertical distance from the smooth gas-liquid interface, the break diameter and the corresponding Froude number. The equation is of the following form,

$$\frac{H}{d} = b_1 (Fr)^{b_2}. \tag{2-1}$$

Where, the values of b_1 and b_2 depend on the type of phenomena (OGE or OLE) and geometry.

Schrock et al. (1986) examined the onset of gas and liquid entrainment for a stratified air-water and steam-water flow in a horizontal pipe with branches oriented downward, sideward and upward. It was found that the experimental data was not consistent with the theoretical results found using Eq. (2-1), for the side and bottom branch discharges for OGE. It was then concluded that this discrepancy was due to the fact that the effects of viscosity, μ and surface tension, σ, were neglected. Correlations relating the viscosity number, Bond number and Froude number were therefore developed, as follows. For the case of gas entrainment through a bottom branch,

$$Fr_L Bo^2 N_\mu^{-0.5} \left(\frac{\rho_L}{\Delta\rho} \right)^{0.5} = 19.4 \left(\frac{H}{\sqrt{\sigma/g\Delta\rho}} \right)^{2.2}, \tag{2-2}$$

and for gas entrainment through the side branch,

$$Fr_L Bo^2 N_\mu^{-0.5} \left(\frac{\rho_L}{\Delta\rho} \right)^{0.5} = 40.6 \left(\frac{H}{\sqrt{\sigma/g\Delta\rho}} \right)^{2.1}. \tag{2-3}$$

Where Bond number, Bo is given by

$$Bo = \frac{d}{\sqrt{g\Delta\rho/\sigma}}, \tag{2-4}$$

and the viscosity number by,

$$N_\mu = \mu_L \left(\frac{g\Delta\rho}{\sigma^3 \rho_L^2} \right)^{0.25}. \tag{2-5}$$

Smoglie and Reiman (1986) performed experiments with air-water flows through breaks simulated by pipe stubs of various diameters located at the bottom, the top or in the side of a horizontal pipe. They observed the illustrated flow phenomena (OGE) with photographs. They reported that gas entrainment starts when a very thin gas tube reaches the branch inlet. This first gas tube is not stable but is swept away after few seconds and a long period of time can pass until another gas tube is formed. As the distance from the branch entrance to the interface is shortened or branch flow rate is increased, the gas tube becomes thicker and more stable. When the distance from the branch entrance to the interface is further reduced, a condition is reached where the flow pattern switches over from a vortex flow to a vortex-free flow. One reason for this transition is the increasing influence of the wall friction with decreasing interface levels. Another transition from vortex to vortex-free flow occurs when the superimposed liquid velocity (cross flow velocity) exceeds a certain value. For a cross flow velocity ≤ 0.06 m/s the vortices are very unstable and for higher values the flow field observed in the experiments was always vortex free. Smoglie et al. (1987) conducted theoretical and experimental work for the onset of gas and liquid entrainment through single discharging side and bottom branch, from a stratified air-water region. From their experimental results, they developed correlations for OGE and OLE, as well as, the quality of two-phase flow.

6

Yonomoto and Tasaka (1988) conducted theoretical and experimental work for OGE and OLE through a small side, top or bottom break in the middle of a duct from a stratified region. The parameters were changed to allow three different types of experiments to be conducted: Air-water flow supplied from one duct end and outlet flow rate equal zero, outlet air or water flow rate equal to zero, and air, water, or air and water are symmetrically supplied from both ends of the duct. They experimentally determined correlations according to the different flow phenomenon and break orientations considered, are of the same as Eq. (2-1). For the case of OGE, it was discovered that the experimental data did not correspond well with the theoretical values, which was believed to have been caused by the basic flow conditions used for the model, vortex free, cross flow free and stagnant during entrainment. Modifications were therefore performed to generate a theoretical correlation of the same form as Eq. (2-1) with the values 0.63 and 0.86 for b_1 and b_2 respectively.

Hassan et al. (1998) performed a series of experiments to produce data for two-phase air-water discharge through a small- diameter branch connected to a large reservoir in which the flow remained stratified. In their experiments the branch diameter remained constant (6.35 mm i.d.), while the reservoir pressure, the pressure drop through the branch and the down-stream hydraulic resistance were varied to give a range of experimental conditions. Two normalized parameters were introduced, a dimensionless interface height involving H, H_{OGE} and H_{OLE}, and a dimensionless mass flow rate involving $\dot{m}_{G,OLE}$, $\dot{m}_{L,OGE}$ and $\dot{m}_{TP}$. Data from various experimental conditions collapsed with the normalized parameters delineating a well-defined trend suitable for correlation equations. Two empirical correlations were developed, one relating the two-phase flow

quality, x, to the dimensionless interface height, and the other relating the dimensionless mass flow rate to the dimensionless interface height. Thus, their correlation provided a complete empirical model for predicting x and $\dot{m}_{TP}$ for any given *H*. The fit of their correlations with their experimental data was found to be good.

Maier et al. (1998) reported four cases of gas entrainment. Initial vortex entrainment (IVE) was characterized by a hair-thin, vortex, gas cone that originated from the flat interface over the branch or the bottom of the depression in the interface formed over the branch. IVE was always intermittent. Continuous vortex entrainment (CVE) was identical in appearance to IVE and formed in the same manner. However, CVE was continuous and always formed at the bottom of the depression. Initial depression entrainment (IDE) was characterized by observing the first instance of the depression in the interface over the branch becoming fully entrained. As the interface was lowered, the depression in the interface over the branch deepened until it entrained. IDE was always intermittent and prior to its occurrence, vortex cones, much like IVE, may have occurred. IDE was either vortical or non-vortical in nature. Continuous depression entrainment, CDE, was identical in appearance to IDE and formed in the same manner, however, CDE was continuous. They found that some data points in which the first instance of entrainment corresponded to continuous entrainment, and for others it corresponded to intermittent entrainment. Hence they considered the critical onset of gas entrainment height at the point of continuous gas entrainment instead of first instance of observable gas that was entrained in the beginning.

Majumdar et al. (1999) predicted the OGE, OLE, and flow quality. They developed an empirical model based on the model by Smoglie et al. (1986). They

8

validated their empirical model by comparing their results with Hassan et al. (1997)'s experimental results. They found a disagreement between their results and Schrock et al. (1987)'s model and attributed the difference to the geometry and medium used.

More recently, Ahmed et al. (2003) modeled the onset of gas entrainment in a single discharging side branch, installed on a flat vertical wall, from a smooth-stratified gas-liquid environment. Two models were proposed by the authors, first a simplified model that treated the discharge as a three-dimensional point sink, and second a more complex model that assumed the discharge to have a finite diameter. They treated each fluid phase independently and assumed both to be incompressible, inviscid, irrotational, and quasi-steady with negligible surface tension. To that end, they used a balance of Bernoulli's equation along the interface to bring both phases into account which were applied between infinity and a point on the wall above where the discharge was installed. To predict the onset of gas entrainment phenomena they used a criterion based on the work of Taylor (1950), who investigated the onset of instability of inviscid liquid surfaces accelerated vertically. It was stated that a liquid surface would become unstable if accelerated at a rate greater than that of gravity. This result was correlated in the equation,

$$\frac{\eta}{\eta_0} = \cosh\left(\left(\frac{4\pi s(a-g)(\rho_L - \rho_G)}{\lambda a(\rho_L - \rho_G)}\right)^{\frac{1}{2}}\right). \qquad (2\text{-}6)$$

Where η/η_0 is the ratio of the disturbance to its initial value, at any time, with λ representing the disturbance wavelength, $(a-g)$ being the difference between the vertical acceleration imposed on the liquid and gravity, and s is the downward distance of

the moving surface. With the onset of gas entrainment criterion being established, along

with Bernouilli's equation, one remaining unknown left, the velocity field. The authors

first assumed the discharge to be a point sink. Using a known potential function to define

the velocity field the authors were able to find a simple correlation in the form of,

$$\frac{H_{OGE}}{d} = 0.625 Fr^{0.4}, \tag{2-7}$$

where,

$$Fr = \frac{4\dot{m}}{\pi\sqrt{gd^5 \rho_L (\rho_L - \rho_G)}}. \tag{2-8}$$

The critical height (H_{OGE}) at the onset of gas entrainment is shown to be a

function of the Froude number. The Froude number is a function of the discharge liquid

mass flow rate ($\dot{m}$), the discharge diameter (d), gravitational acceleration (g) and the

fluid densities ($\rho_L - Liquid$ and $\rho_G - Gas$). For the second model, called the finite

branch model, the authors accounted for the branch diameter by solving Laplace's three-

dimensional equation, which results from a potential function subjected to appropriate

boundary conditions. This second model was found to be more representative of the

phenomena with $Fr < 10$ where the difference between both models was approximately

5% and increased dramatically afterwards. With $Fr = 1$ the difference in prediction

between the two models was approximately 20%.

Ahmad and Hassan (2006) experimentally investigated the onset of gas

entrainment phenomenon from a stratified region through branches located on a

semicircular wall configuration, in close dimensional resemblance with a Canada

Deuterium and Uranium (CANDU) header-feeder system. New experimental data for the onset of gas entrainment was generated during single and multiple discharge from an air/water stratified region over a wide range of Froude numbers (0 to 100). They provided sets of data for single, dual, and triple discharges. Also, they discussed the effect of the secondary branch on the H_{OGE} in the primary branch.

Following Ahmed et al. (2003), Andaleeb et al. (2006) used a similar approach to model multiple discharge on a curved surface. Their model accounted for the effect of wall curvature, with a main pipe diameter of 50.8 mm and discharge diameter of 6.35 mm. Two models were proposed, first a simplified model that treated the discharge as a three-dimensional point sink, and second a more complex model that assumed the discharge to have a finite diameter. They treated each fluid phase independently and assumed both to be incompressible, inviscid, irrotational, and quasi-steady with negligible surface tension. They presented their results for the bottom branch, the 45° branch and the side branch. They found relatively good agreement with Ahmad and Hassan (2006)'s experimental data. With their finite branch model at low Froude numbers, their results showed the need to include the surface tension in modeling. Hence, their results did not agree with Ahmad and Hassan (2006)'s experimental data for low Froude numbers.

In summary the functional relationship in Eq. (2-1) has been corroborated for quasi-steady unsymmetrical flow conditions approaching the discharge (Reimann and Khan, 1984; Smoglie and Reimann, 1986; Maciaszek and Micaelli, 1990; Yonomoto and Tasaka, 1991) and symmetrical flow (Maier et al., 2001; Ahmad and Hassan, 2006). These studies recorded the critical height based on flow visualization and purported that

the flow field was vortex-free at the onset of gas entrainment. These experimentalists described the critical height to be achieved with the steady entrainment of the gas phase - usually described as a cone-like flow structure.

2.2 Multiple Discharge Investigations

Several authors investigated experimentally the critical height at the onset of gas entrainment in dual and triple discharge branches. Kowalski and Krishnan (1987) experimentally examined a two-phase steam-water flow in a large manifold typical of the CANDU reactor header-feeder system. The manifold consisted of a flow channel, also known as a header, of 4.15 m long and 32.5 cm inner diameter, with a number of small openings, or feeders, located at angles of 0˚, 45˚ and 90˚ on the sidewall through which the fluid enters or leaves the header. The feeders are of 50.8 mm diameter steel pipes that are connected to the headers by nozzles. The experimental measurements of the critical height were found to be inconsistent with the predicted values of Smoglie and Reimann (1986), for both the onset of liquid and gas entrainment. The cause of this inconsistency was believed to have been caused by the simultaneously occurring effects of the liquid entrainment and steam pull-through in the multiple feeders; whereas the system considered by Smoglie and Reimann (1986) was for single discharge and hence the above flow phenomenon was not a factor of consideration.

Parrott et al. (1991) investigated the phenomenon of gas-pull through from a stratified air-water mixture at a pressure of 510 kPa, during dual discharge through vertically aligned orifices of 6.35 mm inner diameter and 127 mm long, located on the sidewall of a reservoir, at a vertical distance L center-to-center. The critical height at the onset of gas entrainment was measured over a wide range of Froude numbers for the

upper (Fr_1) and lower (Fr_2) orifices as well as distances between orifices with L/d set to 1.5, 2, 3, 4 and 6. This span of independent parameters permitted three possible gas pull-through patterns to be observed during the experiments, which proved the parameters' strong relevance to the onset phenomenon and the critical height at the onset of gas entrainment. The first pattern observed at very low (or zero) Fr_1 and high Fr_2, consisted of the gas pull-through occurring in only the lower orifice. The second pattern was perceptible with a slight increase in Fr_1 with the maintenance of a high Fr_2, where the gas pull-through took place in both the upper and lower orifices. Finally, the last pattern was observed after a further increase of Fr_1, which caused the gas pull-through to occur in the upper orifice only. In addition, a meniscus of a height of approximately 3.3 mm of liquid was found to form along the inner walls of the large reservoir. This height remained quite significant compared to the orifice diameter and therefore it was concluded that the critical height, measured from the branch centerline, at the onset of gas entrainment could be measured by either including (h_m) or excluding (h_f), the meniscus height, depending on the discharge rate and liquid height. For the case of discharge occurring in the top orifice only, the experimental results for h_m were found to be consistent with Smoglie and Reimann's (1986) correlation, whereas the results for h_f deviated considerably.

Hassan et al. (1996) examined the onset of gas and liquid entrainment, mass flow rate and quality of two-phase (air-water) discharge from a stratified two-phase region in two branches located on a vertical wall. Two branches, located in the same vertical (1996a) or horizontal line (1996b), were investigated. Their experiments were performed at pressures of 316 and 517 kPa, test section-separator pressure difference of 40 - 235 kPa, branch separating-distance-to diameter ratios of 1.5 - 8 and different hydraulic

resistances of the lines connecting the test section to the separators. Empirical relations were developed for the prediction of the onsets of gas and liquid entrainments.

Hassan et al. (1997) obtained experimental data for the mass flow rate and quality during single, dual and triple discharges from a stratified air-water region through small side branches installed on a semicircular wall. In their investigation, all the branches were adjusted to have the same hydraulic resistance and for the cases of dual and triple discharge, the same pressure drop ΔP was imposed across all active branches. Their tests were conducted at two system pressures Po = 316 and 517 kPa and the pressure drop varied within the range of 40 to 235 kPa. They studied the effect of the wall curvature on the values of $\dot{m}_{TP}$ and x for single and dual discharge by comparing the results between the data from a flat wall and the corresponding data from a semicircular wall. They reported that, the wall curvature has an insignificant effect on the values of $\dot{m}_{TP}$ and x for single discharge case and it has a small effect on the results at the upper branch and a significant effect on the results at the lower branch for the case of dual discharge.

There have been a handful of relevant analytical studies done since 1990 that deal with both the onset of gas entrainment with single and multiple discharges. Ahmed et al. (2004) modelled the onset of gas entrainment critical height in dual discharging side branches, installed on a flat vertical wall, vertically aligned, from a smooth-stratified gas-liquid environment. Two models were proposed by the authors: first, a simplified model that treated the discharge as a three-dimensional point sink, and second, a more complex model that assumed the discharge to have a finite diameter. They treated each fluid phase independently and assumed both as incompressible, inviscid, irrotational, and quasi-steady with negligible surface tension. The critical height at the onset of gas entrainment

14

was obtained over a wide range of Froude numbers for the upper (Fr_1) and lower (Fr_2) orifices as well as distances between the orifices (L/d). Their results showed a good agreement with the available experimental data. Following this, Ahmed (2006 and 2008) applied his two models on two side oriented branches mounted on a vertical wall but the two branches were not vertically aligned and on two branches mounted on an inclined wall (aligned on an inclined line inside the inclined wall). Again his results showed a good agreement with the available experimental results.

Bartley et al. (2003) developed a purely theoretical model relating the height of the gas-liquid interface to the mass flow rates of gas and liquid for the case of two branches separated by a vertical distance. Their theory was based on the existence of a control point upstream of the branches at which the flow is critical. The critical conditions at the control point were used to link the flow region far upstream of the branches, along streamlines parallel to the interface, to the flow conditions at the branch locations and thereby determine the interface height. Their theory showed good agreement with the data for dual discharge when the vertical space between the branches, L/d, was 1.5, 2, or 3. Deviation of their theory from experiments was the greatest near the extreme onset conditions: beginning of OGE, and beginning of OLE. A criterion was developed for determining the maximum (L/d) for the application of the dual-branch model and this criterion determines when the flow through each branch should behave independently.

In summary, the previous experimental studies provided data for the H_{OGE} for different configurations and the effect of the controlled parameters on this height but they did not provide any description of the flow field characteristics such as the three

components of the velocity, the vorticity, and the acceleration flow field. The previous analytical studies succeeded to predict the H_{OGE} for different flow scenarios excluding the work on the circular wall configuration, which is in close dimensional resemblance with a Canada Deuterium and Uranium (CANDU) header-feeder system.

2.3 Two-Phase Flow Structure and Visualization

Although there is a significant amount of analytical and experimental work done to simulate the process of two-phase flow (OGE, OLE, and quality of flow) during multiple discharges from a header, there still exists some disagreement between the predicted and experimental results. As a result this has prompted research to map the flow structure in order to search for new parameters, to guide and support in the modeling process.

Singh (2004) performed experiments regarding a steel teeming process using two scale models. A 2-D PIV technique was used to obtain the radial distributions of tangential velocity. The results showed that the initial tangential velocity was responsible for the vortex formation. Singh outlined three distinct regions; (i) at low initial tangential velocities, the critical height is nearly zero and independent of the tangential velocity (non-vortexing funnel regime); (ii) as initial tangential velocity increases, the critical height increases rapidly to reach about 40-50 % of the initial liquid height. This is the vortical region in which there is a linear increase in the critical height with the initial tangential velocity. (iii) With further increase in initial tangential velocity, the critical height slowly increases asymptotically to the initial liquid height. He also made an argument in understanding the relative importance of the governing forces in the observed phenomenon (the gravitational, inertial, and viscous forces). Singh concluded

that the gravitational forces are most dominant in the teeming process followed by the inertial forces and then the viscous forces.

Bowden (2007) investigated the onset of gas entrainment in a single discharging bottom branch. The flow field was divided into four separate non-simultaneous two-dimensional planes. The velocity fields were measured in each plane using a 2-D PIV technique. The results showed a strong tendency of the flow to be dominated by the radial velocity, towards the branch center. The effect of increasing the discharge flow rate on the velocity field was also demonstrated. It was concluded that simultaneous three dimensional measurements of the complex flow field were required. Significant difficulties were met in measuring the liquid velocity flow field during two-phase flow by PIV.   The results obtained did not include any details about the coherent flow field structure. The results were almost just an average for the flow field, which canceled a lot of details about the flow phenomena.

Honkanen and Saarenrinne (2002) investigated the properties of a turbulent bubbly flow in a cylindrical mixing vessel. The results were utilized in the development of a two-phase CFD model of an industrial mixing vessel. The measured attributes were bubble quantity, bubble size, the axial and radial velocities of bubbles, the local volume fraction of bubbles, and the fluid velocity field and turbulence properties in a measurement plane. Their measurement area was illuminated by a laser light sheet with a thickness of about 5 mm, and the profile of the laser light sheet was similar to a Gaussian curve. The thicker laser light sheet provides a wider profile with a flatter intensity peak. Thus, the overexposure of the bubbles can be avoided. Also, the thicker laser light sheet decreases the number of out-of-plane loss particle pairs. The performance of different

kinds of PIV multiphase measurement methods was compared in their study. Satisfactory results were gained with laser light illumination. When a back lighting was used, the measurement volume became too opaque to detect the bubble shadows from the background noise. The contrast between bubble shadows and the background of the image was too low. The back lighting method gave precise estimates of bubble sizes and shapes, but it was not appropriate for long optical paths with high concentrations of bubbles. The background noise in the bubble images could be minimized with a 2-dimensional median filter or with a levelization procedure, and a digital mask was used to block the light reflected from surfaces.

Noguchi et al. (2003) applied PIV measurements and visualization by LIF (Laser Induced Fluorescence) to a sink vortex of water, with a free surface, produced in a cylindrical tank rotating about the vertical axis. The controlling parameters were the rotating rate of the tank and the volume flux of a water withdrawn from a hole on the bottom of the tank, located at the center. They found that a Rankine-like vortex was produced in the steady state when the volume flux of water withdrawn from the hole was 150 cm^3/s. When the volume flux was 50 cm^3/s, however, the conservation of the angular momentum around the central axis of the vortex was not established. They injected a fluorescence dye (rhodamine B) at the periphery of the cylindrical tank and discovered that the water introduced at the periphery of the tank descended to the bottom, along the side wall, and flowed to the center of the tank in the boundary layer at the bottom of the tank. However, the dye ascended in a thin vertical layer around the core of the vortex suggesting that the upward flow was formed around the sink vortex. When they reduced the rate of rotation of the tank from 0.4 rad/s to 0.2 rad/s, while keeping the

withdrawal rate of the water (to maintain a vortex), they observed horizontal plumes appearing near the side wall due to inertial instability. At the same time ring-shaped disturbances developed in the interior region.

2.4 Summary and Thesis Objectives

The two-phase flow modeling at header-branch junctions is characterized by the critical heights at the onset of two-phase H_{OGE} and H_{OLE}, respectively. Previous studies have demonstrated three models for predicting H_{OGE} in a single discharging branch. The first is an empirical model, and it depends on the liquid and gas densities, the two-phase reservoir geometry, and the branch orientation. The second model is based on the point-sink assumption and it predicts well the H_{OGE} at high Froude numbers. The point-sink model failed to approach the lower physical limit at low Froude numbers. The third is the finite-branch model which could predict the H_{OGE} at high Froude numbers, and approaches the physical limit at low Froude numbers. However, the prediction at low Froude numbers was not satisfactory, due to neglecting the surface tension effect.

The experimental work in literature ranged from studying single to dual discharge and triple discharge. The developed correlations could predict the quality and two-phase mass flow rate over a range of Froude numbers and geometrical conditions. It is evident from the literature review that the gravitational forces are the most dominant in the discharging process, followed by the inertial forces and then the viscous forces. Including the surface tension force in modeling, especially at low discharging flow rate is important. Flow structure in two-phase flow process changes according to the configuration of the discharging vessel, the type of flow (single or dual or triple discharge) and velocity through branches. The previous studies did not provide any

measurements of the flow structures, such as vorticity profiles, stream lines, flow field development and coherent structure, at the onset of gas entrainment. This is essential in understanding the related two-phase flow phenomena and is required for the validation of the two-phase discharge models.

The main objectives of this research work are to bridge the gap in knowledge of two-phase flow structure and regimes in two-phase headers, and to provide information that supports the designers of two-phase header-channel systems. Comprehensive experimental and numerical research programs are developed through this thesis. The Particle Image Velocimetry is used to provide the flow details within a three-dimensional volume. The specific objectives are:

- To design and construct a PIV flow facility to provide detailed measurements of the flow field inside two-phase headers with multiple branches.

- To obtain experimental data for the mean velocity, flow field development and vorticity field in the near region of header-channel junctions, during single, dual, and triple discharge from a large stratified region through branches mounted on a semi-circular wall, over different flow conditions.

- To perform a visual "quantitative" study of the different flow phenomena (e.g., the onset of gas entrainment) that may occur during single, dual, and triple two-phase discharge from a stratified region. Different branch orientations will be tested.

- To develop appropriate analytical models and correlations to estimate the observed flow phenomena of the tested cases, as a function of Weber number, Froude number, and geometric parameters.
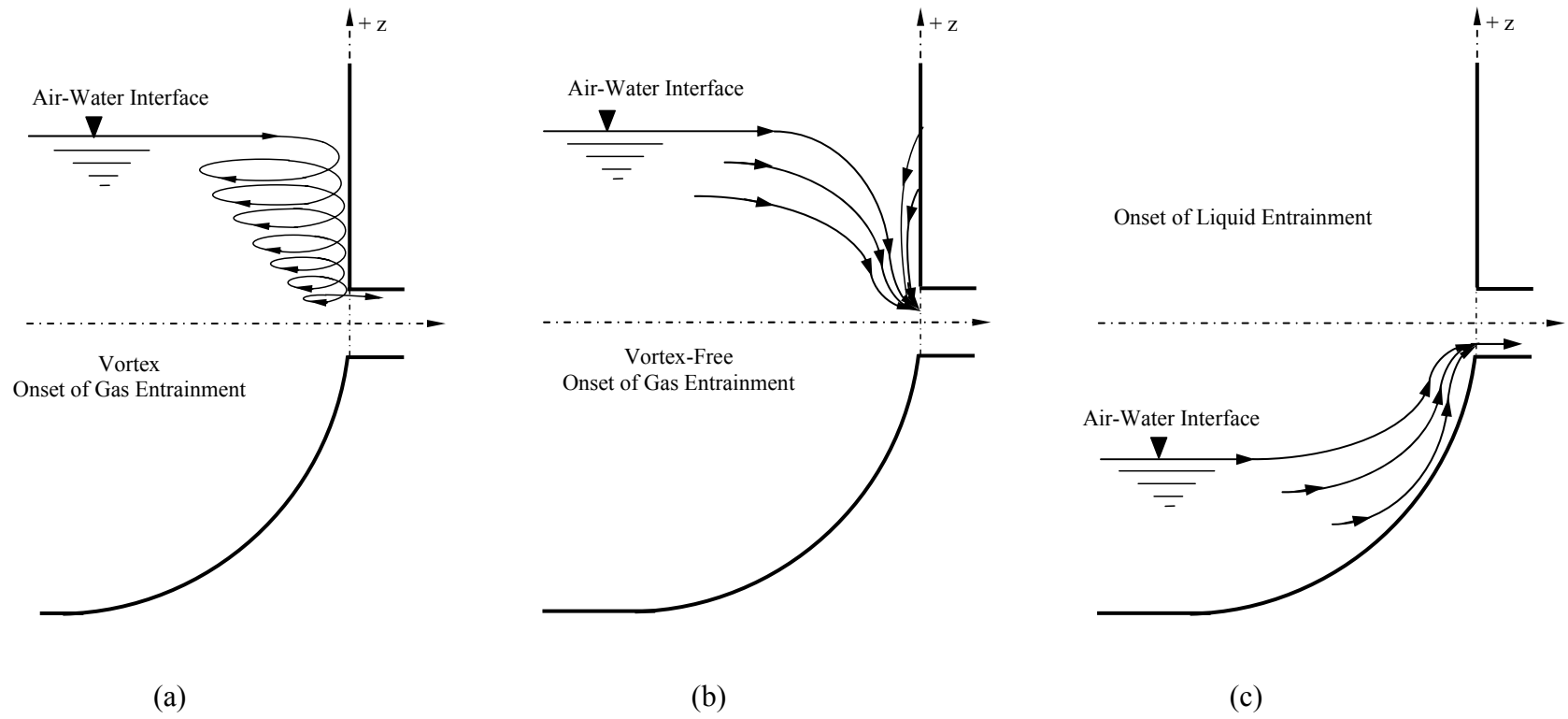
Figure 2.1 Schematic diagrams for onset of gas and liquid entrainment.

(a) Vortex OGE, (b) Vortex-Free OGE, and (c) OLE.

Chapter 3

Experimental Investigations

A typical CANDU header has a circular cross section and measures approximately 6 meters in length, and between 0.36 and 0.41 meters in I.D, and is closed on both ends. Flow enters the top of the header through a number of orifices called turrets, and exits through a network of feeder banks. Each feeder bank contains five 50.8 mm openings located at radial positions of 0°, 45°, 90°, 135° and 180° from the horizontal axis. Hassan et al. (1997) obtained experimental data for the mass flow rate and quality during single, dual and triple discharge from a stratified air-water region through small side branches installed on a semicircular wall. Then they reported that the flow out of the bottom branch C was found to be essentially independent of whether or not there was flow out of the side branch A and the 45° branch B within the tested range. Therefore, it is unlikely that the two missing branches from a full circular section would affect the results of branch C. As well, the two missing branches would likely have been too far from branches A and B to cause significant effect there. As a result, the data from their test section should be representative of those for full-header geometry. Therefore, the geometry used to simulate a typical CANDU header-feeder system by Ahmad and Hassan (2006) has a semi-circular cross section with branches located at 0°, 45° and 90° from the horizontal axis, which are referred to as branches A, B and C, respectively.

3.1 Two-Phase Flow Test Tacility

A schematic diagram for the test section used is shown in Figure 3.1(a). Also Figure 3.1(b) shows the test section installed in the two-phase test facility. It was

designed to optimize optical access from multiple views, while maintaining the required geometry.   It was manufactured from a solid piece of clear cast acrylic. Three 6.35 mm diameter holes were drilled into the quarter-circle surface at 0°, 45° and 90° and extended until a minimum of four diameters and then enlarged to 9.56 mm. The difference between this acrylic test section and the brass test section which used by Ahmad and Hassan (2006), is that the top quarter of the semi-circular cross section was replaced by a flat vertical wall. The acrylic test section was validated by comparing the critical heights obtained by Ahmad and Hassan (2006) with the brass test section. Figure 3.2 shows a schematic diagram of the acrylic test section with one of the investigated planes.

The test facility is shown in Figures 3.3 and 3.4. Ahmad and Hassan (2006) established the test facility at Concordia University in Montreal, Canada. The two-phase reservoir was made from two stainless steel pipes welded together in a T-shape; flanges were welded onto the three ends. The bottom flange was capped with a stainless steel cover equipped with two drilled holes. One of these holes was used to supply water to the two-phase reservoir; while the other hole was used to drain the tank. One of the vertical flanges was capped with an aluminum cover with a circular Plexiglas window with a height of 10 cm. On the third flanged end, a clear acrylic tube was fastened and its open end capped with a stainless steel cover. The test section was installed through a hole machined at the center of this cover. The test section was bolted to the cover and an O-ring provided adequate sealing. The three test section discharges, branches *A*, *B*, and *C*, were controlled by downstream ball valves installed at their outlets. Downstream of the ball valve, each discharge was connected to a flow meter that was regulated with an inline needle valve. Four water flow meters, with overlapping flow rates up to a

maximum of 75 L/min, were used. The flow meters were selected to provide different orders of magnitude of the discharge Froude number ($0.001 \leq Fr \leq 60$). Regulated air was supplied to the two-phase reservoir by a Fisher Pressure Controller. The discharge air was released to atmosphere downstream of the flow meters. The air pressure in the two-phase reservoir was monitored by a Rosemount LCD pressure transducer with a factory calibrated range of 0-830 kPa. Water was stored in a 208 L tank and supplied to the two-phase reservoir by a 3 hp SSV 8-stage vertical pump. The discharged water downstream of the flow meters was circulated back to the tank. The water height was measured by a Rosemount LCD differential pressure transducer with a factory calibrated range of zero to 255 mm H_2O. Plumbing between the two-phase reservoir and all other devices – which include the pump, pressure regulator, pressure transducer, differential pressure transducer and flow meters – was established using flexible PVC tubing. The hydraulic resistance of tubing and valves downstream of the test section was equal for each branch.

3.2 Stereoscopic PIV System

The particle image velocimetry (PIV) has been thoroughly discussed (Willert and Gharib, 1991; Raffel et al., 1998; Adrian, 2005). It is a non-intrusive flow mapping technique that uses particles immersed in the fluid to enable flow tracking. The medium is seeded with tracer particles that are sufficiently small to follow the flow closely. The basic components needed are a digital camera to capture the particle displacement and a light source to illuminate the particles at two distinct instants in time. Quantitative information on the velocity field can be extracted from the image sequence. In PIV, the displacement of particle patterns between subsequent images is determined. For this

purpose the recorded images are divided into rectangular sections, called interrogation areas. The displacement is found by cross correlation of corresponding interrogation areas in two subsequent recordings. Maximum correlation occurs when the particle image patterns match best. This results in the average displacement within one interrogation area, (Δx, and Δy). Since the time Δt between two subsequent recordings is known, the velocity per interrogation area is found. Advanced PIV codes use iterative methods to improve the accuracy by pre-shifting the interrogation areas with the displacement from a previous PIV computation.

Earlier PIV systems were developed to provide planar, two-component, fluid velocity measurements but more recent advances using two-camera systems have produced planar three-component velocity fields (Prasad, 2000). This three-component technique is commonly referred to as stereoscopic PIV (3d-PIV) and it has been used successfully to record velocity fields in single liquid phase systems (Zhang and Hugo, 2006) or even two-phase systems (Hassan et al., 2001). In stereoscopic PIV, two cameras record the same area from a different point of view, as shown in Figure 3.5. The third velocity component can be extracted from the information of two cameras. For each vector in a 3D vector map, the three true displacements (ΔX, ΔY, ΔZ) are reconstructed from the corresponding two dimensional displacements (Δx, Δy) from both cameras. A drawback of this setup is the mismatch between the best plane of focus, which is parallel to the image plane (CCD), and the object plane (laser sheet). A complete focus of the object plane can be achieved when the image plane is tilted relative to the lens such that the object plane, the plane of the imaging lens and the image plane intersect at one common line. This so called Scheimpflug arrangement is visualized in Figure 3.6.

25

Another disadvantage is the perspective distortion, reducing the field of view when the images from both cameras are combined. In order to enable the computation of the velocity field, it is necessary to determine how coordinates from the object plane are imaged onto the CCD plane. This is achieved by a calibration procedure in which images of a well-defined calibration grid are taken with both cameras at multiple heights. Comparing known marker positions with corresponding marker positions on each camera image, model parameters are adjusted to give the best possible fit.

3.2.1 System Specifications

A commercial stereoscopic PIV system, by Dantec Dynamics, was used. The basic components of the system are also shown in Figure 3.3. It consisted of a New Wave Research Solo XT 120 Nd:YAG dual cavity pulsed laser with a 532 *nm* wavelength that was capable of achieving 120 mJ/pulse at an approximate pulse rate of 15 Hz. Light sheet optics converted the single beam output into a light sheet of variable thickness. Two HiSense MkII 12 bit digital output CCD cameras, of 1344 x 1024 pixel resolution, were installed on two precision camera mounts. A maximum image pair capture rate of 5.67 Hz could be achieved with the system. A Nikon objective lens, mounted to the camera, provided focal and illumination adjustments. A National Instruments NI-IMAQ PCI-1426 frame grabber card was used in conjunction with each camera to capture and store the images. A National Instruments NI-DAQ PCI-6601 timer board was used to synchronize the camera imaging with the laser pulses. A double layer target with calibrated dot spacing was used for spatial calibration. The commercial software, Flow Manager, provided image processing and analysis and was run on a 3.6

GHz dual processor workstation with 4 GB of RAM, a 500 GB hard disk, frame grabber, and synchronization cards.

3.2.2 System Components - Challenges and Solutions

The two-phase test facility has on its own several technical challenges and an experienced user may find measurements a daunting, and often, time consuming task. Past studies using the two-phase facility (Ahmad and Hassan, 2006; Bowden and Hassan, 2008) were solely based on qualitative flow visualization and were highly dependant on the level of experience of the experimentalist in observing the phenomena. The PIV measurements are meant to enhance the observations of the experimentalist through quantitative flow visualization by providing, for example, a description of the velocity field. The PIV measurement system has, in its own right, technical challenges. Adapting it to the two-phase apparatus merely compounded those challenges, particularly since the original design of the facility by Ahmad and Hassan (2006) was not conducted with PIV in mind. Barring a complete redesign of the two-phase facility, a costly endeavour to say the least, it was decided to adapt the PIV system to the existing facility. Some major challenges needed to be addressed before even the first image could be taken – these were directly related to the calibration target, camera, and laser placements.

Calibration Ttarget

A single sided, double layer, rectangular calibration target with a 7 by 9 dot matrix of 63 white dots on a black background, and manufactured by Dantec Dynamics, was used. The dot matrix was comprised of 62 smaller 3 mm diameter dots with a single 5 mm dot located at the center. The dot matrix was located on a 7.5 mm x 9.5 mm aluminum plate, painted black, with 2 mm spacing between top and bottom layers. The

calibration target definition was included in the Flow Manager library as part of the Image Model Fit (IMF) algorithm, described later in Sec. 3.3.2.

Two key factors were used to determine the placement of the calibration target, the desired imaging planes and their position relative to the test section. To determine the imaging planes some knowledge of the flow phenomena, as well as expectations of the desired results, was needed. In their earlier work Bowden and Hassan (2007) had demonstrated, using 2D-PIV, horizontal image planes could be used to characterize the onset of gas entrainment flow field. The vertical image planes they investigated did pose an inherent problem with light reflections, on solid surfaces and the air-water interface, causing some distortion and loss of image quality. It was determined, based on their study, that horizontal image planes would be the best candidate. The calibration target dot matrix aligns with the desired image planes thereby requiring horizontal placement of the target.

With a well defined dot matrix it was necessary to locate the calibration target at a known position relative to the test section. Doing so later enabled a correlation between the image plane and the actual position of the plane in the flow field. A convenient choice was to align the center of the 5 mm dot – the larger central dot - vertically with the center of branch *C*. This allowed a known location within the dot matrix to be correlated with a known location on the test section – the image planes could thereby be correlated to known planes in the flow field. The final challenge was to establish a method to traverse the horizontally oriented calibration target vertically through the flow field, effectively scanning the desired volume at discrete vertical intervals. Size constraints prevented the calibration target from being aligned with the desired image plane while

the test section was installed. If the calibration target had been smaller the curved test section wall would have still restricted the traversing range – some interference between the target and wall would have ultimately occurred at some vertical position. The most feasible option was to install the target in the facility, still maintaining a known position, and removing the test section during the calibration procedure. This also relaxed some size restrictions on selecting, or designing, a suitable traversing mechanism.

A simple vertical traverse was designed and built; a schematic is shown in Figure 3.7. The entire traversing mechanism is small enough to fit through the 100 mm hole in the blind flange, where the test section is normally installed, and large enough to provide a span of 70 mm in vertical displacement to the calibration target – the total volume of interest is only 50.8 mm high for the entire test section. Its simple design is easy to use and allows the planes of interest to be traversed in a matter of minutes during experimentation. The design consists of a flat platform that rests horizontally on the interior wall of the cast clear acrylic tube. A threaded hole was machined into the center of the platform. A 70 mm long threaded rod, with a thread pitch of 1.0 mm, was attached to the bottom of the target and then threaded into the platform hole, a locking nut was used to secure its position. Rotating the target a full turn resulted in a 1.0 mm vertical displacement and a half turn a 0.5 mm displacement. Since only full or half turns could be measured accurately (no angular scale was used to determine fractions of turns) at this traversing resolution up to 100 individual image planes could be selected.

The calibration target was aligned with the horizontal image plane and the light sheet, in turn, was aligned with the calibration target. A horizontal light sheet was therefore required. The calibration target dot matrix faced upwards since the test section

would obstruct the view from below. The cameras were therefore oriented with their field of view looking down at the light sheet from above. While necessary, these conditions were not sufficient to determine the final laser and camera placements.

Camera and Laser

With the desired imaging plane orientation established the location of the two cameras, and laser, needed to be determined. Since the test section was contained within a closed reservoir, optical access to the measurement volume was achieved through the cast clear acrylic tube. As a result, reflected light from illuminated particles must pass through a curved surface, 12.7 mm thick. It was also evident that the clear acrylic tube was not entirely optically homogeneous and imperfections were suspected to be due to the casting process used in manufacturing. All these factors were expected to have an effect on the image quality and would contribute to the uncertainty of the measurement in the form of optical refractions and reflections. To address these unknowns it was first considered to replace the circular cross-sectional acrylic tube with a square cross-sectional tube. The reasoning for this was to remove the acrylic tube wall curvature as a factor. It was concluded that this design change would result in several other concerns dealing with safety (due to the operating pressure), manufacturability (lack of availability in the marketplace), and optical uncertainty (increased wall thickness and degradation of material optical homogeneity). This design change was not pursued for these reasons.

A second approach to deal with the cast clear acrylic tube wall curvature was to consider refractive index matching. This technique required a second external reservoir to be constructed on the exterior of the cast acrylic tube. The second external reservoir would have a flat exterior wall made from the same cast acrylic as the curved wall and

the space between the two walls filled with a fluid of similar refractive index as the cast acrylic (refractive index of 1.49). This approach was pursued since it did address reducing the wall curvature effect while not adding any additional concerns with regards to safety, and manufacturability. A reservoir was constructed onto one exterior side of the cast clear acrylic tube, as shown in Figure 3.8, and the space between the two walls filled with water (refractive index of 1.33). With the two-phase reservoir filled with water, the optical path to the measurement volume was visibly improved.

The refractive index matching technique was used by aligning the horizontal light sheet such that it passed perpendicularly through the flat vertical exterior reservoir wall. The cameras were installed above the test section, as shown in Figure 3.8, on a support structure. The design of the support structure was based on aligning the camera axes perpendicularly with the cast acrylic tube exterior surface. In their study, Bowden and Hassan (2007) also aligned the single camera axis vertically, with the field of view looking down on the light sheet. With 3D-PIV the two cameras are mounted in the same plane with their CCD axes (line passing through and parallel to the CCD chip) generally aligned at 90 degrees to each other. After some testing it was observed that the arrangement of cameras and laser, as shown in Figure 3.8, did not provide quality images of illuminated particles in both cameras. Images taken using the camera facing toward the incoming laser light sheet (camera 2) were of good quality and the particles were brightly illuminated, adequately sized, and focused in the image. Images taken using the camera facing away from the incoming light sheet (camera 1), however, were of poor quality with particles being dimly lit and blurry. This difference between images taken with the two cameras was a result of the light scattering modes. The camera facing the

31

incoming light source viewed forward scattered light while the away facing camera viewed back scattered light. The light scattering oversight was corrected by placing the light sheet such that both cameras captured images of forward scattered light. The result was the setup shown in Figure 3.3 with the light sheet entering the two-phase reservoir through the left side flange. This enabled both cameras to capture images of forward scattered light and was a significant improvement to image quality.

3.3 Experimental Procedures

3.3.1 Onset of Gas Entrainment

The procedure for recording the critical height, at the onset of vortex-free gas entrainment (OGE), using air and water as the two fluids, was as follows. Water was first pumped into the two-phase reservoir until the height of the air-water interface was sufficiently above the discharge branch inlet. Typically, this starting liquid height was around 45 mm above the discharge inlet. The objective of positioning the air-water interface was to ensure initial single phase liquid flow when the discharge was activated. The two-phase reservoir was then pressurized to approximately 206 kPa. The valve downstream of the discharge was then opened, thereby activating it, and the discharge flow rate was adjusted to the desired value using the rotameter. The water level in the reservoir was then slowly decreased, at a rate of approximately 1 mm per minute to achieve the steady state condition (this was achieved by observing the reservoir water level transducer reading over time), until the onset of vortex-free gas entrainment occurred in the discharge branch, at which point the critical liquid height (H_{OGE}) was recorded using the differential pressure gauge. From flow visualization, OGE was defined when a gas tube extended from the interface to the discharge branch inlet, and

gas steadily entrained into the branch. The OGE was considered steady when the gas tube tip did not oscillate between the discharge inlet and the interface. This criterion was important to discern between vortex induced, where gas entrainment was unsteady, and vortex-free gas entrainment, where gas entrainment was relatively stable. The water level was then maintained steady by approximately matching the reservoir's inlet flow rate (adjusting pump flow) and the discharge's flow rate (set using the rotameter).

3.3.2 PIV Calibration

With the critical height recorded, the volume of interest, for a single discharge flow rate, could be determined. The volume of interest extends vertically from the bottom of the test section to the air-water interface and extends horizontally to the edges of the test section. The size of the volume of interest is needed first in order to determine the number and location of the horizontal image planes. A sample image of the OGE phenomena and volume of interest, captured as an elevation view, is shown in Figure 3.9. The OGE is in the side branch A with the volume of interest discretized into six horizontal image planes. Each image plane required a separate spatial and temporal calibration for PIV measurements.

Spatial calibration was done in a methodical step-by-step process. With the test section removed, the calibration target height was adjusted such that the dot matrix was aligned with the desired horizontal image plane. The water level within the two-phase reservoir was then increased until it coincided with the previously determined critical height (H_{OGE}). The cameras were then positioned such that their lines of sight were directed towards the target and with their axes displaced by approximately 45 degrees. Due to the perspective distortion, only a portion of each image overlapped in the two

fields of view, this overlapping area defined the final combined field of view. The Flow Manager software provided a real-time grey scale histogram of each image and was also used to achieve an optimal calibration image. An optimal histogram presented two distinct peaks at extreme ends of the grey scale spectrum indicating the white and black colors on the calibration target surface. The histogram was also highly influenced by external light sources since shadows, produced by the air-water interface on the target surface, skewed the contrast between the white dots and the black background. To address this issue local lighting was used to illuminate the calibration target surface, external sources such as room lights were shut off during this process.

Two images of the calibration target, one taken from each camera, were then captured. Using the Image Model Fit (IMF) algorithm (Flow Manager) the original image captured from each camera was then converted to a binary black and white image. In the black and white image, neighboring pixels of identical color were grouped as objects – for example each dot corresponded to an object. The area and centroid position of each object was then calculated by the software, objects with areas below a minimum specified value, or touching the image boundary, were discarded as high-frequency noise. The IMF algorithm then proceeded to recognize valid objects, or dots, from a library of standard calibration target values. This procedure resulted in grid, for each image, that corresponded to the relative size and orientation of the calibration target dot matrix. In many instances the dot matrix was not recognized in the final grid and minor adjustments to lighting or image focus needed to be done. The image was then said to be spatially calibrated. The light sheet was aligned with the dot matrix and then the calibration target was removed from the two-phase reservoir. The dot matrix's central 5 mm dot was

vertically aligned with branch C's centerline then the origin (x = 0, y = 0, z = 0) of the coordinate system was transferred using simple geometrical relations, for each image plane, to the center of branch A inlet, as shown in Figure 3.10.

A temporal calibration process was also required to match the fluid speed with the laser pulse and image capture timing. The dual cavity laser delivers two pulses, with as low as 1 μs time interval between pulses, which are synchronized with each image pair. Two sequential images per camera are needed to produce a single vector field and these two images are referred to as the image pair. The pulse timing, dt, is the time interval between these two images. The pulse timing was estimated based on an expected range of flow speed and interrogation area size and was determined by trial and error for each experimental setup (flow conditions, imaging plane). Using 20 μm mean diameter polyamide (PSP-20) tracer particles which are nearly neutrally buoyant (density of 1030 kg/m^3) in water (density of 999 kg/m^3), images of the flow field, from each camera, were captured. A sample of the PIV images in plane #3, captured from each camera, is shown in Figure 3.11. The images were captured after having first achieved the desired flow conditions at OGE by following the procedure outlined in Sec. 3.3.1. Temporal calibration was achieved by verifying that particle displacement did not exceed 25% of the interrogation areas through visual inspection. This process was iterated by adjusting the pulse timing, dt, until a satisfactory particle displacement was achieved. The pulse timing used for each setup is presented in Table 3.1.

3.4 Data Reduction

With both spatial and temporal calibration established the systems were then said to be appropriately setup to conduct measurements. The data set size, or number of

image pairs, supported by the PIV system could reach up to 150 per experimental run – this number was dependant on the available computer memory. The post processing of images to produce vector maps was handled by the software provided by the manufacturer, Flow Manager. The software was capable of a variety of correlation techniques, which may be selected by the user, and include cross-correlation, auto-correlation, adaptive correlation, and average correlation. Adaptive correlation provided increased dynamic range and was used for data processing. The interrogation area can be adjusted by the user anywhere from 8 x 8 pixels up to 256 x 256 pixels. The accepted standard peak validation of 1.2 was also used in the correlation method. A 3 by 3 pixel moving average filter was used to replace spurious vectors by a locally averaged value of neighboring vectors.

3.5 Experimental Uncertainty

The two fluids used were air and water at an operating pressure of approximately 206 kPa and experiments were conducted at room temperature. All measurement devices were calibrated by the manufacturer as per component specifications. The maximum uncertainty in the calculation of the Froude number was found to be ± 5%. The instrument uncertainty in measuring the two-phase reservoir static pressure was ± 0.83 kPa of which an acceptable range during experimentation was 206 ± 6.8 kPa. The instrument uncertainty in measuring the height of water, H, in the reservoir was found to be ± 0.17 mm H_2O. In Sec. 3.6, a detailed description of the PIV error analysis was provided. Experiments were conducted (for PIV error analysis) for three separate discharge Froude numbers, namely, Fr = 3.48 (low), 10.56 (medium), and 31.69 (high) which resulted in recorded critical height values of H_{OGE} = 30.5 mm, 34.4 mm, and 39.7

mm, respectively. The volume of interest was divided into four, five, or six, horizontal image planes for the low, medium, and high discharge Froude numbers, respectively. The location of each image plane, total number of vectors in each image plane, and the number of image pairs recorded, are shown in Table 3.1.

The critical height at the onset of vortex-free gas entrainment, in branch *A*, was investigated for three discharge Froude numbers. The flow field was recorded using stereoscopic PIV. A sample image recorded from each camera in plane # 6, for the high (*Fr* = 31.69) discharge Froude number, was presented in Figure 3.11. The resulting instantaneous velocity field for each image was found using the adaptive correlation technique, a sample was presented for *Fr* = 31.69 in Figure 3.12. Using the 3D vector statistics algorithm from Flow Manager, the resulting instantaneous 3D velocity field, from the two planar vector fields in Figure 3.12, are shown in Figure 3.13. The resulting flow field shows the bulk flow to be approaching the discharge inlet at the origin of the coordinate system (0, 0, 0) as might be expected. The vortex-free OGE is generally accepted in the literature as a steady-state phenomenon, which implies that a single instantaneous velocity field, at each plane, is sufficient. By selecting five random locations, in each image plane, the number of images required to describe the steady-state was investigated. These locations are shown in Figure 3.10, relative to the original coordinate system, at planar (x, y) locations (0, -25), (12, -25), (-12, -25), (0, -13), and (0,-37) with dimensions in mm. The instantaneous velocity components (*u*, *v*, *w*), recorded at these points, were used to calculate the time averaged velocities for a set of sequential images – the number of which could not exceed 150 image pairs. The time averaged velocity, V_N, after N number of image pairs, *i*, was calculated as,

$$V_N = \frac{\sum_{i=1}^{N} V_i}{N}.$$
(3-1)

A sample of the time averaged velocity at point (0, -13) was shown in Figure 3.14 (a) and selected velocity components at several points in Figure 3.14(b). The total velocity, determined as the square-root of the sum-of-squares of individual velocity components, was also included in Figure 3.14(a). It was found that at least 50 images were needed to achieve no more than 3% deviation in V_N for the five points considered over the range of Froude numbers and investigated planes in Table 3.1. This number was used as the minimum number of image pairs used to calculate the temporally averaged 3D vector field, a sample of which is shown in Figure 3.15.

The Cartesian coordinates (x, y, z) and velocity components (u, v, w) in the temporally averaged vector field were converted into cylindrical coordinates (r, θ, z) and velocity components (V_r, V_t, V_z) using trigonometric relations. The flow field is expected to be strongly dependant on the radial dimension, r, as was previously discussed by Bowden and Hassan (2007). The velocity profiles were extracted from the temporally averaged 3D vector fields by averaging the velocity at constant radial distances. A sample of the velocity profiles resulting from this method is shown in Figure 3.16 for *Fr* = 31.69 and three out of the six investigated planes. The average radial (V_r), tangential (V_t) and vertical (V_z) velocities are shown in Figures 3.16(a), (b), and (c), respectively. These figures demonstrate that the radial velocity has the strongest contribution to the total velocity profile and is corroborated by Bowden and Hassan (2007). The magnitude of the radial velocity is shown to be greatly dependant on the radial distance, r. The tangential and vertical components are weakly related to the radial distance.

3.6 PIV Error Analysis

Before estimating the error in the present complex flow field study a Poiseuille flow experiment was constructed to test the methodology. A steady water flow rate through a circular tube in the turbulent regime was achieved and flow rate was measured using a rotameter. Velocity fields were recorded using PIV within the fully developed region. The flow rate was calculated using the PIV data through conservation of mass, and then compared with the rotameter reading. The experiment was repeated for several Renolds numbers, based on the pipe diameter, and the maximum error was estimated to be ± 3% of the flow meter reading.

In their study Bowden and Hassan (2007) had developed a method to determine the error of their 2D-PIV measurements. The basis of this method was to compare the recorded rotameter flow rate with their calculated flow rate using the PIV data and a control volume conservation of mass approach. A similar approach control volume conservation of mass approach is used here to determine the relative error of the 3D-PIV measurements.

A semi-cylindrical control volume, intersecting the test section wall, was developed as shown in Figure 3.17. The entire control volume was divided into horizontal elemental volumes. The number of horizontal element volumes coincided with the number of investigated PIV measurement planes – in the figure six elemental volumes are shown. The flow rate entering the control volume elements were calculated by considering the flow rates through each of the four control surfaces, as shown in Figure 3.17. For centrally located elemental volumes, such as Nos. 2, 3, 4, and 5, there was no contribution through the top and bottom control surfaces – all flow into these

39

volumes were through the curved lateral surface. The flow rate, $Q_{j,R}$, of elemental volume, j, into the lateral curved surfaces at radius, R, were calculated as,

$$Q_{j,R} = Vr_{j,R} \left(2\,\delta\,R\,dz \right).$$
(3-2)

Where the radial elemental velocities, $Vr_{j,R,\theta i}$, enter through the lateral elemental surface of area $\left(2\,\delta\,R\,dz \right)$. The angle, δ, is the intersecting angle between the control volume and the test section surface and the element height is dz. The average elemental radial velocity, $Vr_{j,R}$, was found as the average value of the whole radial elemental velocities at the same radius, R.

$$V_{r_{j,R}} = \frac{\sum\limits_{i=1}^{i=n} V_{r_{j,R,\theta_i}}}{n}.$$
(3-3)

For the top and bottom elemental control volumes (#'s 1 and 6) the vertical flow rate is calculated as,

$$Q_{j,z} = \sum\limits_{r=1+\frac{dr}{2}}^{R-\frac{dr}{2}} V_{z_{j,r}} \left(2\,\delta\,r\,dr \right).$$
(3-4)

Where the vertical elemental velocities, $V_{z_{j,r,\theta i}}$, enter through the horizontal annular elemental surface of area $\left(2\,\delta\,r\,dr \right)$ with the width of dr. The average vertical elemental velocity, $V_{z_{j,r}}$, was found as the average value of the whole vertical elemental velocities at the same annular elemental surface of area $\left(2\,\delta\,r\,dr \right)$.

$$Vz_{j,r} = \frac{\sum\limits_{i=1}^{i=n} Vz_{j,r,\theta_i}}{n}.$$
(3-5)

The outer radius of the control volume was at a distance R. The total flow rate, Q_R, entering the control volume of radius R was calculated as,

$$Q_R = \sum_{j=1}^{6} Q_{j,R} + \sum_{j=1\&6} Q_{j,z} \, . \tag{3-6}$$

The flow rates recorded from the rotameter, Q_m, were 15 L/min, 5 L/min, and 1.65 L/min for discharge Froude numbers of Fr = 31.69, 10.56, and 3.45, respectively with a maximum uncertainty in the calculation of the Froude number was found to be $\pm$ 5%. The relative error was found by comparing the flow rates between the rotameter and the control volume analysis as,

$$Error \, (\%) = \left| \frac{Q_m - Q_R}{Q_m} \right| \times 100 \, . \tag{3-7}$$

The resulting error calculated from Eq. (3-7) for the three discharge Froude numbers is shown in Figure 3.18(a). The error is shown to increase dramatically as the control volume radius, R, decreases. This trend is similar to that reported by Bowden and Hassan (2007) for a bottom discharge. It was speculated to be due the two-phase flow structure – the cone of air – that forms at OGE at low values of R and also due to the decrease in the number of velocity vectors which contribute in calculating the volume flow rate. The air cone could likely obstruct the path of reflected light from the particles and the air cone itself represents a void of particles. This reasoning helps to explain why at the high Froude number, where the air cone was observed to be largest, the error was also the highest (in the range of R < 15 mm). On the other range of R > 15, where the

number of velocity vectors is greater in high Froude number than in low Froude number which causes the error in the latter to be higher than the former.

To test the control volume approach, the contribution of each elemental volume flow rate to the total volume flow rate, Q_T, was presented in Figure 3.18(b). The total flow rate is Q_R at a constant control volume radius, R, the figure presents results for $R = 10, 15, 20,$ and 25 mm The accumulated volume flow rate, Q_{acc}, is the sum of the flow rates from contributing elemental volumes calculated as,

$$Q_{acc,N} = \sum_{j=1}^{N} Q_{j,R} \, . \tag{3-8}$$

For example, if the number of planes used to calculate Q_{acc} is one ($N = 1$) then $Q_{1,acc} = Q_{1,R}$ or simply volume #1 is Q_{acc}. Similarly, if the number of planes is five ($N = 5$) then $Q_{5,acc} = Q_{1,R} + Q_{2,R} + \ldots + Q_{5,R}$. This means is that the contribution from each elemental volume is not even over the entire control volume – an even distribution would have produced lines oriented at 45 degrees up from horizontal. This figure further shows that the flow rate in volumes #2 and #3 yield the highest contribution to the flow rate which is sensible since these are closest to the discharging branch. Increasing the number of investigated planes, particularly in the volumes closest to the discharge branch, could be expected to improve the represented distribution of flow rates. This would lead to an improvement in the calculated error due to an improved representation of the velocity distribution.

The number of vectors used to determine that average velocity components, at a particular radius, will also influence the control volume's reliability. A sample of the functional relationship between the control volume radius and the number of vectors

found at this radius is presented in Figure 3.19(a). The relationship between the calculated error and the number of vectors is presented in Figure 3.19(b). It is obvious from these figures that the calculated error is highly dependant on the number of vectors used to calculate the volume flow rate for a particular control volume radius. As the control volume shrinks in size the number of vectors dramatically decreases while the error increases. A straightforward conclusion from this is to say that to improve the error at low radii, in the region near the OGE air cone, the number of vectors should be increased. Since the camera's CCD chip has fixed dimensions, in both physical size and number of pixels, one possible solution could be to reduce the physical area in the camera's field of view to improve the image resolution (pixels/mm).

The numbers of vectors along a particular radius are directly related to the method used to find valid vectors. An algorithm had been developed to search the temporally averaged 3D vector fields, which is on a rectangular grid, for valid vectors at a given radius. At any given radius, r, an area of width dr through an angle $d\theta$, as shown in Figure 3.17, was used to find the valid vectors. The size of dr did have an influence on the number of valid vectors found: too small causes little or no vectors to be found, too large and the velocity distributions are inaccurate. It was therefore important to find an optimal size of dr. To test the efficiency of the optimization used in the search algorithm, the effect of the grid spacing size was tested. The effect of the angle was also tested by subdividing the full angle 2δ into smaller sectors of angle $d\theta$ in Figure 3.17, and resulted in an annular sector element. The range of values of dr and $d\theta$ tested are shown in Table 3-2. There was very little improvement in the calculated error with decreasing the sizes of dr or $d\theta$, a sample of these results is presented in Figure 3.20 (a). The time interval, dt,

between image pairs will also influence the error, it's effects were investigated and a sample is presented in Figure 3.20(b). It is apparent that the time interval will drastically affect the relative error. The highest error is shown to be related to the highest time interval, $dt = 30 \times 10^{-6}$ s, and is more than likely due to the increased particle displacement within interrogation areas. This increased displacement could result in out-of-plane particle motions which lead to erroneous vectors within these interrogation areas. Testing the smallest scales to ensure accurate results is not new. In computational fluid dynamics, these tests are typically done to ensure grid independent solutions with the grids being related to both space (dr, $d\theta$, dz) and time (dt).

3.7 Summary and Test Matrix

The main objective of these experimental trails was to provide an assessment of using stereoscopic PIV to measure the liquid side flow field at the onset of gas entrainment. The investigation was conducted with three discharge Froude numbers with each resulting in their own critical value of liquid height where onset occurred. The volumes of interest were divided into horizontal planes where PIV measurements were conducted. A thorough discussion of the techniques used to adapt the PIV system to the established two-phase experiment was provided. Many challenges associated with the spatial and temporal calibrations were found and the practical solutions used to address them were discussed in detail. The measurements showed a highly radial flow field, directed towards the discharge center, which was used to devise an appropriate control volume conservation of mass approach to estimate the relative error of the PIV measurements. The relative error was determined based on comparing the flow rate measured from the rotameter with that calculated from the control volume approach. A

high error was found in the region near the discharge branch and was found to decrease with an increase in the radial distance from the branch center. This lead to an analysis of the control volume methodology which found in this region a very small number of vectors were being used to calculate the volume flow rate, and consequently the error. The control volume approach was also tested for grid independence, both spatially and temporally, and showed little improvement in the error by changing the element size. A drastic change, however, was observed by modifying the time interval between image pairs – increasing the time interval resulted in an increase in relative error. The effect of the number of planes and the repeatability were estimated by repeating the high and medium Froude number experiments for the side branch with more investigated planes Table 3-3 and Table 3-4. Then the study extended to include the investigation of the inclined and bottom branches, *B* and *C*, in single discharge cases Table 3-5. Also the study covered the dual discharge cases *A* and *B* with high and medium Fr_A Table 3-6, dual discharge cases *A* and *C* with high and medium Fr_A Table 3-7, and triple discharge cases *A*, *B*, and *C* with high and medium Fr_A Table 3-8.

Table 3-1 Operating conditions – PIV validation.

Froude Number	H_{OGE}	Investigated plane number	Calibration Target Level	Total number of vectors	I	J	N. of images pair	dt (μs)
31.69 (High)	39.7	6	35	1804	44	41	150	2000
		5	33	1890	45	42	150	2500
		4	29	1886	46	41	150	2500
		3	25	2058	49	42	50	3000
		2	16	2100	50	42	50	4000
		1	8	2100	50	42	50	5000
10.56 (Medium)	34.4	5	32	1927	47	41	150	2500
		4	28	1968	48	41	150	5000
		3	25	1974	47	42	50	5000
		2	16	2016	48	42	50	5000
		1	8	2100	50	42	50	5000
3.48 (Low)	30.5	4	28	2100	50	42	50	5000
		3	25	2100	50	42	50	7500
		2	16	2058	49	42	50	15000
		1	8	2058	49	42	50	15000

Table 3-2 Grid independence parameters – PIV validation.

Case #	dr (mm)	$d\theta$
1	2.0	10.0
2	2.0	5.0
3	1.0	5.0
4	0.5	5.0
5	0.3	5.0
6	0.2	5.0
7	0.5	2.5
8	0.3	2.5

Table 3-3 Test matrix for single discharge, side branch at $Fr_A = 31.69$.

Case # and description	H_{OGE}	Investigated plane number	Calibration Target Level	Total number of vectors	I	J	N. of pictures pair
Case 1: OGE in branch *A*, single discharge. High Froude number in branch *A* where Fr_A equals 31.69. Flow field was investigated with 6 investigated planes.	39.7	6	35	1804	44	41	150
		5	33	1890	45	42	150
		4	29	1886	46	41	150
		3	25	2058	49	42	50
		2	16	2100	50	42	50
		1	8	2100	50	42	50
Case 1r: To check the repeatability and the effect of the number of investigated planes, case 1 was reinvestigated with 9 investigated planes.	39.7	9	36	1938	51	38	100
		8	32	1938	51	38	100
		7	28	1950	50	39	100
		6	24	2050	50	41	100
		5	20	2091	51	41	100
		4	16	1989	51	39	100
		3	12	1950	50	39	100
		2	8	1989	51	39	100
		1	4	2000	50	40	100

Table 3-4 Test matrix for single discharge, side branch at Fr_A = 10.56 and Fr_A = 3.48.

Case # and description	H_{OGE}	Investigated plane number	Calibration Target Level	Total number of vectors	I	J	N. of pictures pair
Case 2: OGE in branch *A*, single discharge. Medium Froude number in branch *A* where Fr_A equals 10.56. Flow field was investigated with 5 investigated planes.	34.4	5	32	1927	47	41	150
		4	28	1968	48	41	150
		3	25	1974	47	42	50
		2	16	2016	48	42	50
		1	8	2100	50	42	50
Case 2r: To check the repeatability and the effect of the number of investigated planes, case 2 was reinvestigated with 8 investigated planes.	34.4	8	32	1786	47	38	100
		7	28	1938	51	38	100
		6	24	2000	50	40	100
		5	20	2000	50	40	100
		4	16	1950	50	39	100
		3	12	1989	51	39	100
		2	8	1862	49	38	100
		1	4	1989	51	39	100
Case 3: OGE in branch *A*, single discharge. Low Froude number in branch *A* where Fr_A equals 3.48. Flow field was investigated with 4 investigated planes.	30.5	4	28	2100	50	42	50
		3	25	2100	50	42	50
		2	16	2058	49	42	50
		1	8	2058	49	42	50

Table 3-5 Test matrix for single discharge, inclined and bottom branches at $Fr_B = 31.69$, $Fr_B = 10.56$, $Fr_B = 3.48$, $Fr_C = 31.69$, and $Fr_C = 10.56$.

Table content:

Case # and description	H_{OGE}	Investigated plane number	Calibration Target Level	Total number of vectors	I	J	N. of pictures pair
Case 4: OGE in branch B, single discharge. High Froude number in branch B where Fr_B equals 31.69.	24.7	3	22	2009	49	41	50
		2	11	1974	47	42	50
		1	2	2100	50	42	50
Case 5: OGE in branch B, single discharge. Medium Froude number in branch B where Fr_B equals 10.56.	18.5	3	14	2214	54	41	50
		2	8	2050	50	41	50
		1	2	2050	50	41	50
Case 6: OGE in branch B, single discharge. Low Froude number in branch B where Fr_B equals 3.48.	14.5	3	12	1932	46	42	50
		2	7	2100	50	42	50
		1	3	2000	50	40	50
Case 7: OGE in branch C, single discharge. High Froude number in branch C where Fr_C equals 31.69.	22.7	3	18	1764	42	42	50
		2	10	1890	45	42	50
		1	2	2142	51	42	50
Case 8: OGE in branch C, single discharge. Medium Froude number in branch C where Fr_C equals 10.56.	13	3	10	2050	50	41	50
		2	6	2142	51	42	50
		1	2	2100	50	42	50

Table 3-6 Test matrix for dual discharge, side and inclined branches at Fr_A = 31.69 and Fr_A = 10.56.

Case # and description	H_{OGE}	Investigated plane number	Calibration Target Level	Total number of vectors	I	J	N. of pictures pair
Case 9: OGE in branch *A*, dual discharges. High Froude number in branch *A* where Fr_A equals 31.69. High Froude number in branch *B* where Fr_B equals 34.4. Flow field was investigated with 9 investigated planes.	41.02	9	36	1938	51	38	100
		8	32	1938	51	38	100
		7	28	1950	50	39	100
		6	24	2050	50	41	100
		5	20	2091	51	41	100
		4	16	1989	51	39	100
		3	12	1950	50	39	100
		2	8	1989	51	39	100
		1	4	2000	50	40	100
Case 10: OGE in branch *A*, dual discharges. Medium Froude number in branch *A* where Fr_A equals 10.56. High Froude number in branch *B* where Fr_B equals 34.4. Flow field was investigated with 8 investigated planes.	35.24	8	32	1786	47	38	100
		7	28	1938	51	38	100
		6	24	2000	50	40	100
		5	20	2000	50	40	100
		4	16	1950	50	39	100
		3	12	1989	51	39	100
		2	8	1862	49	38	100
		1	4	1989	51	39	100

Table 3-7 Test matrix for dual discharge, side and bottom branches at $Fr_A = 31.69$ and $Fr_A = 10.56$.

Case # and description	H_{OGE}	Investigated plane number	Calibration Target Level	Total number of vectors	I	J	N. of pictures pair
Case 11: OGE in branch *A*, dual discharges. High Froude number in branch *A* where Fr_A equals 31.69. High Froude number in branch *C* where Fr_C equals 34.4. Flow field was investigated with 9 investigated planes.	39.75	9	36	1938	51	38	100
		8	32	1938	51	38	100
		7	28	1950	50	39	100
		6	24	2050	50	41	100
		5	20	2091	51	41	100
		4	16	1989	51	39	100
		3	12	1950	50	39	100
		2	8	1989	51	39	100
		1	4	2000	50	40	100
Case 12: OGE in branch *A*, dual discharges. Medium Froude number in branch *A* where Fr_A equals 10.56. High Froude number in branch *C* where Fr_C equals 34.4. Flow field was investigated with 8 investigated planes.	34.16	8	32	1786	47	38	100
		7	28	1938	51	38	100
		6	24	2000	50	40	100
		5	20	2000	50	40	100
		4	16	1950	50	39	100
		3	12	1989	51	39	100
		2	8	1862	49	38	100
		1	4	1989	51	39	100

Table 3-8 Test matrix for triple discharge, side, inclined and bottom branches at $Fr_A = 31.69$ and $Fr_A = 10.56$.

Case # and description	H_{OGE}	Investigated plane number	Calibration Target Level	Total number of vectors	I	J	N. of pictures pair
Case 13: OGE in branch *A*, triple discharges. High Froude number in branch *A* where Fr_A equals 31.69. High Froude number in branch *B* where Fr_B equals 34.4 and high Froude number in branch *C* where Fr_C equals 34.4. Flow field was investigated with 9 investigated planes.	41.8	9	36	1938	51	38	100
		8	32	1938	51	38	100
		7	28	1950	50	39	100
		6	24	2050	50	41	100
		5	20	2091	51	41	100
		4	16	1989	51	39	100
		3	12	1950	50	39	100
		2	8	1989	51	39	100
		1	4	2000	50	40	100
Case 14: OGE in branch *A*, triple discharges. Medium Froude number in branch *A* where Fr_A equals 10.56. High Froude number in branch *B* where Fr_B equals 34.4 and high Froude number in branch *C* where Fr_C equals 34.4. Flow field was investigated with 8 investigated planes.	36.5	8	32	1786	47	38	100
		7	28	1938	51	38	100
		6	24	2000	50	40	100
		5	20	2000	50	40	100
		4	16	1950	50	39	100
		3	12	1989	51	39	100
		2	8	1862	49	38	100
		1	4	1989	51	39	100

Figure 3.1 (a) Test section geometry, (b) Clear cast acrylic test section, shown installed in a two-phase test facility.

Water Surface
Level

+ Z

Side
Branch

- X

H

Horizontal Investigated Plane
Through the Side Branch

θ

+X

r

-Y

25.4

45 º Branch

Acrylic test
section

Bottom
Branch
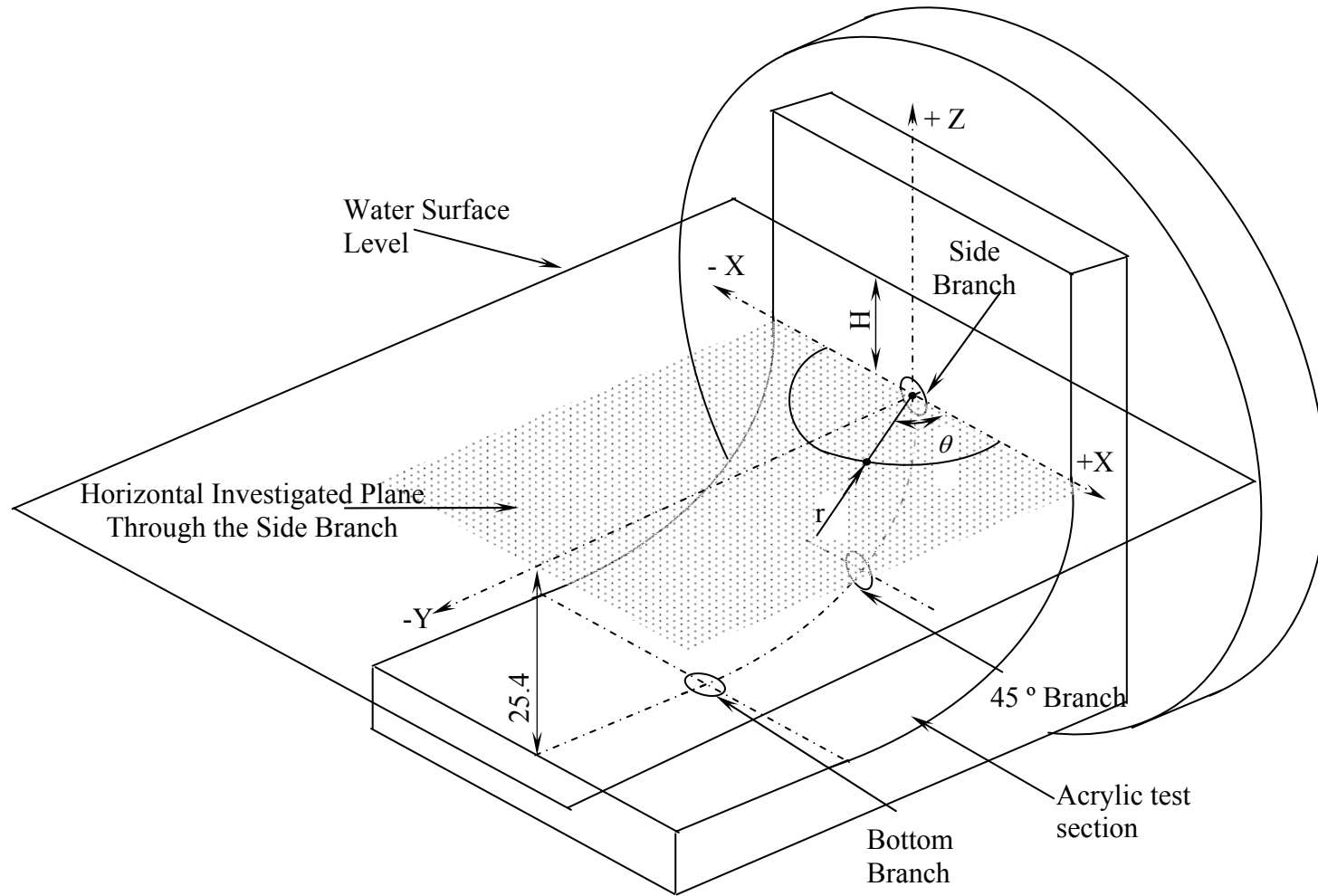
Figure 3.2 Schematic diagram of the clear cast acrylic test section with one of the investigated planes.
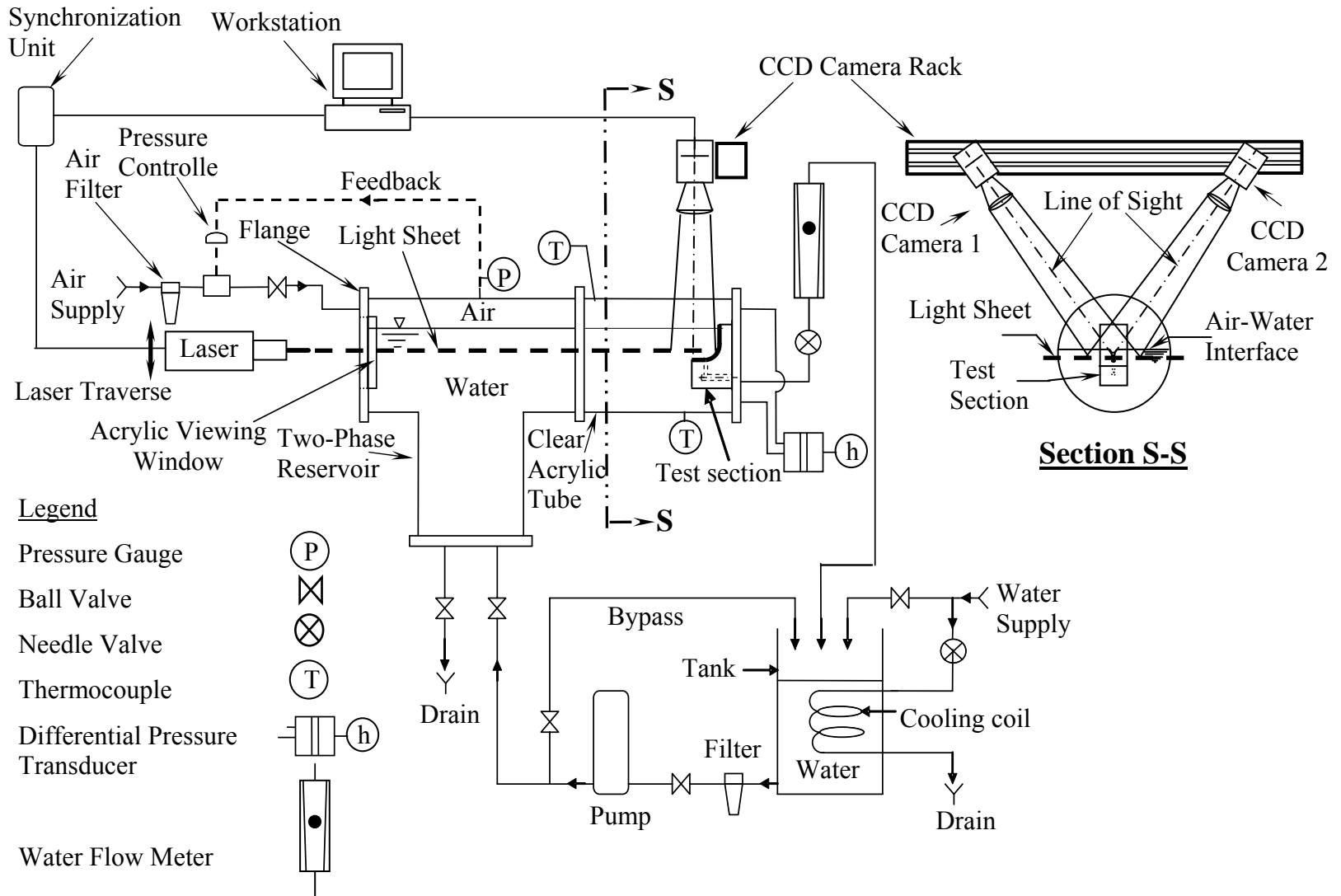
Figure 3.3 Schematic diagram of the experimental test facility with PIV measurement system.

CCD Camera
Rack

Two-Phase
Reservoir

Light Sheet
Optics

Laser
Head

Two Cameras

Pressure
Regulator

Flowmeters

Test Section

Air Supply

Work Station

Synchronization
Unit

Pump

Water Tank

56
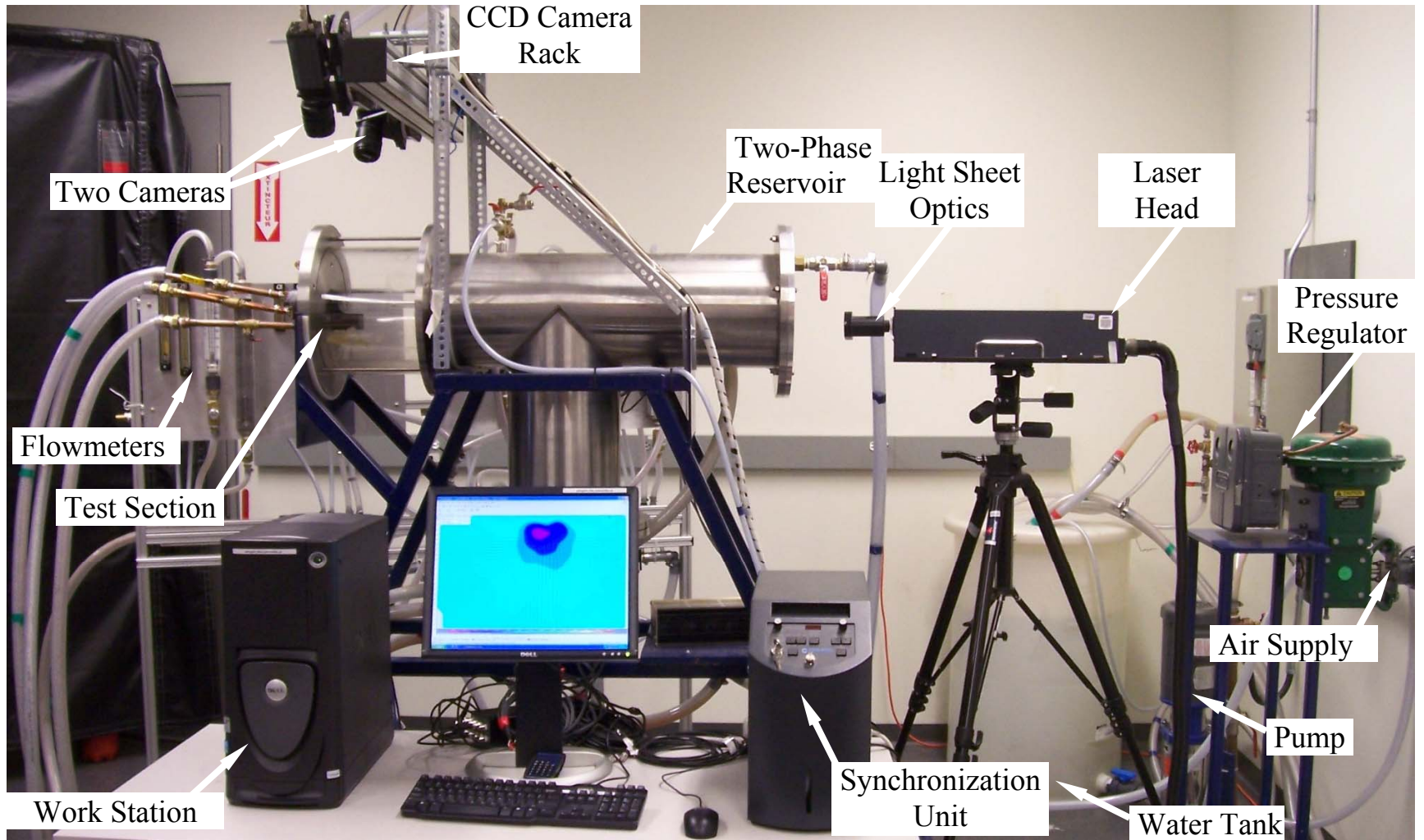
Figure 3.4 Photo of the test facility.

Displacement
seen from left

True
displacement

Displacement
seen from right

Focal plane =
Centre of light
sheet

45°   45°

Left
camera
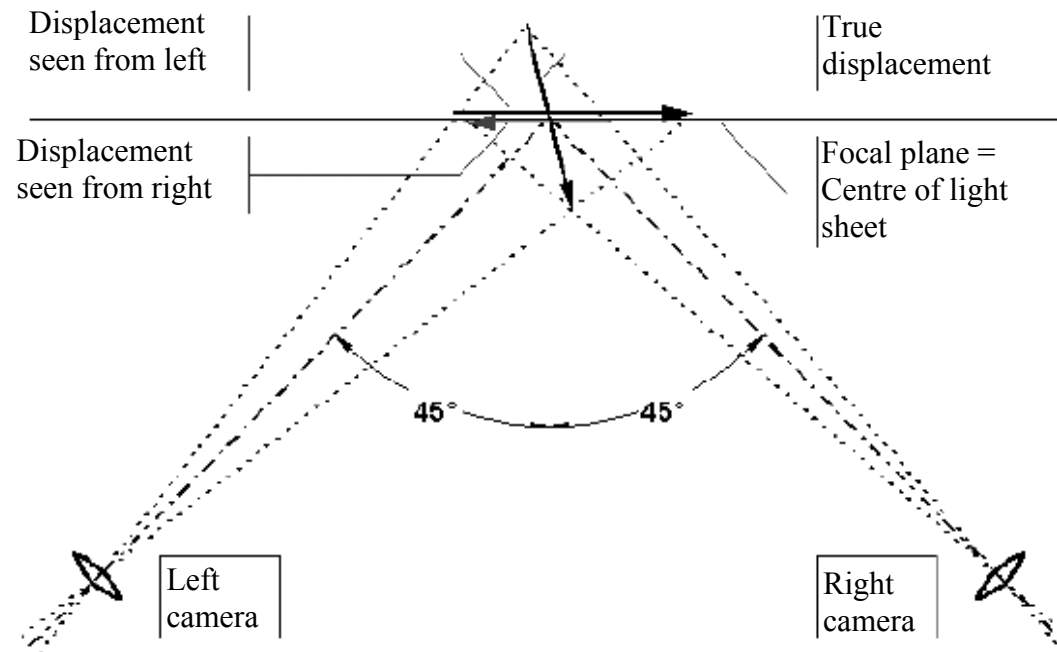
Right
camera

Figure 3.5 Principles of stereoscopic PIV. The displacements derived from the images recorded by the left and right camera are used to reconstruct the true displacement, including the third component.
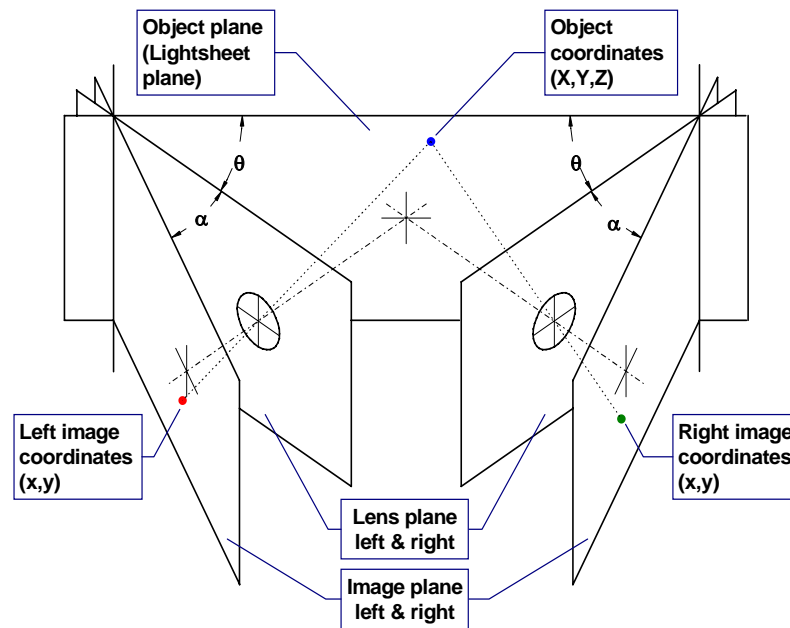
Figure 3.6 Focusing an off-axis camera requires tilting of the CCD-chip (Scheimpflug condition).
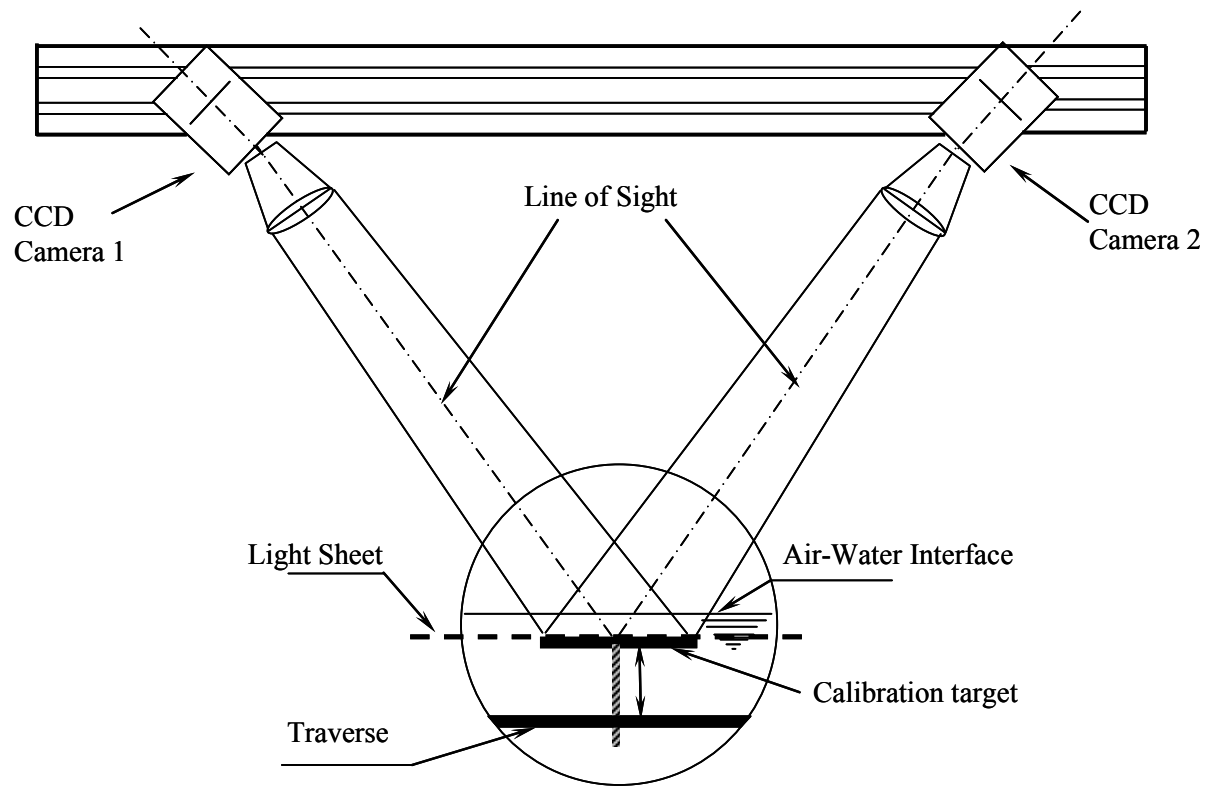
Figure 3.7 Schematic of the 3d-PIV calibration target and vertical traverse shown installed in the two-phase reservoir.
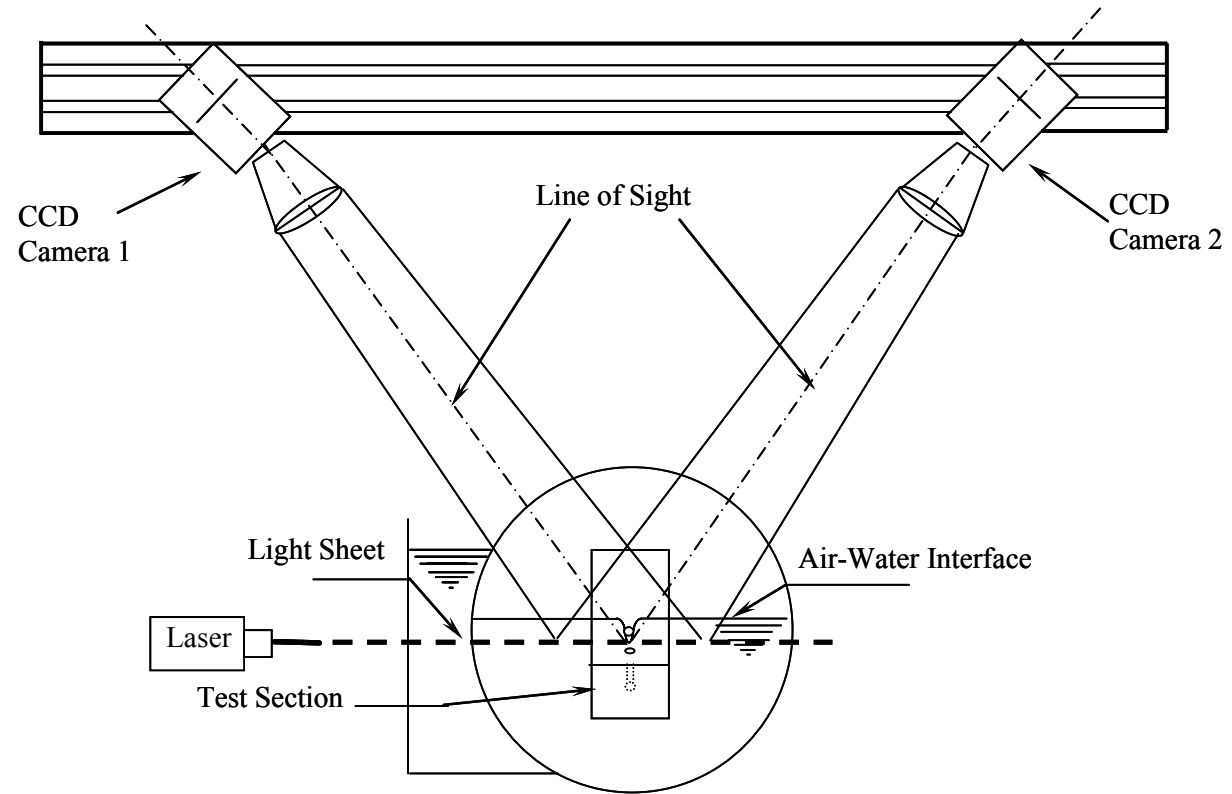
Figure 3.8 Schematic of the refractive index matching technique shown with test section installed in the two-phase reservoir.

Figure 3.9 A sample side view image of the test section showing OGE in the side branch and PIV image planes.
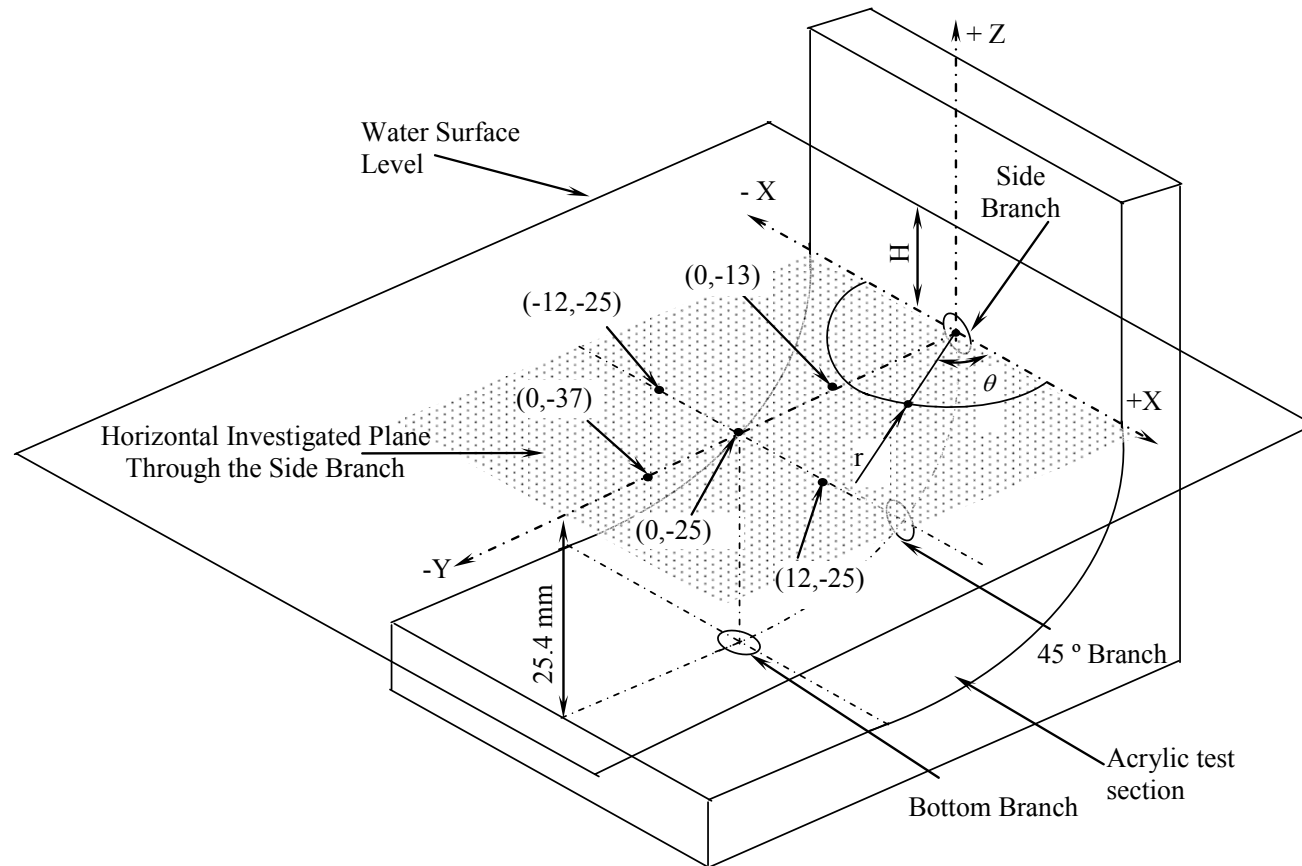
Figure 3.10 Polar coordinate (r, θ, z) transformation with origin located at side branch center.

Side branch

Inclined branch

Bottom branch
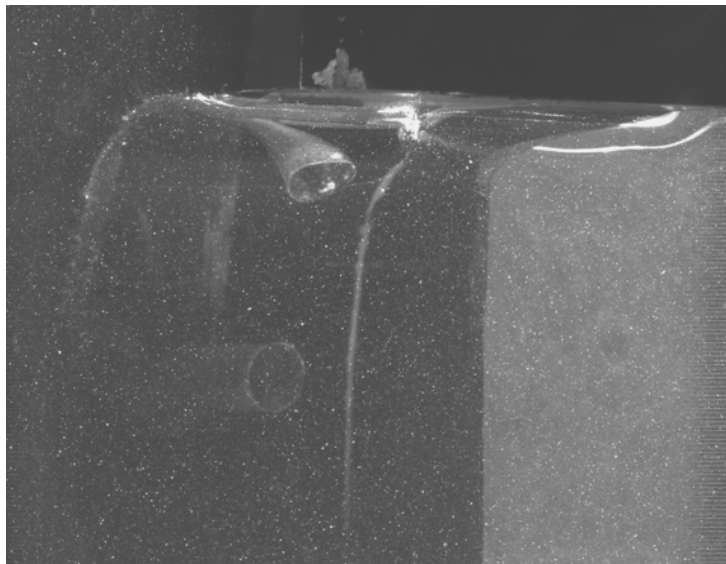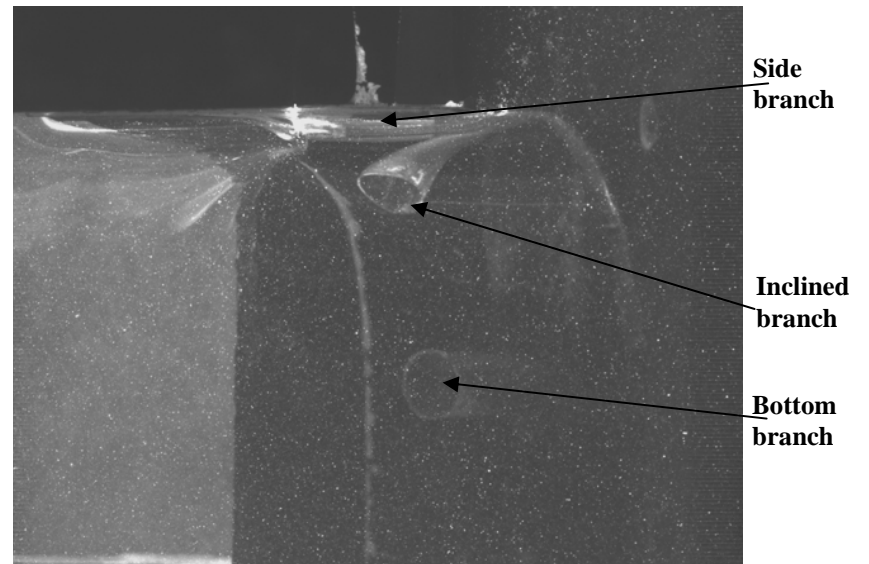
(a)   (b)

Figure 3.11 Sample of stereoscopic PIV images of flow field captured from (a) camera 1 and (b) camera 2.
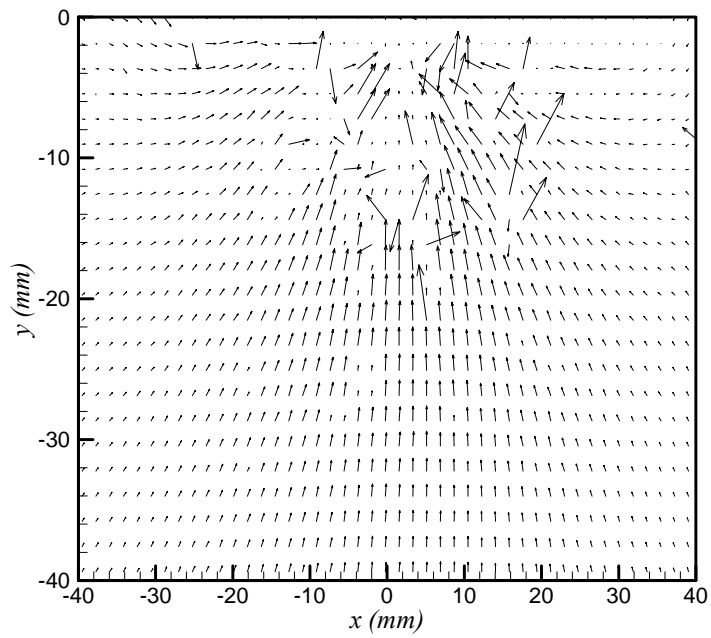
(a)
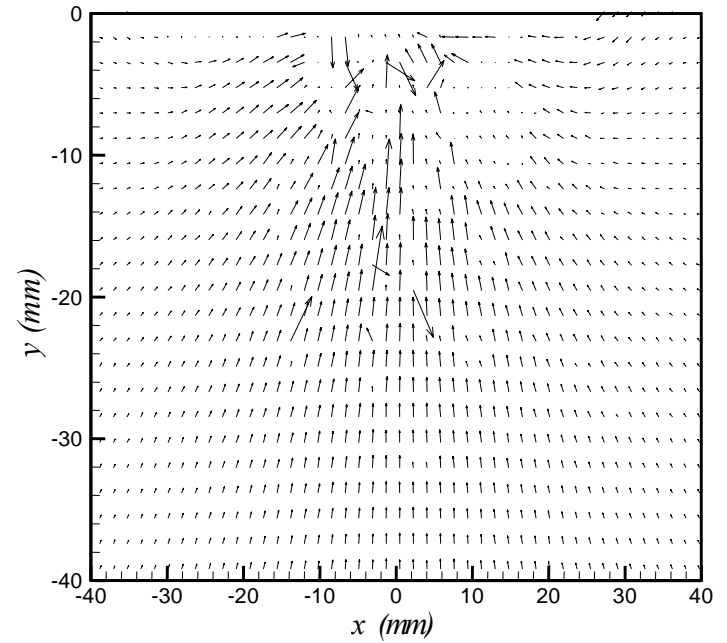
(b)

Figure 3.12 Instantaneous velocity obtained using adaptive correlation obtained from
(a) camera 1 and (b) camera 2 ($Fr = 31.69$, plane 6).
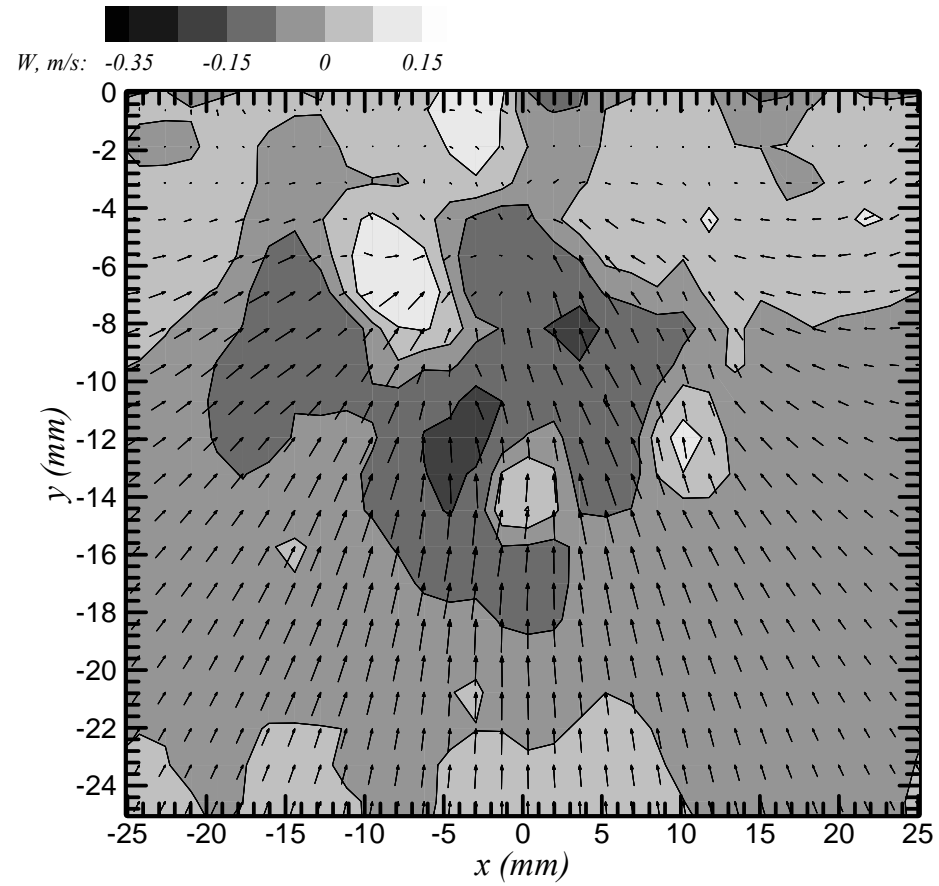
Figure 3.13 Correlated instantaneous 3d vector field (*Fr* = 31.69, plane 6).
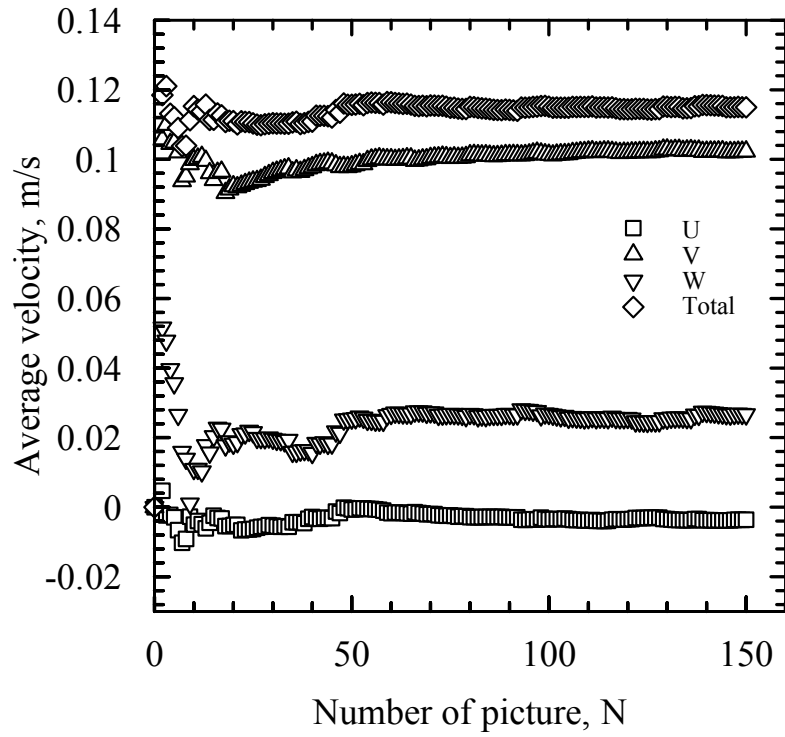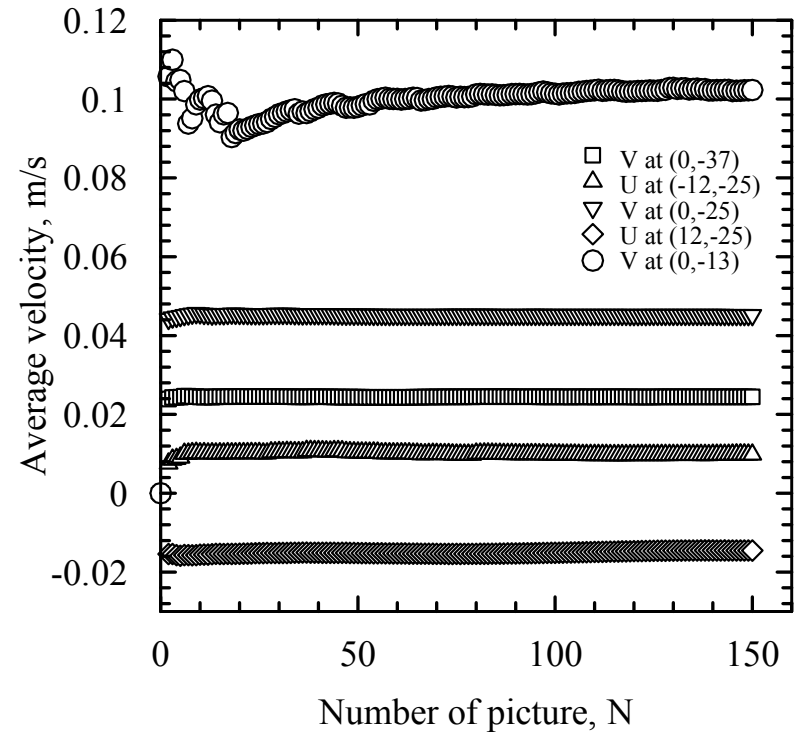
(a)   (b)

Figure 3.14 Effect of number of images on velocity at selected positions.
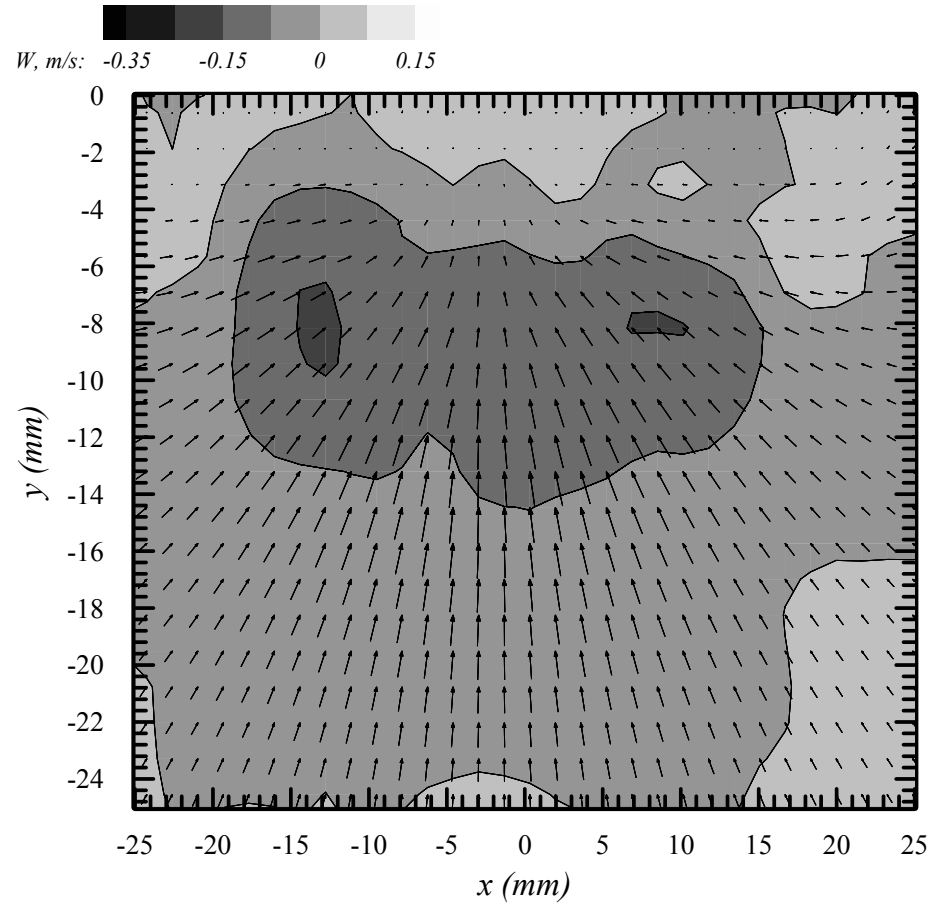
Figure 3.15 A temporally averaged vector field (*Fr* = 31.69, plane 6).
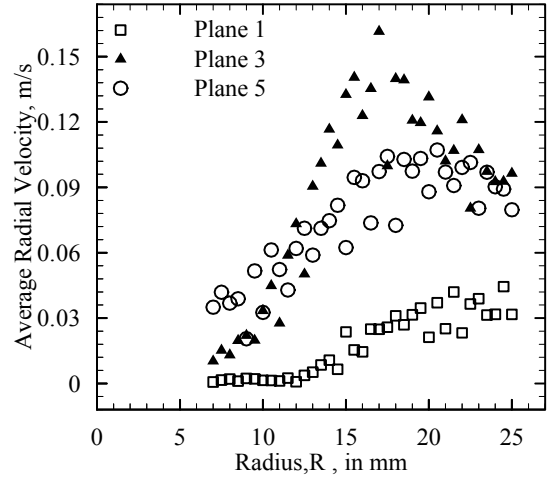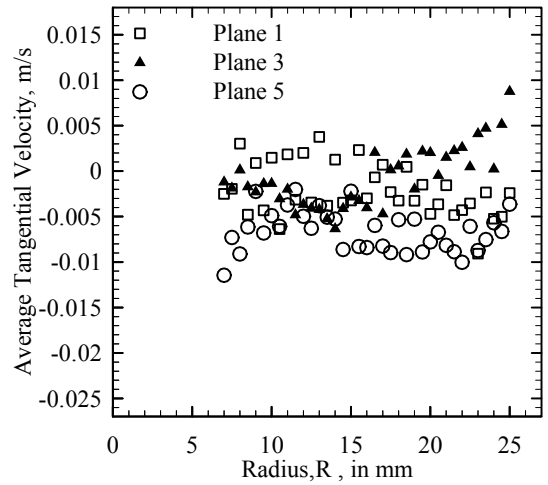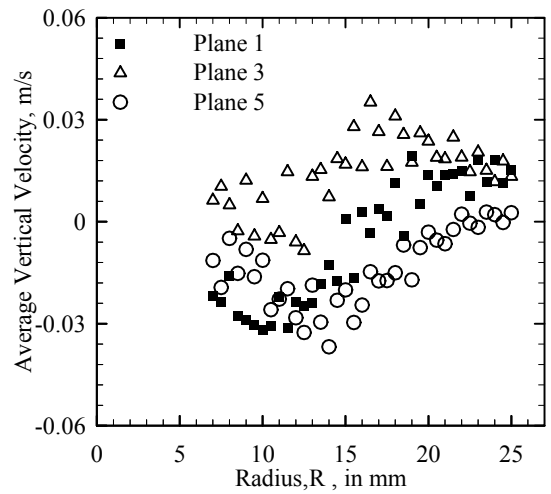
Figure 3.16 Velocity profiles averaged at constant radial distances (*Fr* = 31.69).
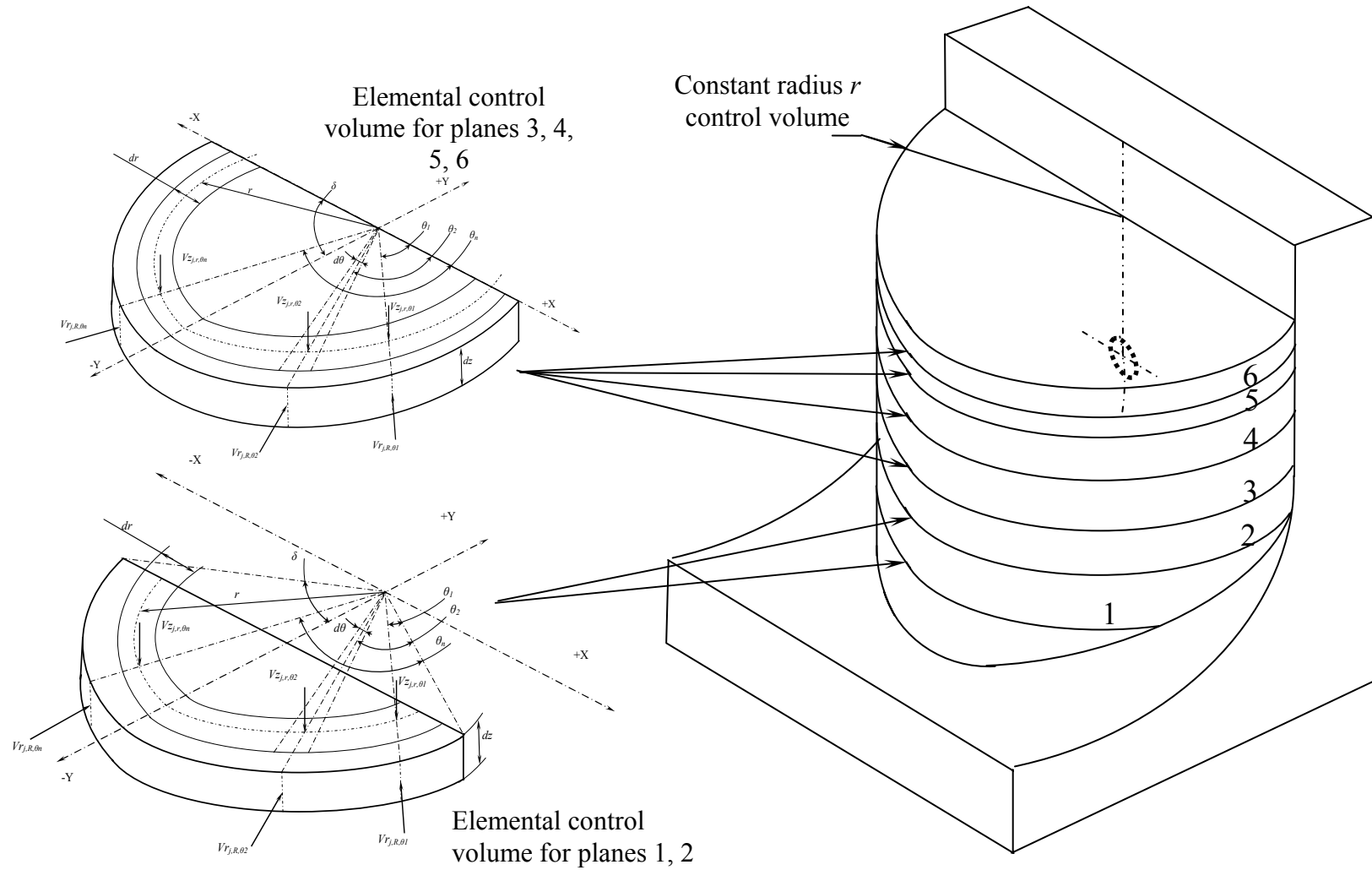
Figure 3.17 Semi-cylindrical control volume, of constant radius, shown intersecting the test section.

(a)

(b)
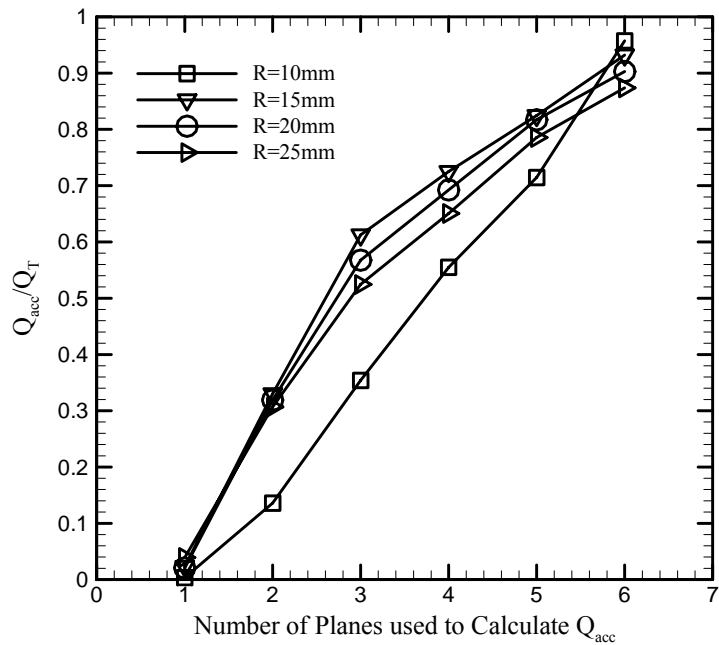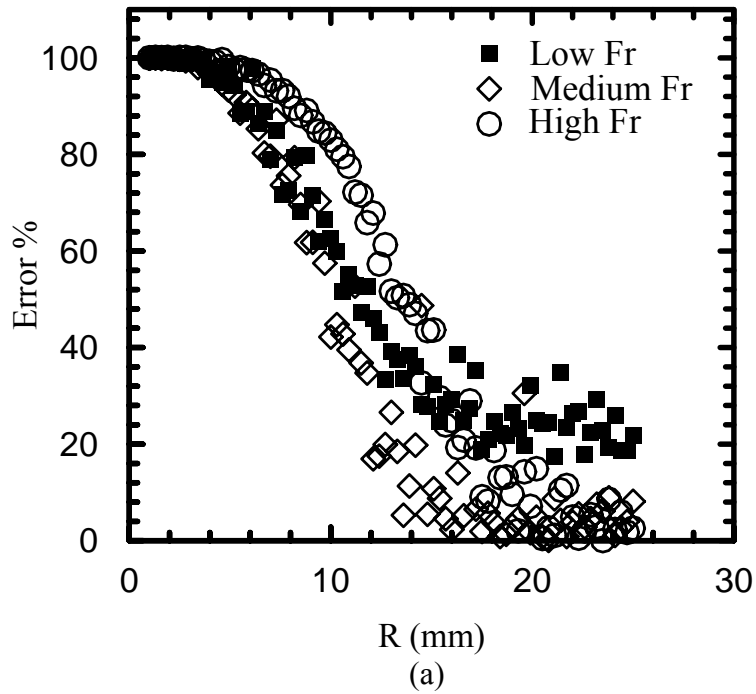
Figure 3.18 (a) Error based on comparison between control volume analysis of PIV data and rotameter flow rate and (b) contribution of each plane to total flow rate in the control volume analysis.
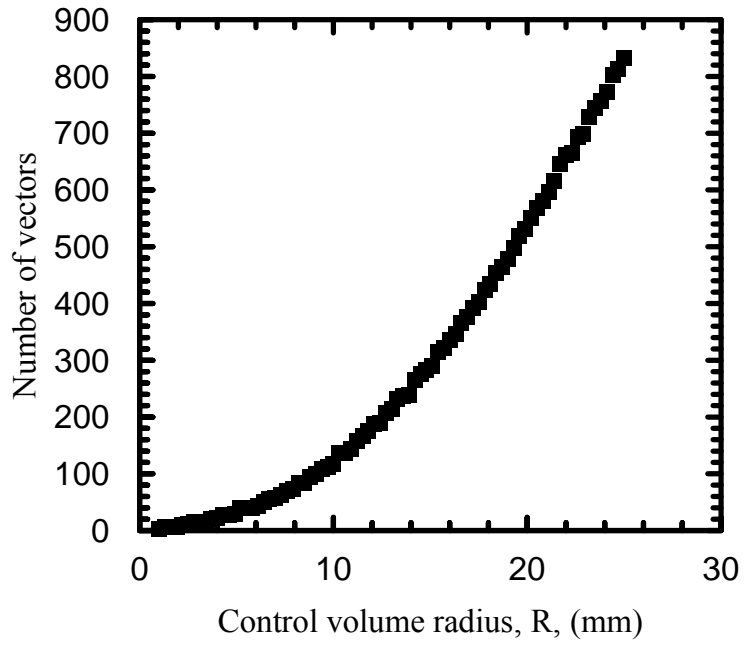
(a)
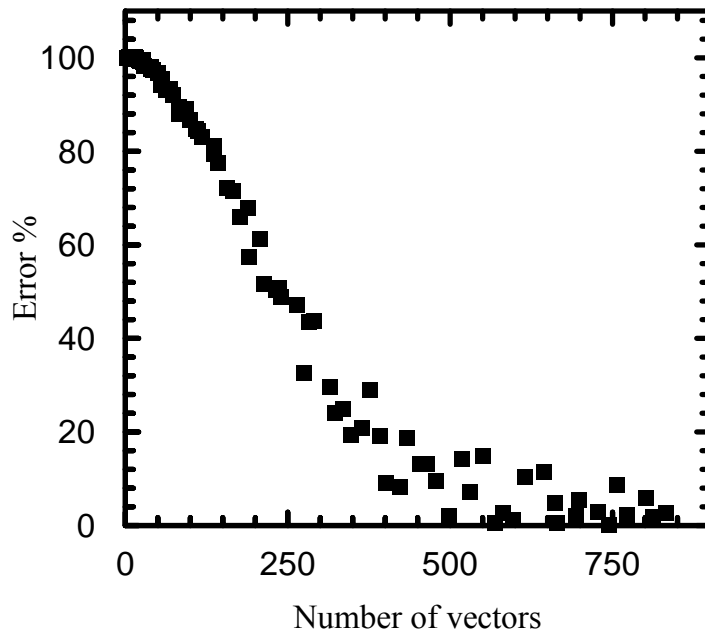
(b)

Figure 3.19 (a) Number of vectors used to calculate flow rate as a function of radial distance and (b) error of control volume method as a function of the number of vectors.
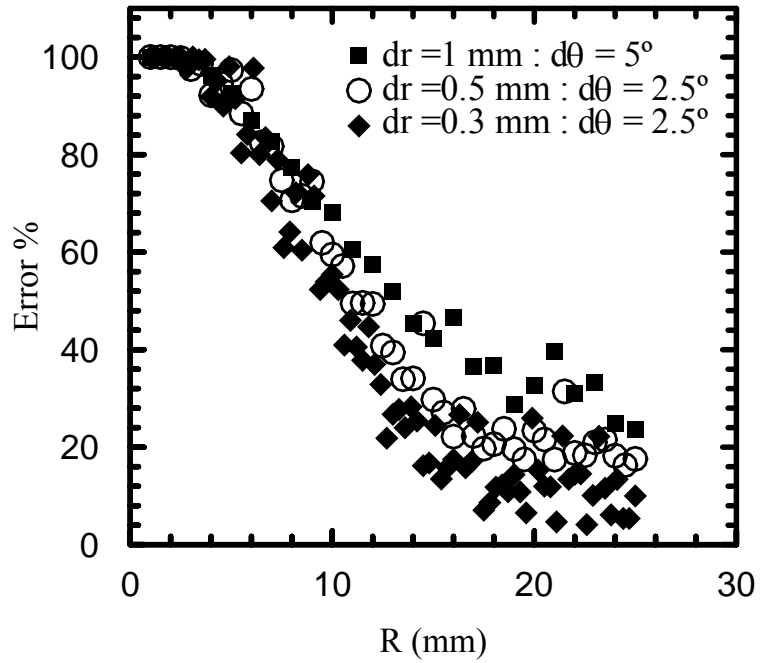
(a)
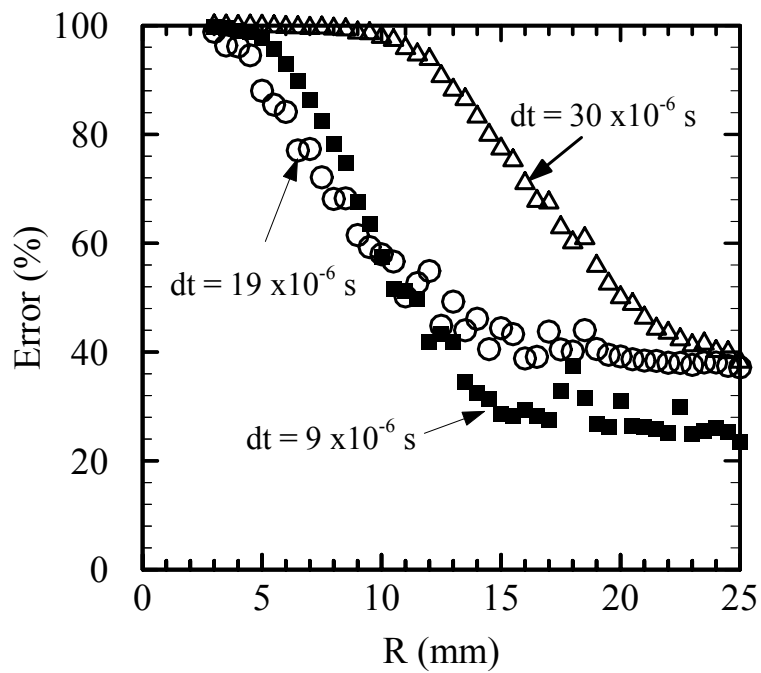
(b)

Figure 3.20 Grid dependence (a) time scale (b) control volume element size.

Chapter 4

Experimental Results of OGE Flow Field - Single Discharge

Eight cases were studied to investigate the liquid side flow field at the onset of gas entrainment during single discharge, using the stereoscopic particle image velocimetry system. The results for one case only, case 1r, will be presented here. The results of remaining cases are tabulated in the Appendix. A single discharge case in branch A, with a high Froude number of 31.69, will be discussed. At this Froude number, the onset of gas entrainment height was 39.7 mm measured, from the bottom branch entrance, O_C. The three dimensional two-phase flow structure was divided into nine horizontal planes. The nine planes are located at heights of 4, 8, 12, 16, 20, 24, 28, 32, and 36 mm above O_C, as shown in Figure 4.1. The results of the velocity fields in the water side of the two-phase environment during continuous gas pull through in branch A will be presented. Throughout the text, the nine horizontal planes will be referred to by their vertical rank starting from plane number 1, at 4 mm height, and ending with plane number 9 at 36 mm height. Results are presented for non-simultaneous measurements of these individual planes.

The presentation of the flow field will be described in four groups of figures. In the first group of figures, from Figure 4.2 to Figure 4.6, the velocity vector field is presented for each plane. In these figures the contour lines represent the magnitude of the vertical velocity, V_z. The vectors refer to the magnitude and direction of the in-plane radial and tangential velocities (V_r and V_t). In the second group of figures, from Figure 4.7 to Figure 4.16, the vorticity field in each plane is presented. The vorticity was

calculated from the velocity components in x and y directions, U and V, respectively. An 8-point circulation vorticity equation adapted from Reuss et al. (1989) where,

$$\omega_{i,j} = \frac{\Delta l}{(2\Delta l)^2} \begin{bmatrix} \left(U_{i,j-1} - U_{i,j+1}\right) + \left(V_{i+1,j} - V_{i-1,j}\right) \\ + 0.5 \begin{pmatrix} -U_{i+1,j+1} + V_{i+1,j+1} - U_{i-1,j+1} - V_{i-1,j+1} \\ + U_{i-1,j-1} - V_{i-1,j-1} + U_{i+1,j-1} + V_{i+1,j-1} \end{pmatrix} \end{bmatrix}. \qquad (4\text{-}1)$$

The vortical structures were extracted from the velocity field using a method adapted from the vortex definition of Jeong and Hussain (1995). They define a vortex region where the second eigenvalue λ_2 ($\lambda_1 \geq \lambda_2 \geq \lambda_3$) of the symmetric tensor ($\Omega^2 + St^2$) is negative at every point inside the vortex core. Where St is the strain-rate tensor (symmetric part) and Ω is the spin tensor (antisymmetric part). For two - dimensional incompressible flows, this means that:

$$\lambda_2 = \left(\frac{\partial U}{\partial x}\right)^2 + \left(\frac{\partial U}{\partial y}\right)\left(\frac{\partial V}{\partial x}\right). \qquad (4\text{-}2)$$

This criterion measures the excess of rotation rate over the strain rate magnitude in a specific plane. In the third group of figures, from Figures 4.17 to 4.19, the average flow field velocities, in each plane, are presented along the radius r which was measured from the side branch entrance, O_A. A half cylindrical surface element was selected, with the area of, $\pi r dz$. The summation of radial velocities along this element was divided by the total number of velocity vectors to yield the average radial velocity at r from the side branch entrance. This procedure was repeated to also obtain the average tangential and

the average vertical velocity along r. In the fourth group of figures, from Figures 4.20 to 4.21, the uniformity, repeatability, and influence of the number of investigated planes used to represent the flow field are presented.

The dimensions of each investigated plane is 50 mm by 30 mm in the x and y directions, respectively. These dimensions enable the flow field area around the three branches to be presented. The negative y dimension was measured from the side branch entrance. Due to its vertical placement each investigated plane will intersect with the test section wall. This intersection is presented as a dashed line in Figures 4.2 to 4.4. On the right of the dashed line the solid wall exists. On the left side of the dashed line, the liquid side flow field PIV data exists. In all Figures the circle represents the bottom branch, C, the oval represents the 45º branch, B, and located at the origin (0, 0, 0) is the side branch.

4.1 Velocity Flow Field

This section presents the velocity fields measured using PIV during continuous gas pull through in branch A. This will be done by showing the nine velocity fields for the nine investigated planes.

4.1.1 In-Plane Velocities

The nine investigated planes show similar trends where in-plane vectors are concerned – the planes present the total in-plane velocity vector which is a summation of radial (V_r) and tangential (V_t) components. The third component, the vertical velocity (V_z) is presented as superimposed contour lines, and will be discussed in the next section. Three distinct regions can be highlighted in each plane, with similar in-plane velocity vector characteristics. The first region is located at the left boundary of the investigated

plane, at y = - 30 mm, and the second region near the middle distance of the plane width (in y direction), and the third region at the right boundary wall. In Figures 4.2 to 4.6, in the first region (y = - 30 mm), the in-plane velocity vectors are relatively small but as the right boundary is approached their magnitude (vector length) will start to increase dramatically and then significantly decrease at the right boundary. At the first region the inlet flow area is very large. As shown in Figure 3.17, a cylindrical surface area centered at the side branch z axis shows the flow to travel nearly horizontally. With increasing flow area, to conserve mass, the in-plane velocity should decrease, as observed. At the second region where the inlet flow area is smaller, conserving mass, the in-plane velocity increases relative to the first region, as expected. At the third region the flow will tend to go toward the side branch entrance by turning vertically down (- V_z) at planes 8, and 9, and by turning vertically up (+ V_z) from the planes 1 to 5. This is because planes 8 and 9 are located above the discharge, while planes 1 to 5 are located below. This transition caused the in-plane velocity in the third region to be significantly decreased.

4.1.2 Vertical Velocities

The vertical velocity, V_z, is represented by the contour lines in Figures 4.2 to 4.6. According to the vertical velocity trend, the flow field will be divided into three groups of investigated planes. The first group includes planes 1 to 5, which are located lower than the side branch entrance. The second group consists of the planes 6 and 7, which pass through the side branch entrance. The third group consists of planes 8 and 9, which are located higher than the side branch entrance. By looking at the region located at -10 mm < x < 10 mm and -30 mm < y < right investigated plane boundary at all the first group of investigated planes, a positive V_z is observed. The peak of this region becomes more

intense and propagates toward the branch entrance as the investigated plane height is increased. This flow structure can be visualized as a conical region with its base located at plane 1 and its apex located at plane 6. The increase in intensity with plane height demonstrates that the flow comes from the planes located lower than the side branch entrance at (0, 0, 0).

There are also some regions where the vertical velocity is shown to be negative, indicating flow in the downward direction and away from the branch inlet. These regions are shown to exist in the area around the intense positive peak – which is attributed to the conical flow structure. One possible explanation is that there are circulation regions, or vortex structures, whose central axis of rotation exists in some horizontal or inclined plane. This would imply that the flow circulates in and out of the horizontal investigated plane. This observation does contradict the flow structure that is generated when the discharge is simulated as a point sink, as in Chapter 7. It is believed, however, that these circulation regions have a minor influence on gas entrainment. This is due to the relatively small size and intensity of the negative peaks with respect to the large central positive peak. Additional work , however, could further enhance our understanding of the flow structure and possibly lead to improvements in the modeling of such phenomena.

At the second group (planes 6 and 7) a positive value of V_z was recorded near the side branch entrance in plane 6, as shown in Figure 4.4(b). This indicates that this part of the side branch entrance is fed by liquid from the lower part of the flow field (planes 1 - 5). A negative value of V_z was recorded near the side branch entrance in plane 7, as shown Figure 4.5(a). This indicates that this part of the side branch entrance is fed by

liquid from the higher part of the flow field (planes 8 and 9). At the third group (planes 8 and 9), which are located at a level higher than the side branch entrance, a negative value of V_z was recorded near the side branch entrance, as shown in Figures 4.5(b) and 4.6 (the peak of this region was large in plane 9 and became smaller in plane 8). Once again, the flow structure of the vertical velocity can be viewed as a conical region with its base located at plane 9 and its apex located at plane 7. This represents that in planes higher than the side branch, the flow comes from above and is directed toward the branch entrance.

Combining observations from planes above and below the side branch inlet yields a more complete picture of the contribution from the vertical velocity to the total flow structure. In higher planes the flow is generally pulled down into the branch, while in lower planes the flow is pulled up. It was found that in both cases (above and below), a large vertical velocity peak formed in region near the branch inlet, and for the most part, this region is centered along the y-axis, which coincides with the branch inlet. These peak regions formed a conical shape when traversing the horizontally oriented investigated planes vertically up, or down, from the branch inlet.

4.2 Vorticity Flow Fields

The vorticity was calculated from the horizontally oriented velocity fields obtained from the PIV measurements. The vortex centers were calculated by following Michard et al. (1997) and Graftieaux et al. (2001), who introduced the scalar function Γ_1. This function characterizes the location of the center of the large-scale vortex, and can be written under the following discrete form,

$$\Gamma_1(P) = \frac{1}{N} \sum_S \frac{(PM \times V_M) \cdot Z}{\|PM\| \cdot \|V_M\|} = \frac{1}{N} \sum_S \sin(\theta_M). \qquad (4\text{-}3)$$

where P is a fixed point in the measurement domain, S is a two dimensional area surrounding P, M lies in S, Z is the unit vector normal to the measurement plane, V_M is the velocity vector at M, θ_M is the angle between the velocity vector V_M and the radius vector PM, and N is the number of points M inside S, as shown in the schematic representation of the terms involved in Γ-criterion, in Figure 4.7. The condition for a point to be a vortex center is,

$$0.9 < |\Gamma_1| < 1. \qquad (4\text{-}4)$$

This method was applied to the whole investigated planes in order to obtain vortex centers, and also to track their displacement with plane location. It was found that none of the points achieved the vortex center criterion in Eq. 4-4. The maximum value in the planes was found to range between 0.7 and 0.8, and may be due to the vorticity being very weak, or perhaps because of the radially dominant velocity field that exists in the horizontal planes.

A schematic diagram for the test section was shown in Figure 3.2. The liquid flow comes from the two-phase environment passing beside the test section edges, towards the side branch entrance. Due to the wake effect, it is expected that two counter rotating vortices will be created near the test section edges, close to the wall. These vorticies were observed throughout qualitative flow visualization experiments.   It was therefore expected that two vorticies would be found near the test section edges in the PIV results.

As was mentioned earlier, the investigated plane right boundary is represented by a dashed line. In Figure 4.8, where investigated plane 1 is 4 mm higher than the bottom branch entrance, the vortices are present at x = - 20 mm and at x = 20 mm. They are identified by peak regions of ω or λ_2 in either Figure 4.8(a) or 4.8(b), respectively. Outside of these peak regions the vorticity is found to be at the lower end of the presented ranges. The 8-point circulation in the peak regions is shown to be ± 7.2 s^{-1} while surrounding regions are around 1 s^{-1} or less. Similarly, the value of λ_2 in peak regions approach values between -10 s^{-2} and -20 s^{-2}, with surrounding regions close to -1 s^{-2}. The vortices are typically located away from the wall (dashed line) and are generated due to the wake effect observed during experimentation.

In Figures 4.9 to 4.16, the vorticity fields follow a similar trend as discussed in Figure 4.8, however the two counter-rotating vortex regions are shown to propagate toward the right edge (solid wall) as the plane height increases. The vorticity in the higher planes becomes stronger relative to the lowest plane 1 – which was also limited because of the low liquid height causing a strong boundary effect. This can be explained by the fact that the upper investigated planes contribute more to the total branch flow rate than the lower investigated planes. The higher the flow rate contribution from the plane, the higher the peak vorticiy is observed. The flow rate of each plane is discussed at the end of this chapter, and presented in Figure 4.20.

4.3 Averaging the Flow Field Data

4.3.1. Radial Direction

The average radial velocity was determined in each plane using the procedure outlined in Chapter 3, Sec. 3.6. Figure 4.17 shows the average radial velocity change along r for the nine investigated planes. In planes 5- 9, a few notable trends are evident. The radial velocity is relatively small far from the branch inlet, near $r = 25$ mm, then as r decreases the velocity increases until it reaches a maximum value around $r = 15$ mm. In planes 1 to 5, the radial velocity decreases to around 0 m/s near $r = 0$, near the side branch entrance. The velocity near the fixed wall, and discharge, is comparatively smaller than the velocity far from the fixed wall. This observation is a glaring contradiction to the expected physics, and this is no more evident than in the two planes located closest to the discharge inlet, planes 6 and 7, respectively. Since these planes actually intersect the discharge inlet, it could be expected that the velocity closest to the inlet is the highest of all investigated planes. However, it is clear from both the velocity field presented in Figures 4.4(b) and 4.5(a), and the computed average radial velocity in Figure 4.17 that this is in fact not the case. It could be argued that in far planes, such as 1 or 9, as the branch inlet is approached, with decreasing r, the flow will begin to curl up or down (depending on the plane location) into the discharge causing the radial component to decrease drastically. While this is a reasonable explanation for the higher planes, it does not suffice for the two planes that intersect the discharge inlet, since the majority of flow near the inlet would in fact be contained within the horizontal plane. Instead, in these two planes the velocity at the discharge inlet is shown to drastically drop off to nearly 0 m/s. The reasons for this have been widely discussed in Chapter 3, but in

summary can be related to two-phase flow structure, and surface reflections, causing a skewed PIV image of the particle displacement within this area. Consequently, the recorded velocity data within this region is not reliable and gives a false impression of the physics of the problem. The calculated error within this region is also discussed in Sec. 3.6.

The influence of plane height on the radial velocity can be seen by comparing the plotted data sets. For example, the velocity in plane 1 is the lowest, and increases in plane 2, and then again in plane 3, and so on until plane 6. In effect, as the height from the branch inlet increases, for $r > 15$ mm, the radial velocity decreases. This trend also continues in planes 7 to 9, however, the flow from the higher planes is directed downward whereas flow from planes 1 to 5 are directed upwards toward the branch inlet. The flow in plane 7, near the side branch entrance, is fed from the higher two planes 8 and 9, and since plane 7 passes through the side branch entrance, most of the vertical flow is converted to radial flow. The result is that the average radial velocity in plane 7, for the most part, is one of the highest when compared to the remaining 8 planes. The same scenario is found in plane 6, in which the flow supplied from planes 1 to 5 is converted to the radial direction, making the average radial velocity in plane 6 also one of the highest. The summation of the flow rates contributed by planes 8 and 9 is greater than summation of the flow rates in planes 1 to 5, as demonstrated in Figure 4.20(a). This is a direct result of the radial velocities in these planes having much larger amplitudes than found in planes 1 to 5. The average radial velocity ranged between 0 and 0.15 m/s in all planes.

4.3.2. Tangential Direction

The average tangential velocity, V_t, was determined in each plane using the same procedure followed to determine V_r as outlined in Chapter 3, Sec. 3.6. Figure 4.18 shows the average tangential velocity change, along r, for the nine investigated planes. The magnitude of V_t ranged between $\pm$ 1.5 cm/s in all planes for r > 15 mm – the range where the velocity data is deemed reliable, as explained in Sec. 4.3.1. A large portion of the data points exist at V_t = 0, which implies that there is little or no tangential component to the velocity profile along r. This is misleading since V_t is actually calculated in each plane using a summation of all tangential velocities located around a given radial distance, r, from the branch inlet origin O_A. In fact, the reason that the near zero average tangential velocity is produced, is that there are both positive and negative tangential values on either side of the y-axis. It is seen from the vector fields, for example Figure 4.6, that there is some symmetry about the y-axis with regards to the vector direction. With x > 0 the velocity vectors curl counterclockwise towards the branch inlet at (0, 0, 0) and implies a positive tangential velocity using the right hand rule. On the other hand, with x < 0 the velocity vectors curl in a clockwise manner implying a negative tangential velocity. If the tangential components on either side of the y-axis are nearly equal at any given r, the summation of these two values yields a value equal or close to zero – the circulation about the discharge could be estimated to be close to zero. This gives further support to the vortex-free assumption that was used in the modeling of gas entrainment. If the average radial and tangential velocity component magnitudes are compared, Figures 4.17 and 4.18, it can be seen that the radial velocity outweighs the tangential component by approximately an order of magnitude. This would seem to indicate that the

flow is dominated by the radial velocity, however, this comparison is misleading because the average tangential velocity is calculated using both positive and negative components rather than the absolute value of the magnitude.

4.3.3. Vertical Direction

The average vertical velocity was obtained as outlined in Chapter 3, Sec. 3.6. Figure 4.19 shows the average vertical velocity change, along r, for the nine investigated planes. Planes 1 to 5 have positive average values while planes 8 and 9 have negative values, for reasons that were discussed earlier. Planes 6 and 7, which intersect the discharge inlet, shows that the average vertical velocity is typically lower than the remaining seven planes. This observation is reasonable since it is expected that the flow should travel almost horizontally into the branch inlet within these planes, requiring a low vertical component. Far a way from the branch entrance at $r = 25$ mm, the flow is mainly horizontal and the vertical flow between the planes is typically low. As the flow approaches the branch inlet, near $r = 13$ mm, the vertical flow between the planes increases – as was found earlier in the vector fields. At the branch inlet, $r = 0$ mm, the average vertical velocity decreases to around $\pm$ 0.05 m/s. Logic states that the vertical velocity should continue increasing towards the branch center, and so this result contradicts the expected physics. This can be explained as follows:

- The calibration process was done in a stratified region. Gas entrainment creates an air cone with its base at the air-water interface and its apex at the side branch entrance. Hence, the PIV data near the side branch entrance are missing, because the flow is not seeded in this region.

- The air-water interface, during gas entrainment, is curved and distorts the seeding particle motion in the investigated planes located under the air-water curved surface.

4.4 Distribution of OGE Flow Rate in the Streamwise Direction

The flow rate was calculated using the velocity information gathered from the PIV vector fields and is followed from the procedure outlined in Chapter 3, Section 3.6. Figure 4.20 shows the change in flow rate along r, for the nine investigated planes and the percentage of the contribution of individual planes to the total flow rate. The velocity near the fixed wall was shown to be typically lower than the velocity far from the fixed wall, as shown in Figure 4.17. The flow rate in plane 1 is less than the flow rate in plane 2, and the flow rate in plane 2 less than plane 3, and so on - this is now proven in Figure 4.20(a). It shows that the flow rate in plane 9 is the highest, while plane 1 has the lowest which does not contradict with Figure 4.17 where the average radial velocity in plane 9 is not the highest. The element height used to define the semi-cylindrical control volume in order to calculate the flow rate in plane 9 is 6 mm, as shown in Figure 4.1. The remaining planes have an element height of 4 mm. The increase in inlet flow surface area, compared to the remaining control volumes, causes plane 9 to have the highest contribution to the total flow rate. As the control volume size approaches the lower limit, as r decreases towards zero, the discrepancies observed in the radial and vertical velocities near the branch inlet that were discussed earlier, become increasingly apparent. It is seen that the calculated flow rate begins to approach a value of zero, which is misleading since the liquid flow rate through the discharge is steady. Looking however

to the region where $r > 15$ mm, the flow rate in each plane begins to approach a steady value, which is more reasonable. The fact that the flow rate in each plane approaches a steady value, with $r > 15$ mm, lends more confidence to the PIV measurements in this range.

The contribution of each plane to the total flow rate was also determined, and is shown in Figure 4.20(b). The figure shows that the flow rates from lower planes, near the fixed wall, are smaller than the flow rates contributed from higher planes, far from the fixed wall. The planes located higher than the side branch entrance (8, 9) for example, provide more flow than planes located below the branch entrance (1 to 5). It is expected that the contribution from plane 9 is the highest, as shown, since it was seen that it had the highest flow rate of all planes in Figure 4.20(a). In addition, the contribution of each plane in Figure 4.20(b) is shown to approach a steady value with $r > 15$ mm, which is consistent with the observations in Figure 4.20(a). With $r > 15$ mm, Figure 4.20 is telling the flow structure that can be expected. From these results, the flow field would have a higher flow rate in regions located above the branch inlet, while lower regions – such as planes 1 to 5 – have lower flow rates. To demonstrate this, planes 5 and 8 will be considered, which are located below and above the branch inlet by 5.4 mm and 6.6 mm, respectively. Comparing these two planes shows that plane 8 has the higher flow rate, or contribution to the total flow rate. Since the distance from the branch inlet is quite similar, in fact plane 8 is 1.2 mm further than plane 5, it is apparent that plane's location – above or below the branch inlet - is significant to the velocity and flow rate in that plane. It could be speculated that since the flow direction from higher planes is downward, it is being assisted by gravitational forces. On the other hand, this force

resists the upward flow from lower planes. The boundary layer of the curved wall also resists the flow from lower planes.

In order to validate whether the calculated flow rates are comparable to the actual flow rate, it was necessary to determine the relative errors comparing the calculated PIV flow rate with the flow meter measurement. The result is presented in Figure 4.21. It is clear that in the branch inlet region, $r = 0$, the associated error is unreasonably high – around 100%. This is expected since the calculated flow rate from the PIV measurements in this region was shown to be around zero. The high error is attributed to the same reasons for the discrepancy in the velocities that were discussed earlier.

The influence of the number of planes used to calculate the error was investigated, as outlined. A second experiment was conducted with the same flow conditions however the test volume was divided into six horizontal planes instead of nine. The idea was to evaluate the effect of decreasing the number of investigated planes, specifically the lower planes (1 - 5) on the flow rate error. The results from the two cases (1 and 1r) are presented in Figure 4.21. The figure shows almost no difference in the flow rate error between the two cases. There was no dramatic change in the lower part of the flow field. This figure also demonstrates the repeatability of the experiment, and that six planes could be sufficient for the single discharge case.

4.5 Summary and Concluding Remarks

This chapter outlined the results from experiments using stereoscopic particle image velocimetry to map the liquid side flow field (velocity, vorticity) at the onset of gas entrainment in a single discharging side branch. The three dimensional volume of

interest was divided into nine horizontal planes where the three-component velocity maps
(V_r, V_t, V_z) were recorded. The main objectives of the experiments were to determine and
quantify the liquid side flow field and structure which is, in part, needed to support or
disprove the potential flow assumptions used in the analytical model in Chapters 6 and 7.
Furthermore, the velocity fields and observations collected can be used by future
researchers to improve existing models, or pursue alternatives to simulate the complex
flow structure.

Two formats were used in the presentation of the flow structure – the whole field
map showing the vector and vorticity fields, and the averaged velocity components (V_r,
V_t, V_z) along a given radial distance, r, from the branch inlet. The main observations
from the flow structure can be summarized as follows,

- The velocity field is dominated by the radial and vertical components.
  Away from the discharge ($r > 20$ mm) the fluid flows primarily in the
  radial direction towards the inlet. Closer to the inlet ($r < 15$ mm) the flow
  curls vertically towards the discharge inlet – up from lower planes and
  down from higher planes.   The peak fluid velocity is found at
  approximately $r = 15$ mm.   The fluid flows with a higher velocity in
  planes located above the discharge inlet, compared with planes located the
  same distance below the inlet.

- The tangential velocity component, within the horizontal planes,
  demonstrates that the flow curls towards the inlet. It was determined,
  however, that the curl did not satisfy the Γ_1 vortex center criterion. The
  vorticity was found to have negligible intensity within the horizontal

planes, and regions of high vorticity were observed due to the wake effect at the test section boundary. It is suspected that vortex structures exist within vertical or inclined planes, as observed from the positive and negative vertical velocities observed in the horizontal planes.

- The flow rate entering the discharge was calculated using the PIV data and then compared with that measured from the flow meter. In the far field, where the radial distance from the branch inlet was greater than approximately 20 mm, there was good agreement between calculated and measured flow rates. Closer to the discharge inlet, radial distance less than approximately 15 mm, the relative error increased dramatically. It was concluded that this was due, in part, to the two-phase flow structure distorting the particle displacement in the PIV images.

The flow structure seems to support the potential flow field assumption, which is used extensively in the literature, and in the theoretical analysis presented in Chapters 6 and 7. Although the potential flow assumption is an approximation of the actual complex flow structure, it provides a good approximation in modelling the critical liquid height. Future researchers may want to consider the effects of secondary elements, such as wake voriticies, or additional vortex structures in vertical planes, since these may help to explain some of the discrepancies found in past and present analyses of the gas entrainment phenomenon.

Dimensions in mm

Air-Water Interface

r measured from z axis for
all planes in all cases

$+ z$

Plane 9

Plane 8

Side Branch A

Plane 7

$+ y$

Plane 6

Plane 5

O_A (0, 0, 0)

Plane 4

Plane 3

O_B (0, -7.44, -17.960)

Plane 2

Plane 1

45º Branch B

Bottom Branch C

$- z$

O_C (0, -25.4, -25.4)

39.7 36 32 28 24 20 16 12 8 4
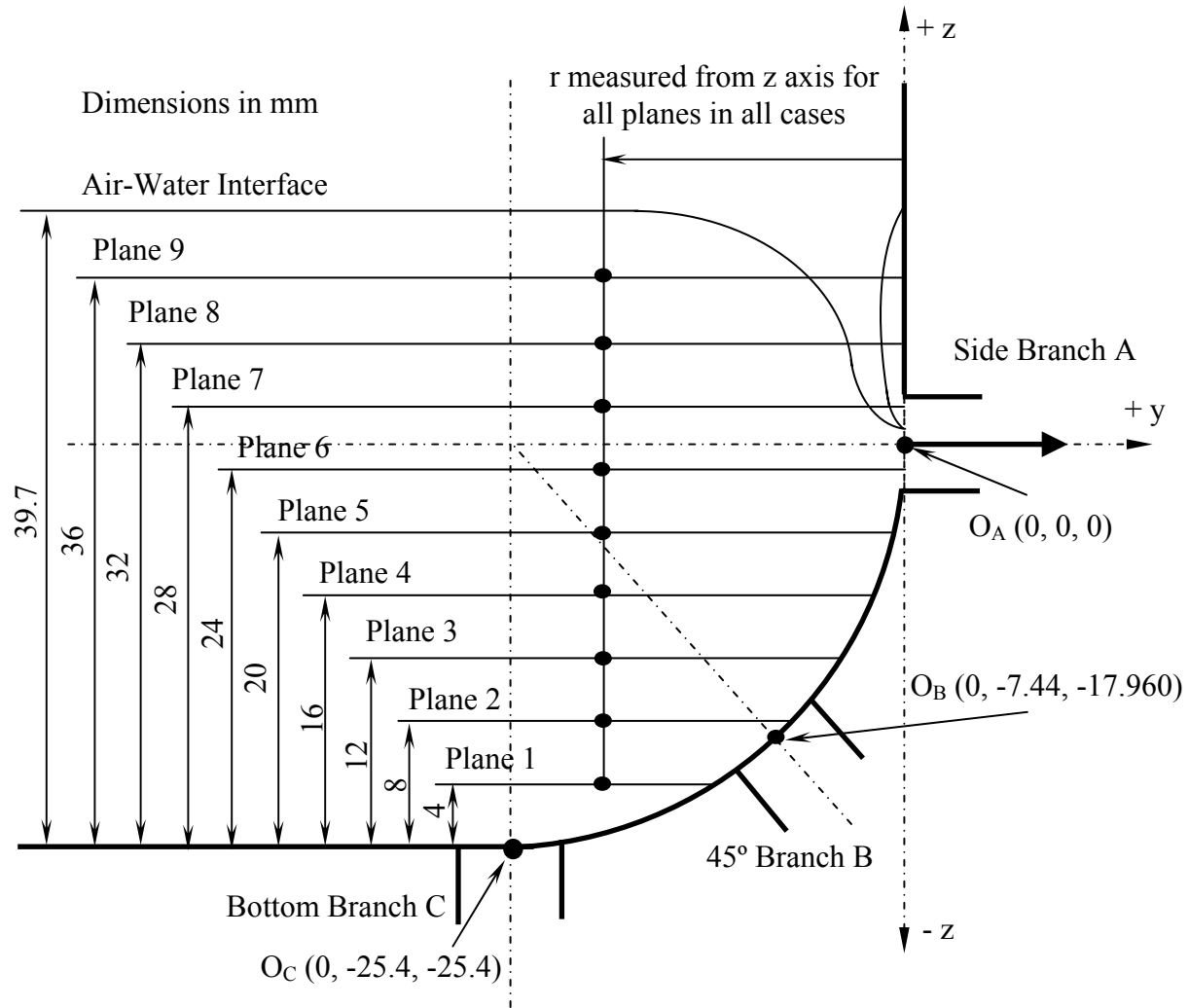
Figure 4.1 Experimental test section with the nine investigated planes.

(a) Plane 1.

(b) Plane 2.
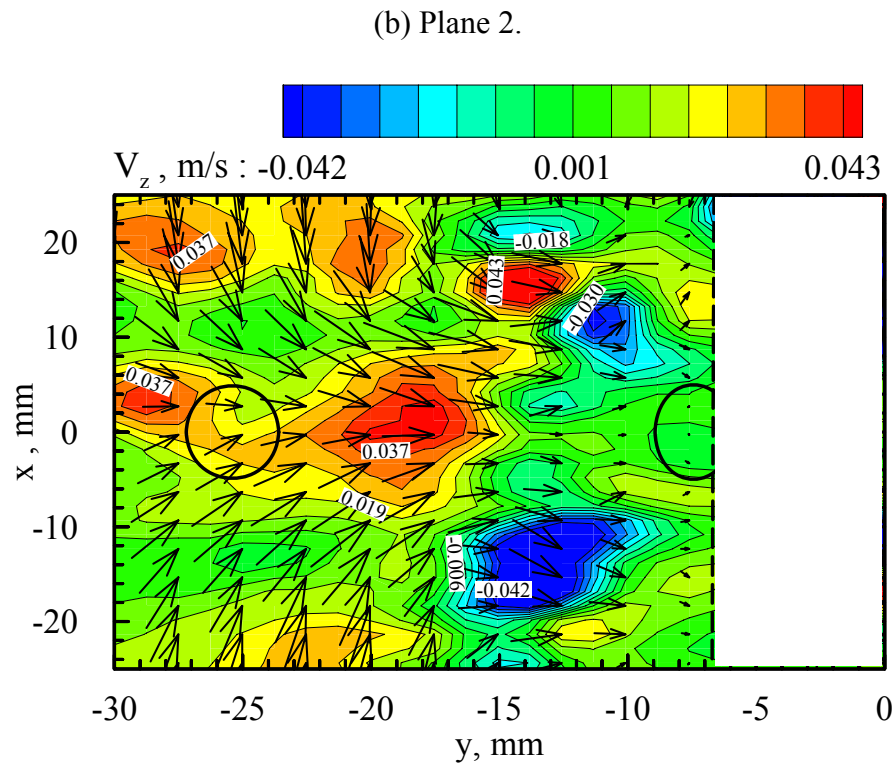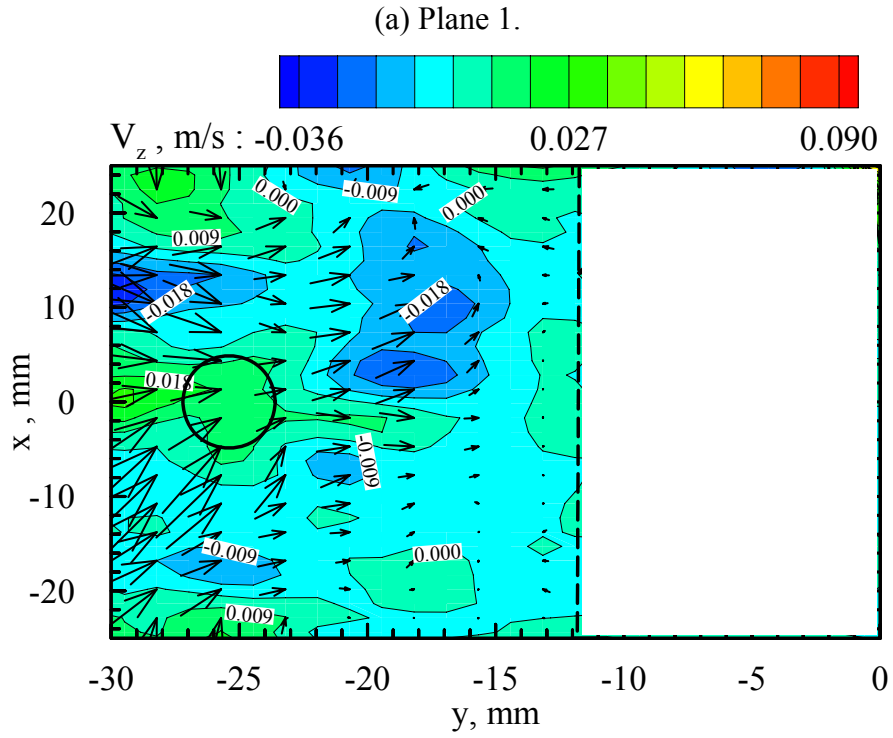
Figure 4.2 Velocity field in horizontal planes number 1 and 2 in case 1r.

(a) Plane 3.

(b) Plane 4.
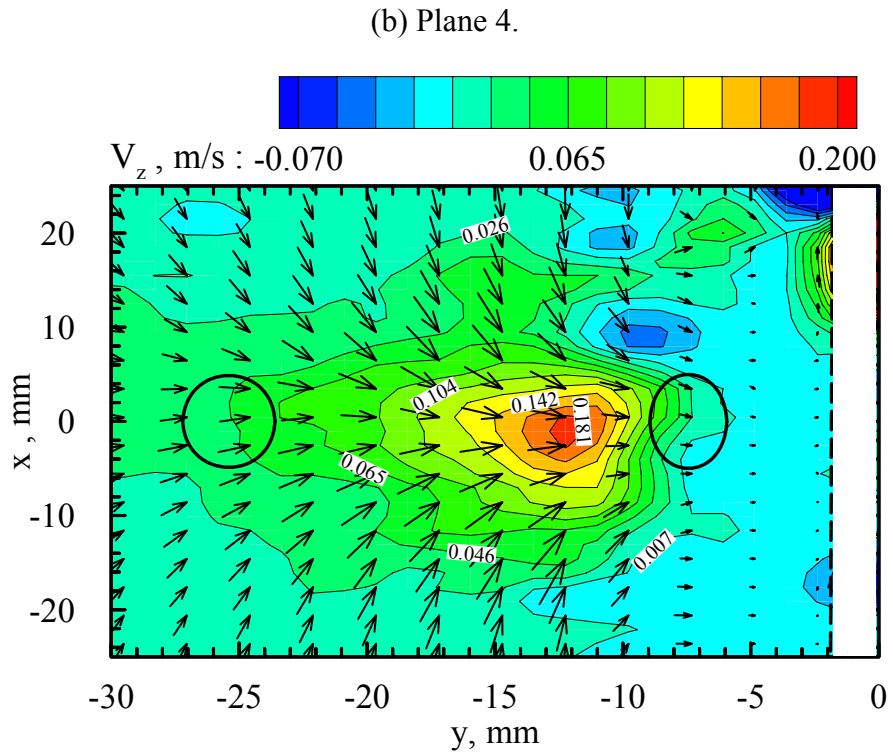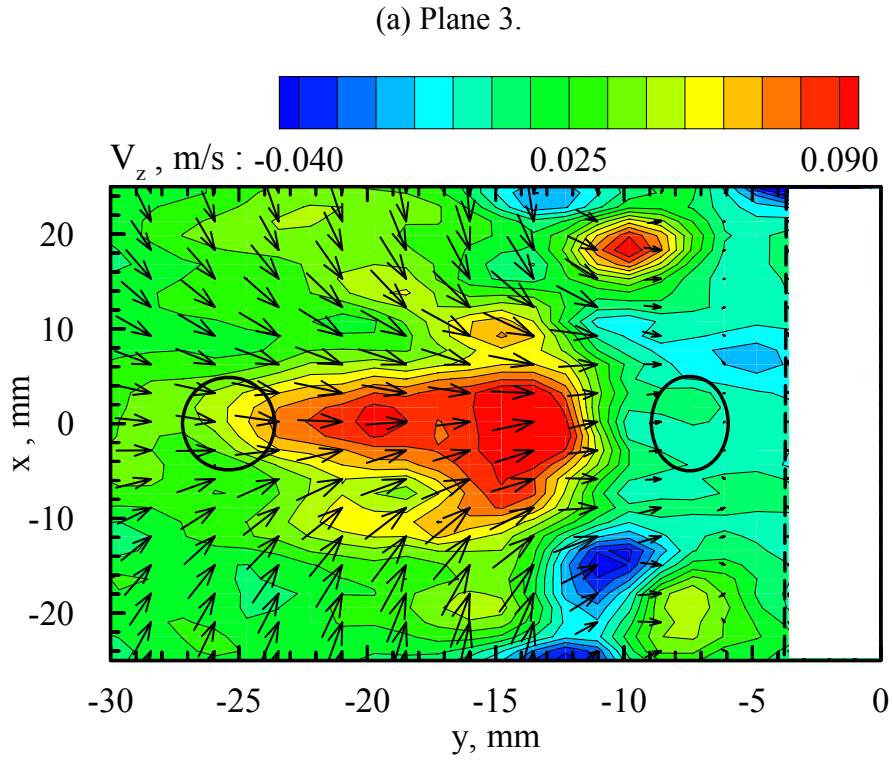
Figure 4.3 Velocity field in horizontal planes number 3 and 4 in case 1r.

(a) Plane 5.

(b) Plane 6.
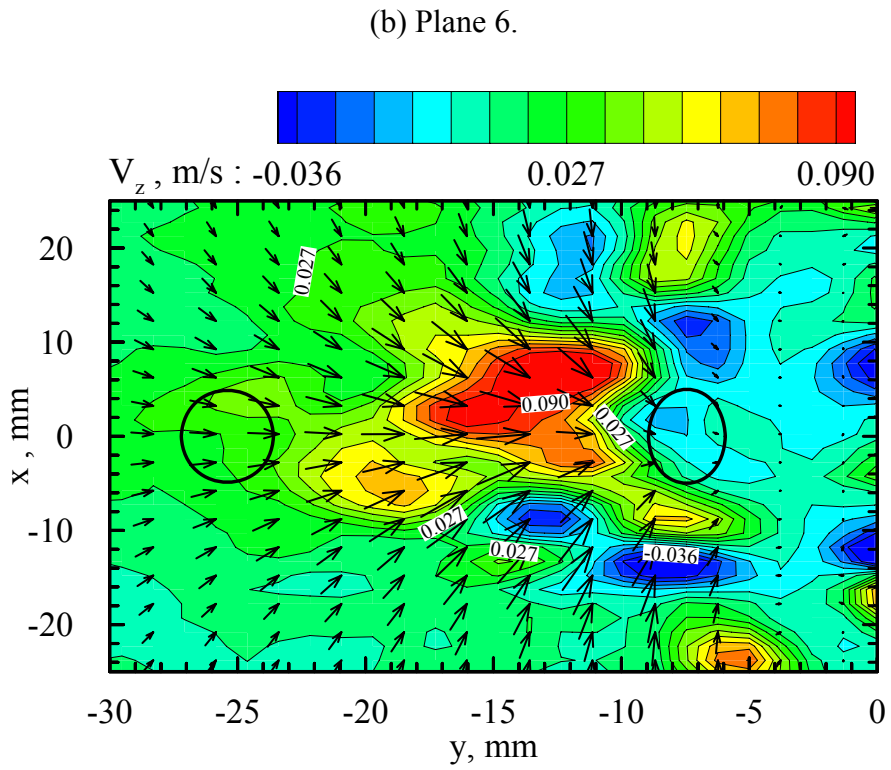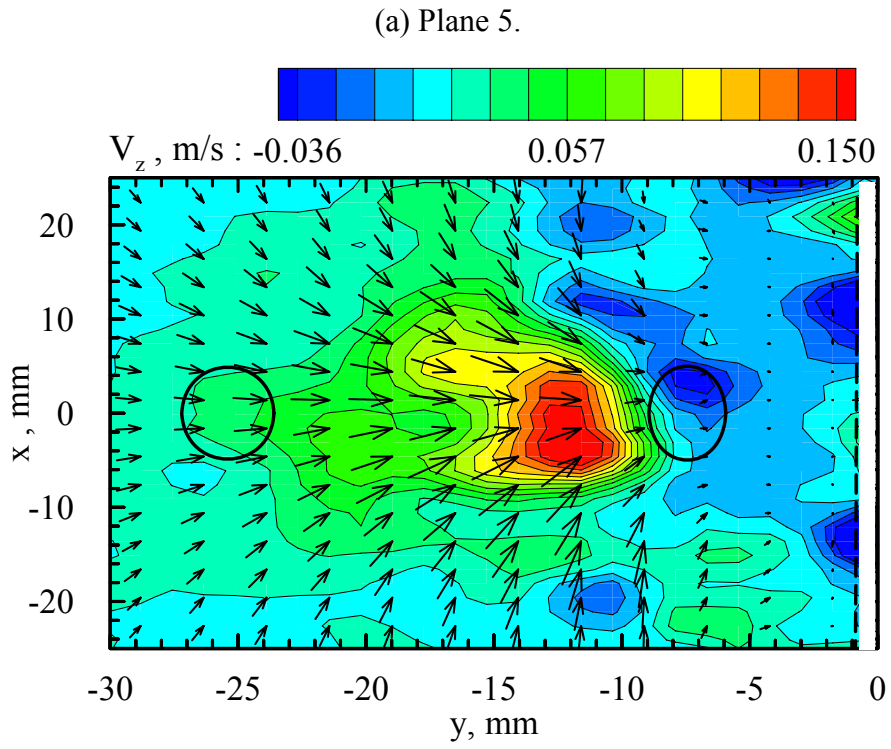
Figure 4.4 Velocity field in horizontal planes number 5 and 6 in case 1r.

93

(a) Plane 7.

(b) Plane 8.
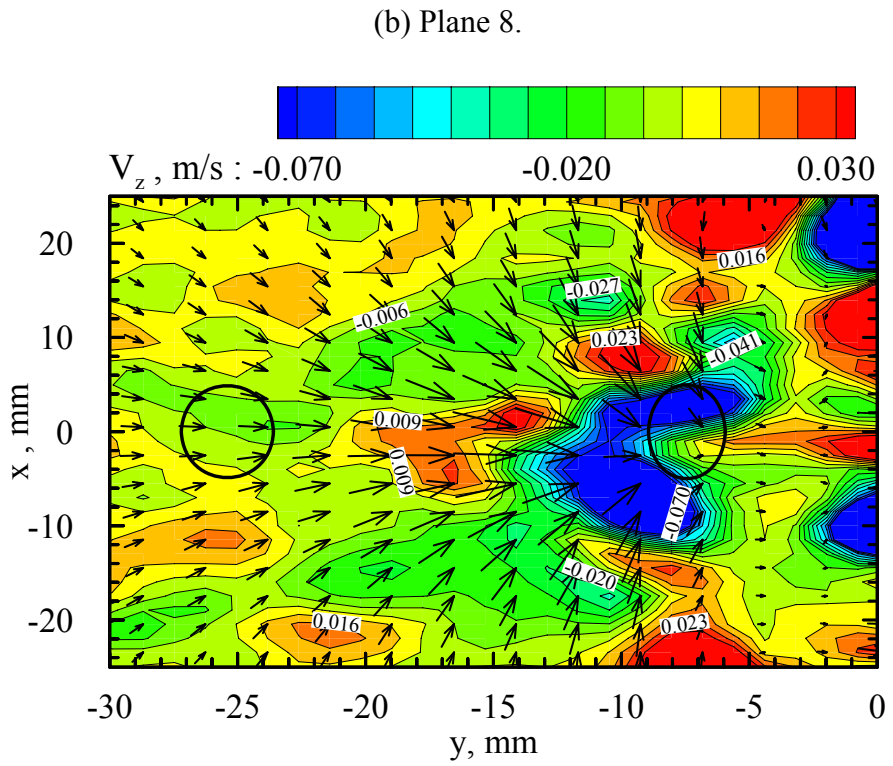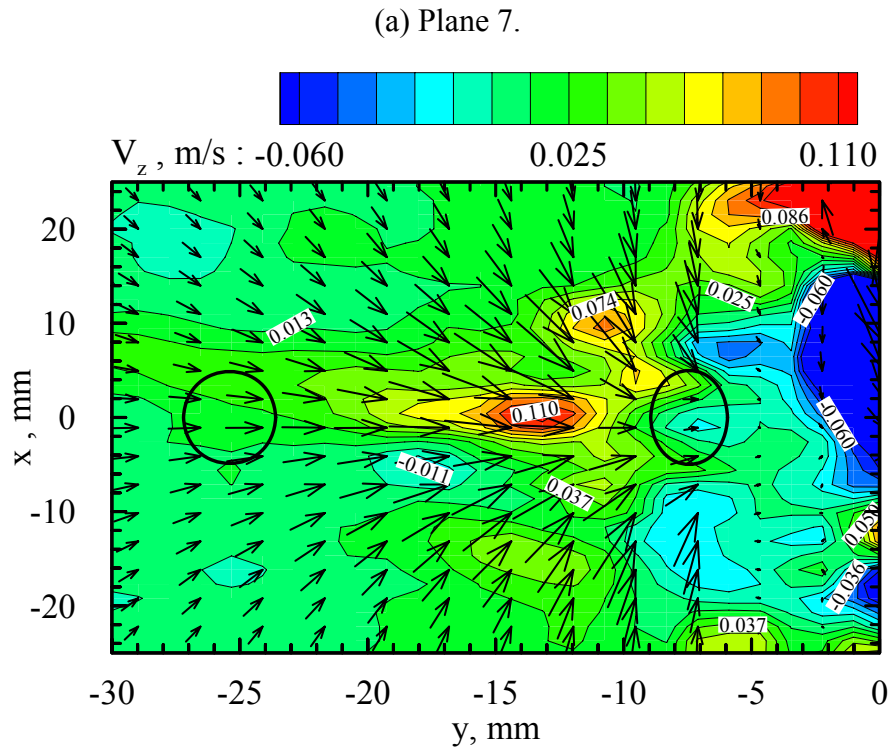
Figure 4.5 Velocity field in horizontal planes number 7 and 8 in case 1r.

94
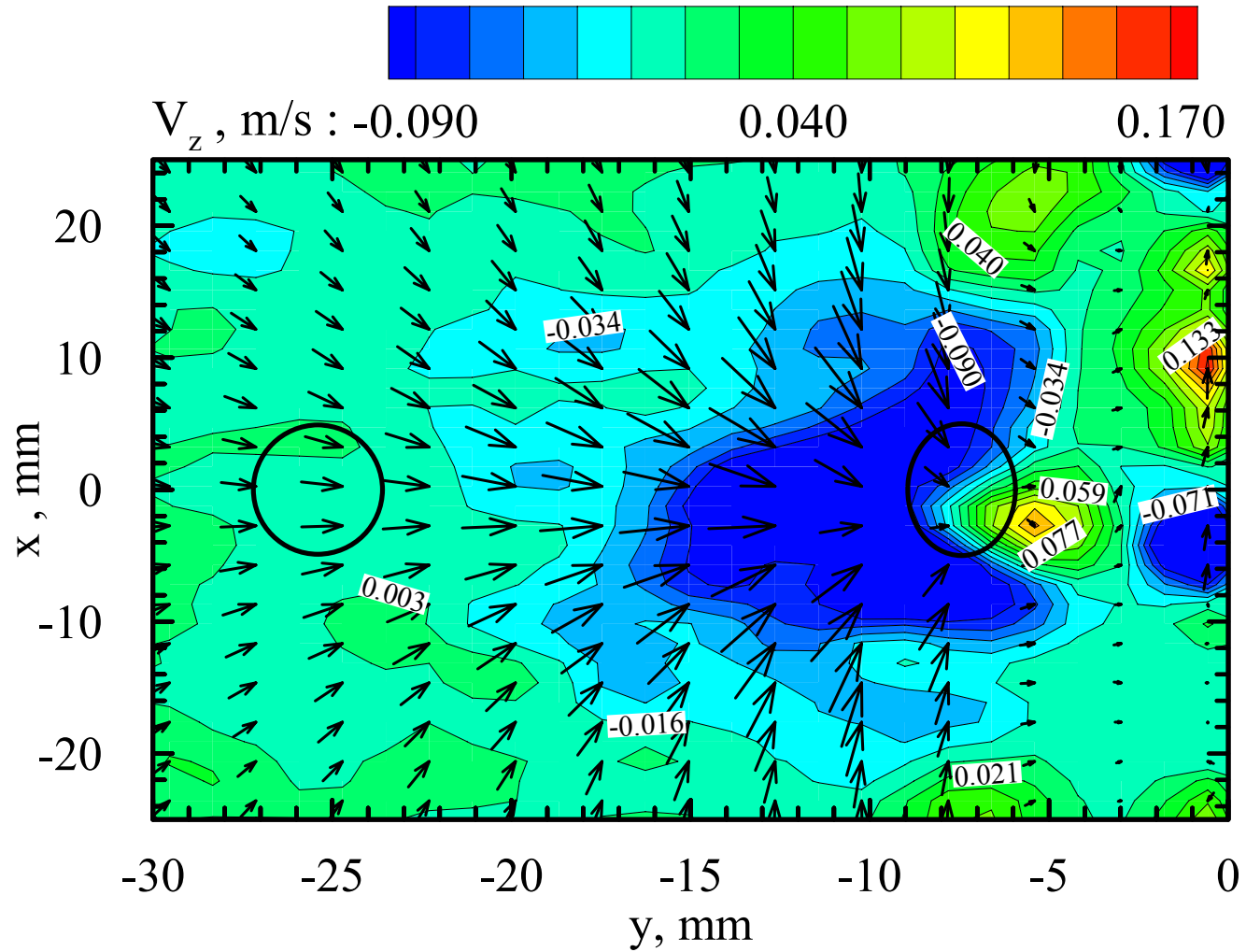
Figure 4.6 Velocity field in a horizontal plane number 9 in case 1r.
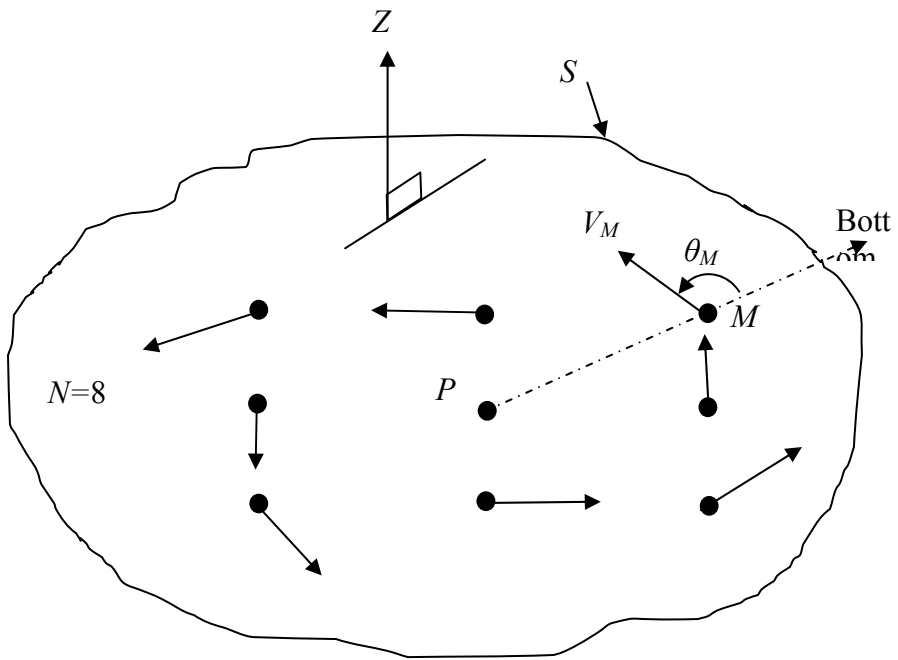
Figure 4.7 Schematic representation of the terms involved in Γ-criterion.

(a) 8-point circulation vorticity in plane 1.
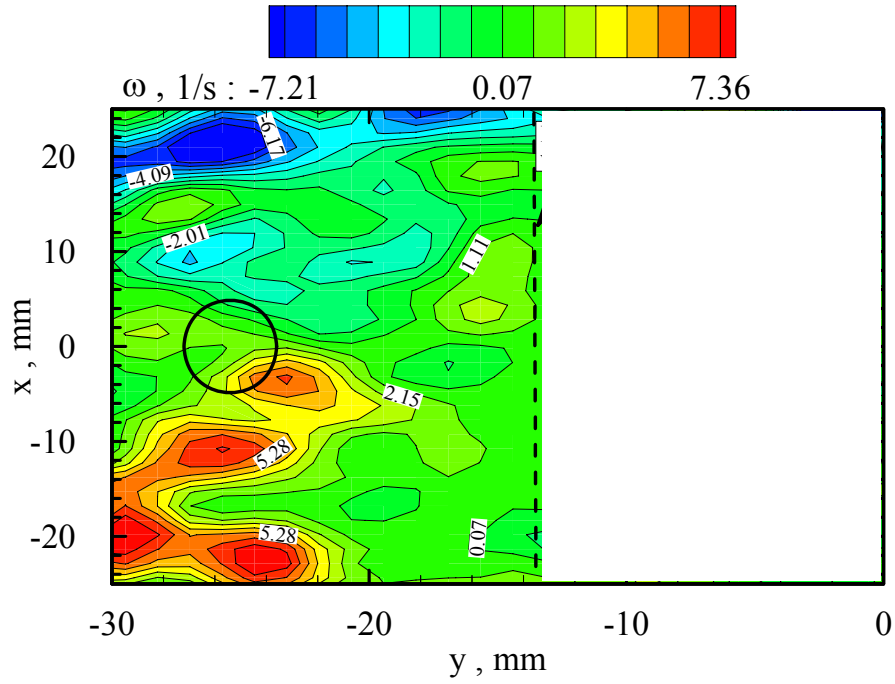
(b) Vortical structures based on λ_2 criterion in plane 1.
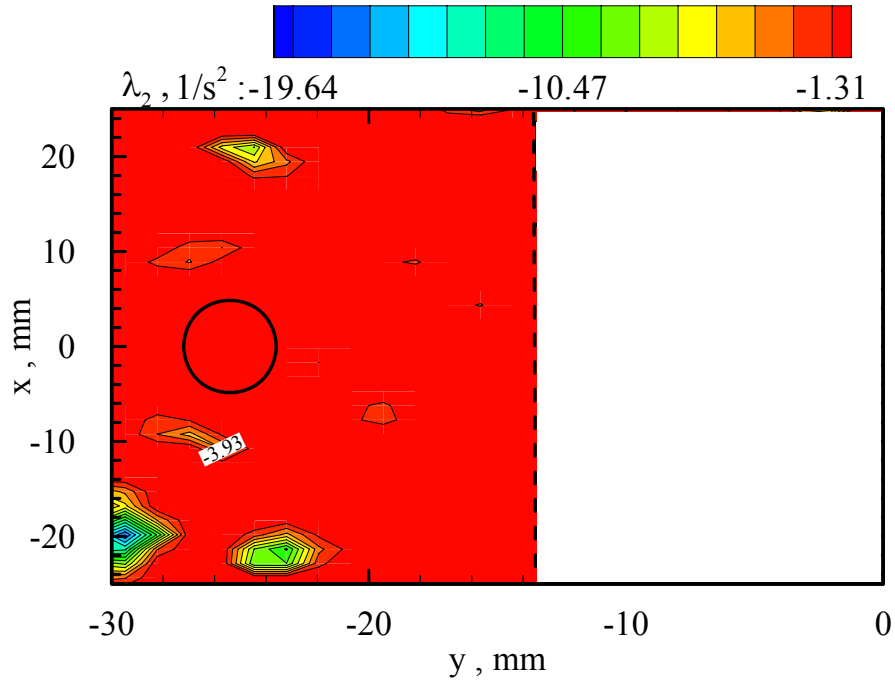
Figure 4.8 Vorticity field in a horizontal plane number 1 in case 1r calculated based on 8-point circulation vorticity equation (a) and vortical structures based on λ_2 criterion (b).

(a) 8-point circulation vorticity in plane 2.
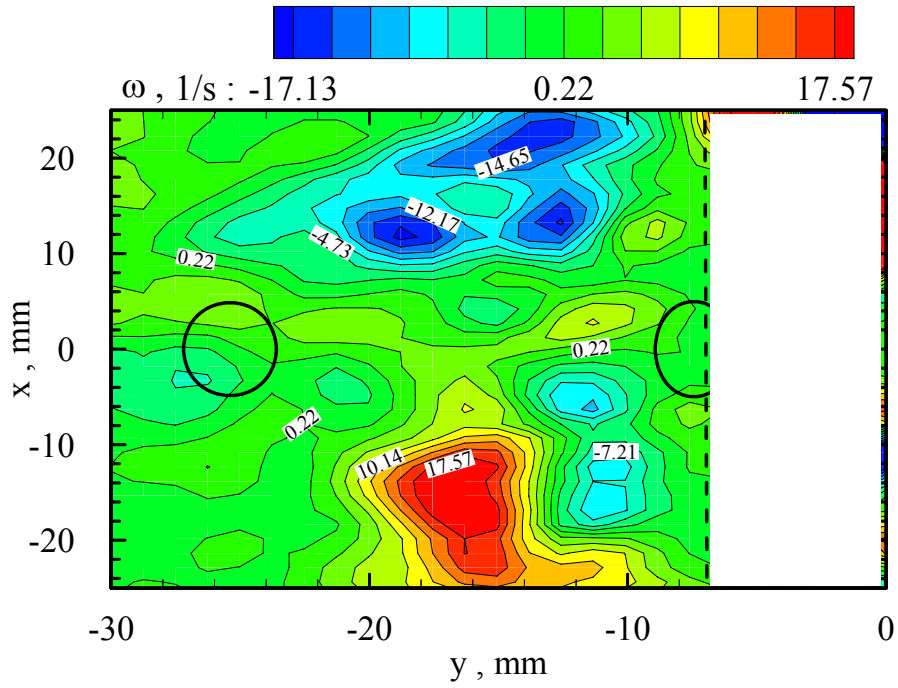
(b) Vortical structures based on λ_2 criterion in plane 2.
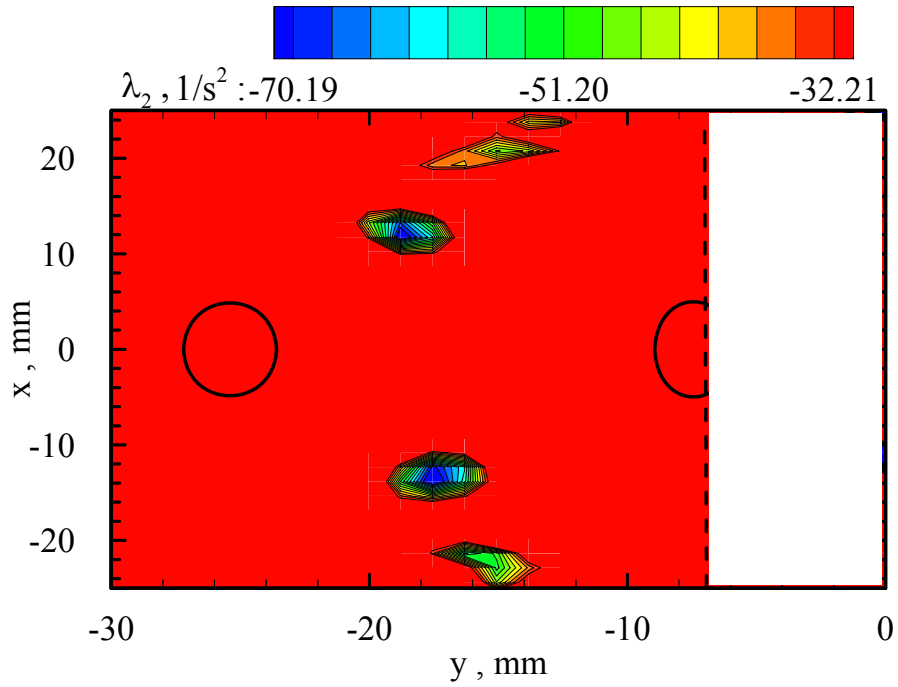
Figure 4.9 Vorticity field in a horizontal plane number 2 in case 1r calculated based on 8-point circulation vorticity equation (a) and vortical structures based on λ_2 criterion (b).

(a) 8-point circulation vorticity in plane 3.
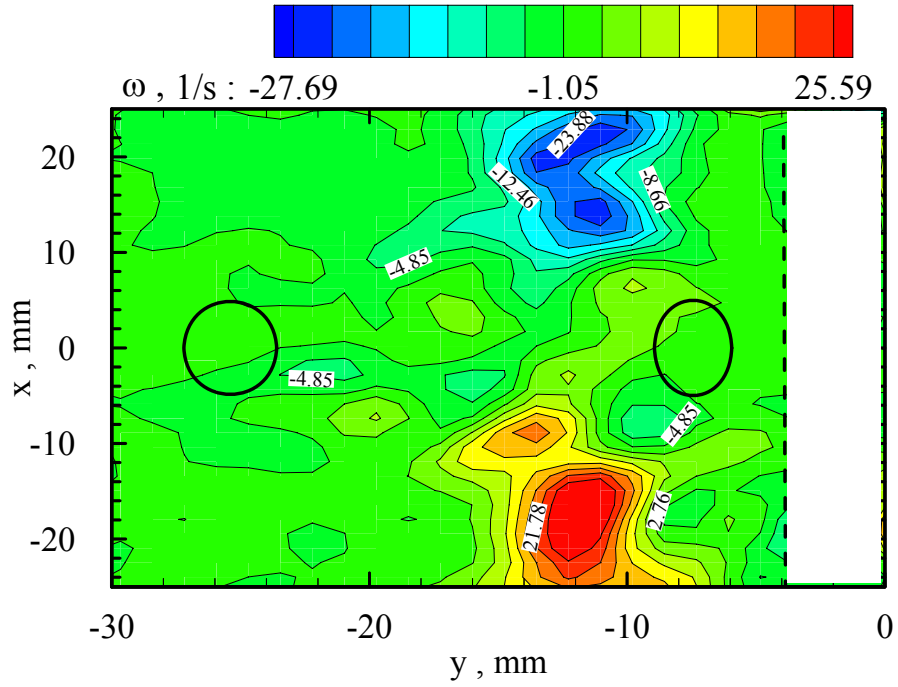
(b) Vortical structures based on λ_2 criterion in plane 3.
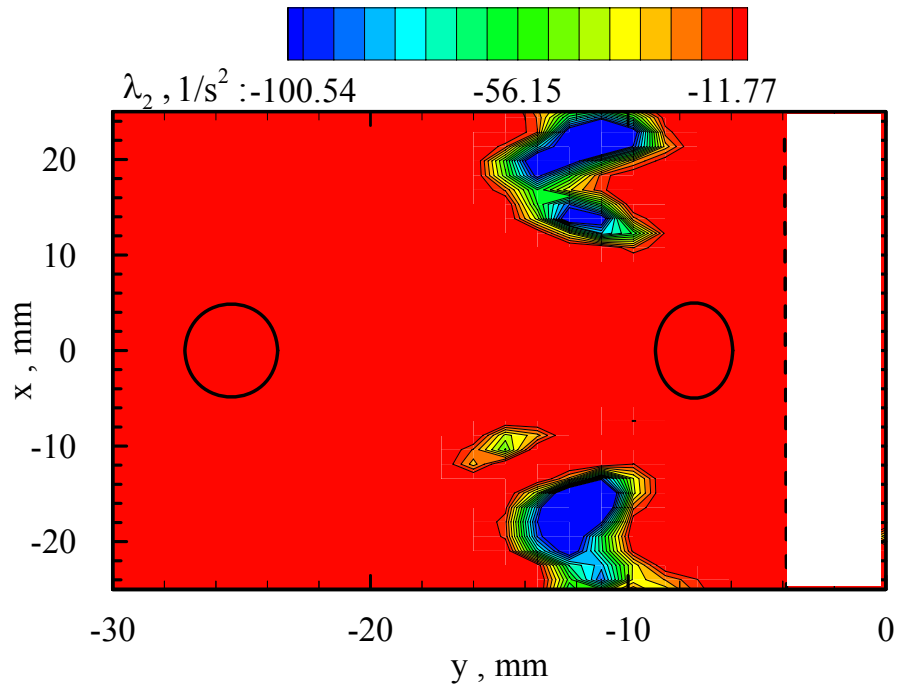
Figure 4.10 Vorticity field in a horizontal plane number 3 in case 1r calculated based on 8-point circulation vorticity equation (a) and vortical structures based on λ_2 criterion (b).

(a) 8-point circulation vorticity in plane 4.
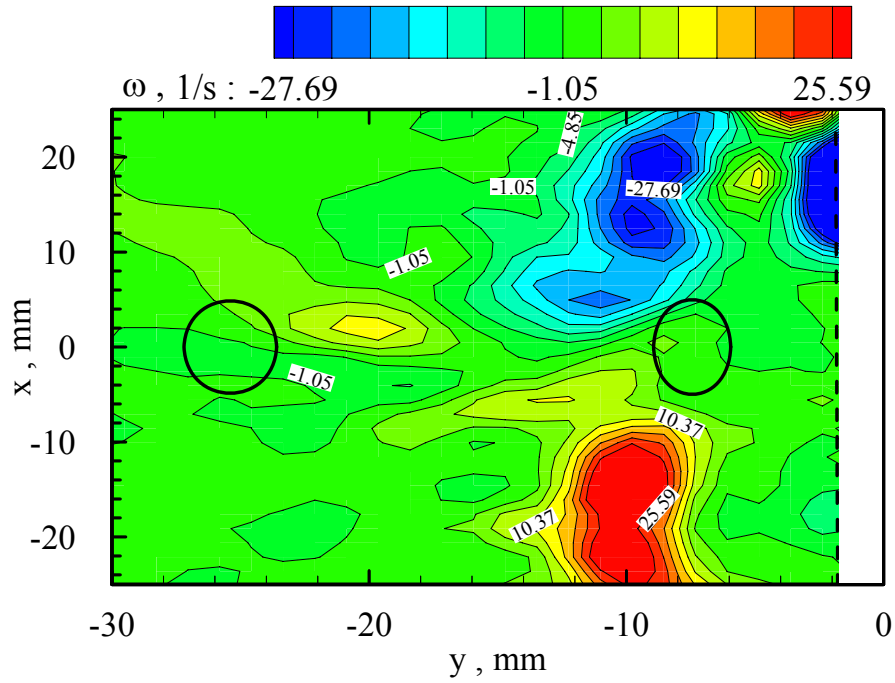
(b) Vortical structures based on λ_2 criterion in plane 4.
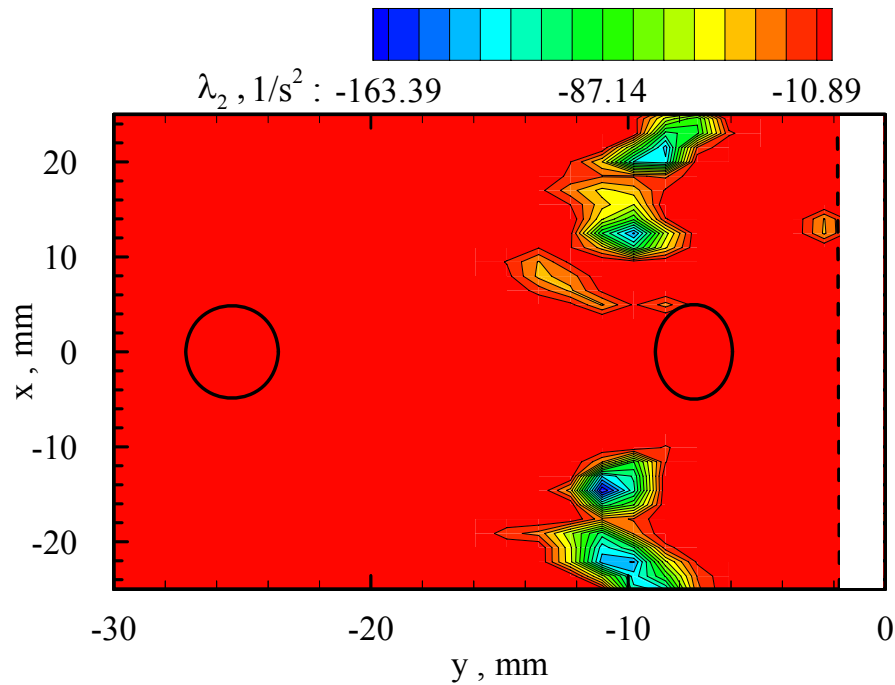
Figure 4.11 Vorticity field in a horizontal plane number 4 in case 1r calculated based on 8-point circulation vorticity equation (a) and vortical structures based on λ_2 criterion (b).

(a) 8-point circulation vorticity in plane 5.
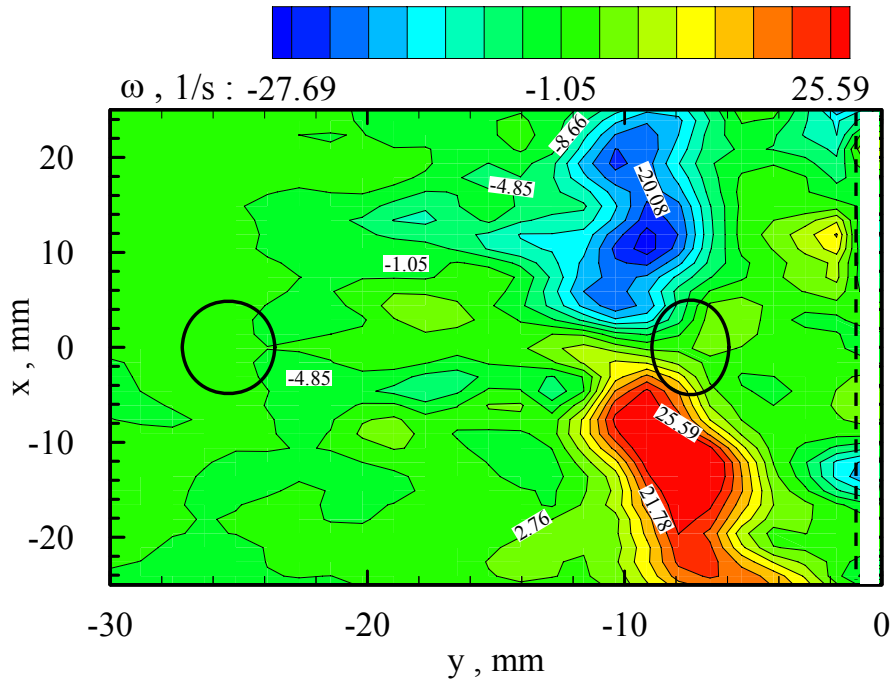
(b) Vortical structures based on λ_2 criterion in plane 5.
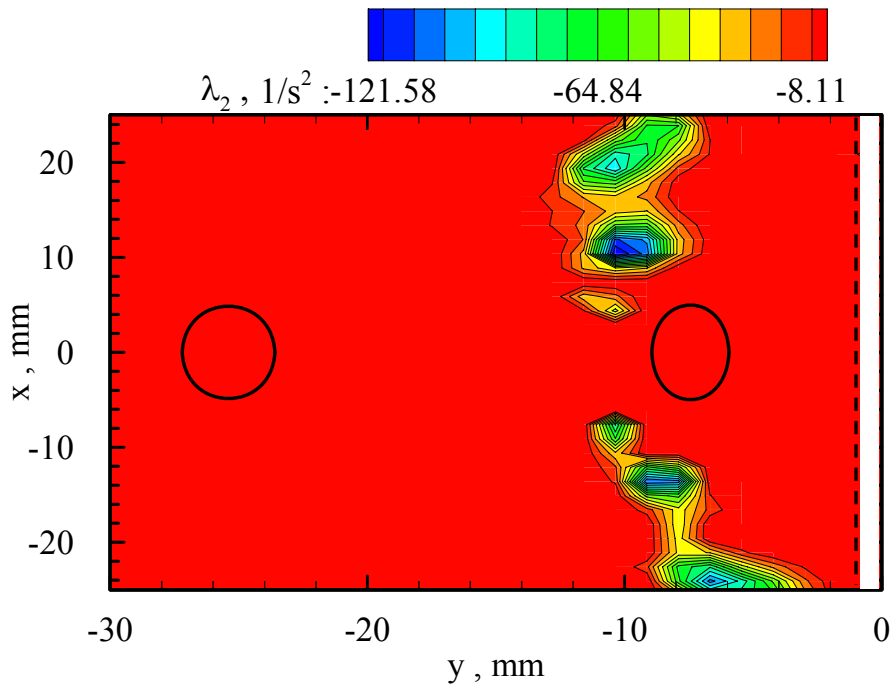
Figure 4.12 Vorticity field in a horizontal plane number 5 in case 1r calculated based on 8-point circulation vorticity equation (a) and vortical structures based on λ_2 criterion (b).

(a) 8-point circulation vorticity in plane 6.
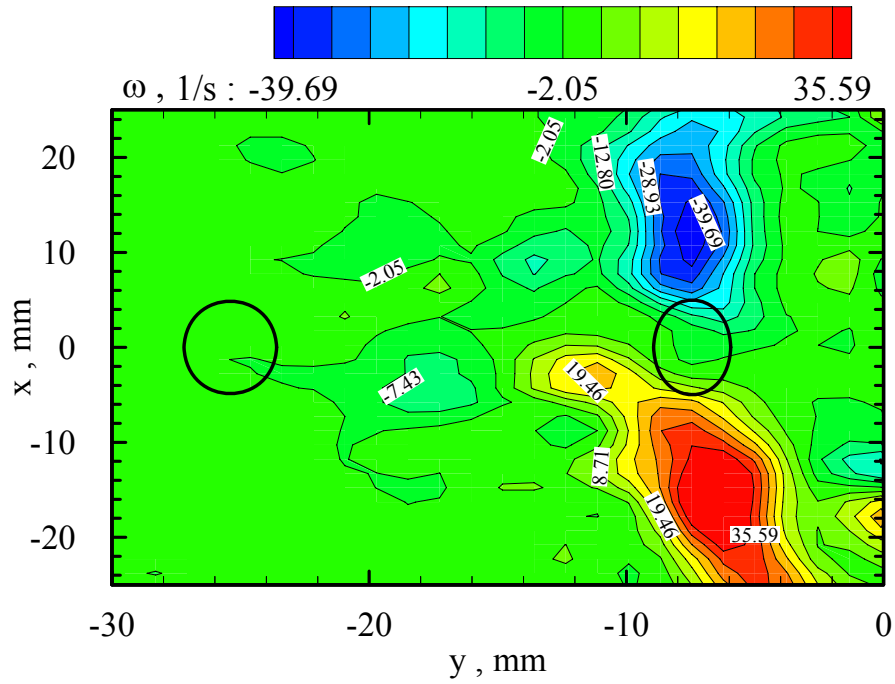
(b) Vortical structures based on λ_2 criterion in plane 6.
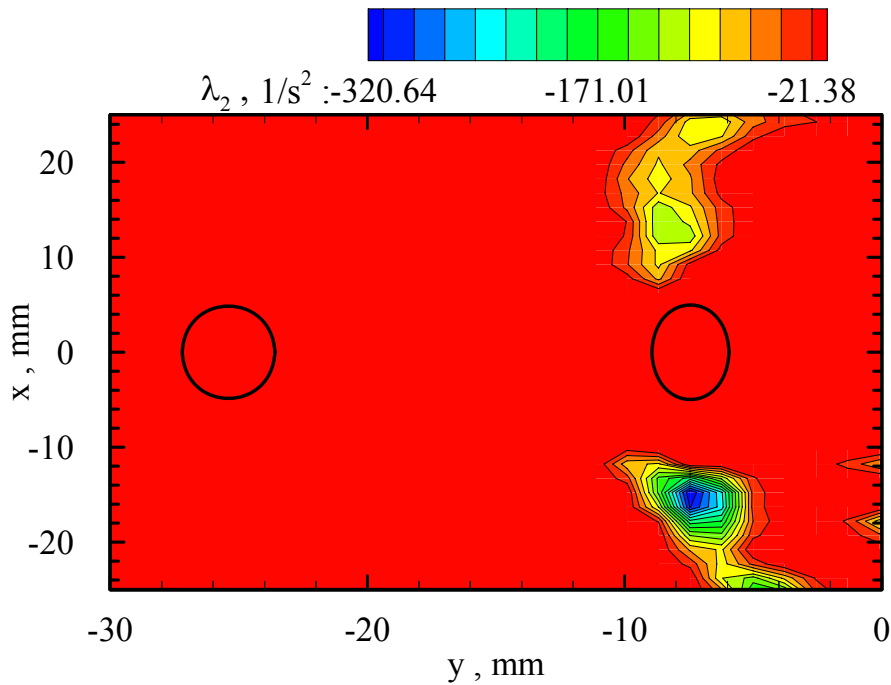
Figure 4.13 Vorticity field in a horizontal plane number 6 in case 1r calculated based on 8-point circulation vorticity equation (a) and vortical structures based on λ_2 criterion (b).

(a) 8-point circulation vorticity in plane 7.
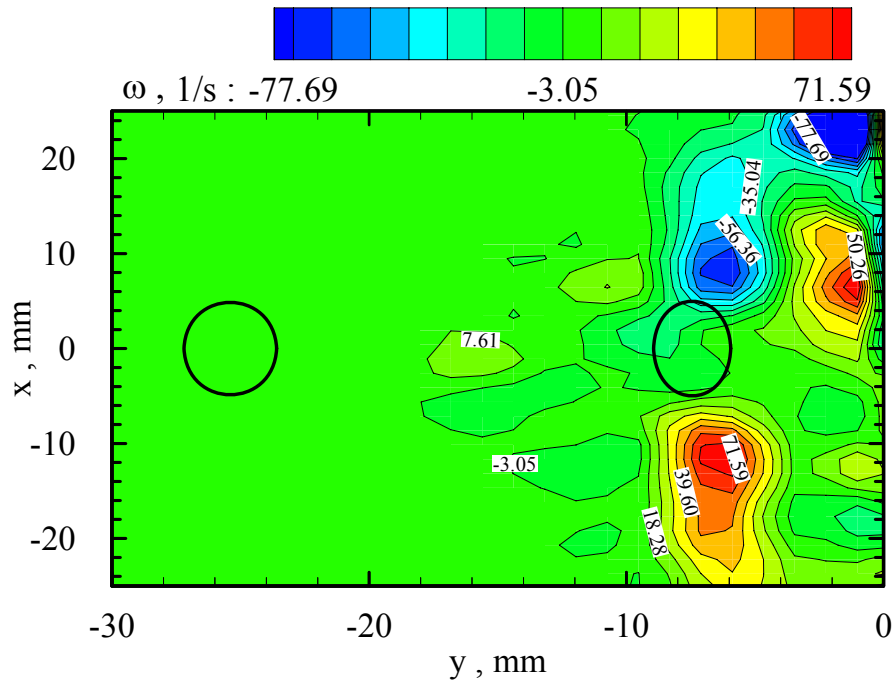
(b) Vortical structures based on λ_2 criterion in plane 7.
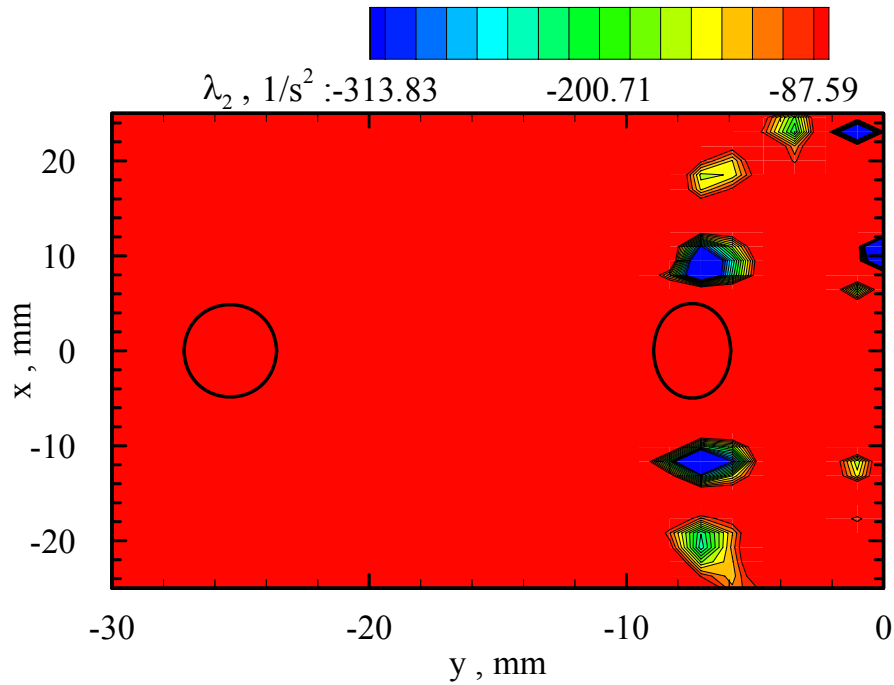
Figure 4.14 Vorticity field in a horizontal plane number 7 in case 1r calculated based on 8-point circulation vorticity equation (a) and vortical structures based on λ_2 criterion (b).

(a) 8-point circulation vorticity in plane 8.
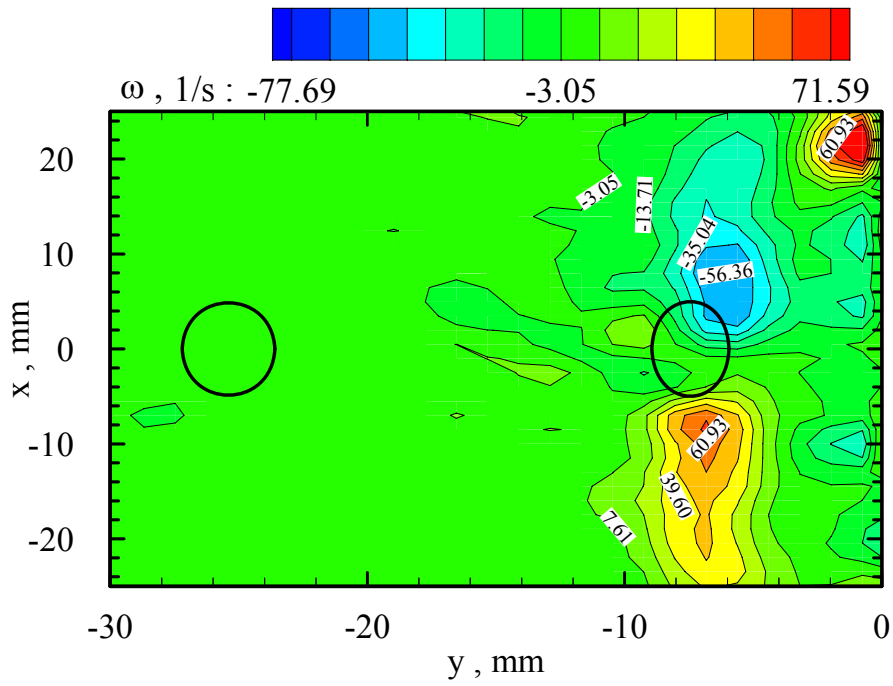
(b) Vortical structures based on λ_2 criterion in plane 8.
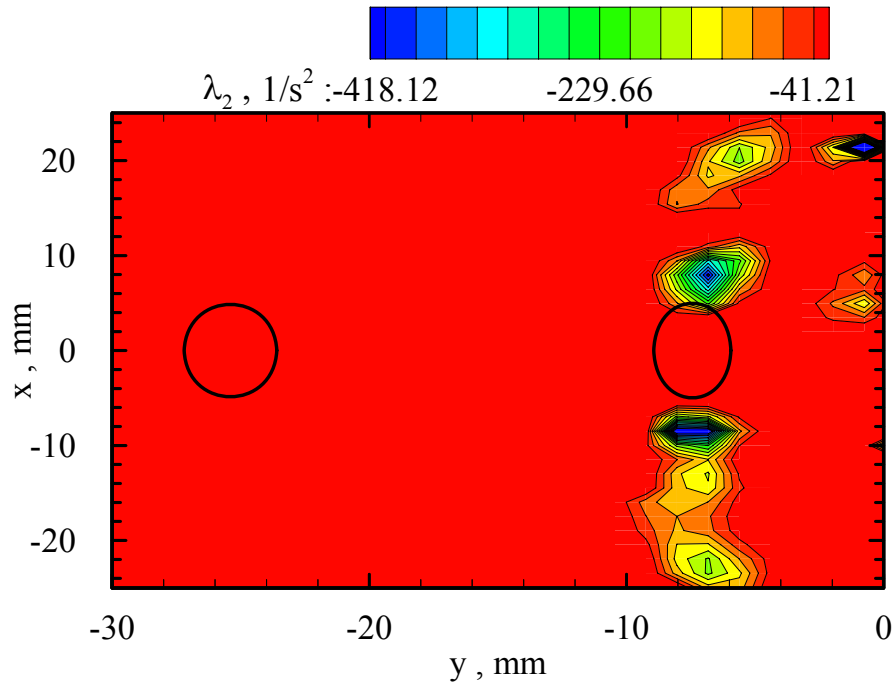
Figure 4.15 Vorticity field in a horizontal plane number 8 in case 1r calculated based on 8-point circulation vorticity equation (a) and vortical structures based on λ_2 criterion (b).

(a) 8-point circulation vorticity in plane 9.
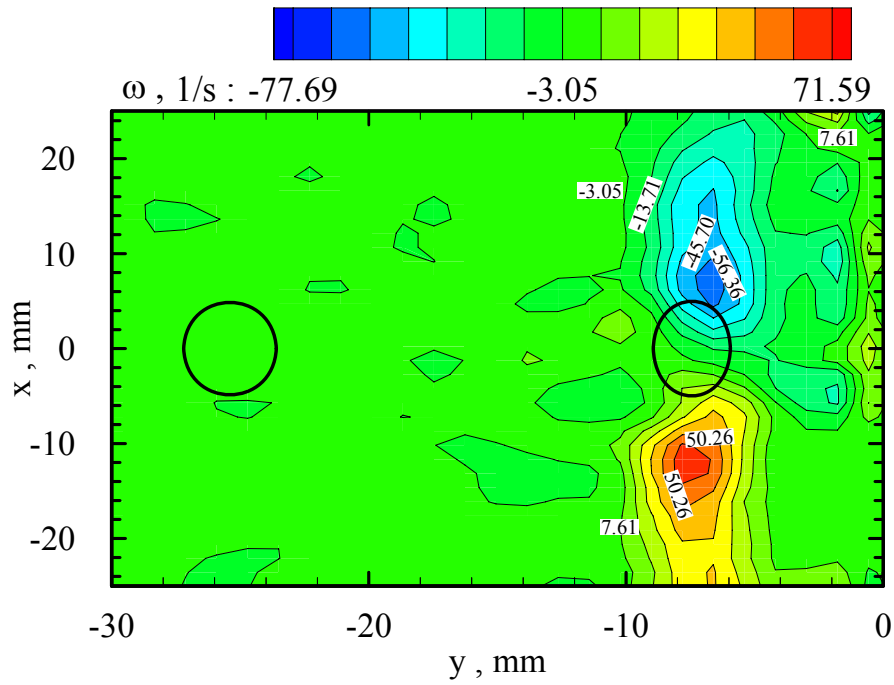
(b) Vortical structures based on λ_2 criterion in plane 9.
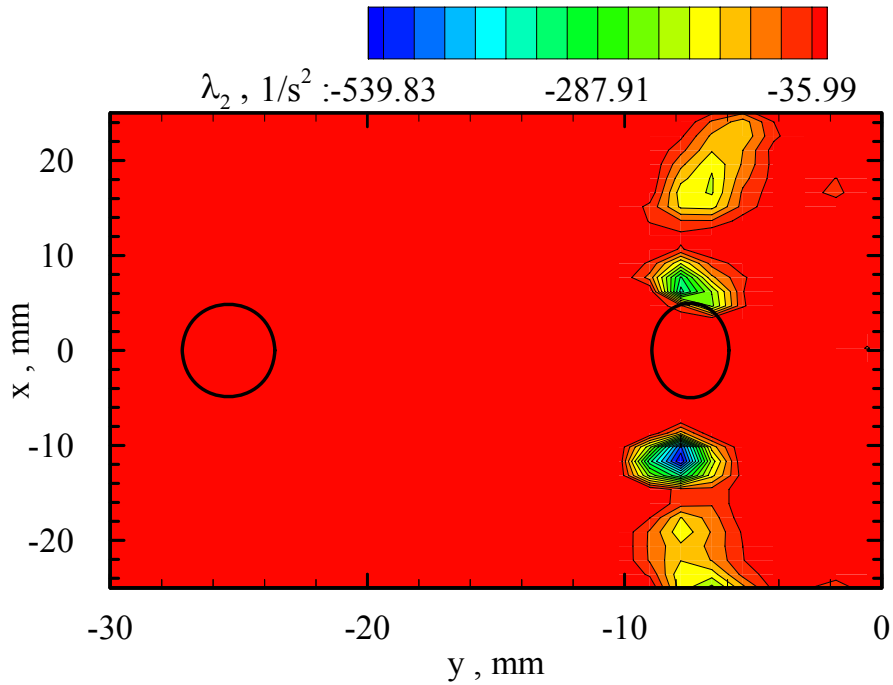
Figure 4.16 Vorticity field in a horizontal plane number 9 in case 1r calculated based on 8-point circulation vorticity equation (a) and vortical structures based on λ_2 criterion (b).
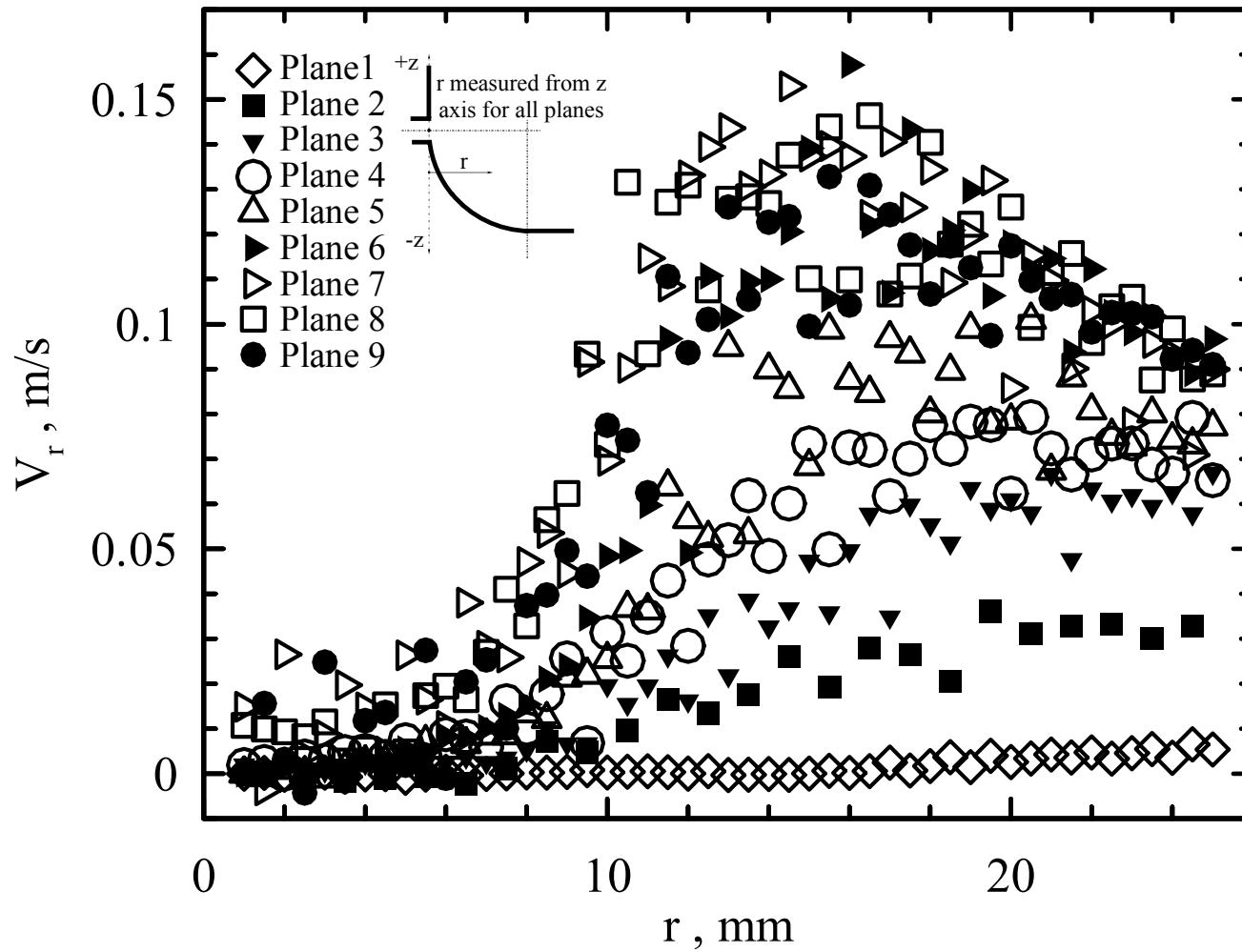
Figure 4.17 Effect of investigated plane height on average radial velocity change along *r*.
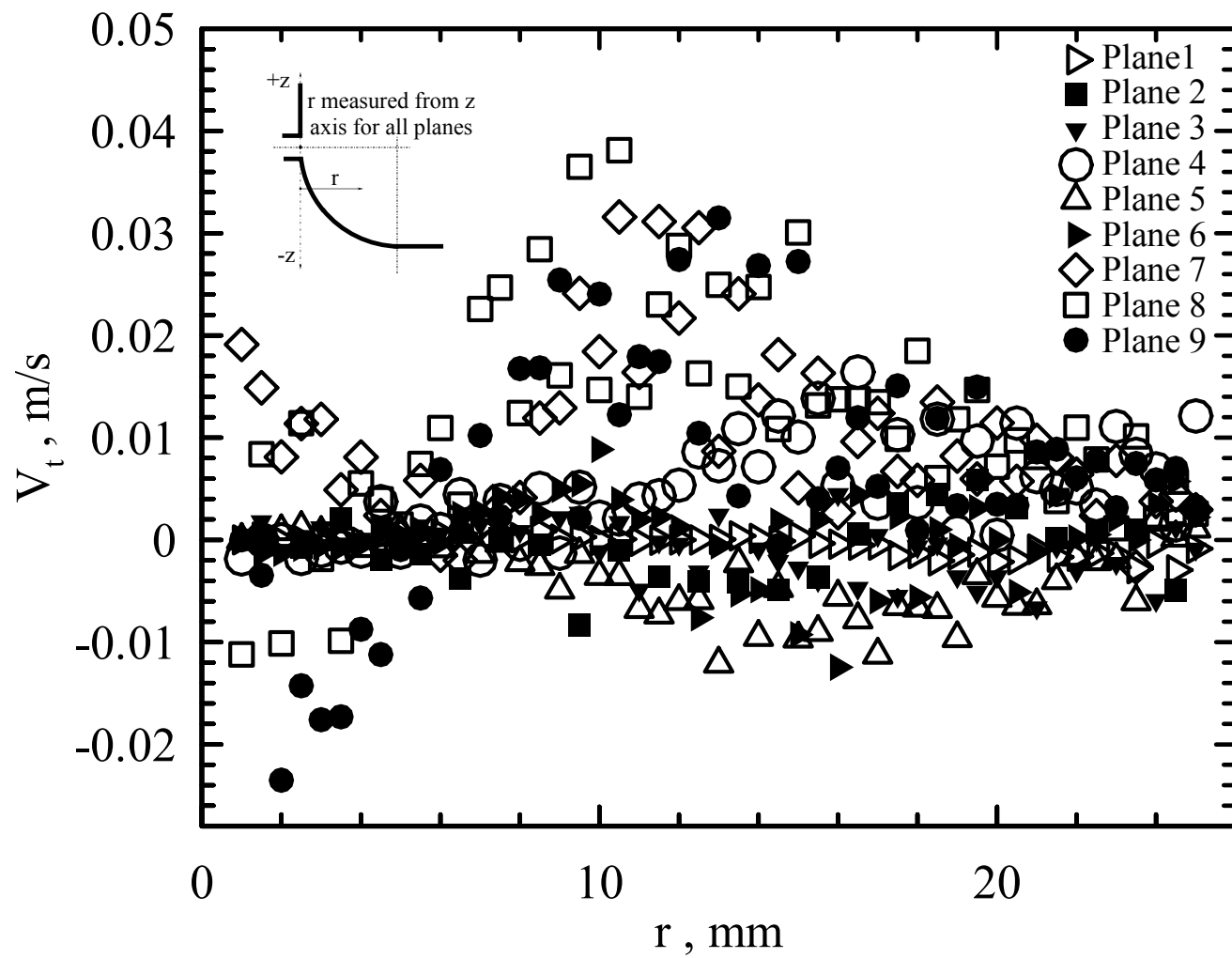
Figure 4.18 Effect of investigated plane height on average tangential velocity change along *r*.
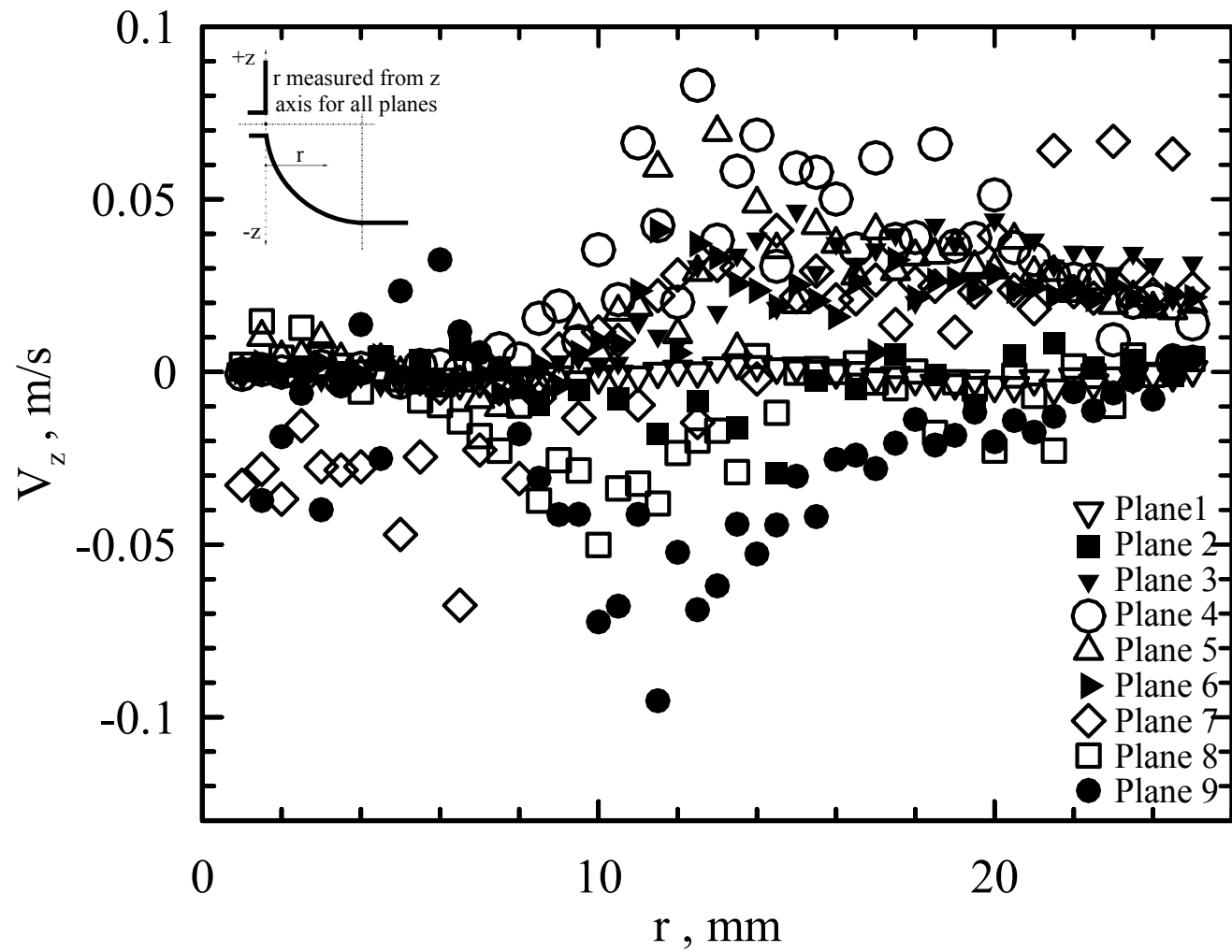
Figure 4.19 Effect of investigated plane height on average vertical velocity change along *r*.

(a) PIV estimated of flow rate in each plane.
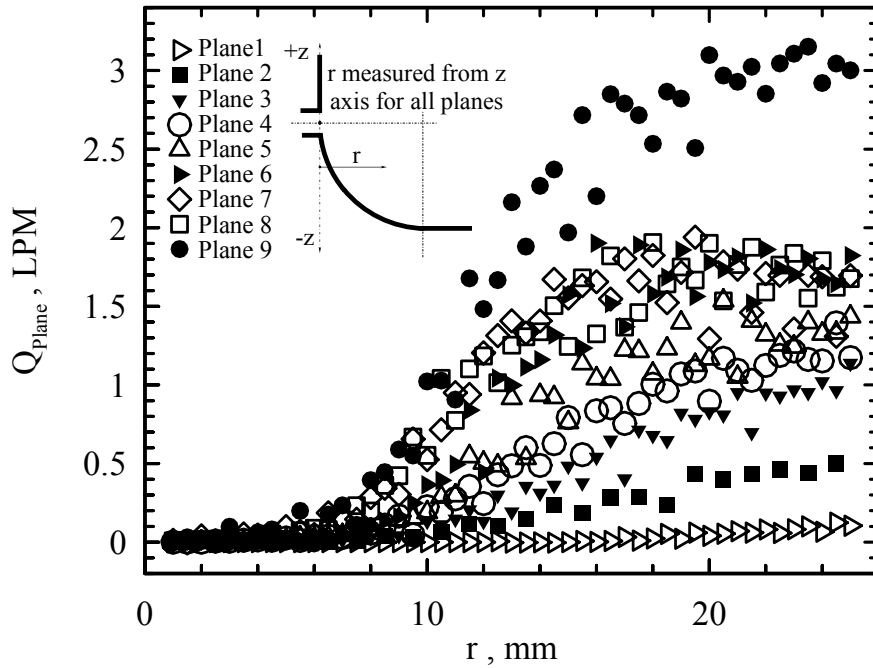
(b) % of flow rate in each plane to the total flow rate.
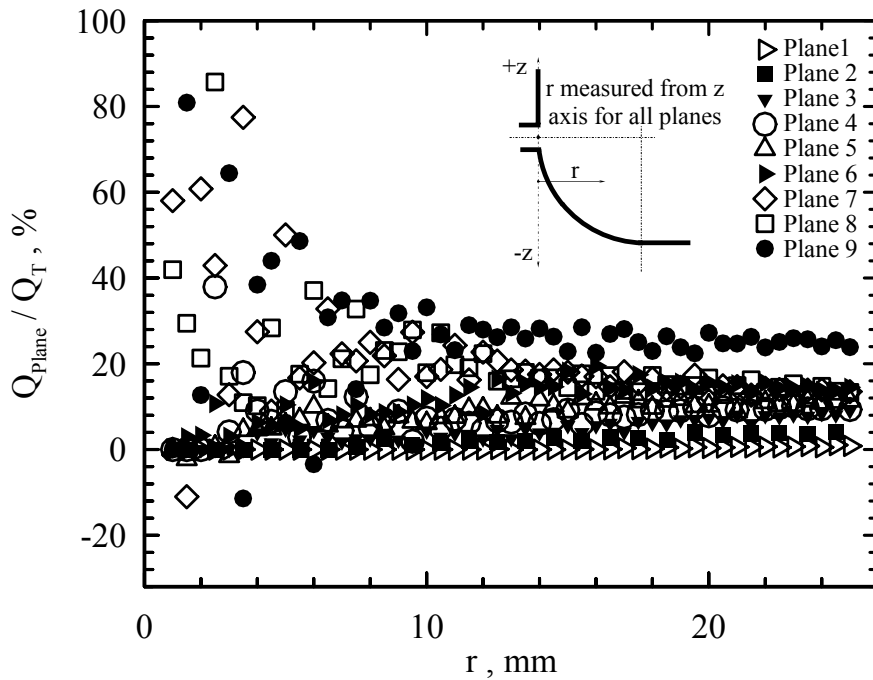
Figure 4.20 Change in plane flow rate contribution in the total flow rate along *r*. (a) PIV
estimated of flow rate in each plane. (b) % of flow rate in each plane
to the total flow rate.
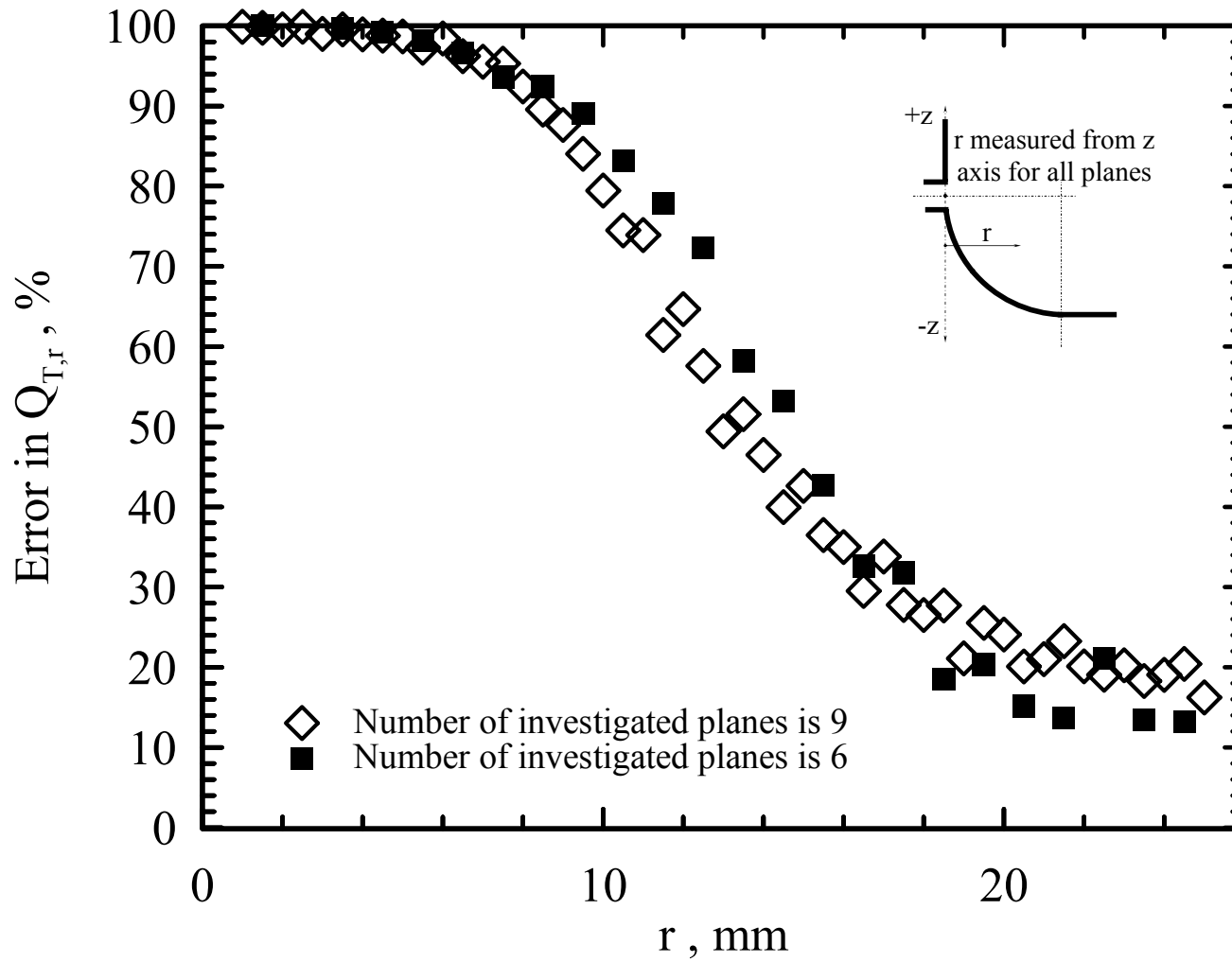
Figure 4.21 Flow rate error calculated for case 1 and case 1r.

Chapter 5

Experimental Results of OGE Flow Field - Dual and Triple Discharges

Six cases were investigated to explore the liquid side flow field at the onset of gas entrainment during dual and triple discharges, using stereoscopic PIV. The results for two cases, case 11 and case 13, will be presented here. The results of remaining cases are tabulated in the Appendix (will be provided with the last version of the thesis). A comparison between single, dual, and triple discharge cases, according to average velocities in the same planes and for two different Froude numbers in branch *A*, will be also presented. This is mainly to show the effect of the secondary branch or branches on the OGE flow field in the primary branch.

5.1 Dual Discharge Flow Structure

Case 11 consists of the side branch *A* and the bottom branch *C* being active and both having a high Froude number of 31.69 and 34.4, respectively. In this case, the onset of gas entrainment height was 39.75 mm measured from the bottom branch entrance, O_C (0, - 25.4, and - 25.4). To investigate the OGE flow field for the dual discharge scenario, the three dimensional two-phase flow structure was divided into nine investigated planes, as shown in Figure 4.1. The velocity fields were measured using stereoscopic PIV during continuous gas pull-through in branch *A* and single phase liquid flow in branch *C*.

5.1.1 Velocity Flow Field

Figure 5.1(a) shows similar trends for the in-plane velocity vectors as found in the single discharge cases. In the single discharge, the in-plane vectors starts with relatively low values at $r = 30$ mm. The vectors increase in magnitude with decreasing r until approximately the middle distance of the plane width. The magnitude then decreases until it reaches almost zero, near $r \approx 0$, near the side branch entrance. The secondary discharge branch C works as a sink and the single discharge in-plane velocity trend repeats twice. In Figure 5.1(a), the trend is shown in the in-plane velocity vectors which are directed toward the right side boundary, called the side branch region, where $- 23$ mm $< y < - 12$ mm and x $= \pm 25$ mm. This trend is also shown where y $< - 23$ mm and x $= \pm 25$ mm, and the flow is directed toward the bottom branch C, called the bottom branch region, and follows an almost axisymmetric path. These two regions are easily distinguished. The two regions, side branch and bottom branch, also show similar in-plane velocity vector trend in plane 2. The region included in ($- 5$ mm $< x < 5$ mm) and ($- 15$ mm $< y < - 7$ mm), called the central region, shows a lower in-plane velocity than the side branch region. The flow in this region tends toward the side branch entrance by following a vertical path and hence dramatically reducing its in-plane magnitude. In planes 3 to 5, Figures 5.2(a) to 5.3(a), the bottom branch effect is still evident as the component of the in-plane velocity in the y direction decreases. This causes the vectors not to be directed toward the side branch entrance when comparing with the single discharge case, Figures 4.3 and 4.4(a). The effect of the bottom branch was not evident in the velocity in planes 6 to 9, Figures 5.3(b) to 5.5. These in-plane velocity fields are similar to the single discharge case as shown in Figures 4.4(b) to 4.6.

Planes 1 and 2 in Figure 5.1 show a large area of negative V_z, which indicates the dominance of the bottom branch effect in these planes. In planes 3 to 5, each of the two branches started to show their effects in localized regions. A negative value of V_z was recorded near the bottom branch, while a positive value of V_z was recorded near the side branch, as shown in Figures 5.2 and 5.3(a). In plane 6, Figures 5.3(b) shows negligible effects of the side branch on V_z, because plane 6 is located at the same height as the side branch. However the effect of the bottom branch on V_z in its region is more evident. In plane 7, Figures 5.4(a), show a negative value of V_z distributed almost in the whole plane with an average value of $-$ 0.12 m/s, whereas the same plane 7 in the single discharge case showed almost an entirely positive value of V_z, and this highlights the influence of the bottom branch. Plane 8 in Figure 5.4(b) shows a negative value of V_z, similar to the single discharge case but with a wide range and a maximum value of - 0.19 m/s, which is two and half times greater than the single discharge case. Plane 9 in Figure 5.5 also shows a negative value of V_z similar to the single discharge case, and the magnitude indicates that the bottom branch effect is diminished at that height.

5.1.2 Vorticity Flow Field

A similar vorticity flow field as in the single discharge case was observed. Two counter rotating vortices were produced near the test section edges, as shown in planes 1 to 9 in Figures 5.6 to 5.14. The vorticity changes with the plane height. In plane 1, where the bottom branch is dominant, the ratio of the value of the vorticity in dual discharge to the value of the vorticity in single discharge was 7. This ratio is decreased to 5 in plane 2, 2 in planes 3 and 4 and almost 1 in planes 5 to 9. The strength of the vortex depends on

the flow rate represented by its plane, higher flow rate resulting in higher vorticity. As a result, the bottom branch increased the flow rate of the lower planes. Therefore, a higher vorticity value was found in the planes 1 to 4. A few satellite vortices were also observed near the bottom branch, in planes 1 to 5. After which, the effect of the bottom branch was insignificant and these vortices were not observed in planes 6 to 9.

5.1.3 Average Velocities

Figure 5.15 shows the average radial velocity change along r for the nine investigated planes. Similar trends for the single discharge side branch are evident here. The radial velocity is relatively small at $r = 25$ mm, then its value increases with decreasing r until it reaches a maximum value around $r \approx 15$ mm. The magnitude then decreases until it reaches almost zero near $r \approx 0$, near the side branch entrance. The velocity near the fixed wall is smaller than the velocity far from the fixed wall, and average radial velocity in plane 7 was found to be the highest. This is due to the followings:

- Plane 7 is at the same height of the side branch and produces almost entirely radial velocity, V_r, when compared to the total velocity value.
- The flow comes vertically from the higher planes, 8 and 9, and tends to be radially oriented toward the side branch entrance.
- Plane 7 is far away from, the curved wall and its effects, and the surface tension in the air-water interface and its effects, which causes more free fluid motion.

The main difference in the dual discharge case is the negative values of V_r which were recorded in plane 1, where the bottom branch attracts the flow toward its center. This

114

effect extends to the higher planes hence the bottom branch reduces the average radial velocity but without achieving the negative values of V_r, as shown in the Figure 5.15. The average radial velocity ranged from -0.02 to 0.2 m/s in all planes.

Figure 5.16 shows the average tangential velocity change, along r, for the nine investigated planes. The data spread is located between ± 0.04 m/s. The dual data shows a greater range of average tangential velocity changes than in the single discharge. This indicates that more flow enters the planes. Plane 1 and 2 show the highest variation of the average tangential velocity, which is expected due to the presence of the satellite vortices caused by the bottom branch. The fluctuation in the average tangential velocity is returned to the two edge vortices accompanying each plane.

Figure 5.17 shows the average vertical velocity change, along r, for the nine investigated planes. Planes 3 to 6 have positive average vertical velocity and plane 7 has fluctuated values around zero while 1, 2, 8 and 9 have negative values. Planes 3 to 5 are located at a height lower than the side branch entrance and it is expected to have positive V_z values. Plane 6 passes through the side branch entrance but, its positive average vertical velocity could be explained as a result of the flow exchange between the planes, or the existence of a neutral point in the side branch entrance which attracts the flow from the lower planes. Plane 7 passes through the side branch entrance but its fluctuating V_z values are around zero because it is located at or closer to the neutral point. Planes 1 and 2 are greatly affected by the bottom branch flow (they are very close to that branch) which produces the negative V_z values. Similary, planes 8 and 9 show negative values of V_z because their location is close and higher than the side branch entrance. The trend of V_z, for planes 3 to 6 and 8 and 9, follows that of the single discharge case. Far away from

the side branch entrance, at $r = 25$ mm, the flow is mainly horizontal and the vertical flow between the planes is small. As the flow approaches the side branch inlet, near $r \approx 13$ mm, the vertical flow between the planes (3 to 6 and 8 and 9) increases and consequently increases the average vertical velocity. Planes 1 and 2 show a similar trend but in an opposite direction. Since they are highly affected by the bottom branch, V_z in these planes is small far away from the bottom branch entrance at $r = 0$ mm. As the flow approaches the bottom branch inlet, near $r \approx 20$ mm, the vertical flow between the planes increases and consequently increases the value of V_z.

5.2 Triple Discharge Flow Structure

The triple discharge scenario, case 13, with the side branch A, the 45° branch B, and the bottom branch C being activated with a high Froude number of 31.69, 34.4, and 34.4 respectively, is discussed here. In this case the onset of gas entrainment height was 41.8 mm measured from the bottom branch entrance, O_C (0, - 25.4, and - 25.4). To investigate the OGE flow field for the triple discharge scenario, the three dimensional two-phase flow structure was divided into nine investigated planes, as shown in Figure 4.1, and their flow fields were measured using Stereoscopic PIV during continuous gas pull-through in branch A, with a single phase liquid flow in branches B and C.

5.2.1 Velocity Flow Field

With respect to the in-plane velocity, Figure 5.18(a) shows the velocity field for plane 1. A similar trend for the in-plane velocity in dual discharge case 11 was observed. The two regions, bottom branch region (left side where y < - 23 mm and x = ± 25 mm) and inclined and side branches region (right side where – 23 mm < y < - 12 mm and x = ±

25 mm), can be distinguished. The single discharge case 1r showed that, far away from the branch center the radial velocity is relatively small then its value increases with decreasing the distance from the branch center, then decreases again until it reaches zero near the branch center.   This trend was observed twice in each of the mentioned regions. The bottom branch region vanished in plane 2 in Figure 5.18(b). The region included in (– 5 mm < x < 5 mm) and (- 15 mm < y < - 7 mm) in plane 2, called the central region, shows a lower in-plane velocity than the others in this velocity field. This region is almost located at a central position between the three branches, and its velocity is a resultant of the effects from the three branches. Plane 3 in Figure 5.19(a), is located higher than the bottom and inclined branches. The central region and vertical velocity are affected by the three branches, because the flow tends to go to the inclined and bottom branches. This causes the central region to have a very low in-plane velocity. Planes 4 to 6 in Figures 5.19(a) and 5.20, show that the bottom branch effect still exists. The component of the in-plane velocity in the y-direction, V_y, is decreased and vectors are not directed toward the side branch entrance as when compared with the single discharge case in Figures 4.3 and 4.4(a). In these planes, the central region is noticeable until plane 7, Figure 5.21(a), where the side branch effect is dominant and the central region limited. The effect of the bottom and inclined branches does not show any changes in the in-plane velocity in planes 7 to 9 and they almost follow the same trend of the in-plane velocity in the single discharge case as shown in Figures 5.21 and 5.22.

With respect to the vertical velocity, plane 1 in Figure 5.18(a) shows a large area of negative V_z and indicates the dominance of the bottom branch in this plane. A balanced positive and negative V_z is shown in plane 2, Figure 5.18(b), which passes through the

inclined plane entrance indicating the balanced effect of the three branches at the same time on this plane. Plane 3 in Figures 5.19(a) shows a great area of negative V_z also indicating the dominance of the bottom and inclined branches in this plane, except some positive V_z spots which indicates that the side branch effect is extended to this plane. Planes 4 to 6, Figures 5.19(b) and 5.20, show the increase of the positive V_z spots indicating that the side branch effect increases while the bottom and the inclined branches effects decrease in these planes. Planes 7 to 9 show a negative value of V_z distributed almost in the whole plane with a larger peak value than the dual discharge case 11, as shown in Figures 5.21 and 5.22. The difference between the maximum V_z value in triple discharge case 13, and the maximum V_z value in dual discharge case 11, is a decrease in magnitude with increasing plane height.

5.2.2 Vorticity Flow Field

Similar vorticity fields were observed in the triple discharge case 13 as in the dual discharge case 11. Two counter rotating vortices were created near the test section edges, in each plane, as well as satellite vortices near the bottom and inclined branches, as shown in planes 1 to 9 in Figures 5.23 to 5.31. The vorticity varied with the plane height. In planes 1 to 5 in Figures 5.23 to 5.27, the vorticity strength is on the same order as the dual discharge case 11, but is more distributed over the plane area. This is due to the effect of the inclined branch, in the triple discharge case 13. The inclined branch flow cause satellite vortices to be observed in plane 6. The effect of the bottom and inclined branches were negligible so that none of these satellite vortices were observed in planes 7 to 9.

5.2.3 Average Velocities

Figure 5.32 shows the average radial velocity change along r for the nine investigated planes. In this figure, three regions can be classified according to the strength of the average radial velocity in each of the planes. Region 1 is located at $r = 23 \pm 2$ mm, region 2 is located at $r = 19 \pm 2$ mm, and region 3 is located at $r = 15 \pm 2$ mm. The highest average radial velocity in region 1 and 2 is found in plane 2. Since plane 2 is located at the same height as the inclined branch, the flow inside this plane is produced by the inclined and side branches. The second highest in these regions are found in planes 7 to 9, and are only affected by the side branch flow. In region 3, the highest average radial velocity was in plane 8. Region 3 is located near the air-water interface and air core where vortices with horizontal axes fed more flow to the higher planes. Planes 5 and 6 were almost the lowest average radial velocity in all regions. These planes are located between the side and inclined branches which produce flow in opposite directions, and consequently the average radial velocity is lowest. The rank of the velocity strength in planes 3 and 4 did not change with the region since the effect of the three branches on them is similar.

Figure 5.33 shows the average tangential velocity change, along r, for the nine investigated planes. Most of the data are shown to be located between - 0.04 and 0.08 m/s. The triple discharge data shows a greater range of average tangential velocity changes than the single or dual discharge cases. This indicates that the flow becomes more active. Planes 1 and 2 show the highest variation in average tangential velocity, which is expected due to the satellite vortices produced and surrounding these planes.

The fluctuation of average tangential velocity is also returned to the two edges vortices that are found in each plane.

Figure 5.34 shows the average vertical velocity change, along r, for the nine investigated planes. Planes 3 and 4 have positive average vertical velocity at $r < 16$ mm. At $r > 16$ mm the average vertical velocity in these two planes is negative. Parts of planes 3 and 4 are located at $r < 16$ mm and are too close to the entrance of the side branch, and since they are also located below the side branch entrance they have values of positive average vertical velocity. On the other hand, parts of planes 3 and 4 that are located at $r > 16$ mm are too close to the entrance of the inclined and bottom branches, and since they are located over these branch entrances they have values of negative average vertical velocity. The remaining planes, 1, 2, and 5 - 9 have negative average vertical velocity values. Planes 1 and 2 are located just higher than the bottom and inclined branches entrances, respectively, and are expected to have negative values of V_z since the effects from these two branches are dominant. Planes 6 - 9 are located higher than the side branch entrance, and are expected to have negative values of V_z, since this branch, and effects of the other two branches, encourage downward flow. Plane 5 is located between the side and inclined branches. Its negative V_z values come from the resultant of the two branches pulling the liquid from that plane.

5.3. Comparisons Between Single, Dual, and Triple Flow Field

This section will discuss the effects of the Froude number and plane height on the average velocities in selected configurations. The selected single discharge cases are in

the side branch A, case 1r for high Froude and case 2r for medium Froude number. Selected dual discharge cases in branches A and B are case 9 for high Froude number in branch A, and case 10 for medium Froude number in branch A. Dual discharge cases in branches A and C are case 11 for high Froude number in branch A, and case 12 for medium Froude number in branch A. Selected triple discharge cases in branches A, B, and C are case 13 for high Froude number in branch A, and case 14 for medium Froude number in branch A. In all cases the OGE occurs in the side branch, A.

5.3.1. Average Radial Velocities

The presentation in this section will start by explaining the development of the average radial velocity from planes 1 to 8 in cases that include the high and medium Froude numbers in branch A, followed by a comparison between the two groups. The side branch center is located at $r = 0.0$ mm, the inclined branch center is at $r = 7.4$ mm, and the bottom branch center is at $r = 25$ mm.

In plane 1, Figure 5.35(a), with high Froude number in A, the trends were explained previously in sections 4.3.1, 5.1.3, and 5.2.3 There is no data in the range of 0 $< r < 11.5$ mm since the wall is located in this region. The value of V_r in the single discharge case 1r was almost zero since plane 1 is so close to the bottom branch wall. In the dual discharge case 11 with branches A and C, the existence of the bottom branch flow increased the flow inside plane 1, but at the same time its effects were resisted by the side branch flow, which is why V_r is greater than in the single discharge case 1r. On the other hand, comparing the dual case 9 with branches A and B, shows the same effect on V_r from each branch since they are both located at the right side of plane 1 in Figure 4.1, and this is why V_r is greater here than in the dual discharge case 11. The triple

discharge is the summation of the two effects (the dual discharge case 11 and the dual discharge case 9) and this is why V_r is largest.

The single discharge case in plane 1, Figure 5.35(b), has a medium Froude number in branch A (Fr = 10.56). The single discharge case showed small negative values of V_r. The velocities within this plane are not uniform or directed toward the right edge of the plane, and hence toward the side branch entrance. The in-plane velocities are directed toward three spots in the plane, two of them have negative values of V_z and the one in between has a positive V_z. The three spots are located along a vertical line parallel to the x axis at the mid-span of the y-axis. The three spots collect liquid from the two sides of the plane (right side boundary and left side boundary) and are responsible for the negative values of V_r that are observed. In case 12, the bottom branch flow increases the flow inside plane 1. At the same time, the bottom branch effect is assisted by the side branch flow (since the single discharge case already contains negative values of V_r). This explain why V_r in case 12 is greater than the single discharge case 2r, Figure 5.35(b) and also greater than the dual case 11, in Figure 5.35(a). On the other hand, in the dual discharge case 10, the existence of the inclined branch flow (which is located at the right side of plane 1, Figure 4.1) increases the negative V_r value since it pulls more liquid inside the plane, and the flow performs similarly to the single discharge case 2r. This effect produces negative values of V_r when compared to case 9. The triple discharge is the summation of the two effects (the dual discharge case A and C and the dual discharge case A and B with a medium Fr_A).

In plane 2, Figure 5.36(a), the radial velocities behaviors are different from plane 1 in Figure 5.35(a). There is no data in the range of $0 < r < 8.0$ mm because of the wall.

In case 11, the velocity behavior in plane 2 is similar to plane 1. In case 9, the value of V_r increases with increasing radial distance, r. This is due to plane 2 being closer to the side branch than plane 1 since the side branch increases V_z as r decreases, and consequently leads to decreasing V_r. A similar behavior is observed in the triple discharge case. In plane 2, Figure 5.36(b), the radial velocities behavior is different from plane 1 in Figure 5.35(b). In the dual discharge case 12, the velocity behavior in plane 2 is the same as in plane 1, however with smaller values of V_r are found since plane 2 is located farther from the bottom branch than plane 1. In case 10, the value of V_r increases with increasing r because plane 2 is closer to the side branch than plane 1, and the side branch flow increases V_z as r decreases and consequently leads to decreasing V_r. A similar behavior is observed in the triple discharge case.

In planes 3 and 4, Figures 5.37(a) and 5.38(a), the radial velocities behavior for the dual discharge case 9, the dual discharge case 11, and the triple discharge case 13 is similar to the velocity behavior for the triple discharge case in plane 2. The flow in planes 3 and 4 is dominated by the inclined branch and the side branch effects are secondary. The side branch flow increases V_z as its entrance is approached with decreasing r, and consequently leads to decreasing V_r. In planes 3 and 4, Figures 5.37(b) and 5.38(b), respectively the behaviors for the dual discharge 10, the dual discharge case 12, and the triple discharge case 14 are similar to the behavior for the triple discharge case in plane 2 for the same reasons as in Figures 5.37(a) and 5.38(a).

In planes 5 and 6, Figures 5.39(a) and 5.40(a) respectively, the velocities behavior for the dual discharge case 9, the dual discharge case 11, and the triple discharge case 13 is similar to the triple discharge case 13 in plane 3. The only difference here is that the

rank of each case's curve is reversed to that found in plane 3. The flow in planes 5 and 6 is dominated by the side branch flow, and the effects of the inclined branch flow are secondary. The inclined branch flow increases V_z with decreasing r and consequently leads to decreasing V_r. In planes 5 - 8, Figures 5.39(b), 5.40(b), 5.41(b), and 5.42(b) respectively, the velocities behavior for the single discharge case is different from planes 1- 3. The single discharge case has no negative values of V_r, since the side branch is located at the right boundary of these planes. In effect, there will be only positive values of V_r. The effect of dual discharge case 10, the dual discharge case 12, and the triple discharge case 14 is to increase the flow inside these planes, 5 to 9. The velocities behavior is similar to the single discharge case with greater positive values of V_r.

In planes 7 and 8, Figure 5.41(a) and 5.42(a), the velocities behavior for the dual discharge case 9, the dual discharge case 11, and the triple discharge case 13 is similar to the triple discharge case 13 in plane 1. The only difference is that the rank of each case's curve varies from that of plane 1. The flow in planes 7 and 8 are dominated by the side branch flow and the flow in the inclined branch pulls more liquid toward these planes. In the triple discharge case 13, the bottom branch flow decreases the effect of the inclined branch on planes 7 and 8. This leads to a decrease in V_r in the triple discharge case compared to the dual discharge case 9. The bottom branch flow pulls more liquid toward planes 7 and 8 in dual discharge case 11 and shows less effect than the dual discharge case 9. The difference in height between the bottom branch entrance and the two planes being is larger than that of the inclined branch entrance.

5.3.2. Average Tangential Velocities

Figures 5.43 to 5.50 show the change in the average tangential velocity, V_t, along r in planes 1 to 8 during OGE in the side branch A for cases 1r, 2r, and 9 - 14. The behavior of the velocity is similar and it fluctuates near $V_t = 0.0$. The amplitude of V_t depends on the flow scenario, the plane height, and the plane position with respect to the active branch entrance. As an example, the single discharge case 1r shows a gradual increase in V_t starting from plane 1 in Figure 5.43, until it reaches maximum amplitude at planes 5 to 7 in Figures 5.47 to 5. 49, then it decreases in plane 8 in Figure 5.50. Planes 5 to 7 are the closest planes to the side branch entrance. It can also be seen that the case 2r of medium Fr_A shows a lower amplitude of V_t in the same plane, for example Figures 5.48(a) and 5.48(b). The results insist on the idea of increasing V_t with increasing the number of active branches, as long as that plane is not very close to one of the active branches. As an example, the triple discharge scenario shows the highest value of V_t in planes 1 to 5 in Figures 5.43 to 5.47.

5.3.3. Average Vertical Velocities

Figures 5.51 to 5.58 show the change in the average vertical velocity along r in planes 1 to 8 during OGE in the side branch A for cases 1r, 2r, and 9 - 14. The velocity behavior of each case depends on the flow configuration (single discharge, dual discharge, or triple discharge) the discharge Froude number, the plane height, and the plane position with respect to the active branch entrance. For example, the single discharge case 1r, in plane 1 in Figure 5.51(a), the velocity behavior of V_z is practically a horizontal with some deviation around $V_z = 0$. This indicates that the side branch does not affect V_z which is because of the large difference in height between plane 1 and the side

branch entrance. Once the flow scenario changes to dual or even triple discharge, the V_z velocity behavior is totally different. The deviation from the single discharge velocity behavior depends on the distance between the activated secondary branch and the plane shown, and also on the relative flow strength of the activated secondary branch to the side branch strength. Figure 5.51(a) emphasizes this idea and the triple discharge velocity behavior shows the largest deviation from the single discharge velocity behavior. These effects can also be seen to have less deviation in the rest of planes 2 to 8. As the plane height increases, the effect of the side branch on the in-plane velocity increases in addition the effects of the activated secondary branch decreases, as shown in Figures 5.52(a) to 5.58(a). Plane 1 is located just above the bottom branch entrance and is aligned parallel to the discharge inlet opening. The plane is also below the inclined branch entrance but is misaligned by 135 degrees. Flow traveling from the horizontal plane 1 to the bottom branch must negotiate a 90 degree downward turn, while flow from the plane to the inclined branch must turn 135 degrees upward. Hence, the plane is exposed to two opposite effects from the bottom and inclined branches, but with a greater effect from the bottom branch due to its proximity to the plane. This is why in Figure 5.51(b) the effect of the bottom branch on V_z is largest in the dual discharge case with branches A and C, even more so than the triple discharge of branches A, B, and C. Starting from Figure 5.52(b) until 5.58(b), planes 2- 8, the bottom and the inclined branches affect the values of V_z in a similar manner. These branches are located on the same side of the investigated plane (lower than the planes), however, the effect of the inclined branch is greater than the that of the bottom branch since it is located closer to the investigated planes. This is

126

why in Figures 5.52(b) to 5.58(b), the greatest effect on V_z is found for the triple discharge case 14, then the dual discharge case10 and finally the dual discharge case 12.

5.4 Summary and Concluding Remarks

This chapter outlined the results from experiments using stereoscopic particle image velocimetry to map the liquid side flow field (velocity, vorticity) at the onset of gas entrainment in a dual and triple discharging side branch. This is addition to the average velocities comparison between eight different cases.

Two formats were used in the presentation of the flow structure – the whole field map showing the vector and vorticity fields, and the averaged velocity components (V_r, V_t, V_z) along a given radial distance, r, from the branch inlet. The main observations from the flow structure of multiple discharge can be summarized as follows,

- Two regions were distinguished in planes 1 and 2 in dual and triple discharge. The side branch region, in which the in-plane velocity vectors are directed toward the right side boundary, and the bottom branch region, in which the in-plane velocity vectors are directed toward the bottom branch C, and follows an almost axisymmetric path. A third region, called the central region, noticed in planes 3 to 5 in dual discharge case and in planes 2 to 6 in triple discharge case, showed a lower in-plane velocity than the side branch region. This is because, the central region and vertical velocity are affected by the three branches, in which the flow tends to go vertically to the bottom and side branches in dual discharge case and to the inclined, bottom and side branches in triple discharge case.

- The tangential velocity components, within the horizontal planes, demonstrate that the flow curls towards the inlet. It was determined, however, that the curl did not satisfy the Γ_1 vortex center criterion. Some of satellite vorticies were found due to the bottom branch existence but with a negligible intensity within the horizontal planes, and regions of high vorticity were observed due to the wake effect at the test section boundary. It is suspected that vortex structures exist within vertical or inclined planes, as observed from the positive and negative vertical velocities observed in the horizontal planes.

- The flow field was affected by the existence of the secondary (bottom) branch in the dual discharge case and with the secondary (bottom and inclined) branches in the dual discharge case if compared with the single discharge side branch case. It is affected also by the Froude number value in the side branch in the dual and triple discharge cases.
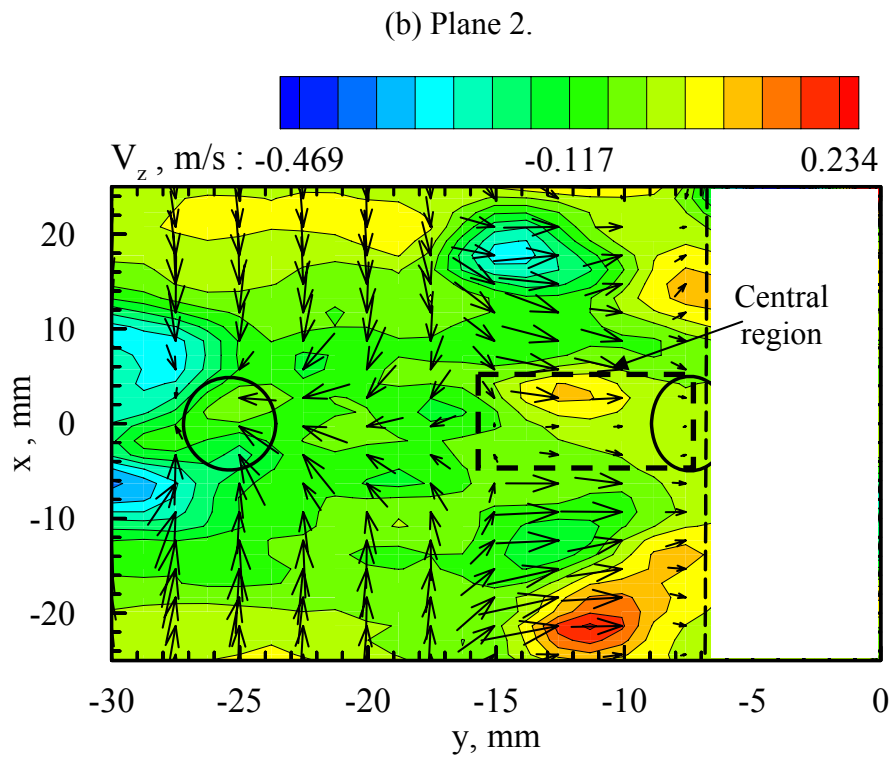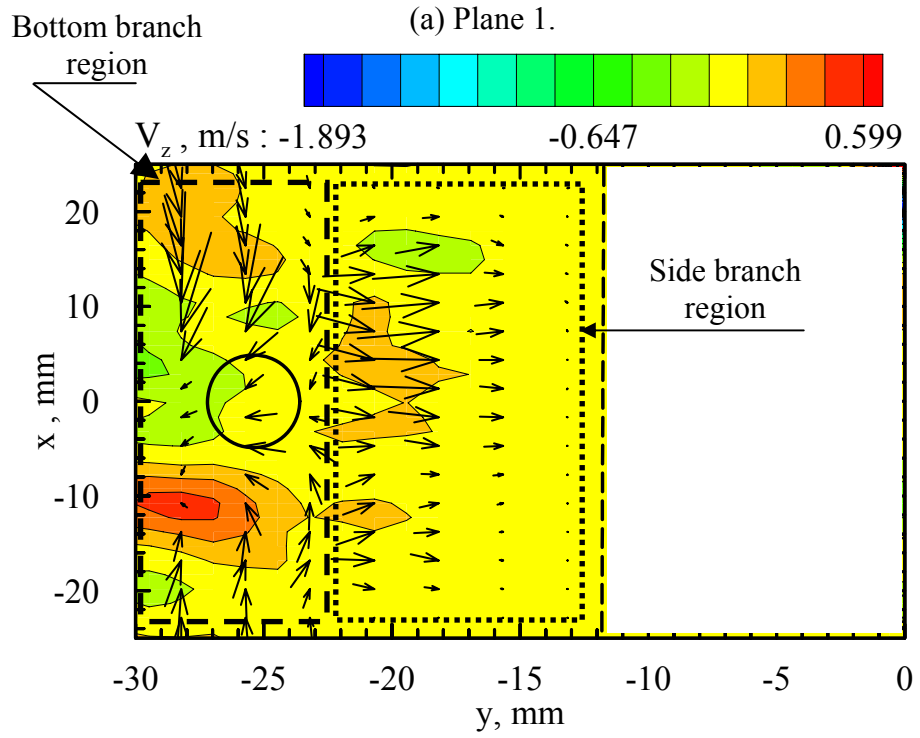
(a) Plane 1.

(b) Plane 2.

Figure 5.1 Velocity field in horizontal planes number 1 and 2 in case 11.

(a) Plane 3.
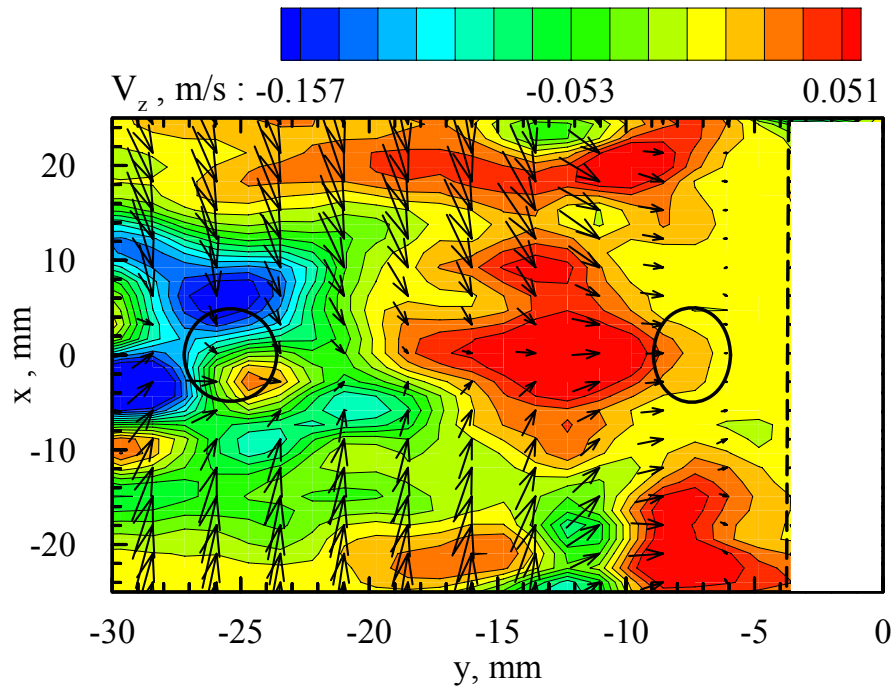
(b) Plane 4.
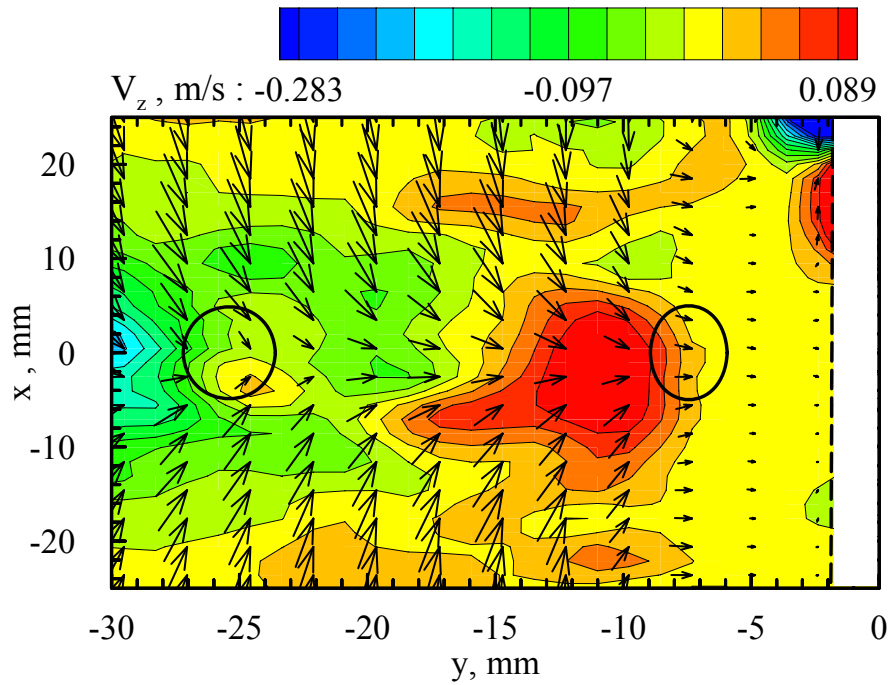
Figure 5.2 Velocity field in horizontal planes number 3 and 4 in case 11.
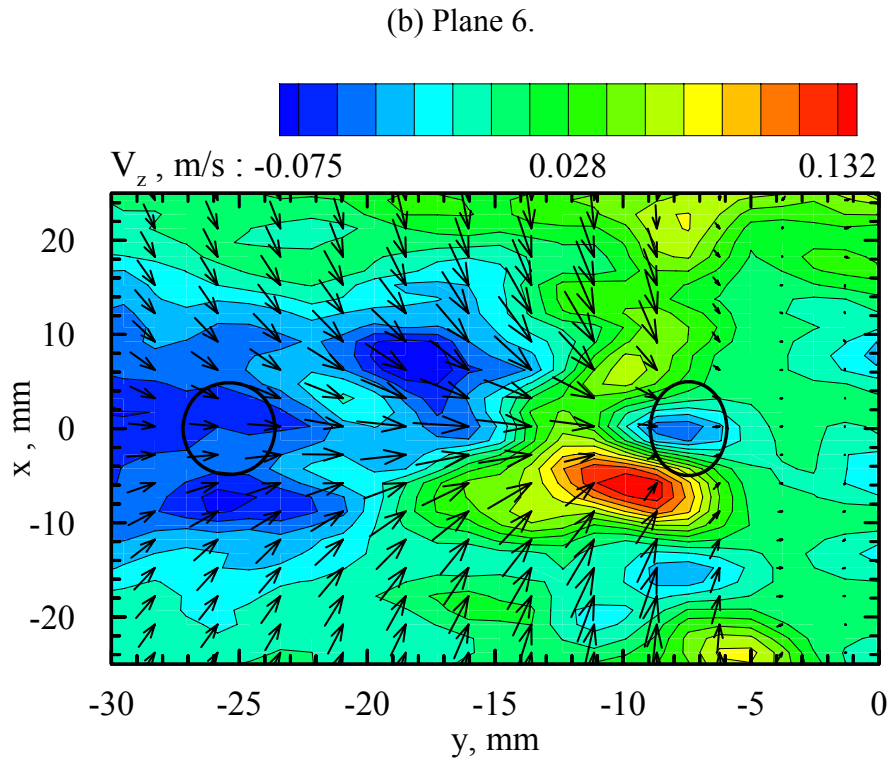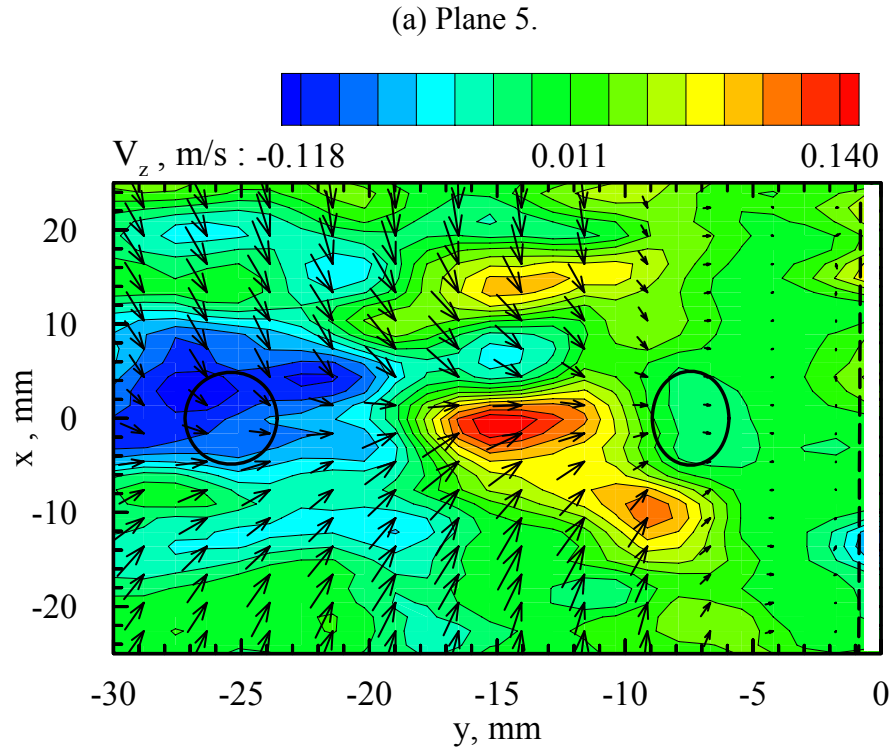
(a) Plane 5.

(b) Plane 6.

Figure 5.3 Velocity field in horizontal planes number 5 and 6 in case 11.

131

(a) Plane 7.
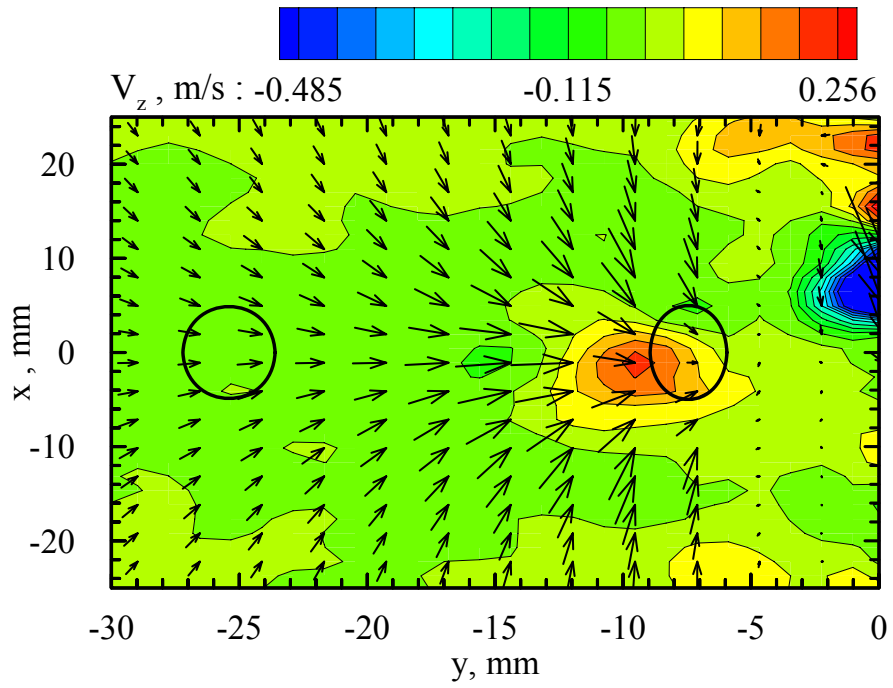
(b) Plane 8.
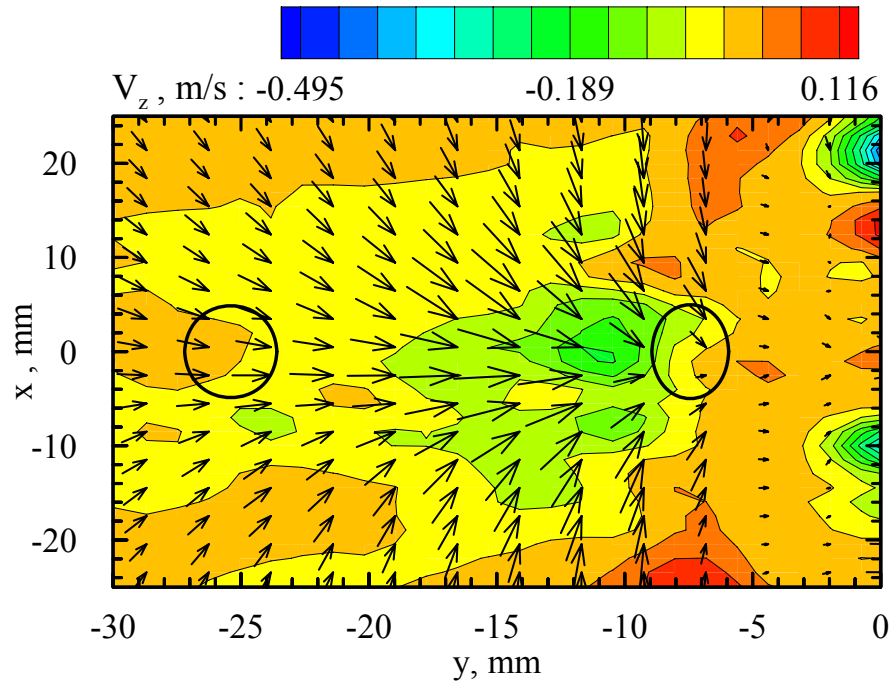
Figure 5.4 Velocity field in horizontal planes number 7 and 8 in case 11.

132
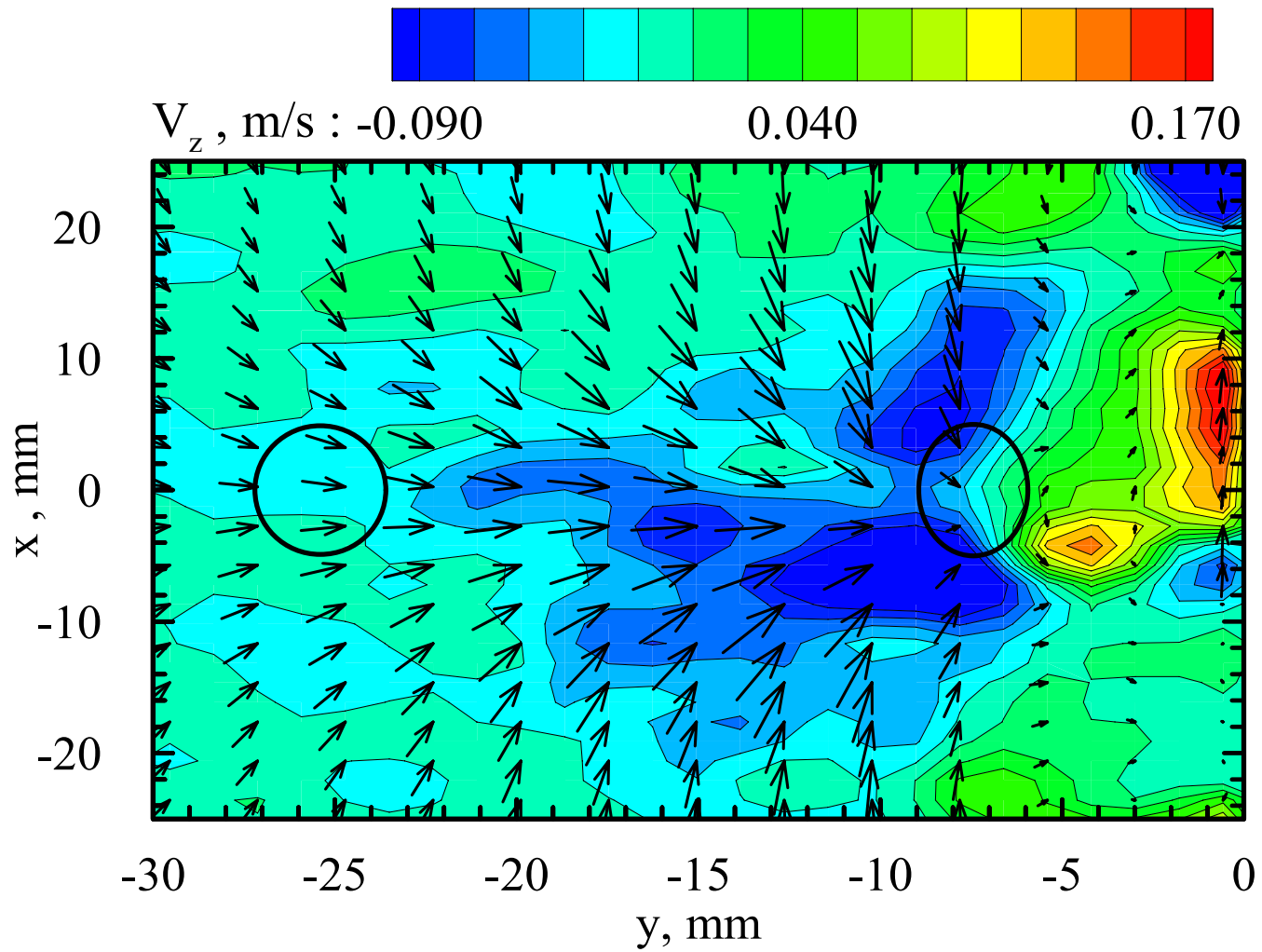
Figure 5.5 Velocity field in a horizontal plane number 9 in case 11.

(a) 8-point circulation vorticity in plane 1.
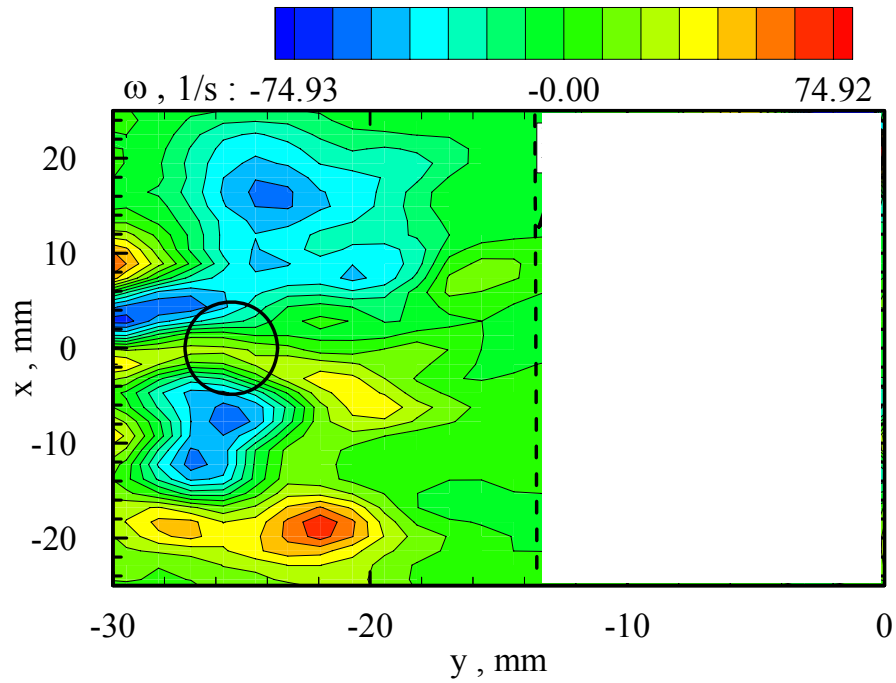
(b) Vortical structures based on λ_2 criterion in plane 1.
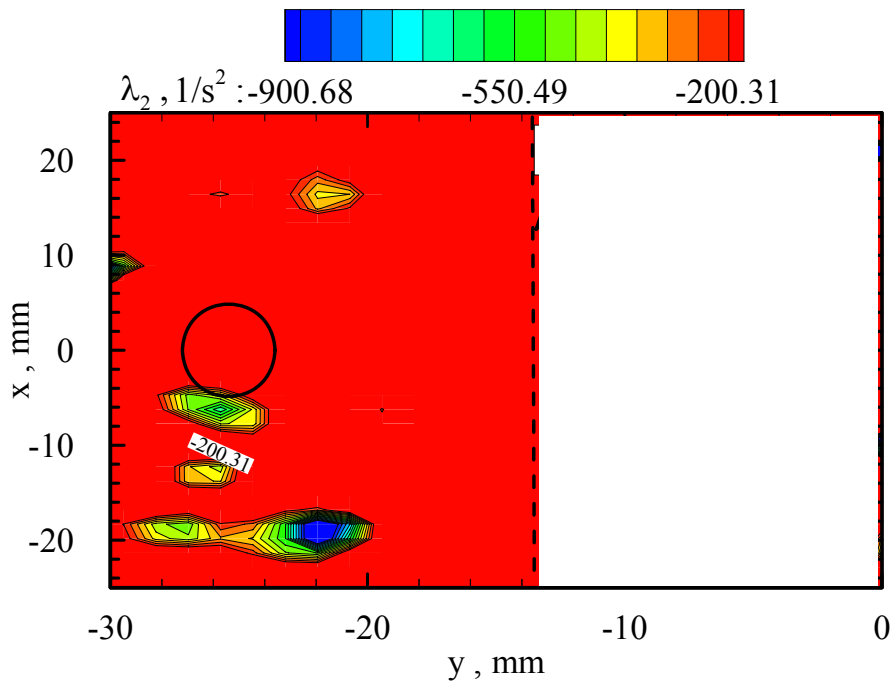
Figure 5.6 Vorticity field in a horizontal plane number 1 in case 11 calculated based on 8-point circulation vorticity equation (a) and vortical structures based on λ_2 criterion (b)

(a) 8-point circulation vorticity in plane 2.
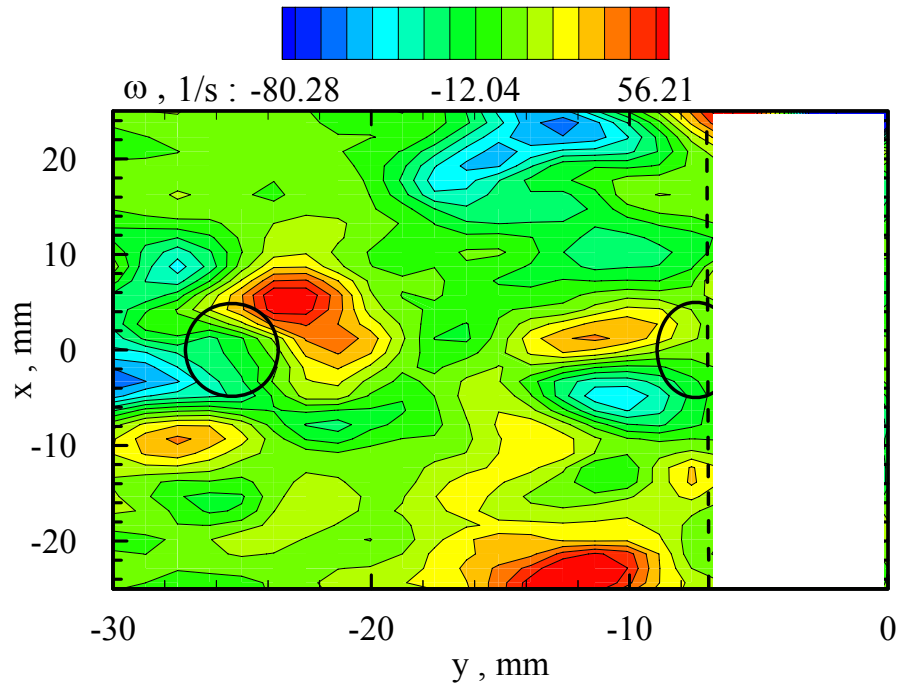
(b) Vortical structures based on λ_2 criterion in plane 2.
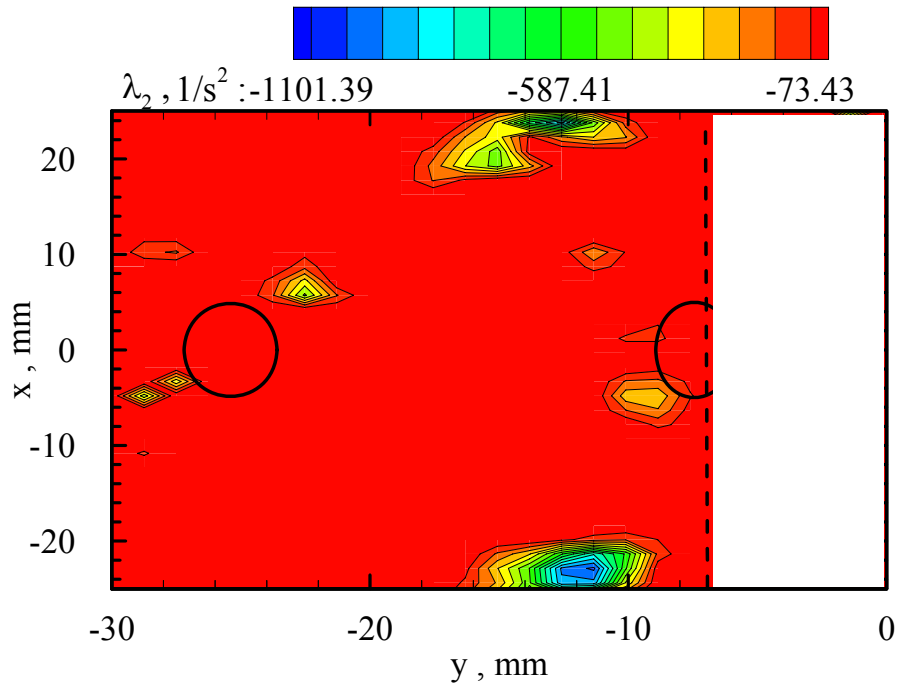
Figure 5.7 Vorticity field in a horizontal plane number 2 in case 11 calculated based on 8-point circulation vorticity equation (a) and vortical structures based on λ_2 criterion (b)

(a) 8-point circulation vorticity in plane 3.
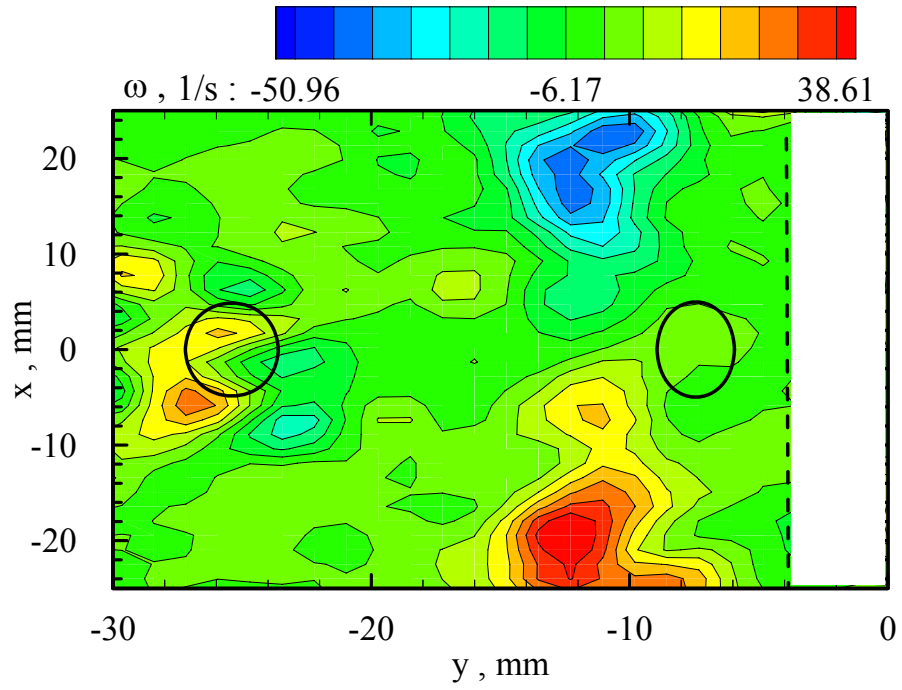
(b) Vortical structures based on λ_2 criterion in plane 3.
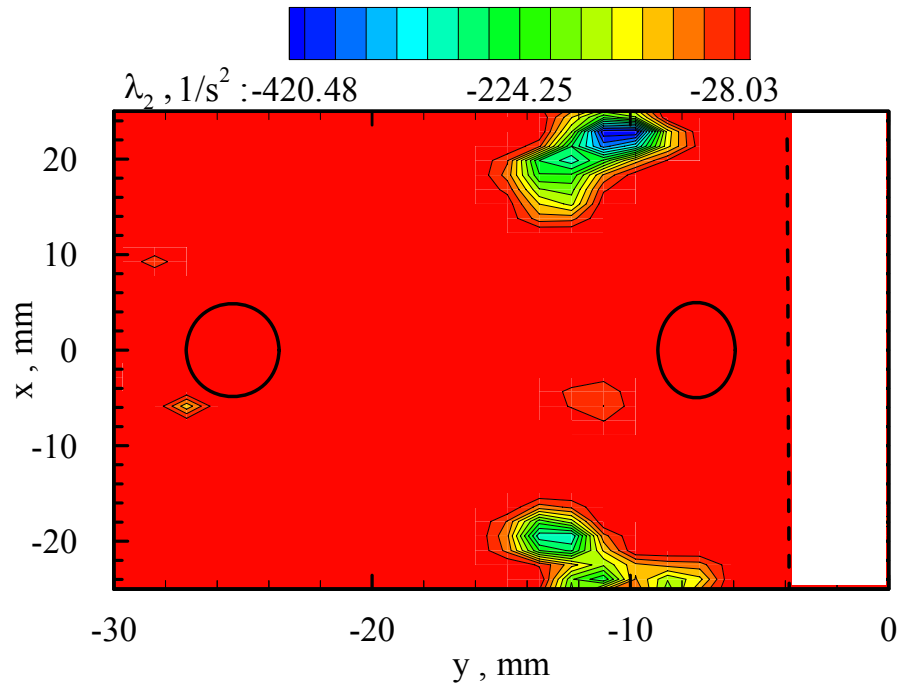
Figure 5.8 Vorticity field in a horizontal plane number 3 in case 11 calculated based on 8-point circulation vorticity equation (a) and vortical structures based on λ_2 criterion (b).

(a) 8-point circulation vorticity in plane 4.
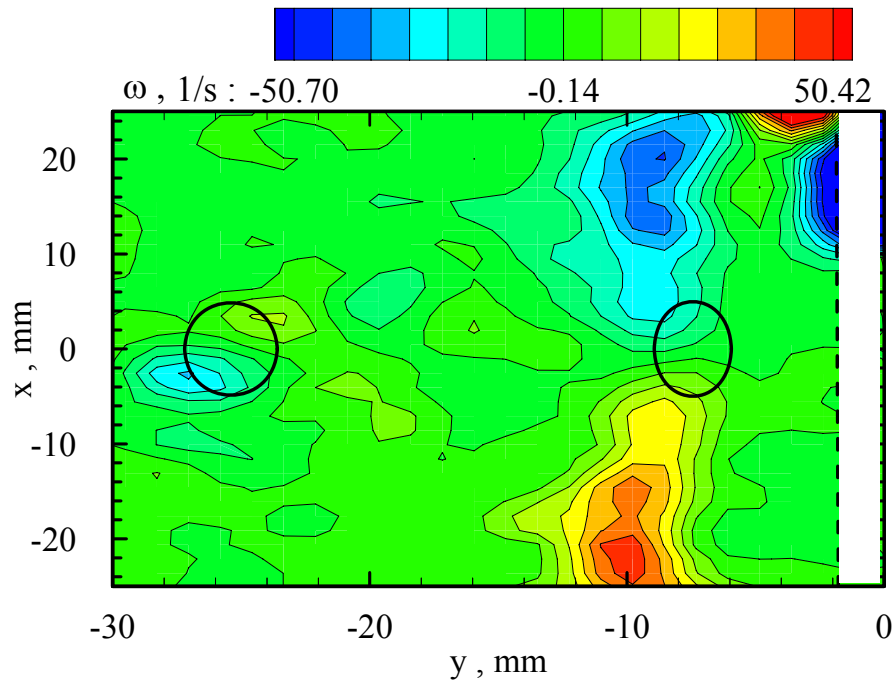
(b) Vortical structures based on λ_2 criterion in plane 4.
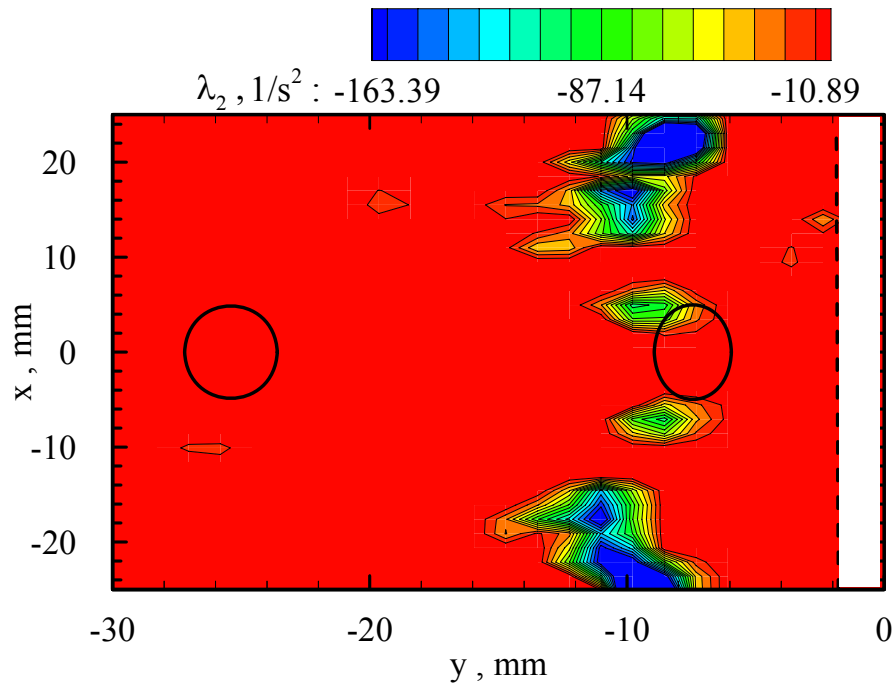
Figure 5.9 Vorticity field in a horizontal plane number 4 in case 11 calculated based on 8-point circulation vorticity equation (a) and vortical structures based on λ_2 criterion (b).

(a) 8-point circulation vorticity in plane 5.
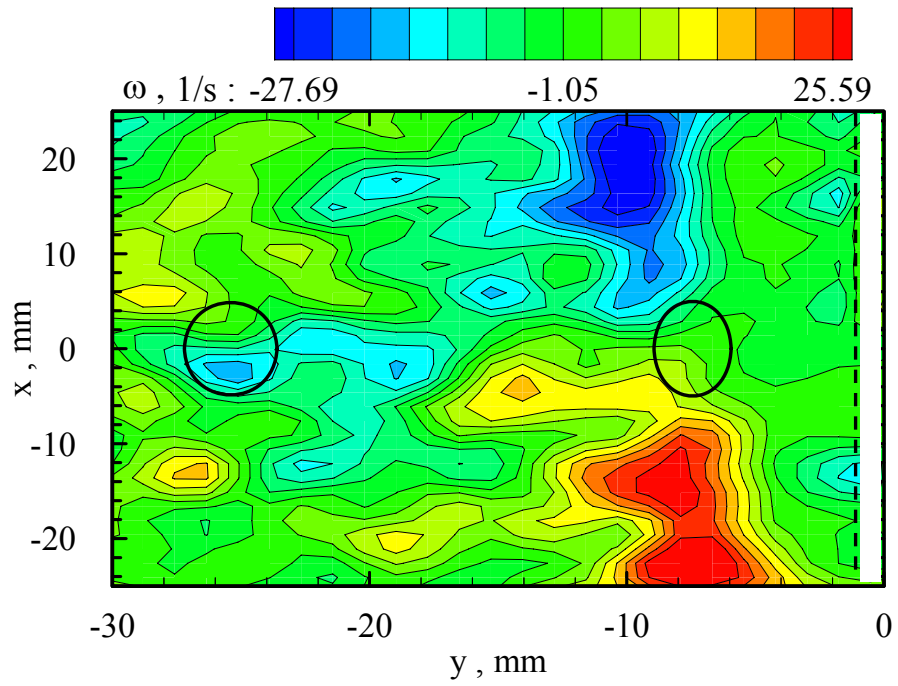
(b) Vortical structures based on λ_2 criterion in plane 5.
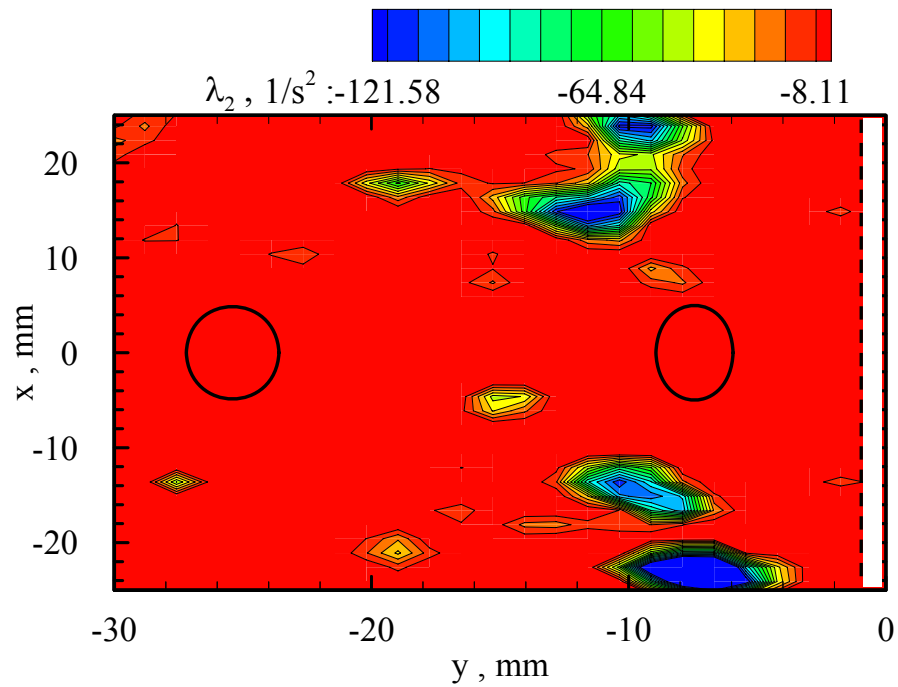
Figure 5.10 Vorticity field in a horizontal plane number 5 in case 11 calculated based on 8-point circulation vorticity equation (a) and vortical structures based on λ_2 criterion (b).

(a) 8-point circulation vorticity in plane 6.
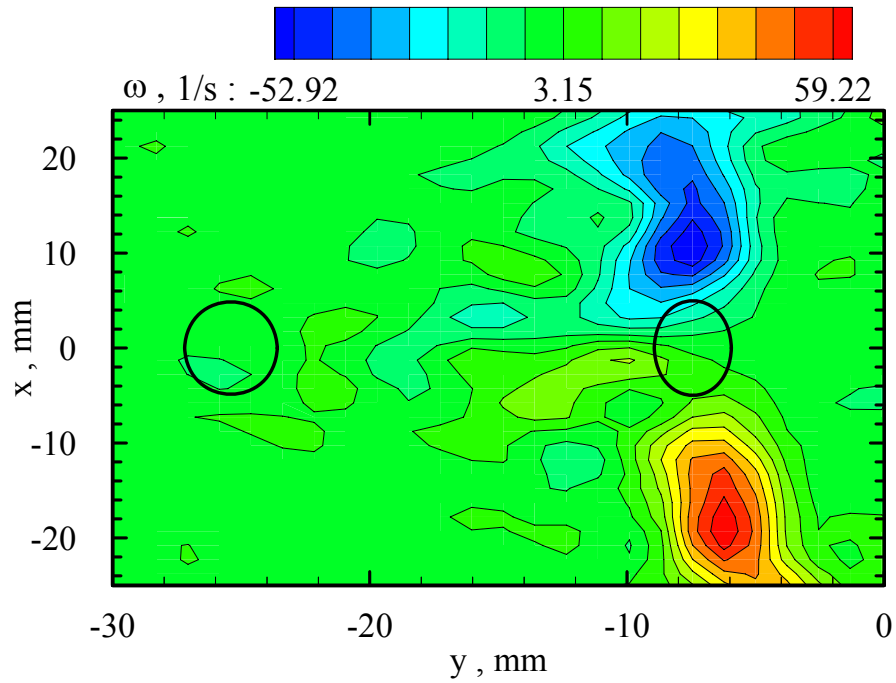
(b) Vortical structures based on λ_2 criterion in plane 6.
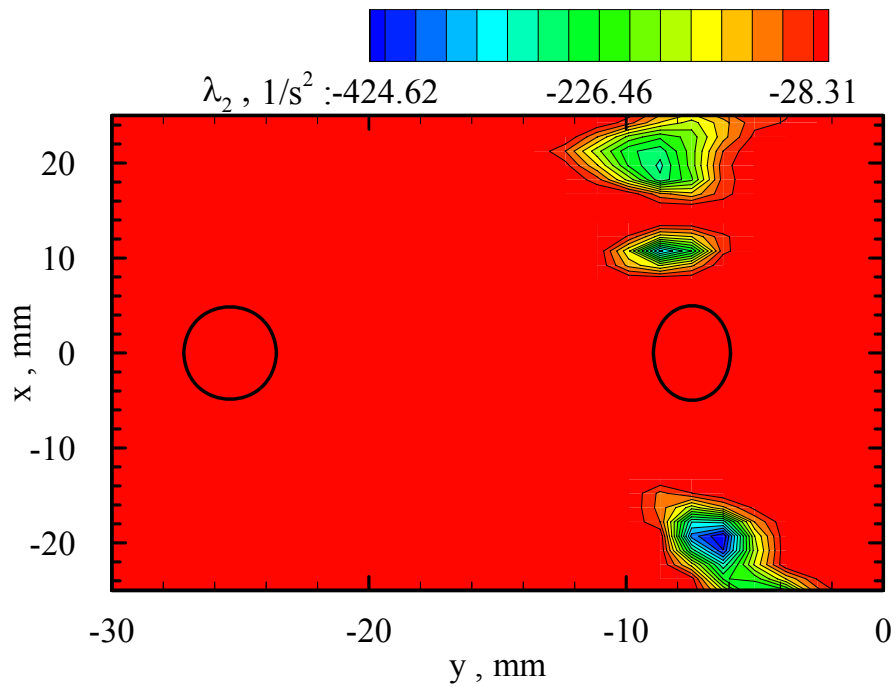
Figure 5.11 Vorticity field in a horizontal plane number 6 in case 11 calculated based on 8-point circulation vorticity equation (a) and vortical structures based on λ_2 criterion (b).

(a) 8-point circulation vorticity in plane 7.
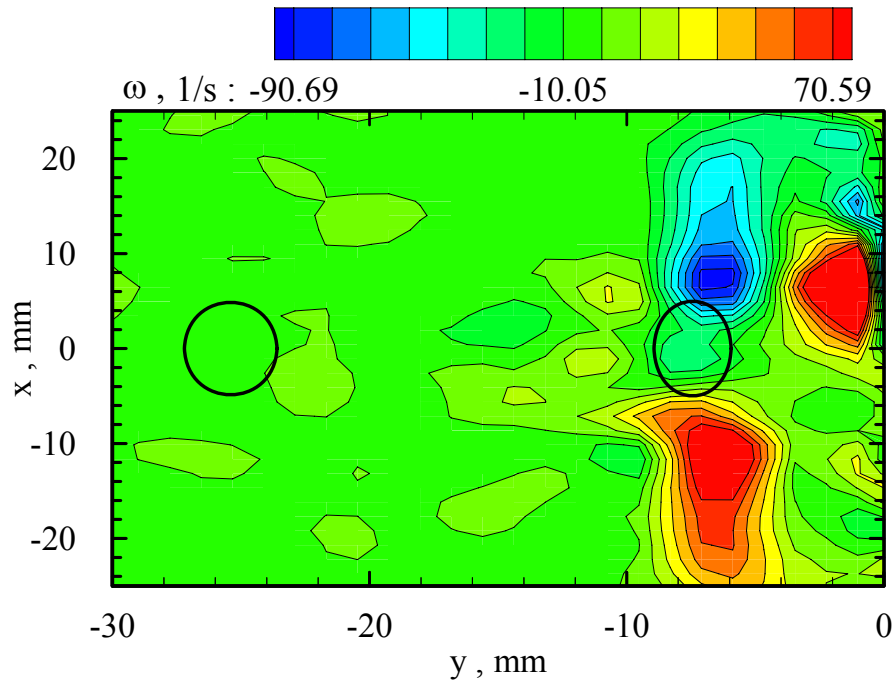
(b) Vortical structures based on λ_2 criterion in plane 7.
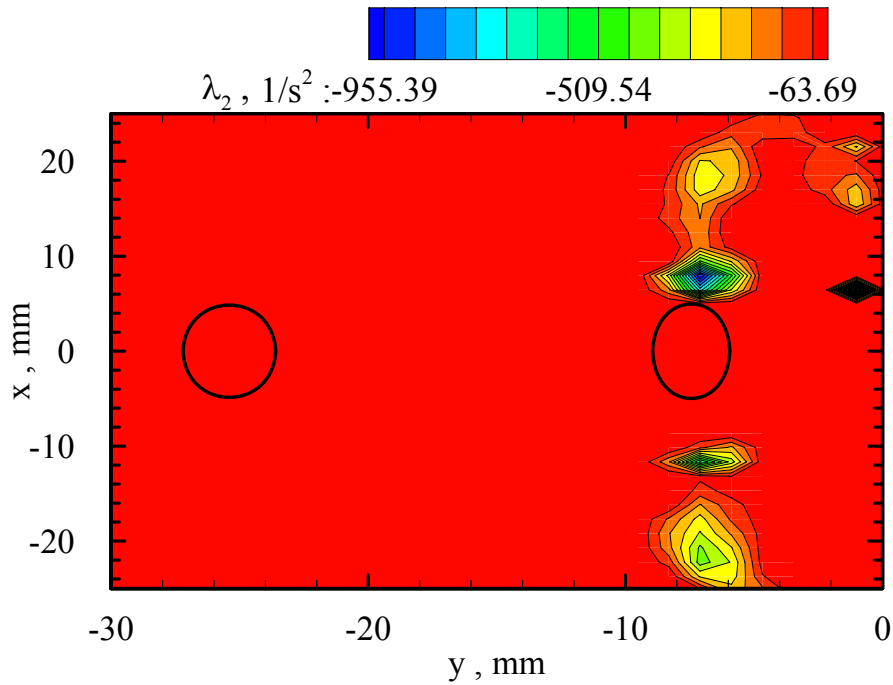
Figure 5.12 Vorticity field in a horizontal plane number 7 in case 11 calculated based on 8-point circulation vorticity equation (a) and vortical structures based on λ_2 criterion (b).

(a) 8-point circulation vorticity in plane 8.

ω , 1/s : -77.69   -3.05   71.59

(b) Vortical structures based on λ_2 criterion in plane 8.

λ_2 , $1/s^2$:-486.33   -259.37   -32.42
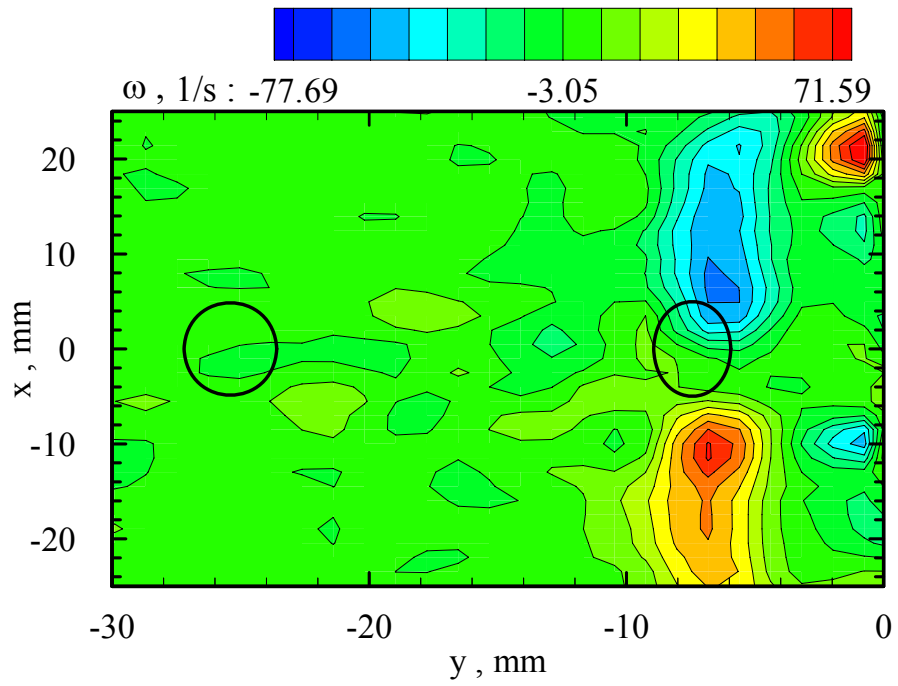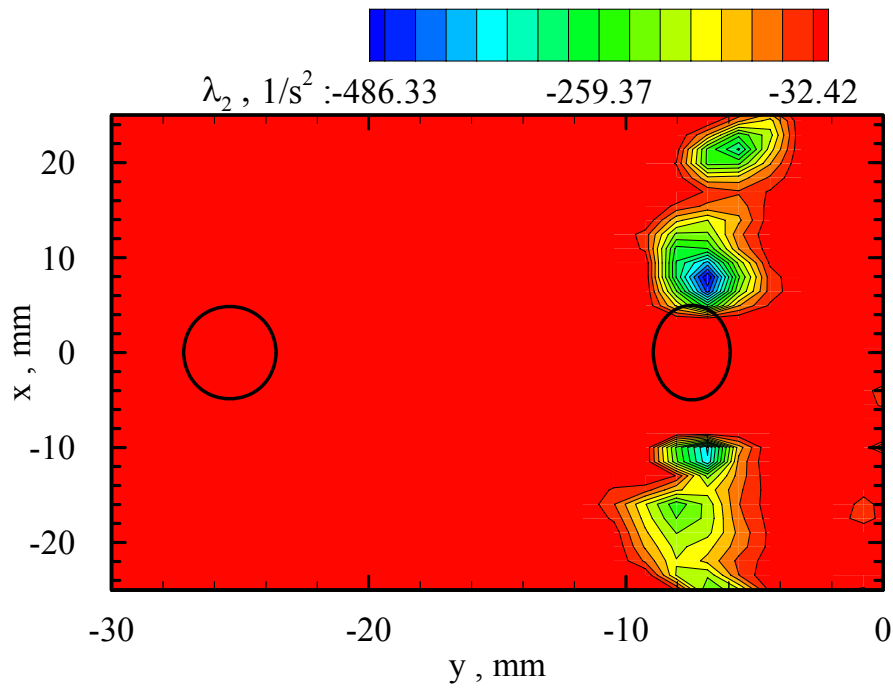
Figure 5.13 Vorticity field in a horizontal plane number 8 in case 11 calculated based on 8-point circulation vorticity equation (a) and vortical structures based on λ_2 criterion (b).

(a) 8-point circulation vorticity in plane 9.
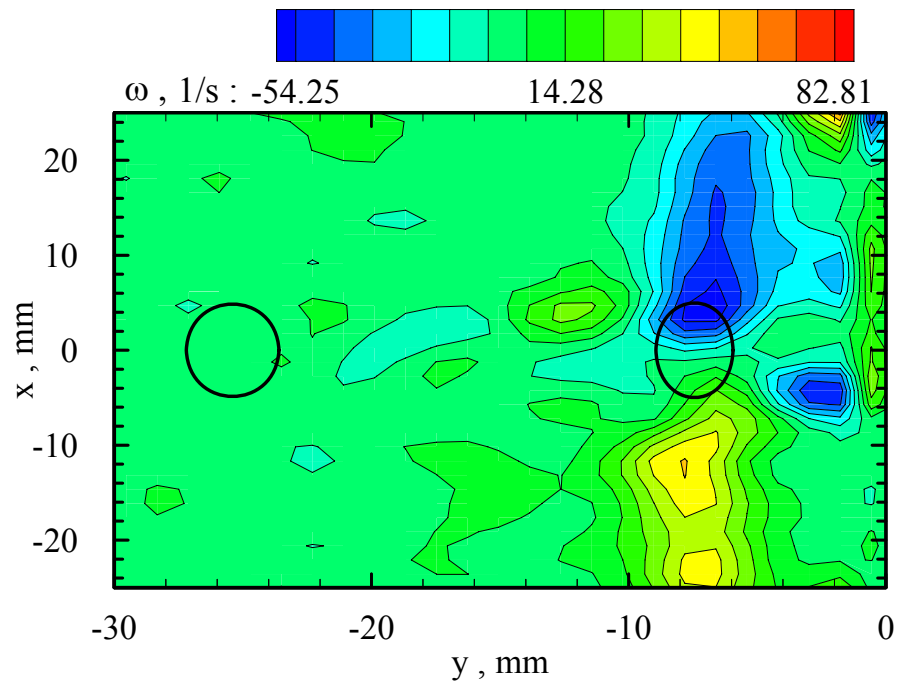
(b) Vortical structures based on λ_2 criterion in plane 9.
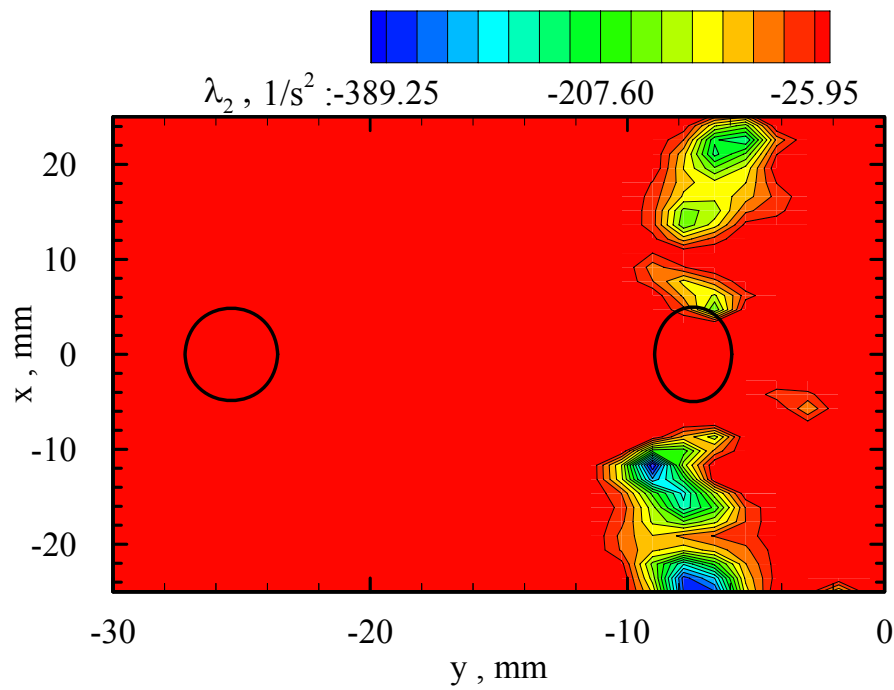
Figure 5.14 Vorticity field in a horizontal plane number 9 in case 11 calculated based on 8-point circulation vorticity equation (a) and vortical structures based on λ_2 criterion (b).
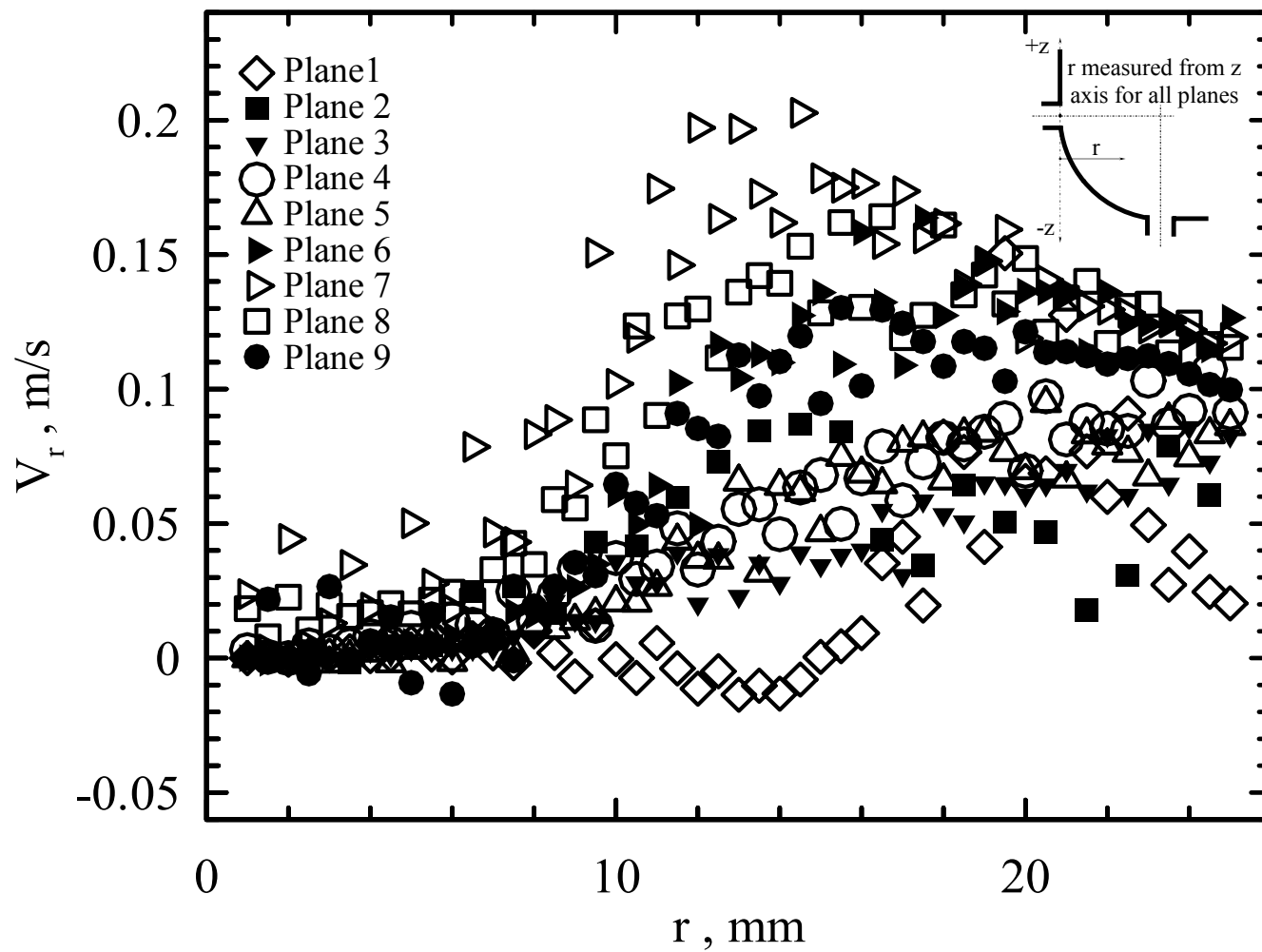
Figure 5.15 Effect of investigated plane height on average radial velocity change along r.
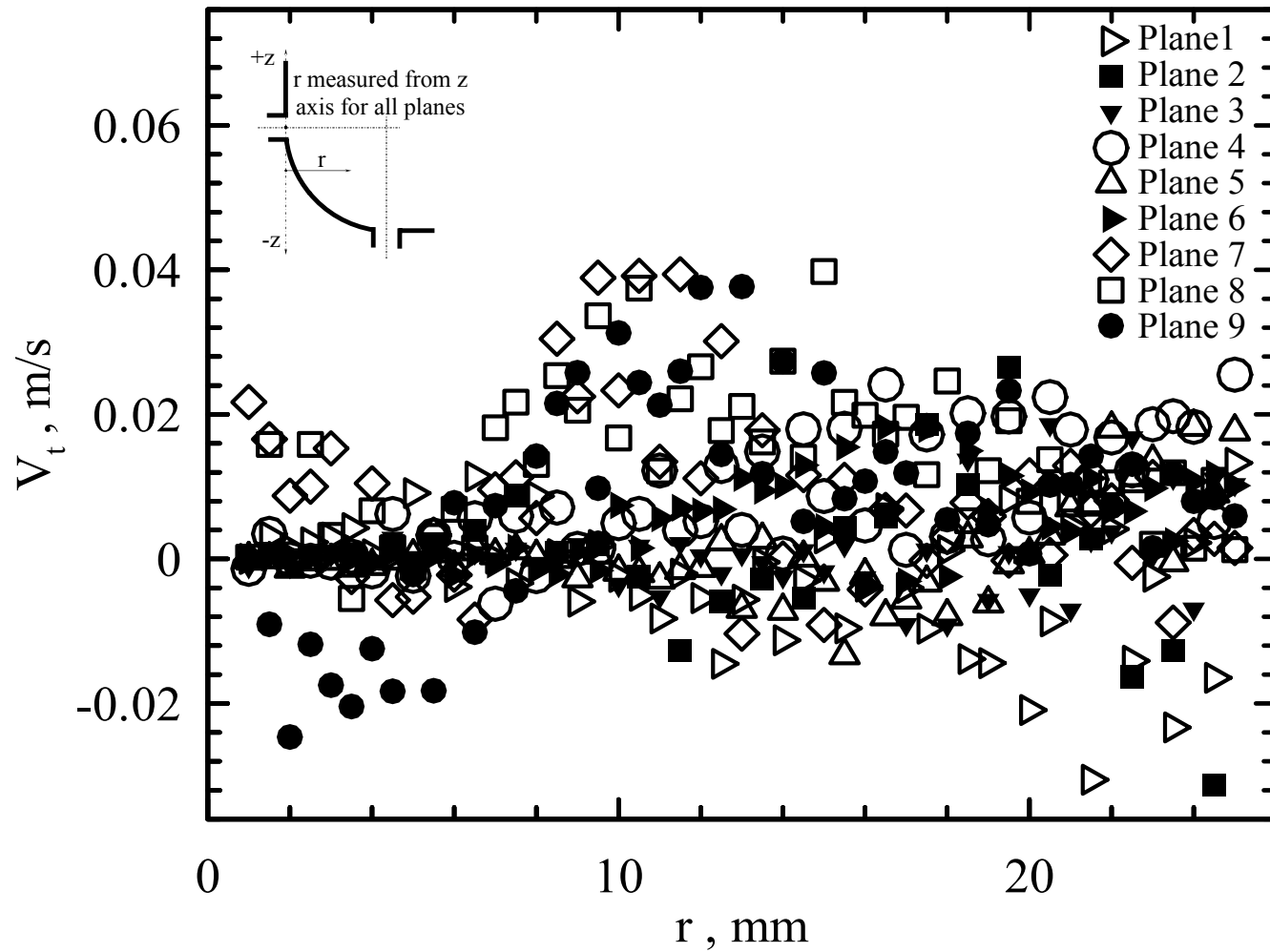
Figure 5.16 Effect of investigated plane height on average tangential velocity change along r.
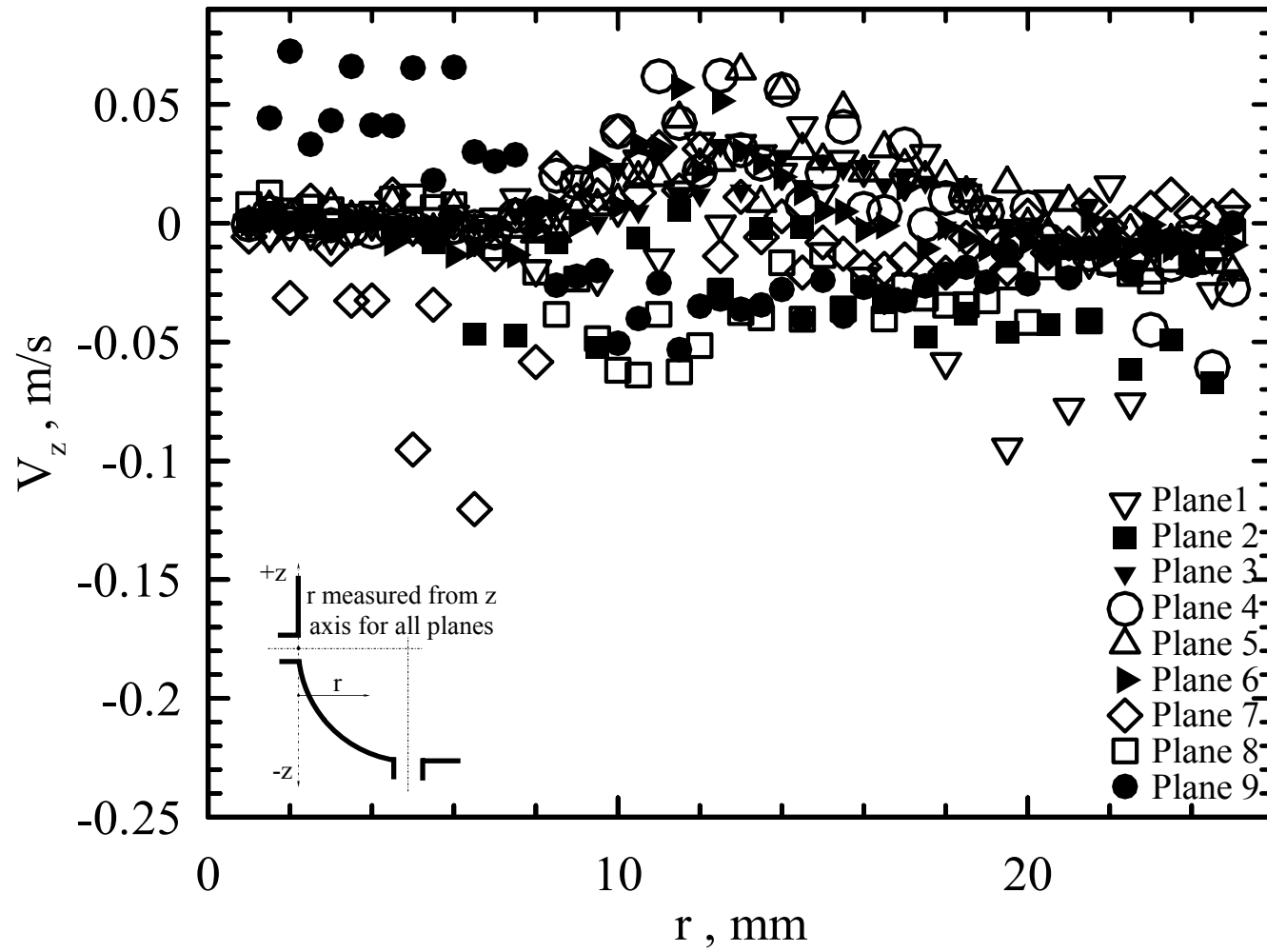
Figure 5.17 Effect of investigated plane height on average vertical velocity change along *r*.
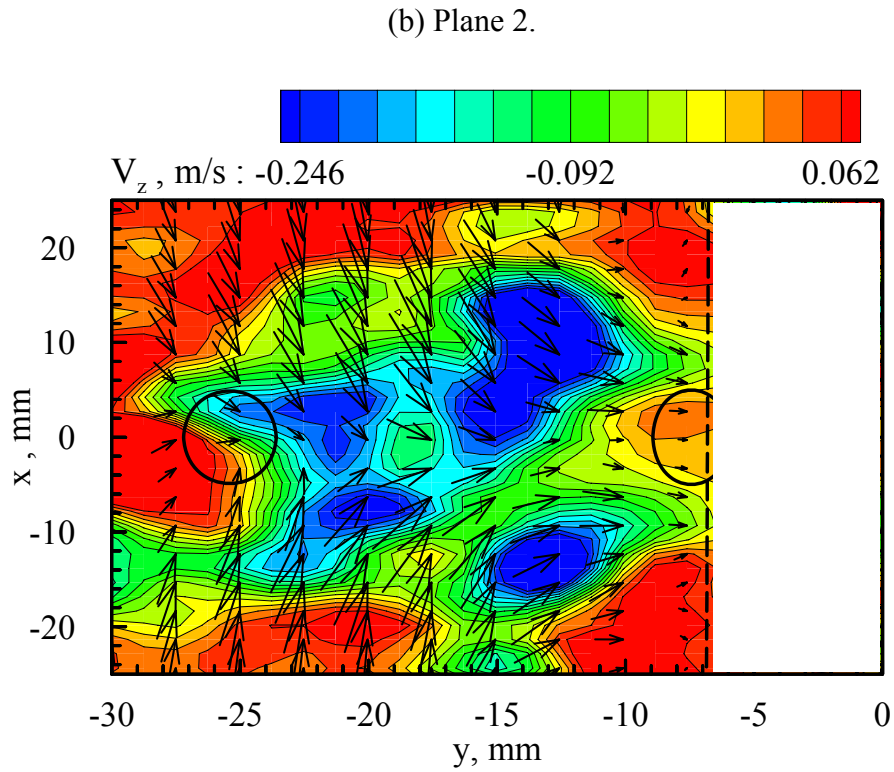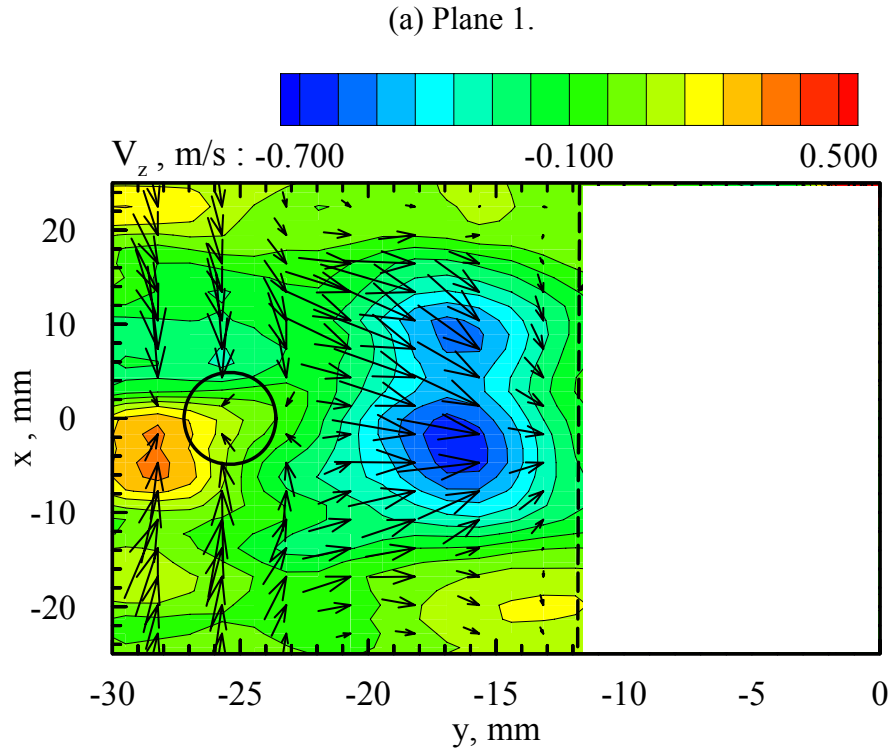
(a) Plane 1.

(b) Plane 2.

Figure 5.18 Velocity field in horizontal planes number 1 and 2 in case 13.

146

(a) Plane 3.

V_z, m/s : -0.209   -0.008   0.193

(b) Plane 4.

V_z, m/s : -0.173   -0.050   0.073
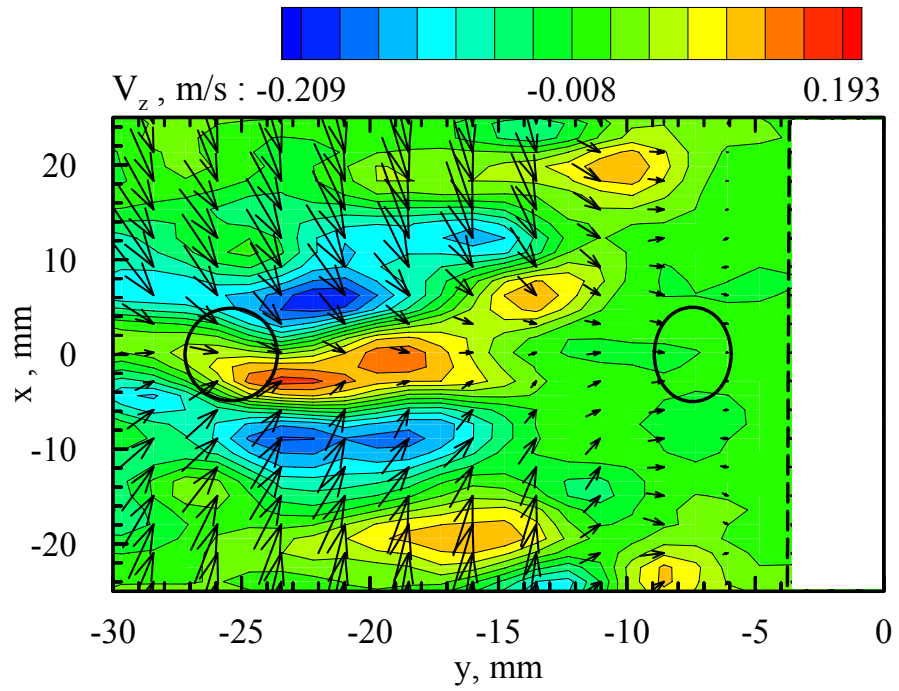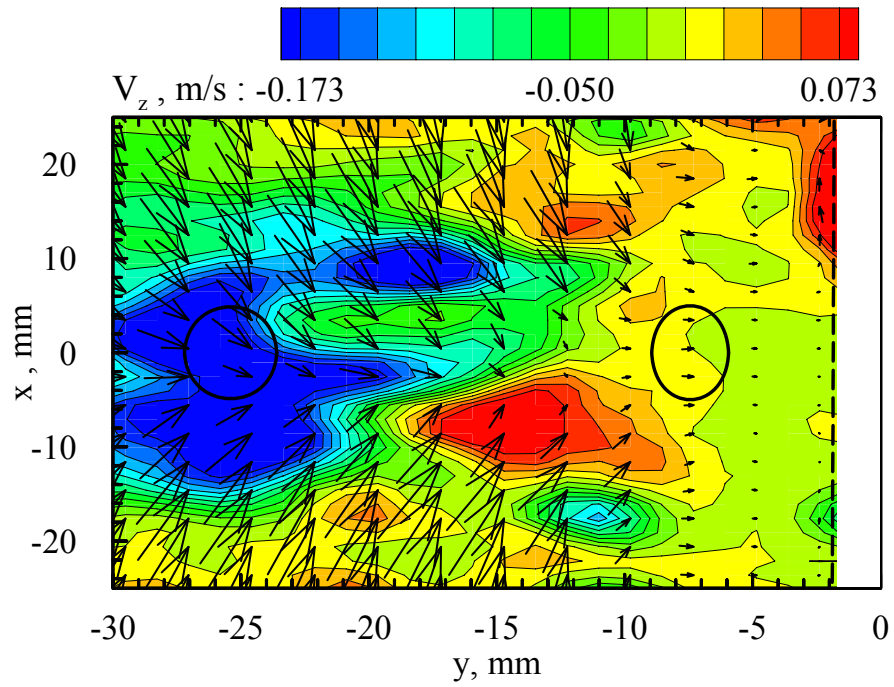
Figure 5.19 Velocity field in horizontal planes number 3 and 4 in case 13.

147

(a) Plane 5.
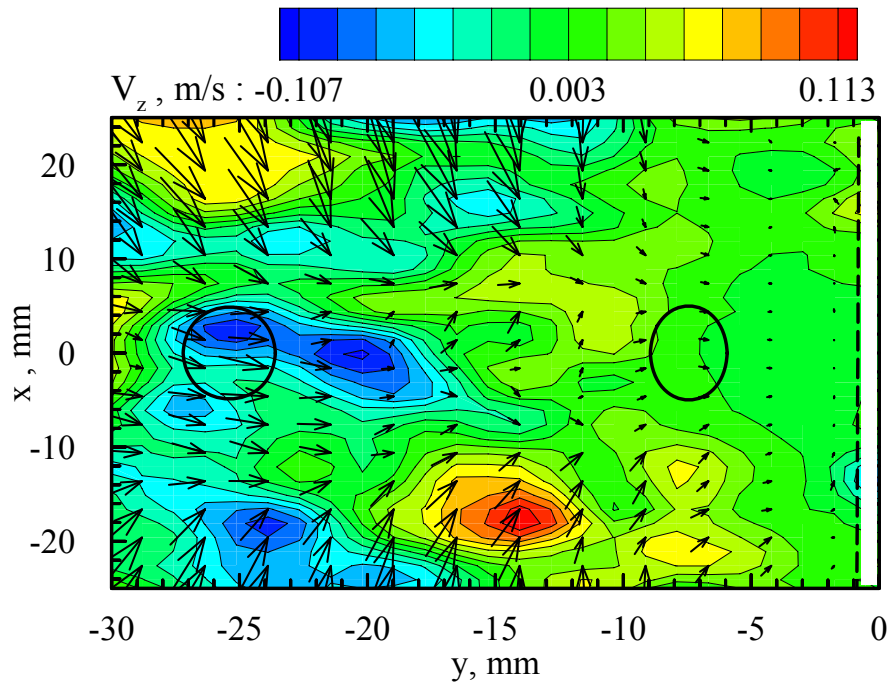
(b) Plane 6.
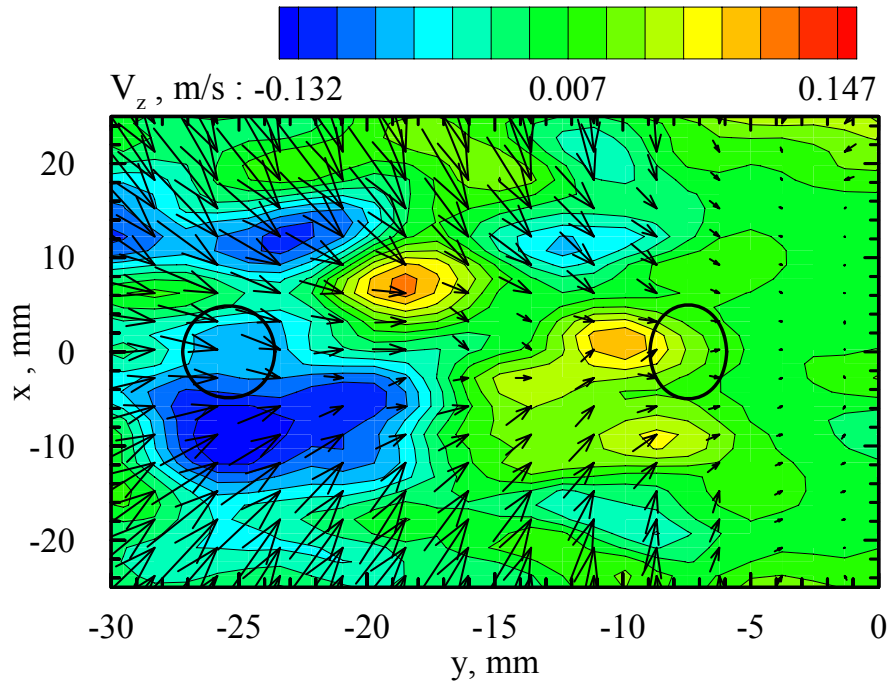
Figure 5.20 Velocity field in horizontal planes number 5 and 6 in case 13.

148

(a) Plane 7.

(b) Plane 8.
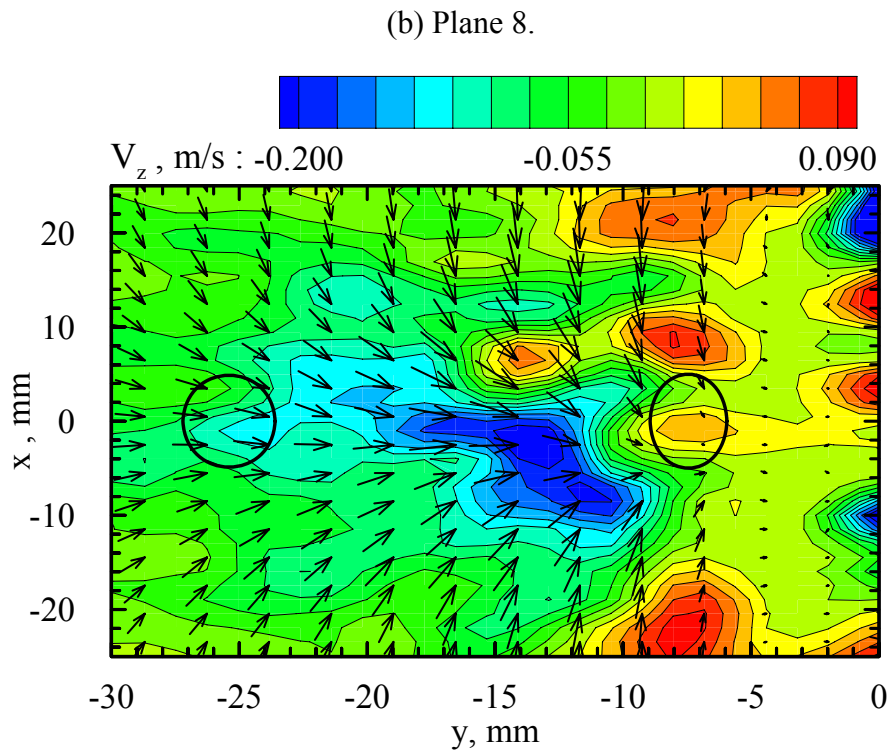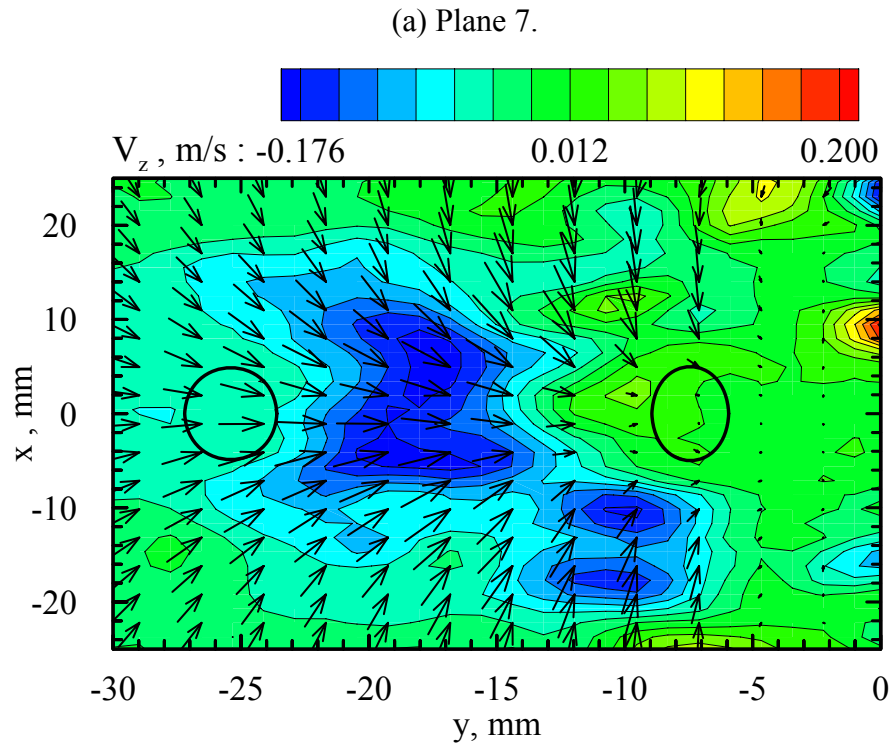
Figure 5.21 Velocity field in horizontal planes number 7 and 8 in case 13.

149
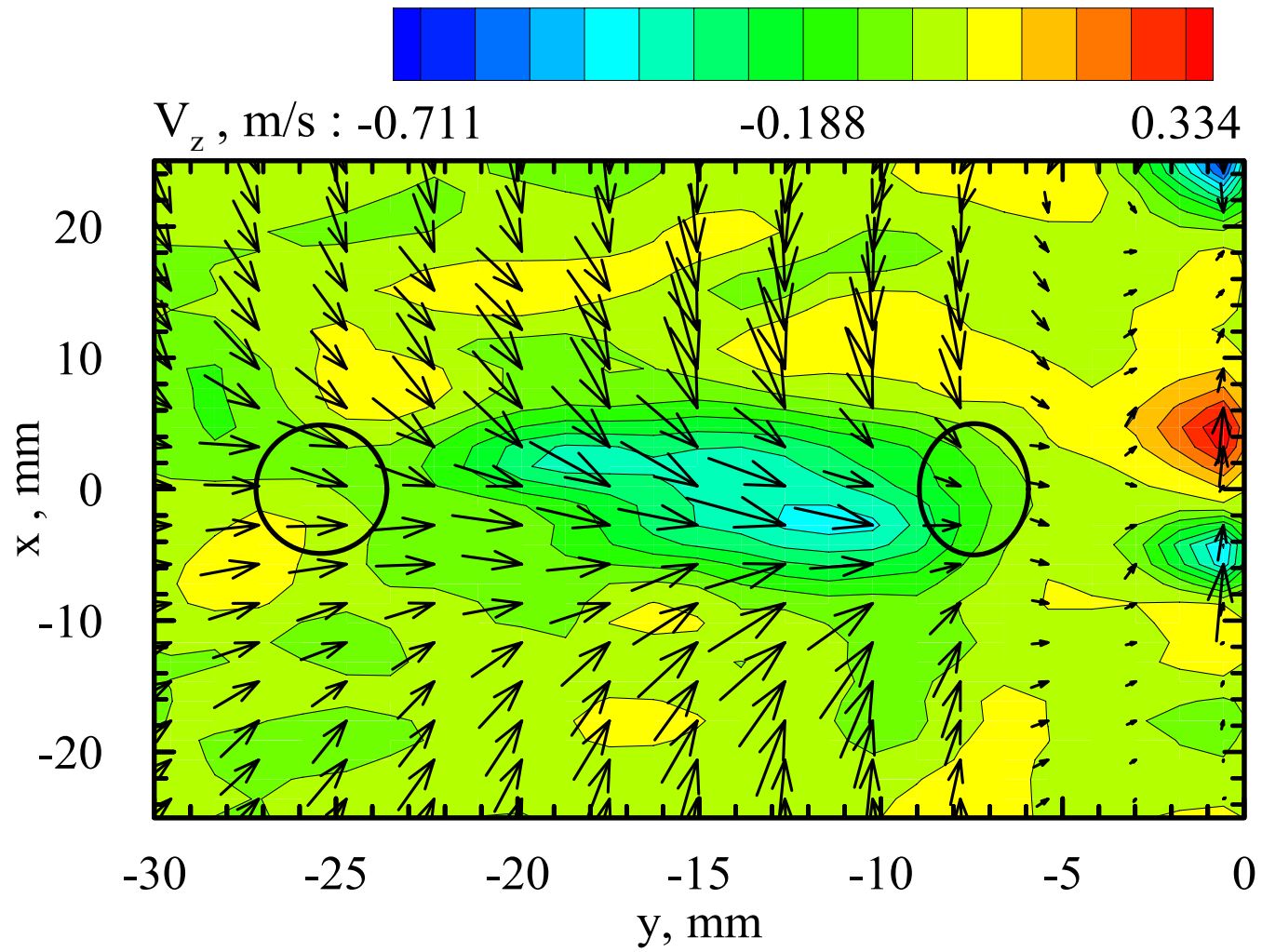
Figure 5.22 Velocity field in a horizontal plane number 9 in case 13.

(a) 8-point circulation vorticity in plane 1.
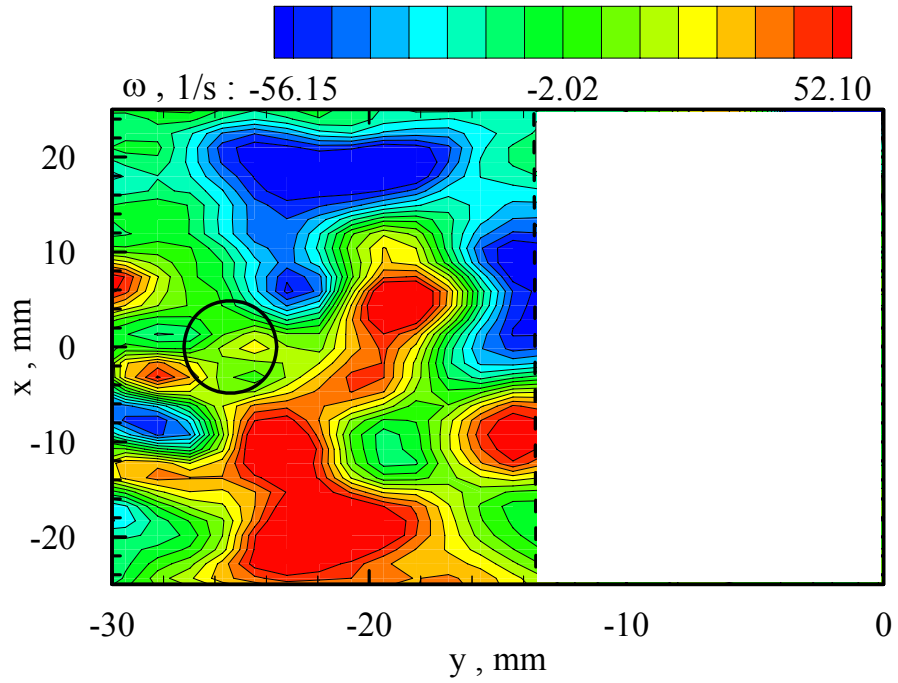
(b) Vortical structures based on λ_2 criterion in plane 1.
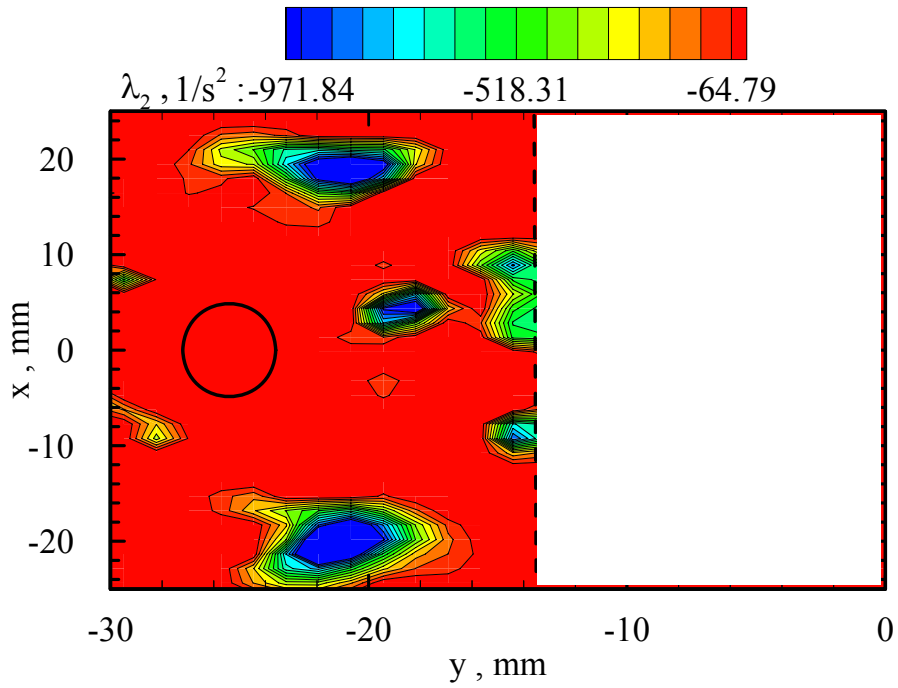
Figure 5.23 Vorticity field in a horizontal plane number 1 in case 13 calculated based on 8-point circulation vorticity equation (a) and vortical structures based on λ_2 criterion (b).

(a) 8-point circulation vorticity in plane 2.
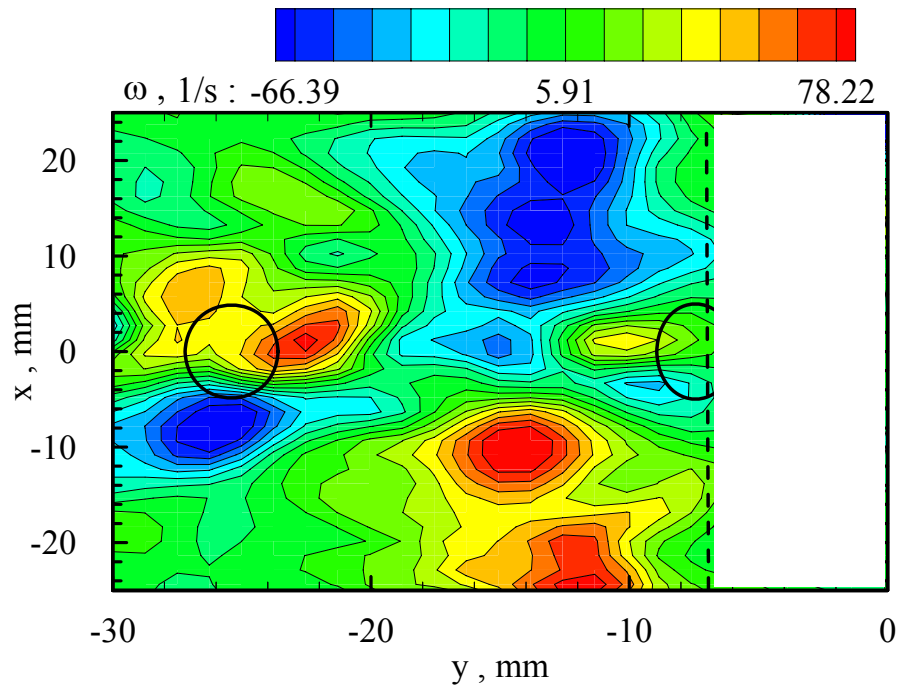
(b) Vortical structures based on λ_2 criterion in plane 2.
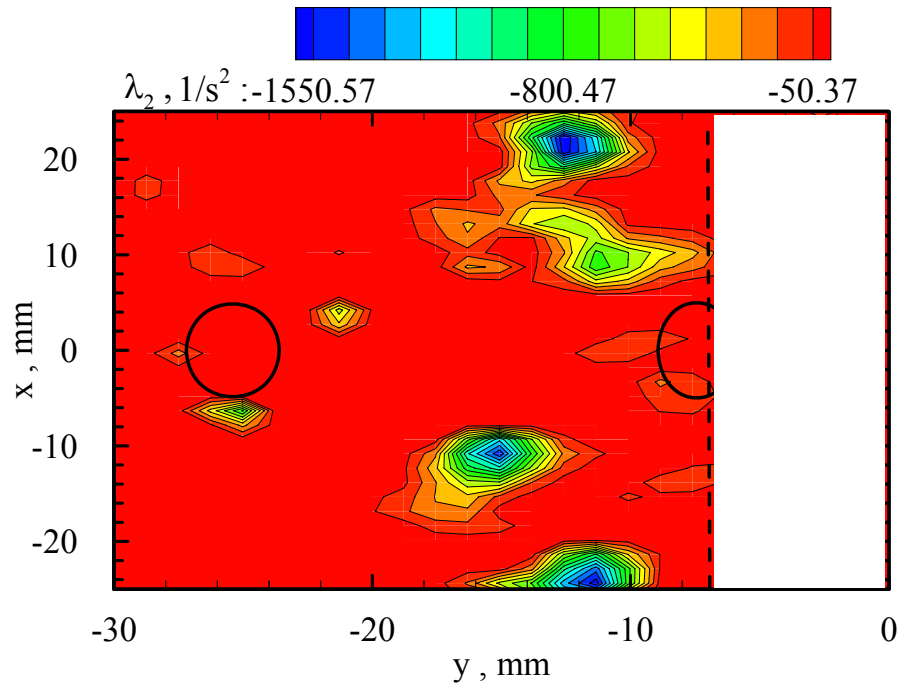
Figure 5.24 Vorticity field in a horizontal plane number 2 in case 13 calculated based on 8-point circulation vorticity equation (a) and vortical structures based on λ_2 criterion (b).

(a) 8-point circulation vorticity in plane 3.
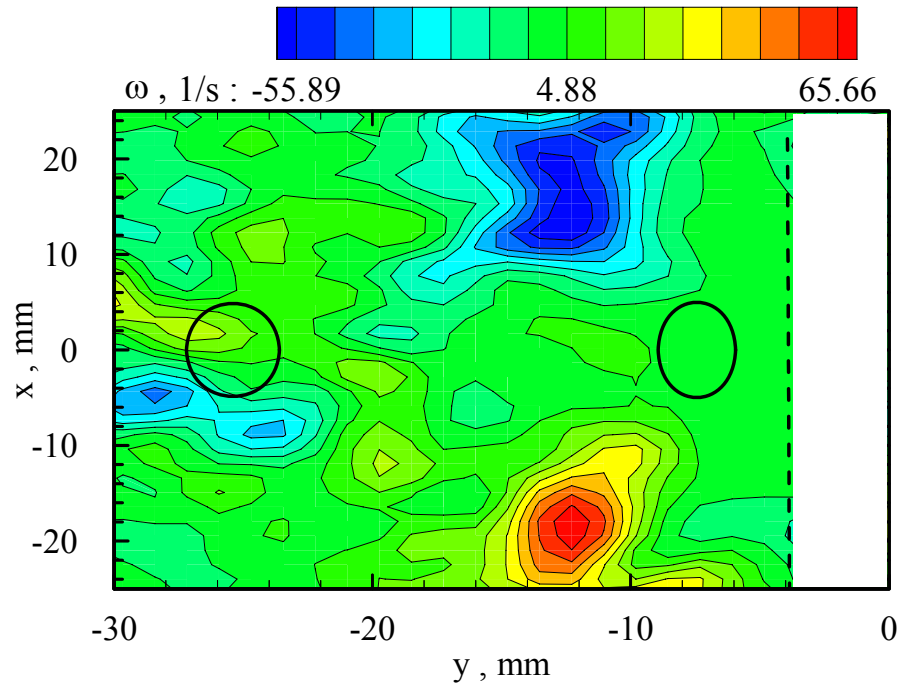
(b) Vortical structures based on λ_2 criterion in plane 3.
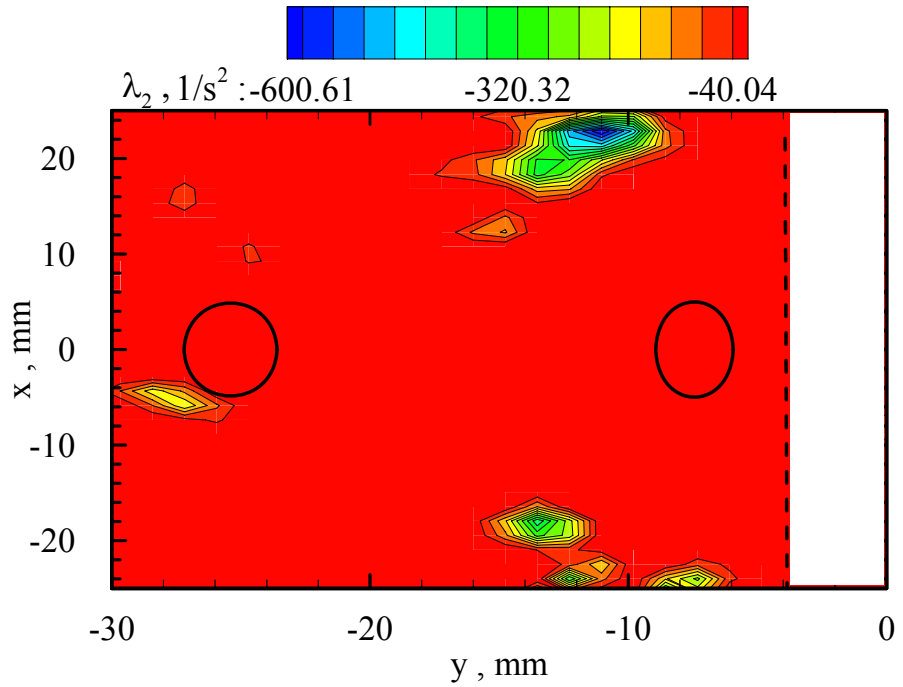
Figure 5.25 Vorticity field in a horizontal plane number 3 in case 13 calculated based on 8-point circulation vorticity equation (a) and vortical structures based on λ_2 criterion (b).

(a) 8-point circulation vorticity in plane 4.
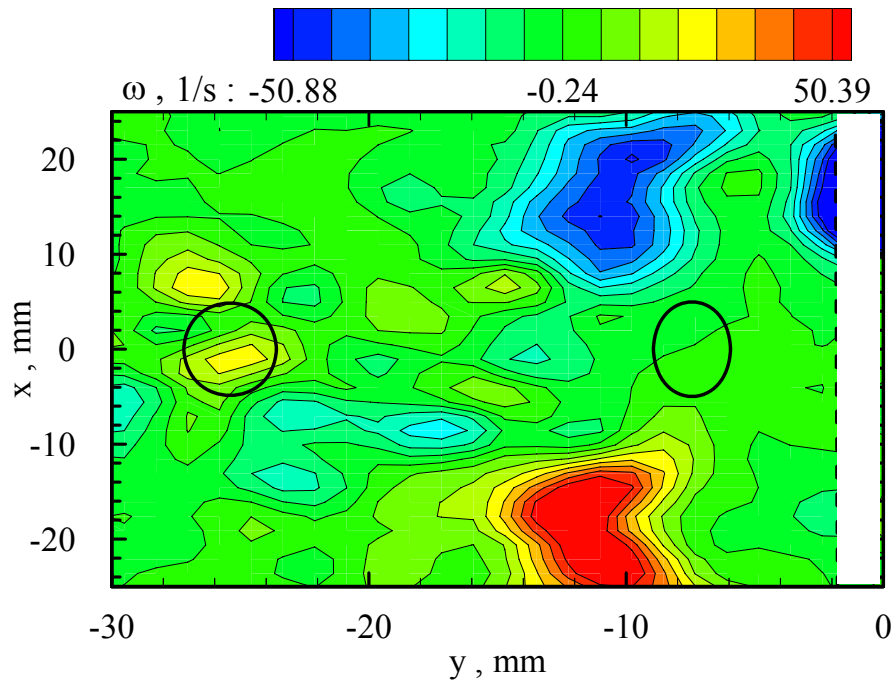
(b) Vortical structures based on λ_2 criterion in plane 4.
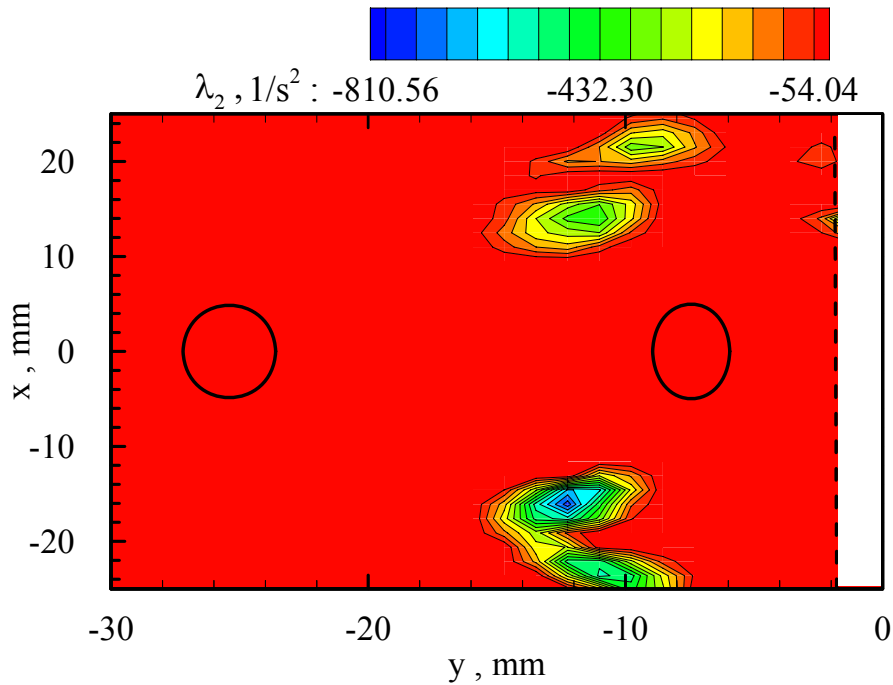
Figure 5.26 Vorticity field in a horizontal plane number 4 in case 13 calculated based on 8-point circulation vorticity equation (a) and vortical structures based on λ_2 criterion (b).

(a) 8-point circulation vorticity in plane 5.
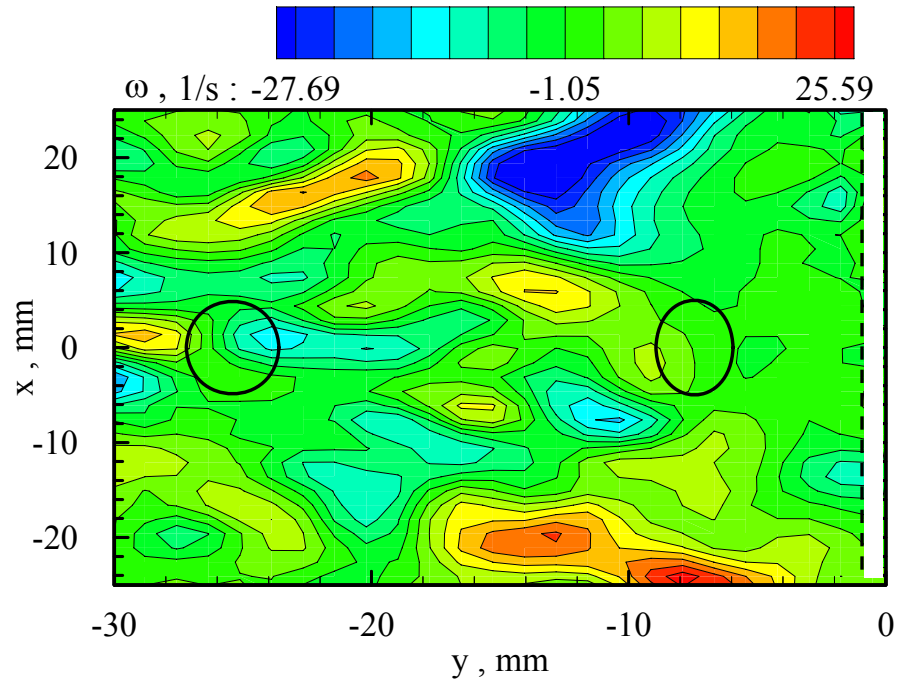
(b) Vortical structures based on λ_2 criterion in plane 5.
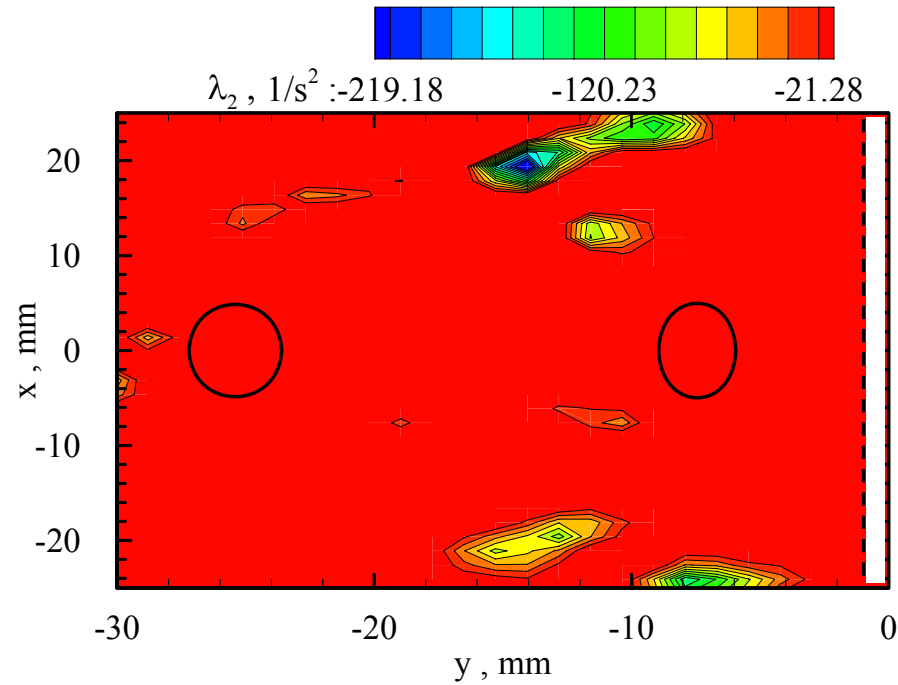
Figure 5.27 Vorticity field in a horizontal plane number 5 in case 13 calculated based on 8-point circulation vorticity equation (a) and vortical structures based on λ_2 criterion (b).

(a) 8-point circulation vorticity in plane 6.
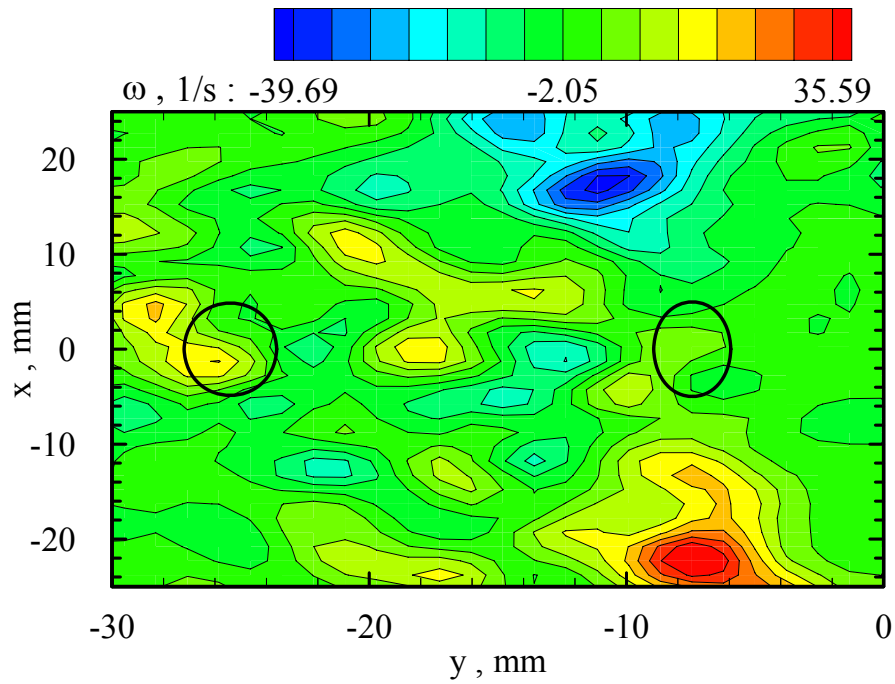
(b) Vortical structures based on λ_2 criterion in plane 6.
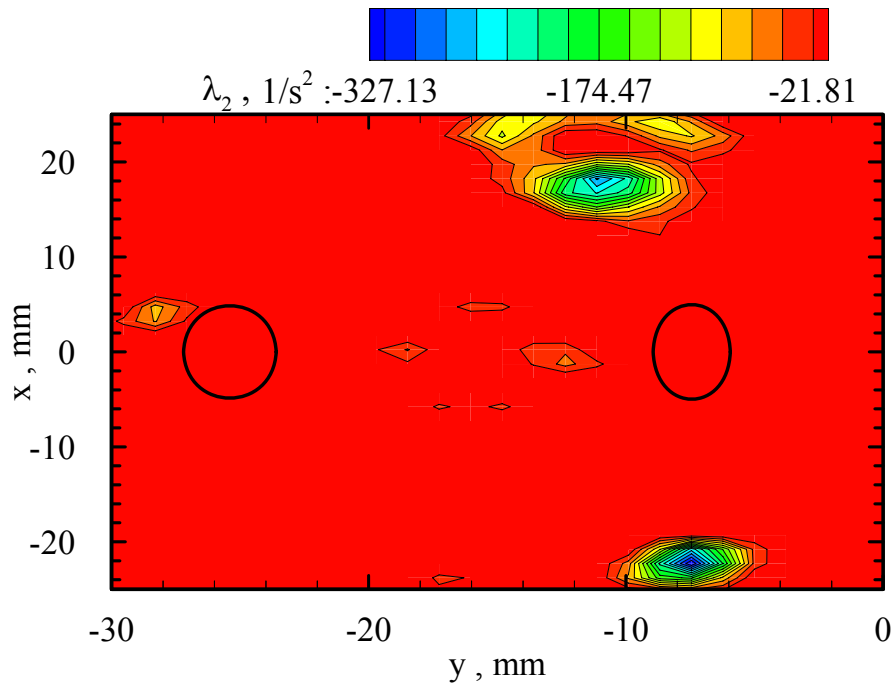
Figure 5.28 Vorticity field in a horizontal plane number 6 in case 13 calculated based on 8-point circulation vorticity equation (a) and vortical structures based on λ_2 criterion (b).

156

(a) 8-point circulation vorticity in plane 7.
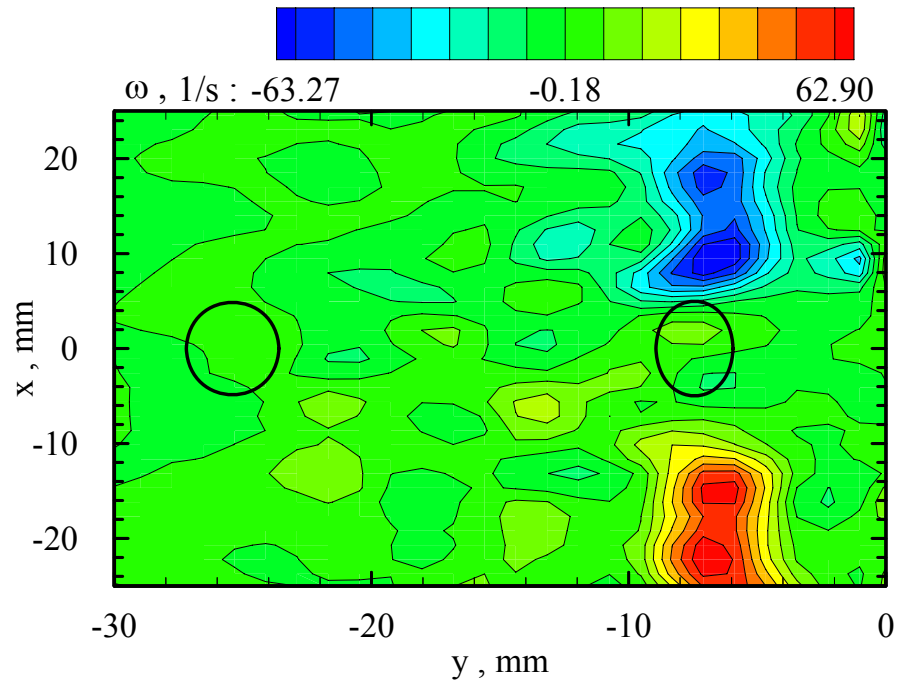
(b) Vortical structures based on λ_2 criterion in plane 7.
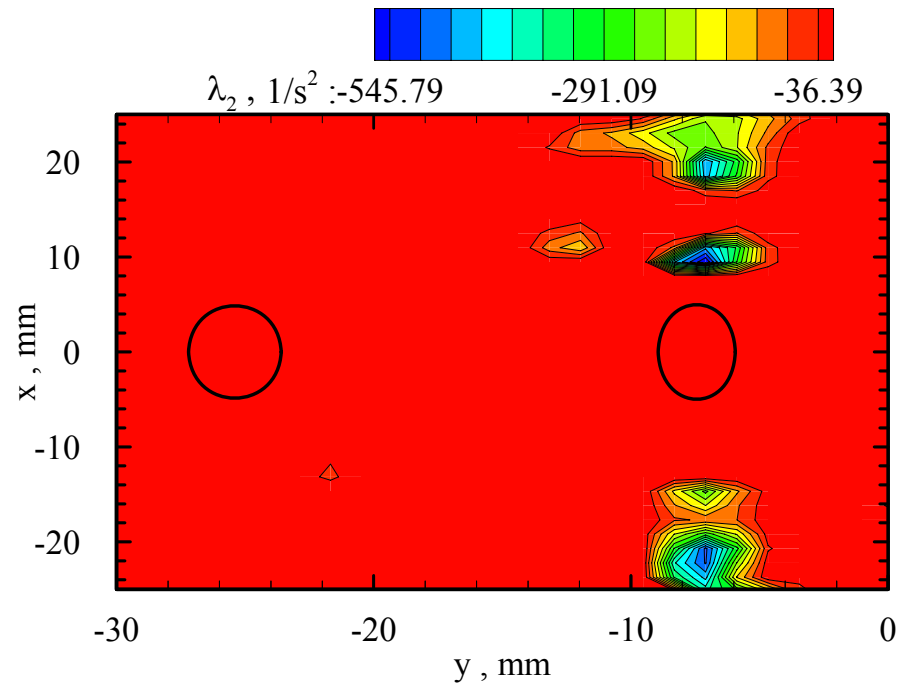
Figure 5.29 Vorticity field in a horizontal plane number 7 in case 13 calculated based on 8-point circulation vorticity equation (a) and vortical structures based on λ_2 criterion (b).

(a) 8-point circulation vorticity in plane 8.
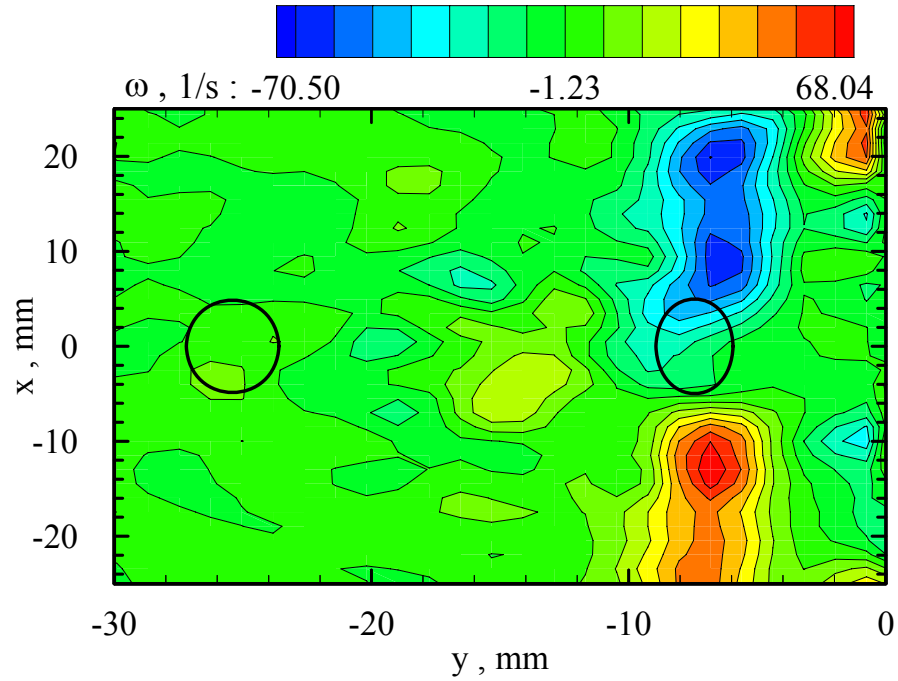
(b) Vortical structures based on λ₂ criterion in plane 8.
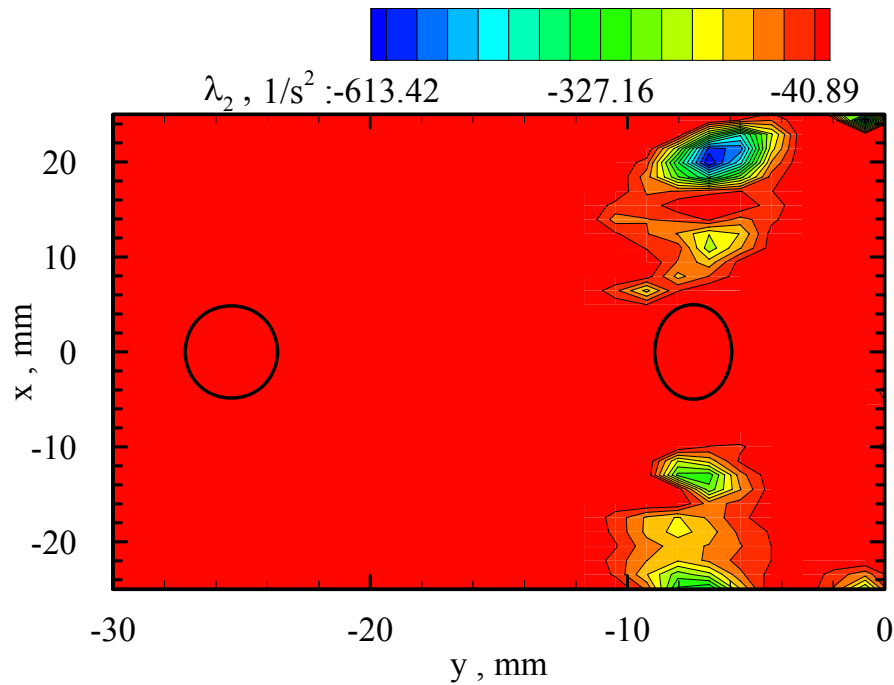
Figure 5.30 Vorticity field in a horizontal plane number 8 in case 13 calculated based on 8-point circulation vorticity equation (a) and vortical structures based on λ_2 criterion (b).

(a) 8-point circulation vorticity in plane 9.
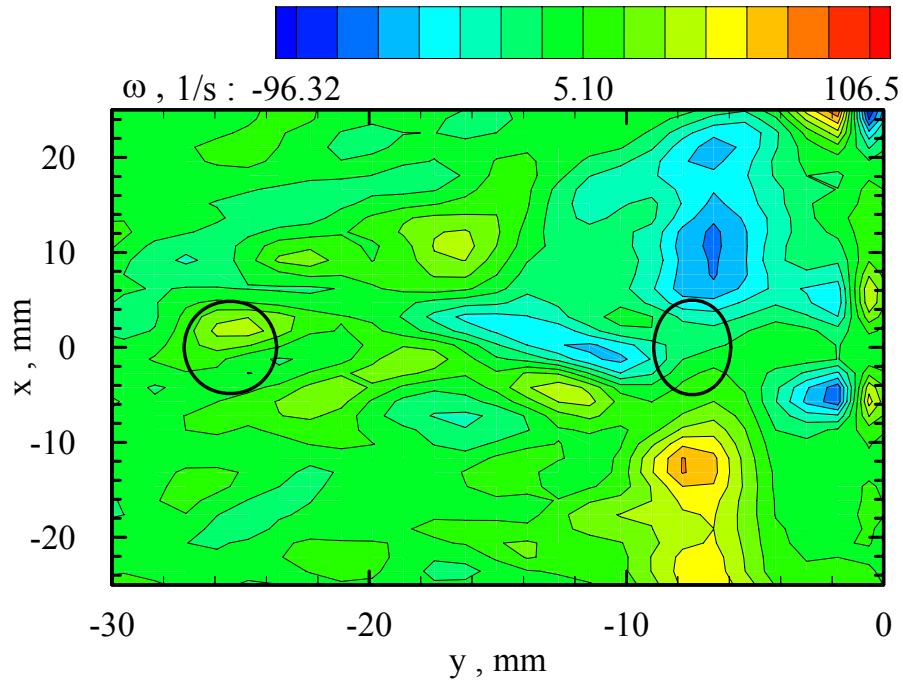
(b) Vortical structures based on λ_2 criterion in plane 9.
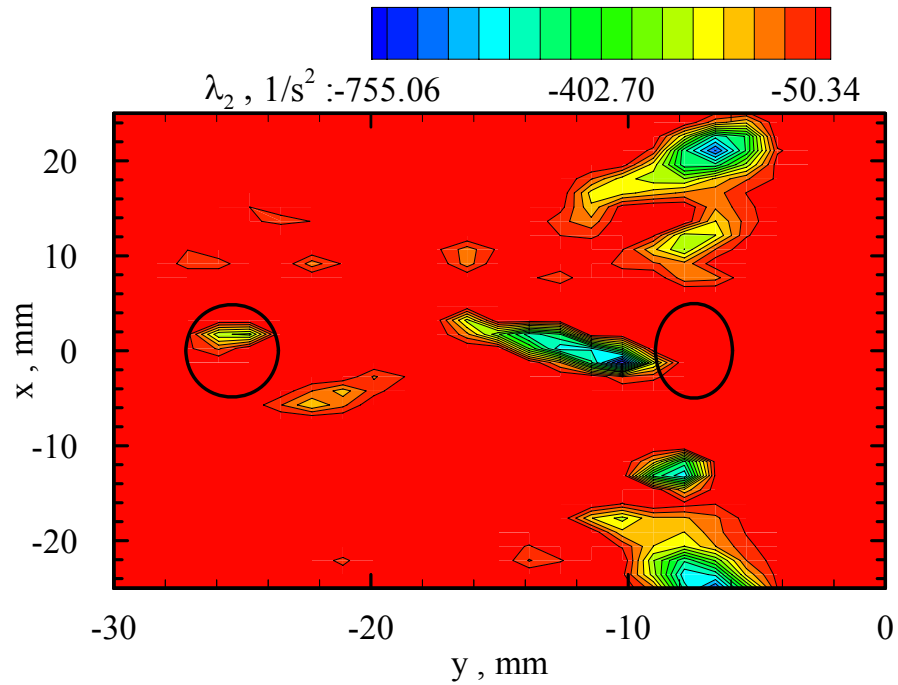
Figure 5.31 Vorticity field in a horizontal plane number 9 in case 13 calculated based on 8-point circulation vorticity equation (a) and vortical structures based on λ_2 criterion (b).
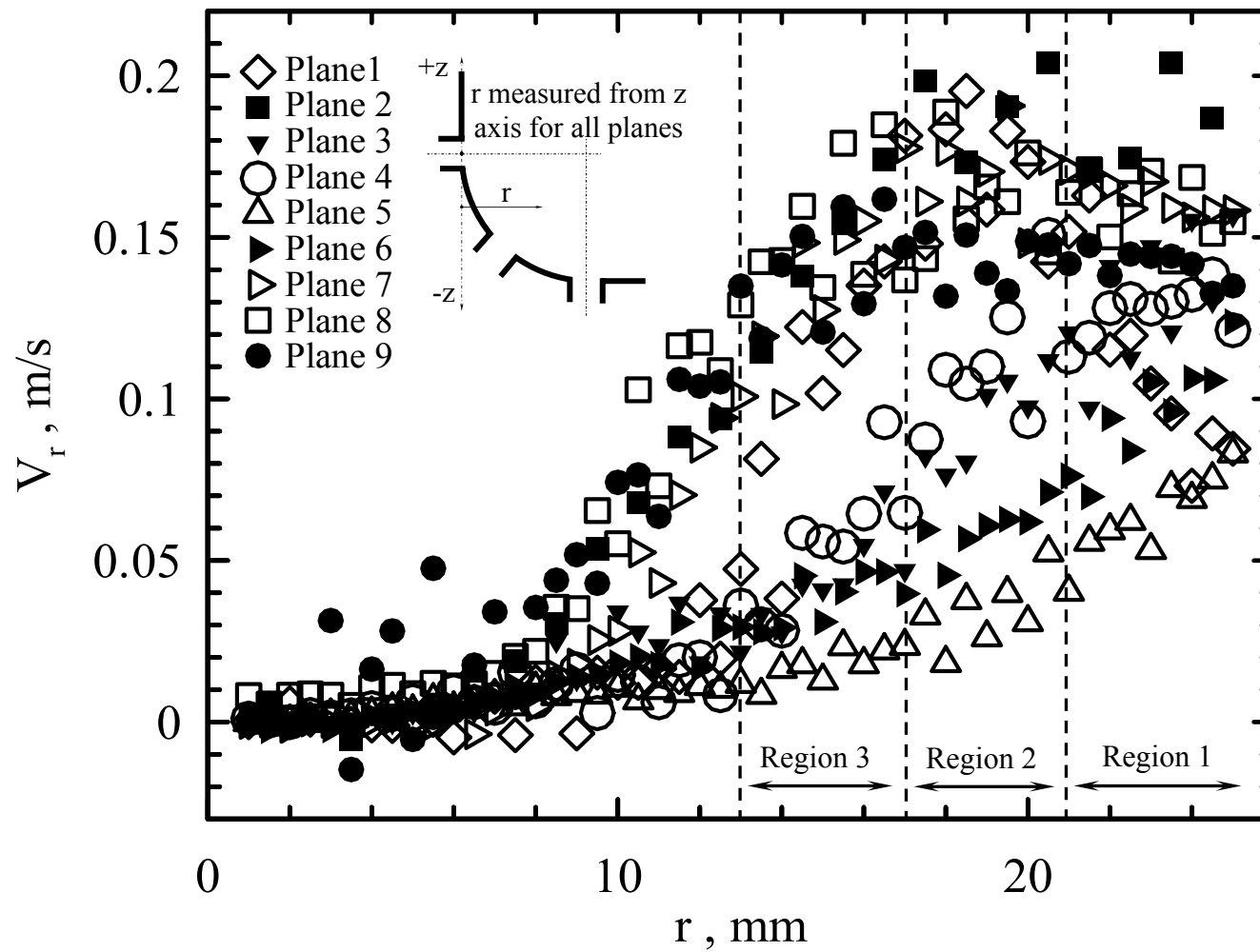
Figure 5.32 Effect of investigated plane height on average radial velocity change along r.
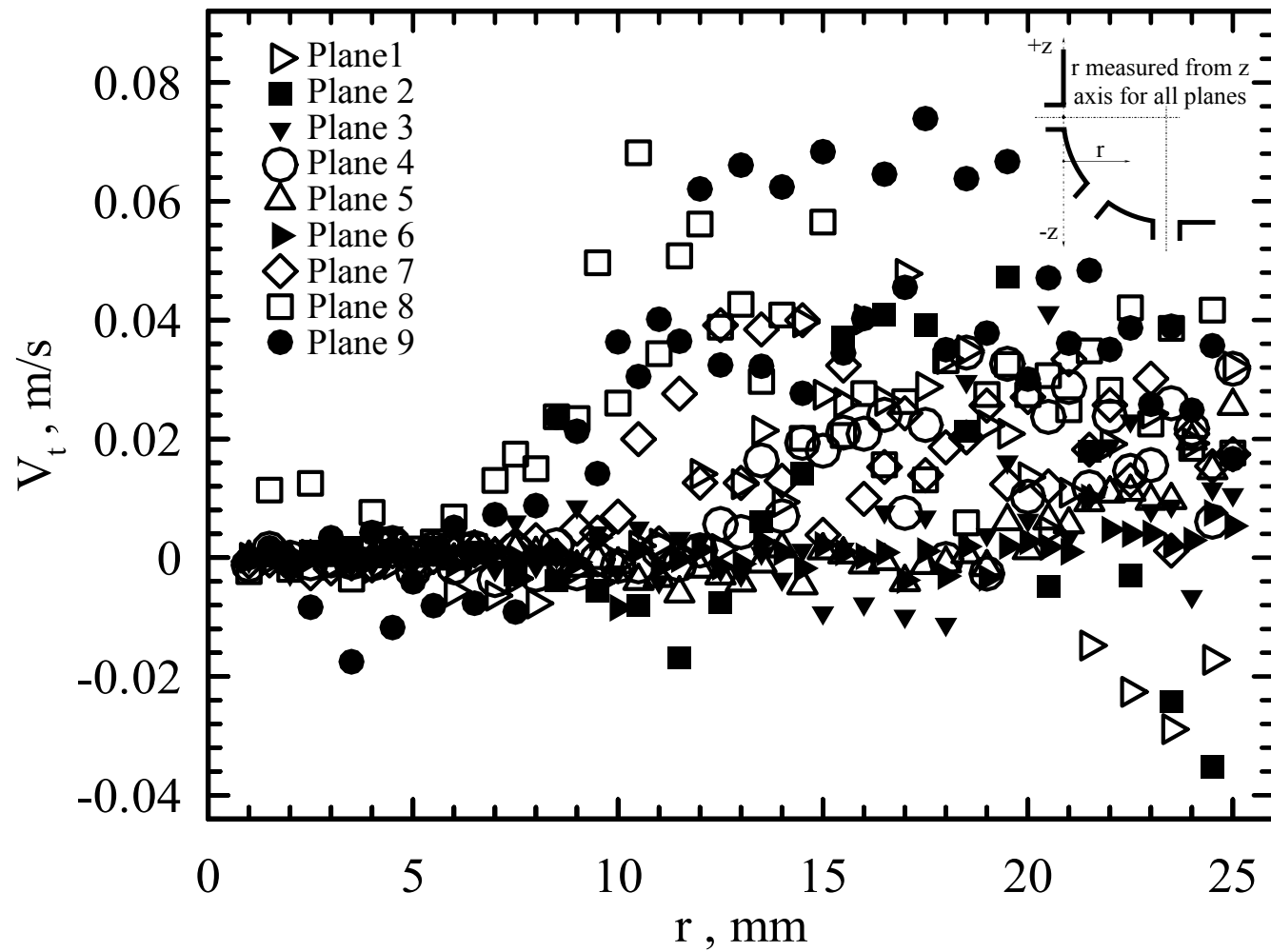
Figure 5.33 Effect of investigated plane height on average tangential velocity change along r.
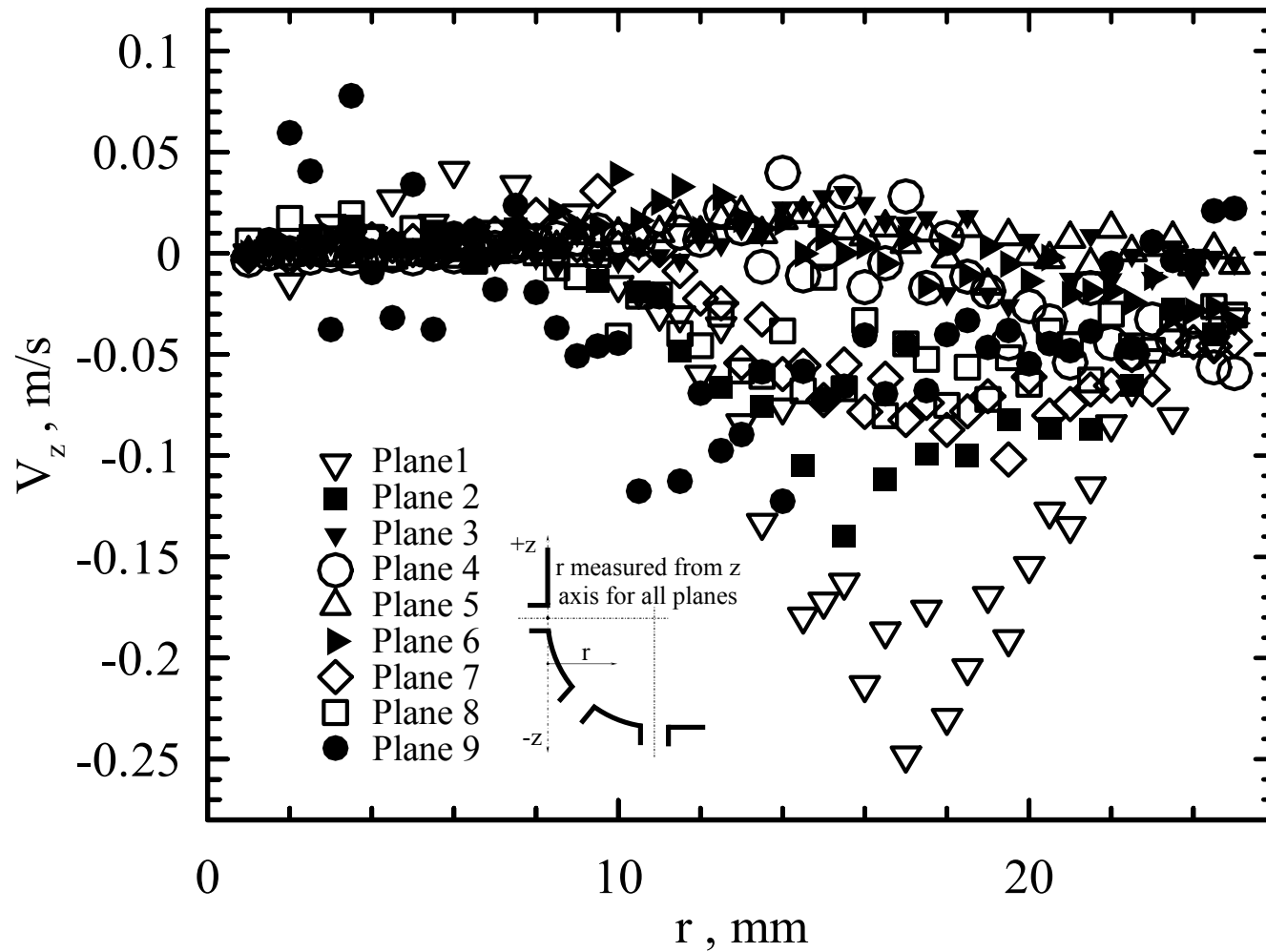
Figure 5.34 Effect of investigated plane height on average vertical velocity change along r.

(a) High Froude number in branch *A*, plane 1.
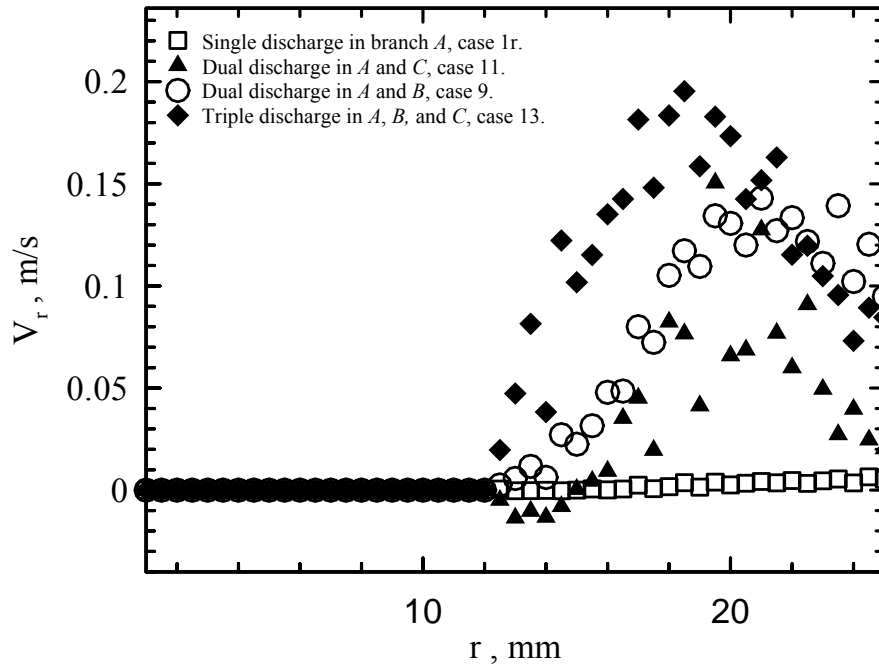
(b) Medium Froude number in branch *A*, plane 1.
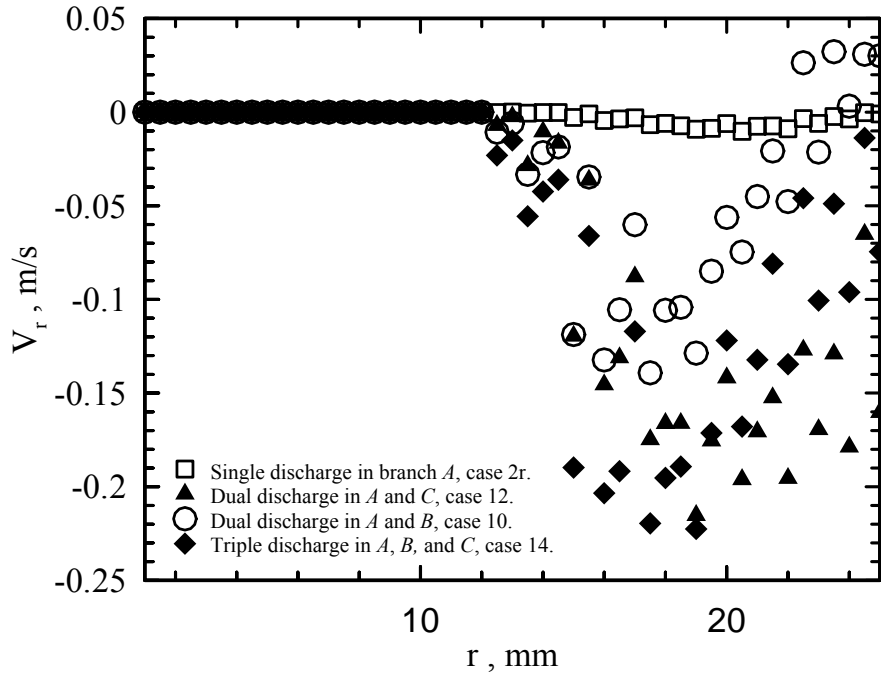
Figure 5.35 Average radial velocity change along r in plane 1 for different flow configurations at (a) High Froude number in branch *A*, and (b) Medium Froude number in branch *A*.

(a) High Froude number in branch *A*, plane 2.
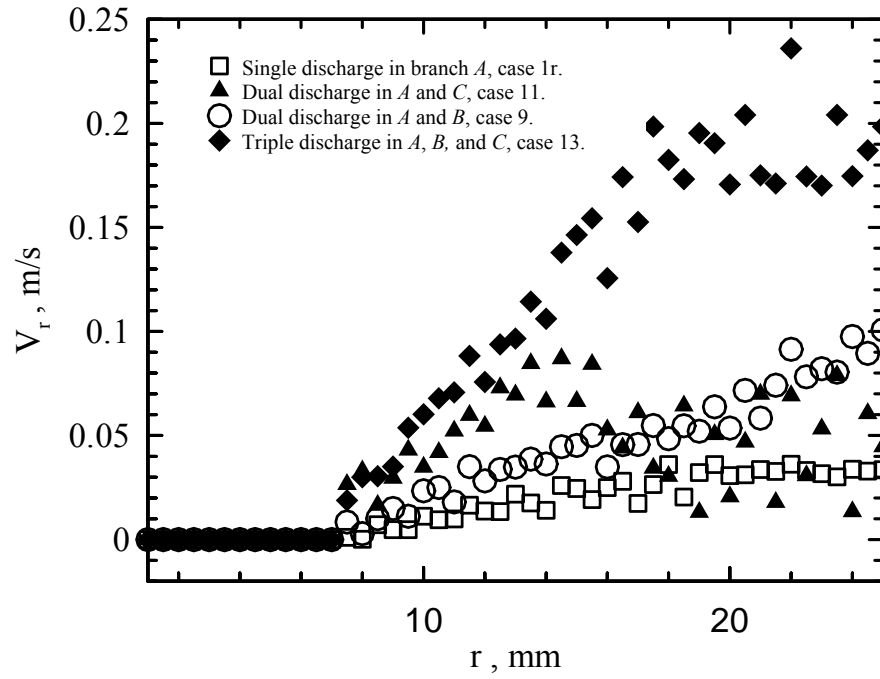
(b) Medium Froude number in branch *A*, plane 2.
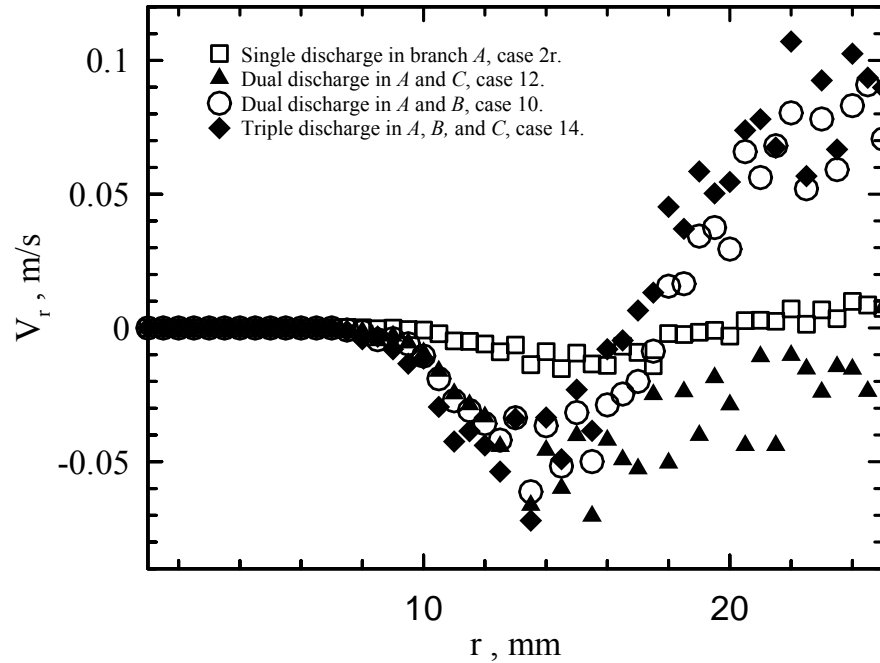
Figure 5.36 Average radial velocity change along r in plane 2 for different flow configurations at (a) High Froude number in branch *A*, and (b) Medium Froude number in branch *A*.

(a) High Froude number in branch *A*, plane 3.
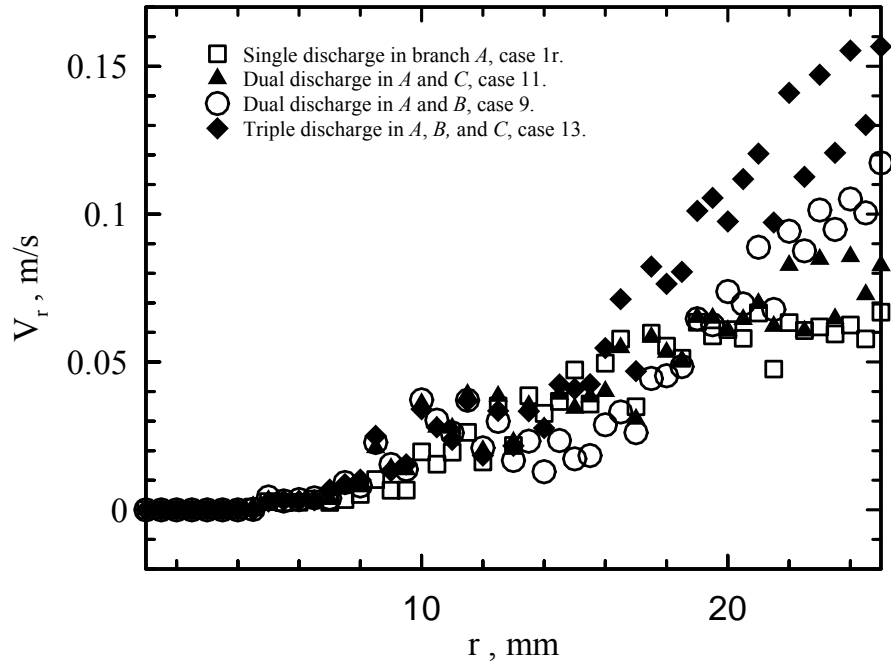
(b) Medium Froude number in branch *A*, plane 3.
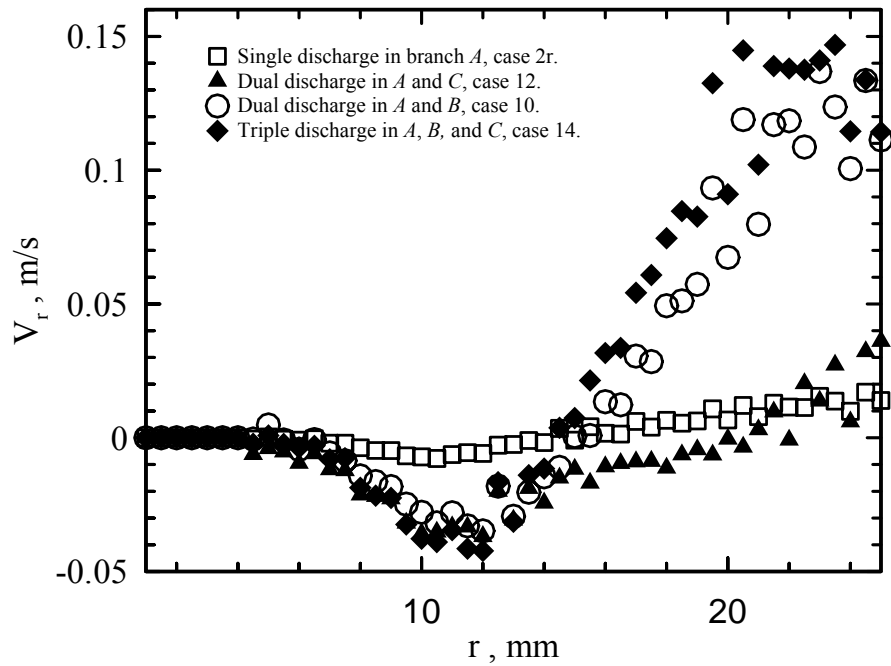
Figure 5.37 Average radial velocity change along r in plane 3 for different flow
configurations at (a) High Froude number in branch *A*, and (b) Medium Froude number
in branch *A*.

(a) High Froude number in branch *A*, plane 4.
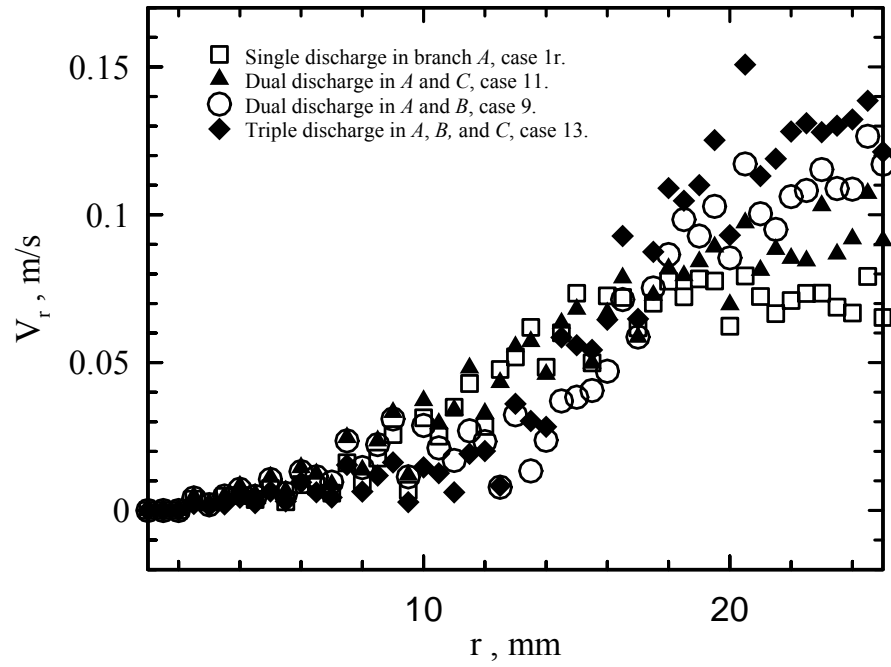
(b) Medium Froude number in branch *A*, plane 4.
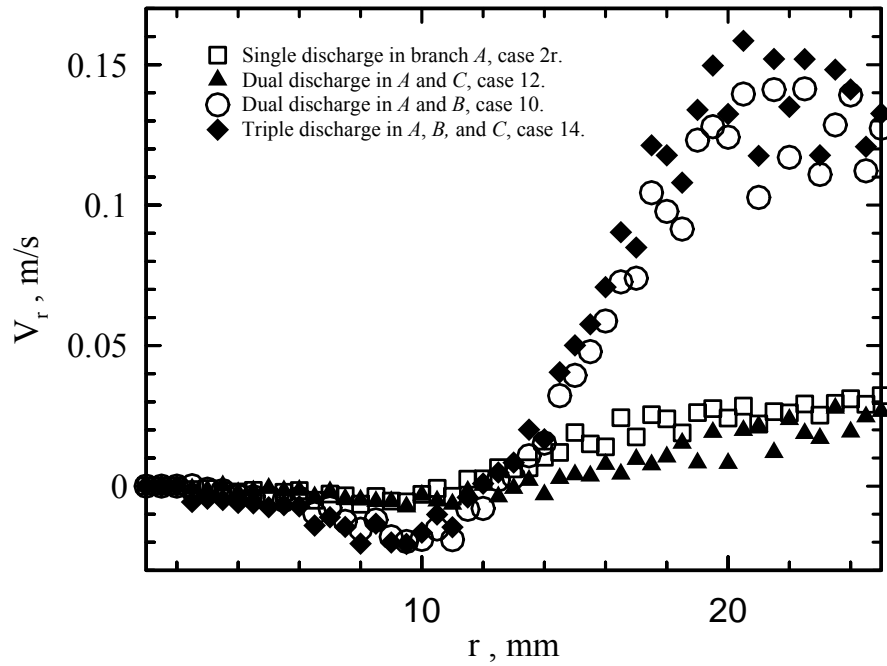
Figure 5.38 Average radial velocity change along r in plane 4 for different flow configurations at (a) High Froude number in branch *A*, and (b) Medium Froude number in branch *A*.

(a) High Froude number in branch *A*, plane 5.
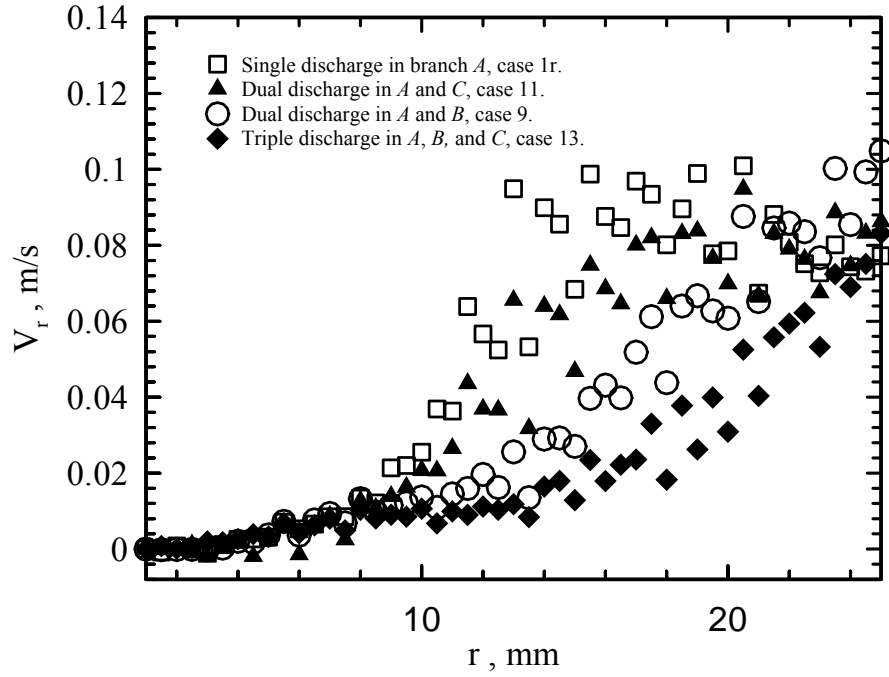
(b) Medium Froude number in branch *A*, plane 5.
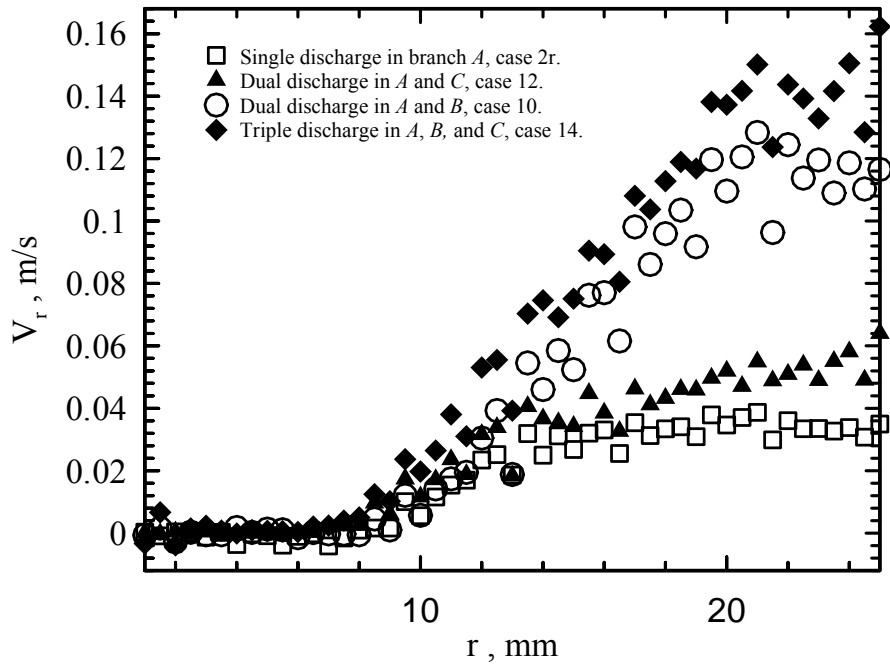
Figure 5.39 Average radial velocity change along r in plane 5 for different flow configurations at (a) High Froude number in branch *A*, and (b) Medium Froude number in branch *A*.

(a) High Froude number in branch *A*, plane 6.
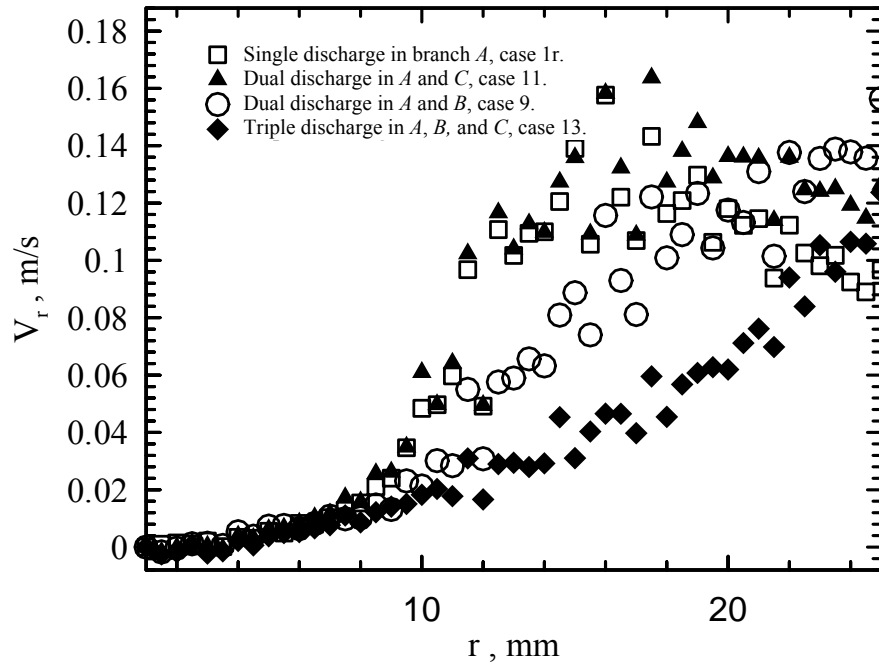
(b) Medium Froude number in branch *A*, plane 6.
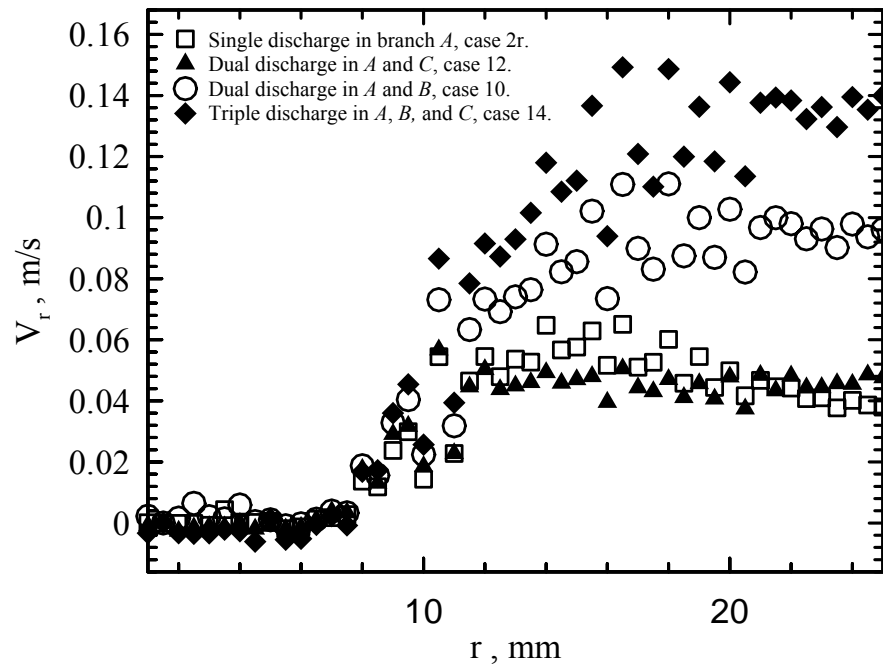
Figure 5.40 Average radial velocity change along r in plane 6 for different flow configurations at (a) High Froude number in branch *A*, and (b) Medium Froude number in branch *A*.

(a) High Froude number in branch *A*, plane 7.
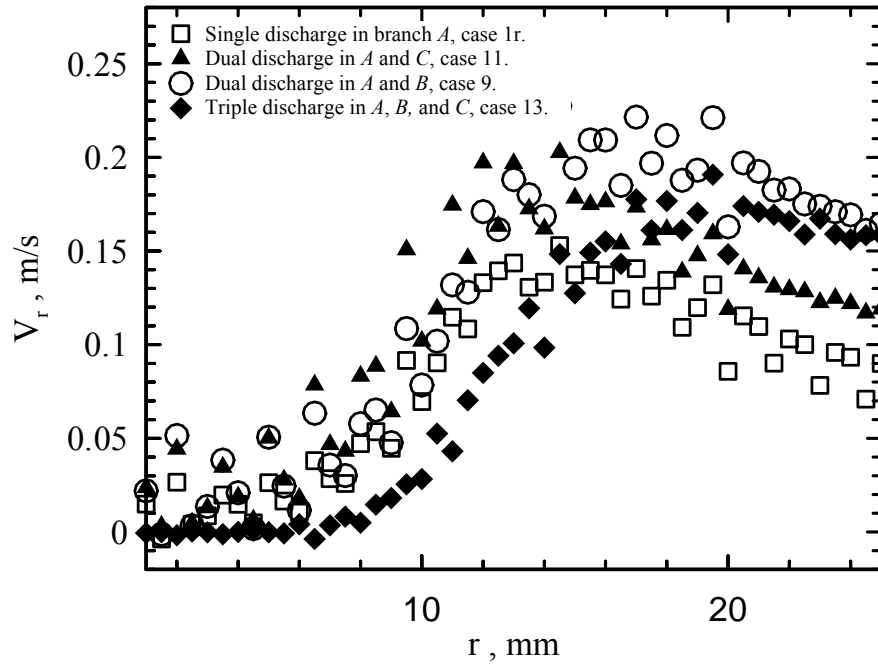
(b) Medium Froude number in branch *A*, plane 7.
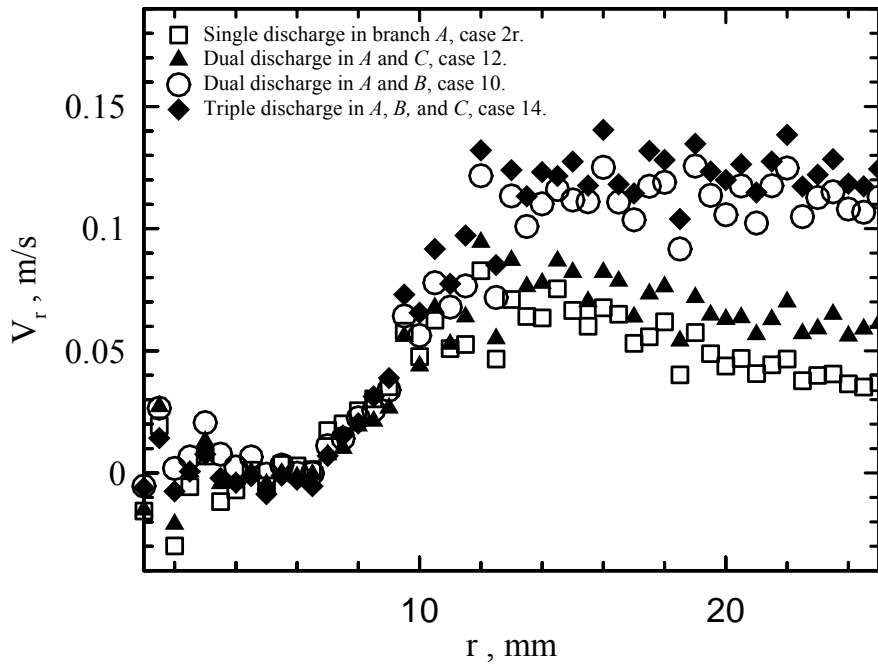
Figure 5.41 Average radial velocity change along r in plane 7 for different flow configurations at (a) High Froude number in branch *A*, and (b) Medium Froude number in branch *A*.

(a) High Froude number in branch *A*, plane 8.
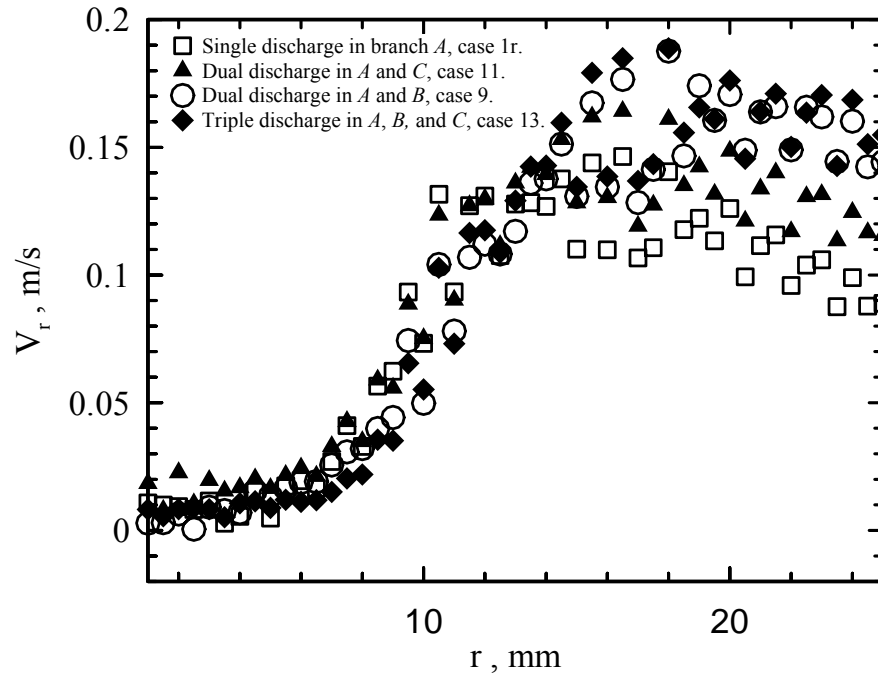
(b) Medium Froude number in branch *A*, plane 8.
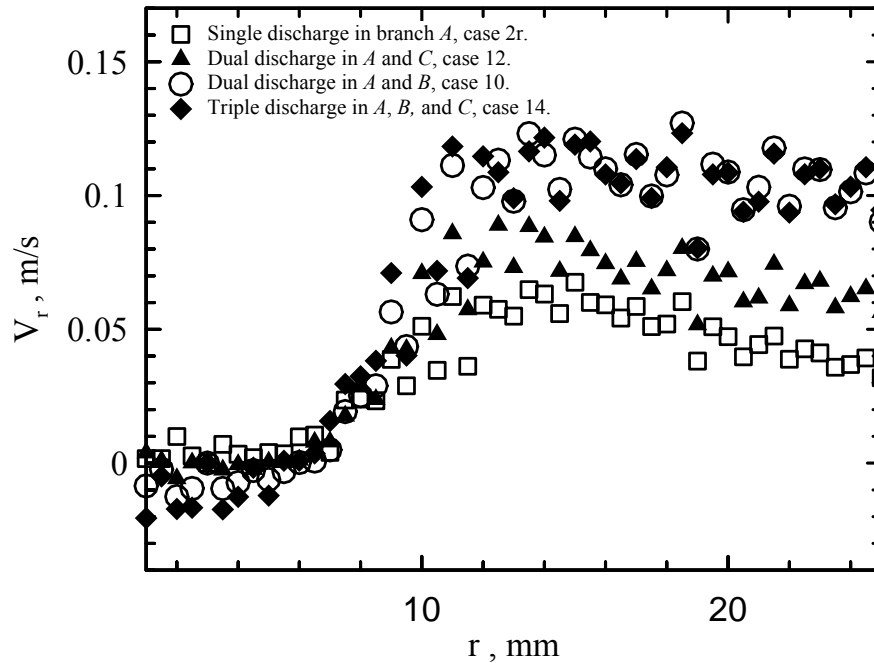
Figure 5.42 Average radial velocity change along r in plane 8 for different flow configurations at (a) High Froude number in branch *A*, and (b) Medium Froude number in branch *A*.

170

(a) High Froude number in branch *A*, plane 1.
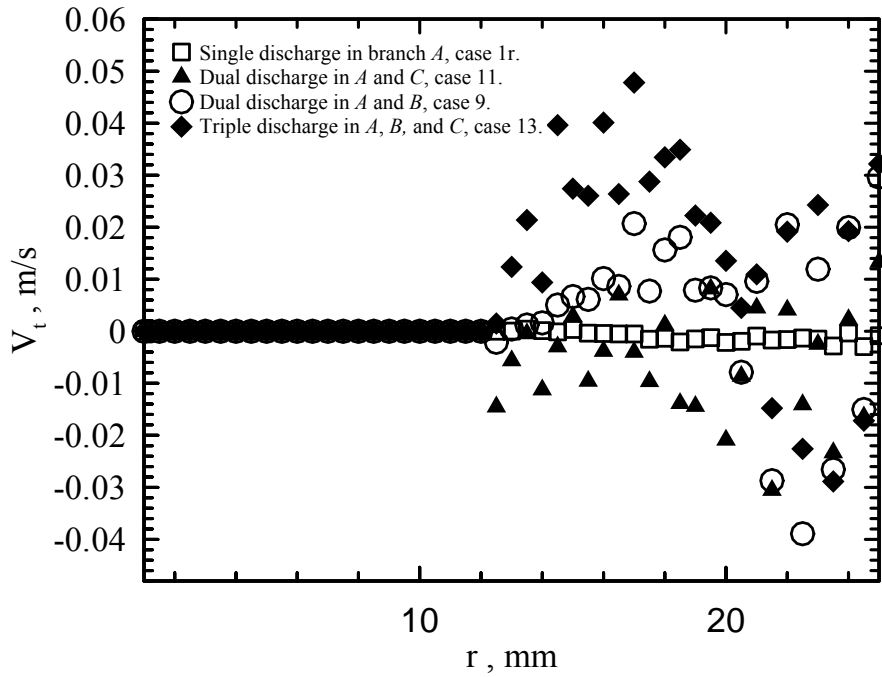
(b) Medium Froude number in branch *A*, plane 1.
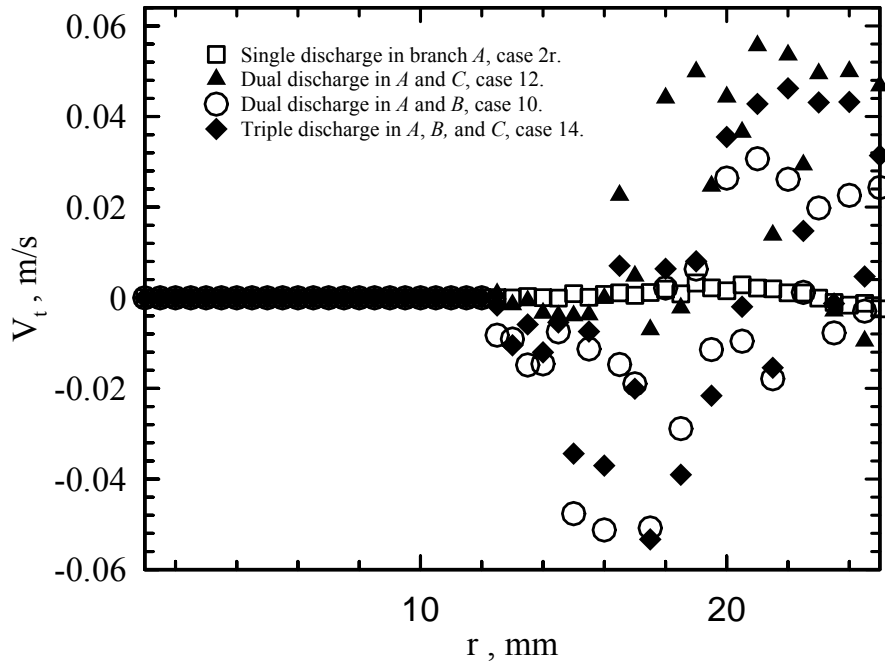
Figure 5.43 Average tangential velocity change along r in plane 1 for different flow configurations at (a) High Froude number in branch *A*, and (b) Medium Froude number in branch *A*.

(a) High Froude number in branch *A*, plane 2.
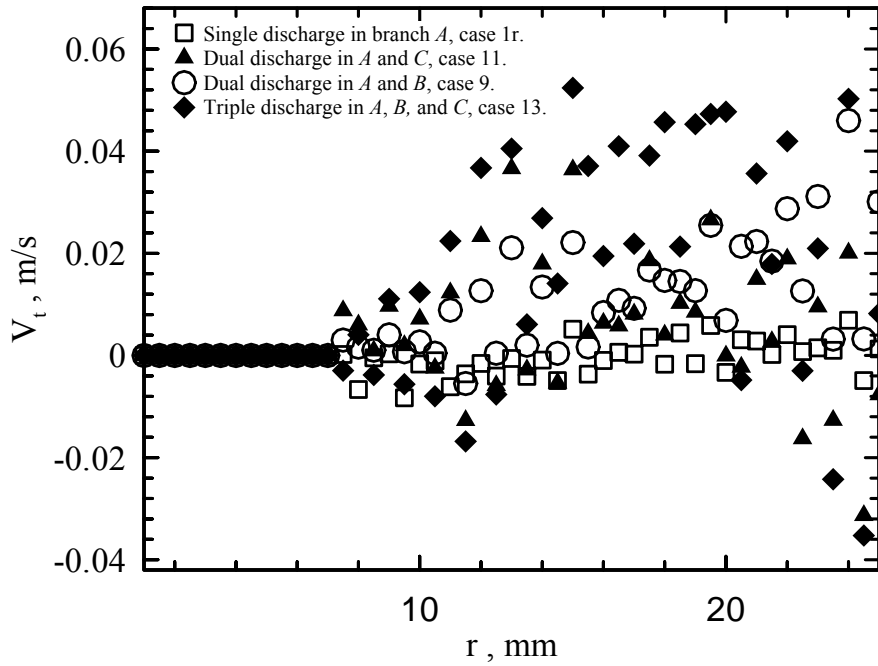
(b) Medium Froude number in branch *A*, plane 2.
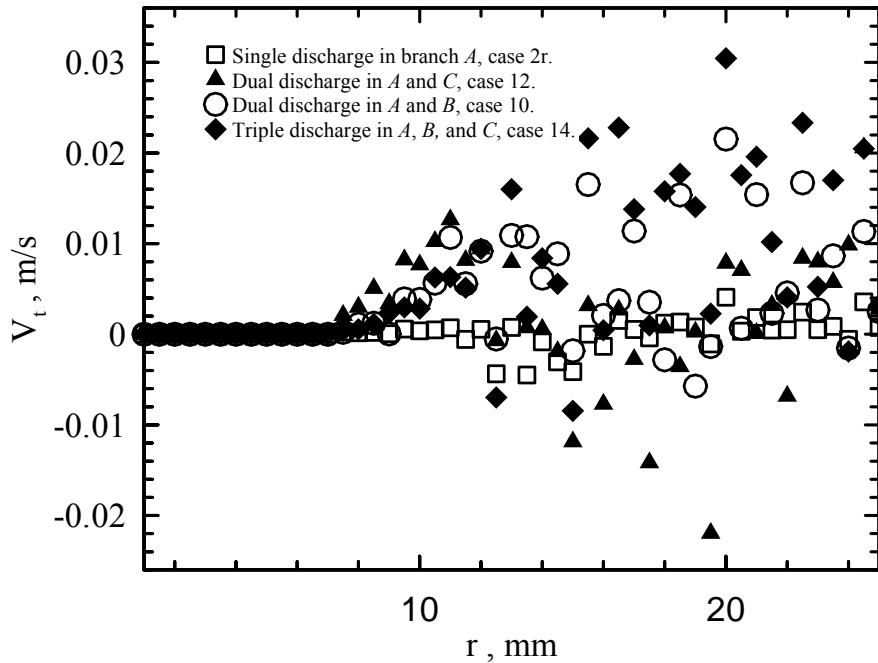
Figure 5.44 Average tangential velocity change along r in plane 2 for different flow configurations at (a) High Froude number in branch *A*, and (b) Medium Froude number in branch *A*.

(a) High Froude number in branch *A*, plane 3.
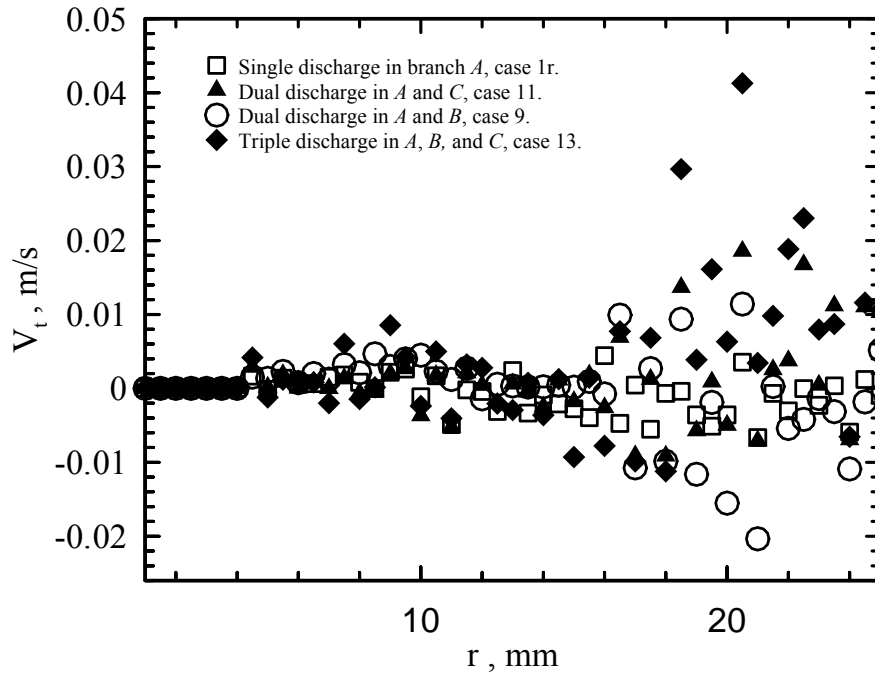
(b) Medium Froude number in branch *A*, plane 3.
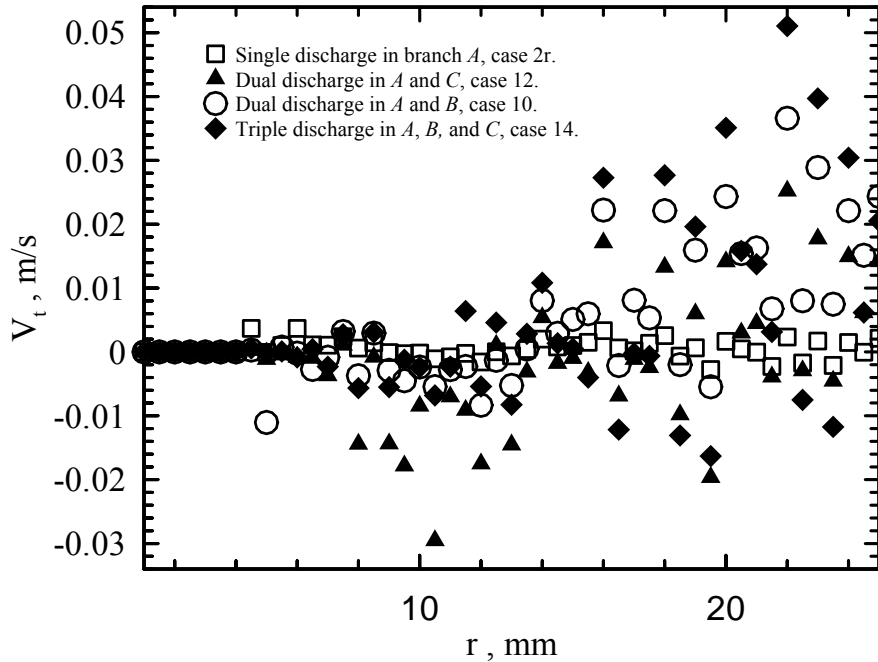
Figure 5.45 Average tangential velocity change along r in plane 3 for different flow configurations at (a) High Froude number in branch *A*, and (b) Medium Froude number in branch *A*.

(a) High Froude number in branch *A*, plane 4.
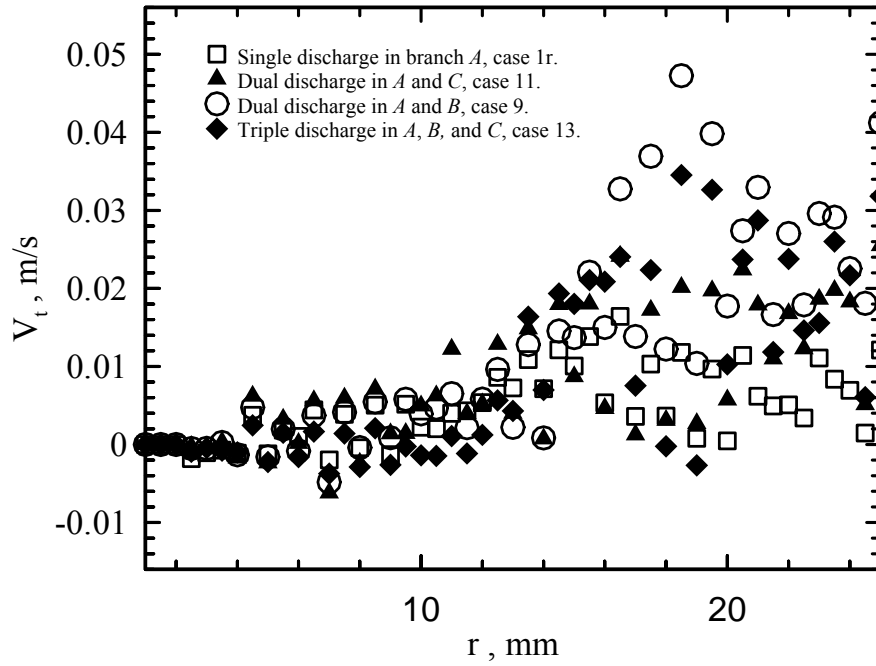
(b) Medium Froude number in branch *A*, plane 4.
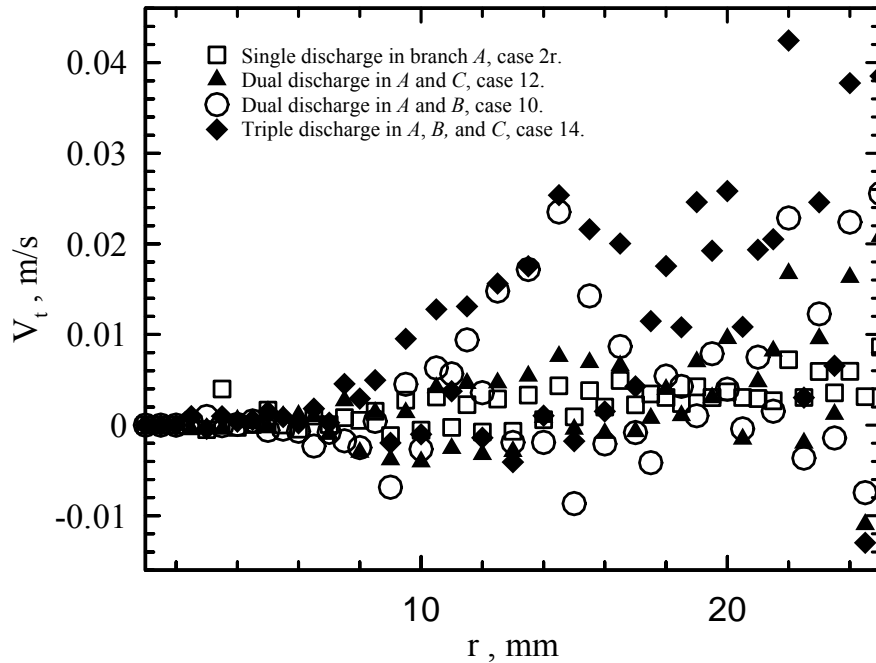
Figure 5.46 Average tangential velocity change along r in plane 4 for different flow configurations at (a) High Froude number in branch *A*, and (b) Medium Froude number in branch *A*.

(a) High Froude number in branch *A*, plane 5.
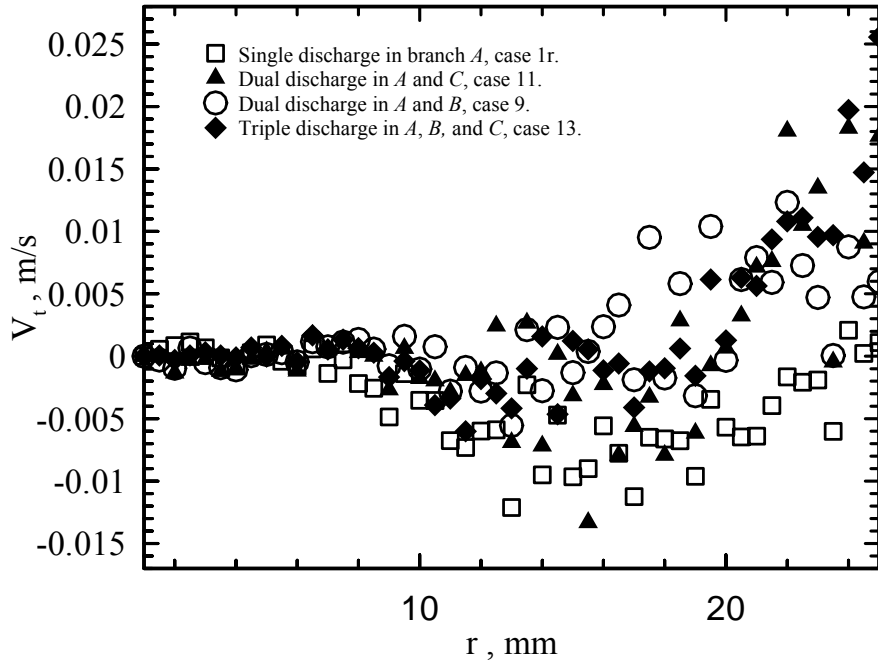
(b) Medium Froude number in branch *A*, plane 5.
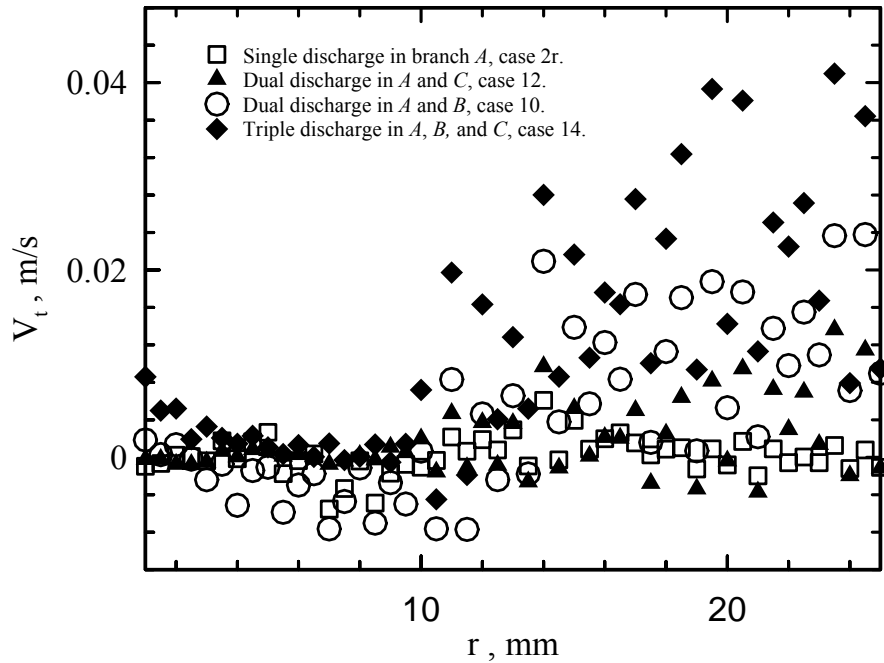
Figure 5.47 Average tangential velocity change along r in plane 5 for different flow configurations at (a) High Froude number in branch *A*, and (b) Medium Froude number in branch *A*.

(a) High Froude number in branch *A*, plane 6.
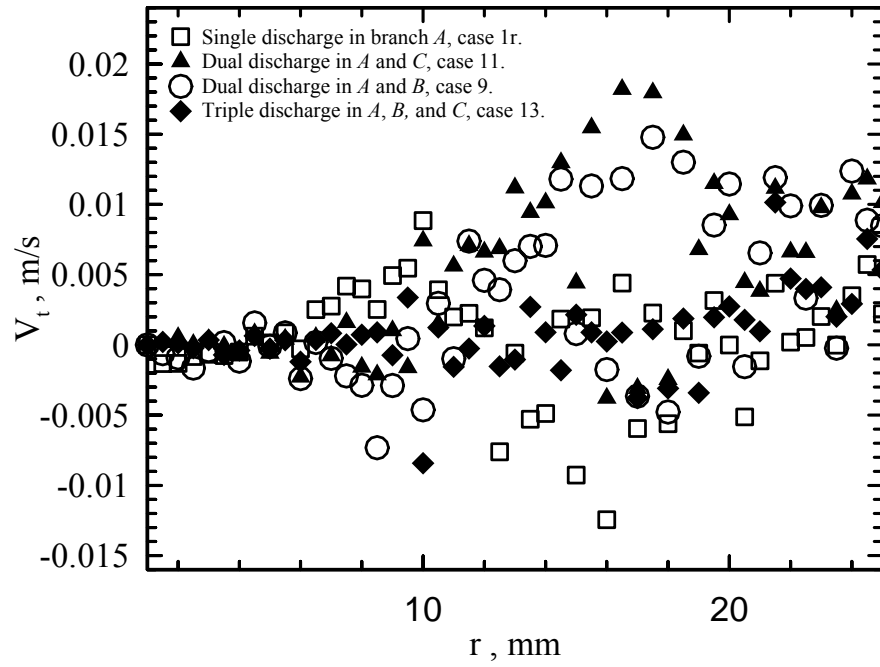
(b) Medium Froude number in branch *A*, plane 6.
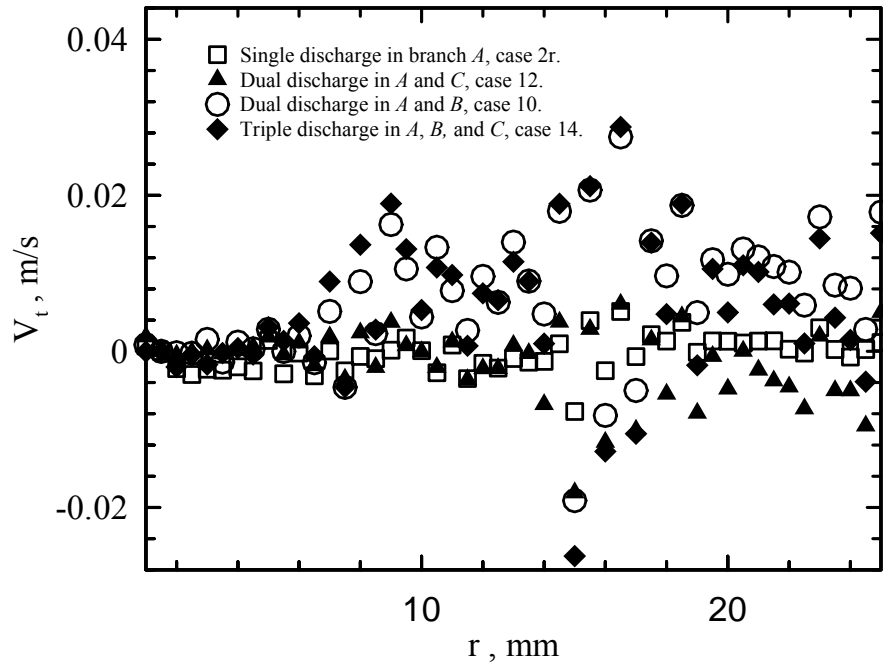
Figure 5.48 Average tangential velocity change along r in plane 6 for different flow configurations at (a) High Froude number in branch *A*, and (b) Medium Froude number in branch *A*.

(a) High Froude number in branch *A*, plane 7.
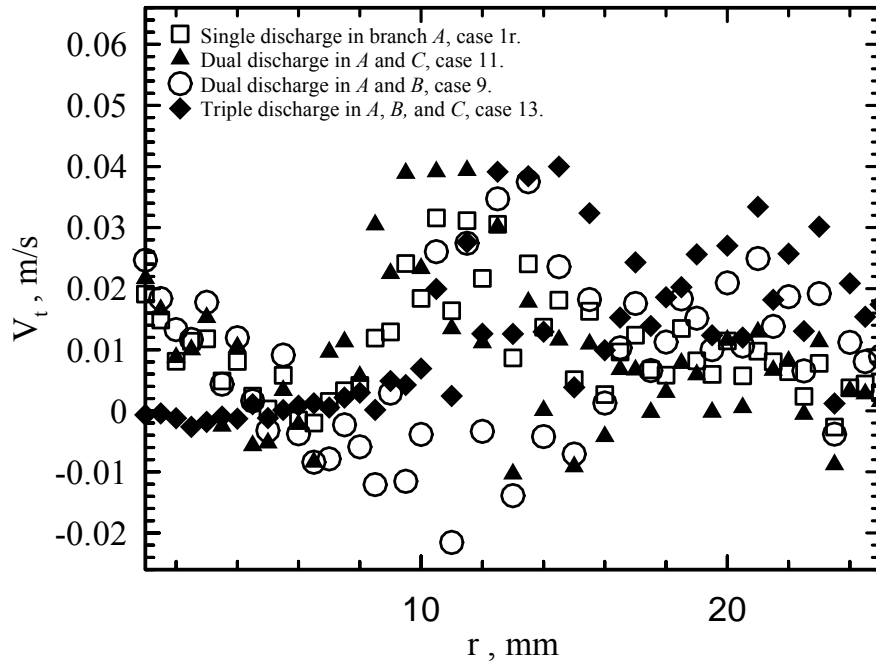
(b) Medium Froude number in branch *A*, plane 7.
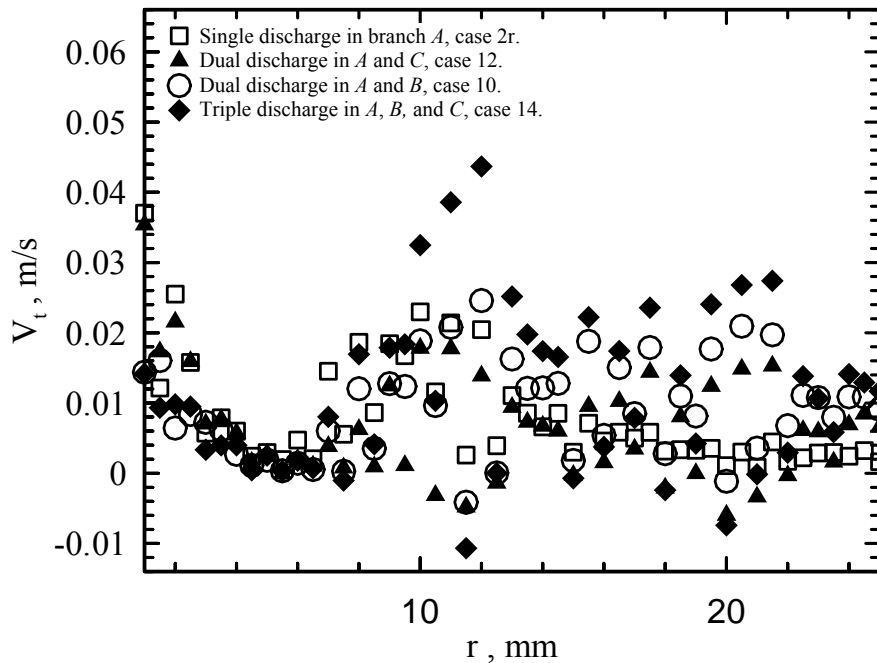
Figure 5.49 Average tangential velocity change along r in plane 7 for different flow configurations at (a) High Froude number in branch *A*, and (b) Medium Froude number in branch *A*.

(a) High Froude number in branch *A*, plane 8.
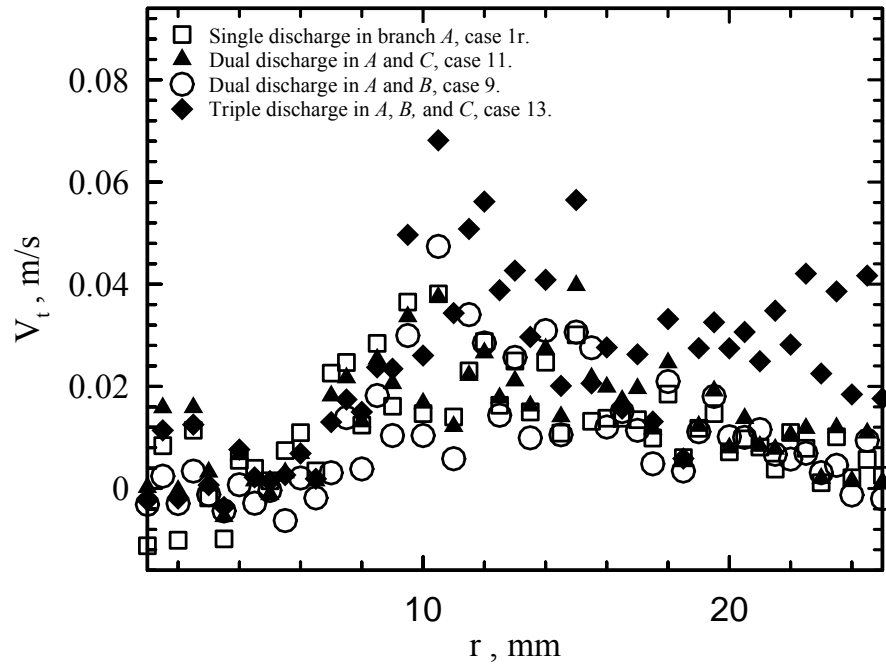
(b) Medium Froude number in branch *A*, plane 8.
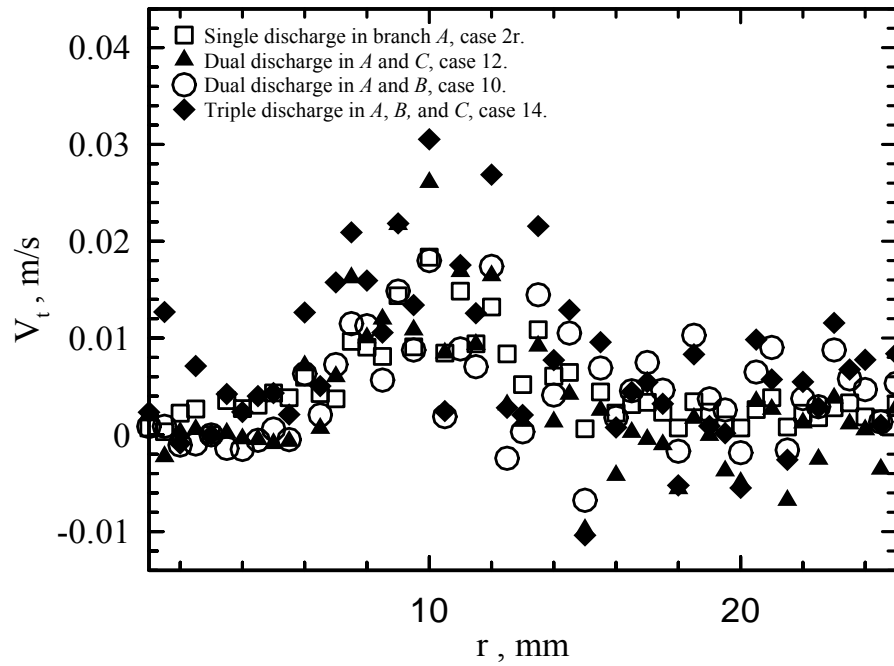
Figure 5.50 Average tangential velocity change along r in plane 8 for different flow configurations at (a) High Froude number in branch *A*, and (b) Medium Froude number in branch *A*.

(a) High Froude number in branch *A*, plane 1.
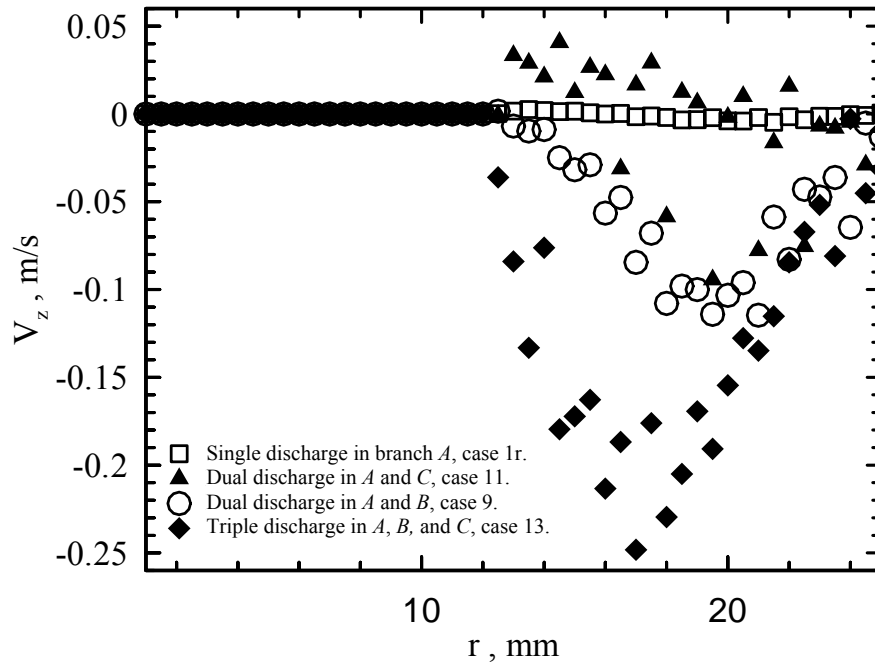
(b) Medium Froude number in branch *A*, plane 1.
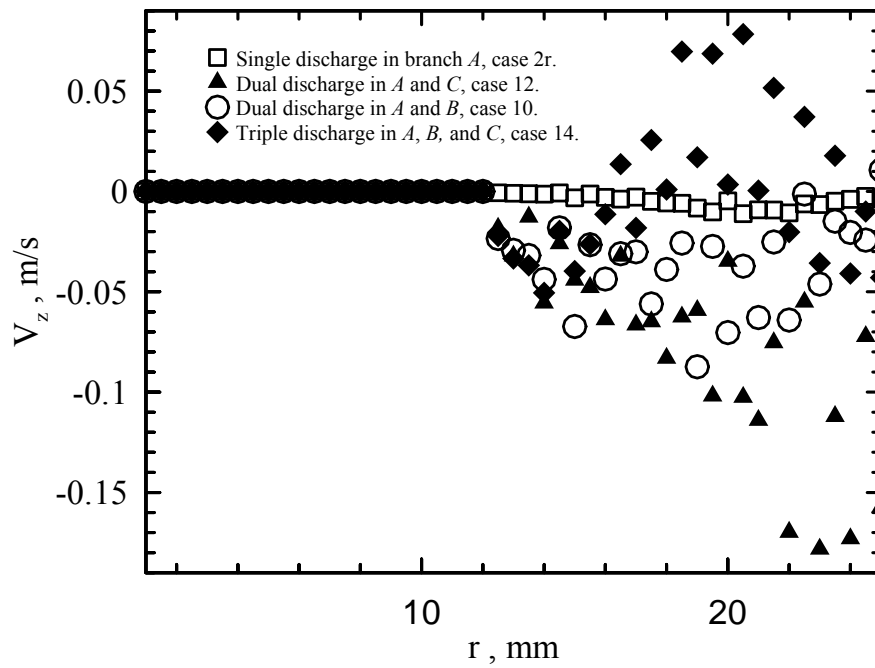
Figure 5.51 Average vertical velocity change along r in plane 1 for different flow configurations at (a) High Froude number in branch *A*, and (b) Medium Froude number in branch *A*.

(a) High Froude number in branch *A*, plane 2.
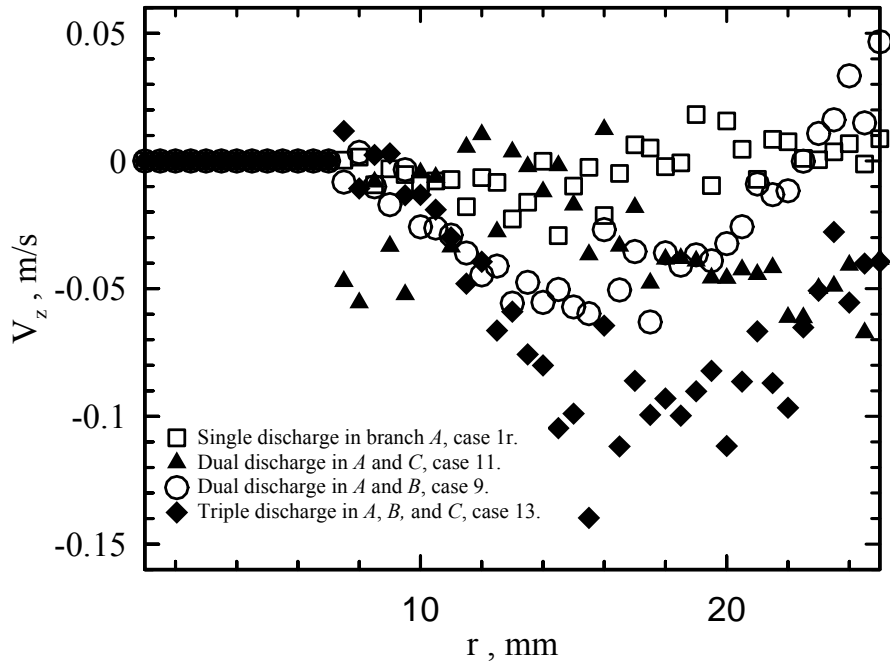
(b) Medium Froude number in branch *A*, plane 2.
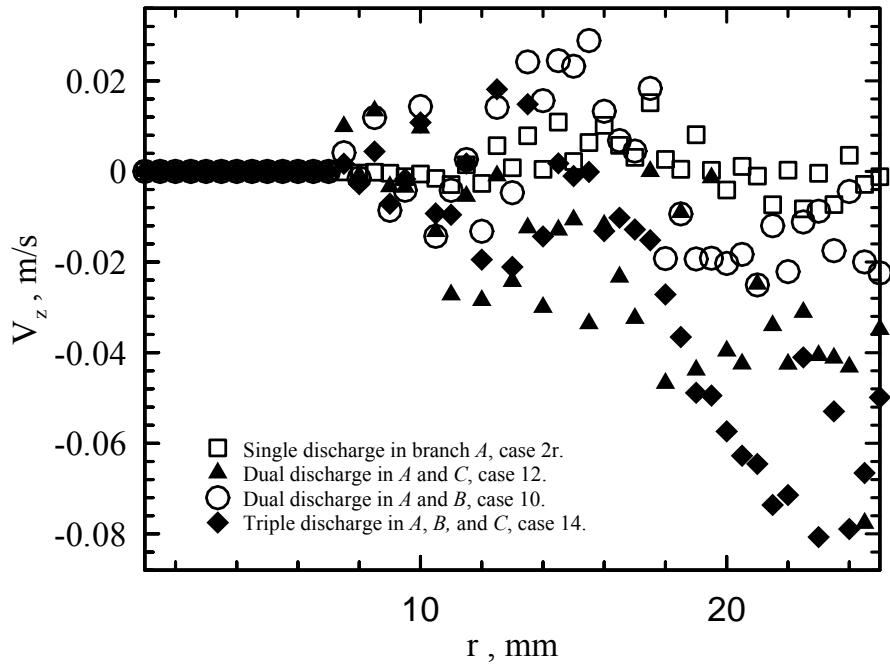
Figure 5.52 Average vertical velocity change along r in plane 2 for different flow configurations at (a) High Froude number in branch *A*, and (b) Medium Froude number in branch *A*.

(a) High Froude number in branch *A*, plane 3.
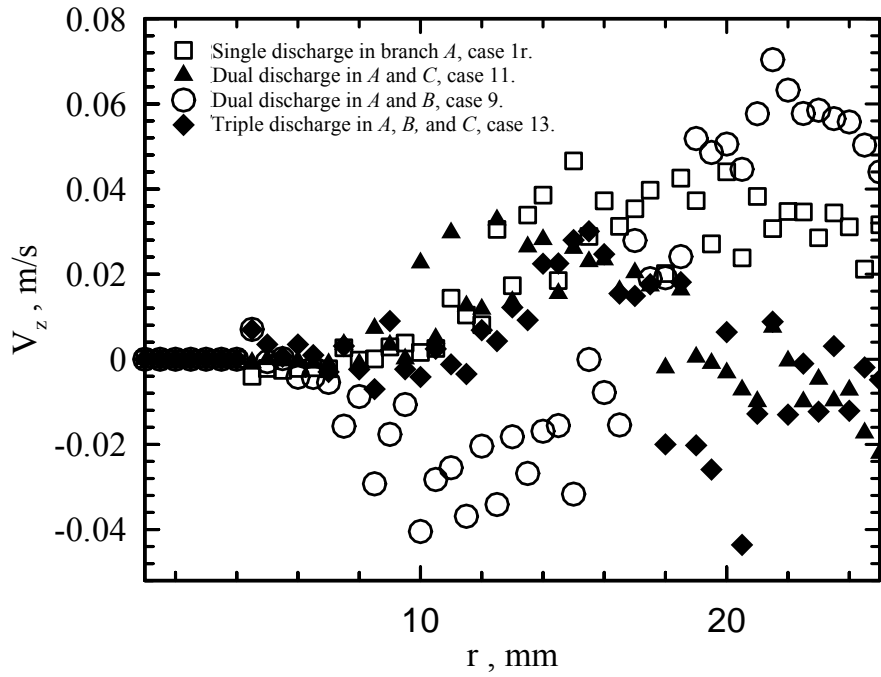
(b) Medium Froude number in branch *A*, plane 3.
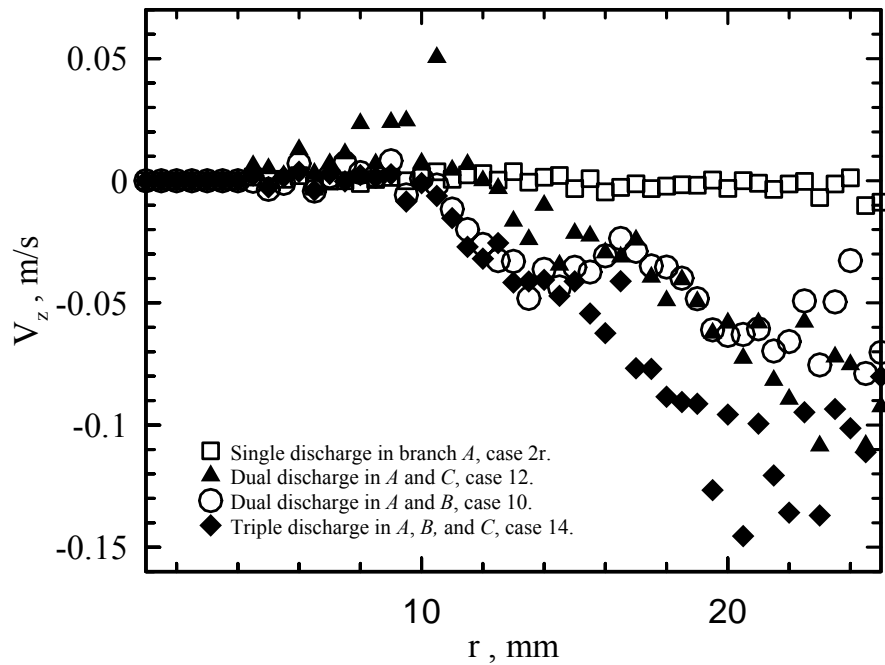
Figure 5.53 Average vertical velocity change along r in plane 3 for different flow configurations at (a) High Froude number in branch *A*, and (b) Medium Froude number in branch *A*.

(a) High Froude number in branch *A*, plane 4.
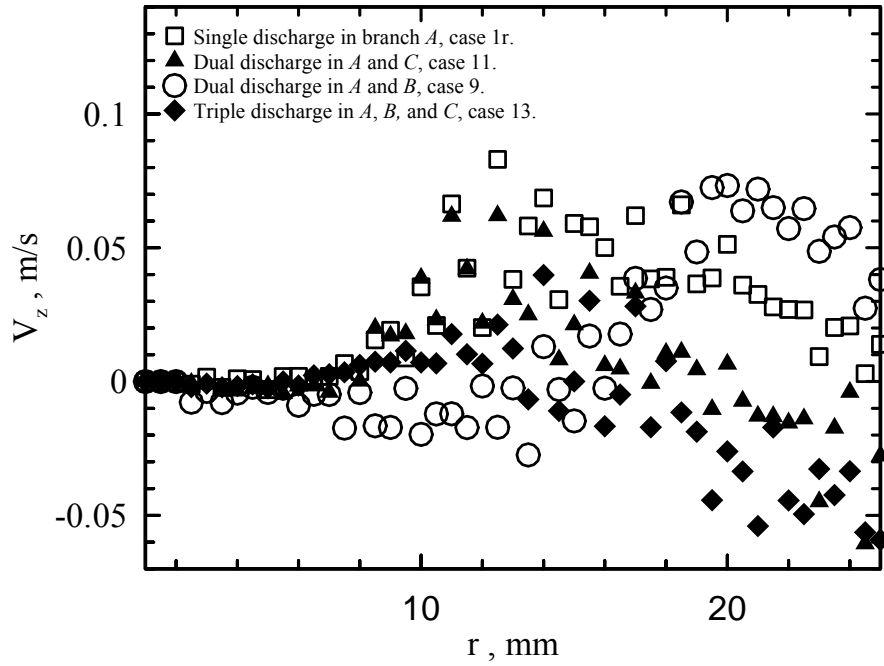
(b) Medium Froude number in branch *A*, plane 4.
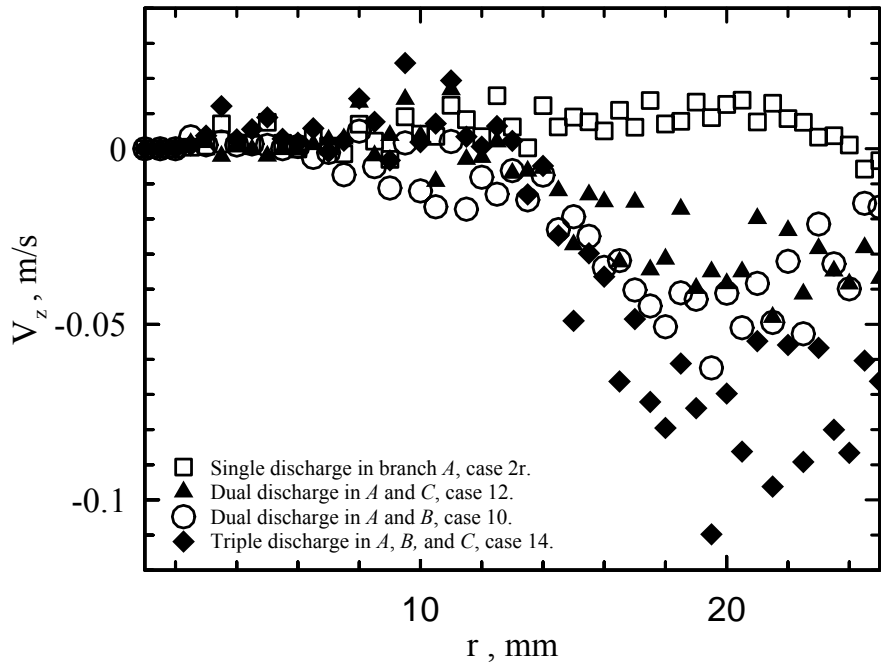
Figure 5.54 Average vertical velocity change along r in plane 4 for different flow configurations at (a) High Froude number in branch *A*, and (b) Medium Froude number in branch *A*.

(a) High Froude number in branch *A*, plane 5.
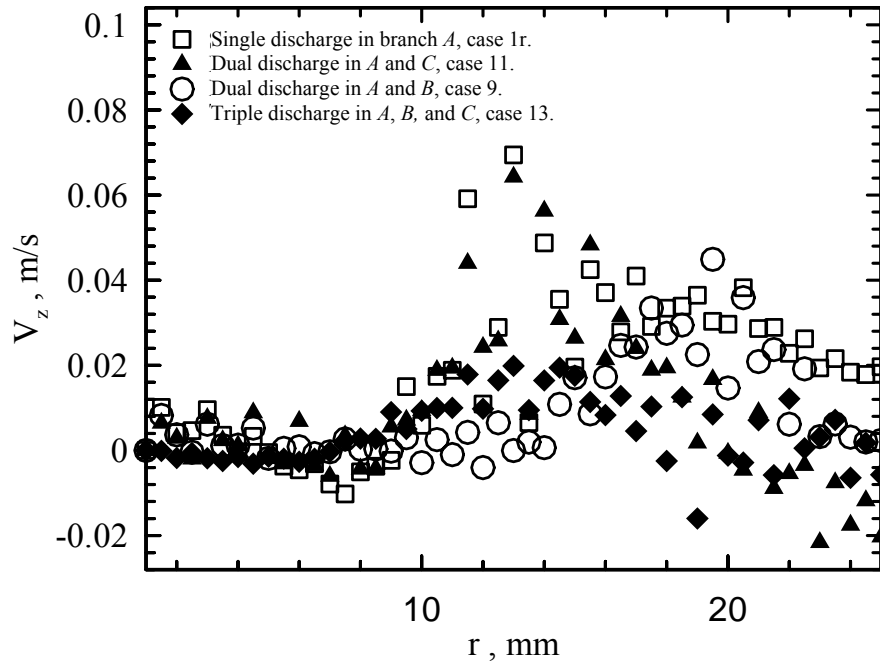
(b) Medium Froude number in branch *A*, plane 5.
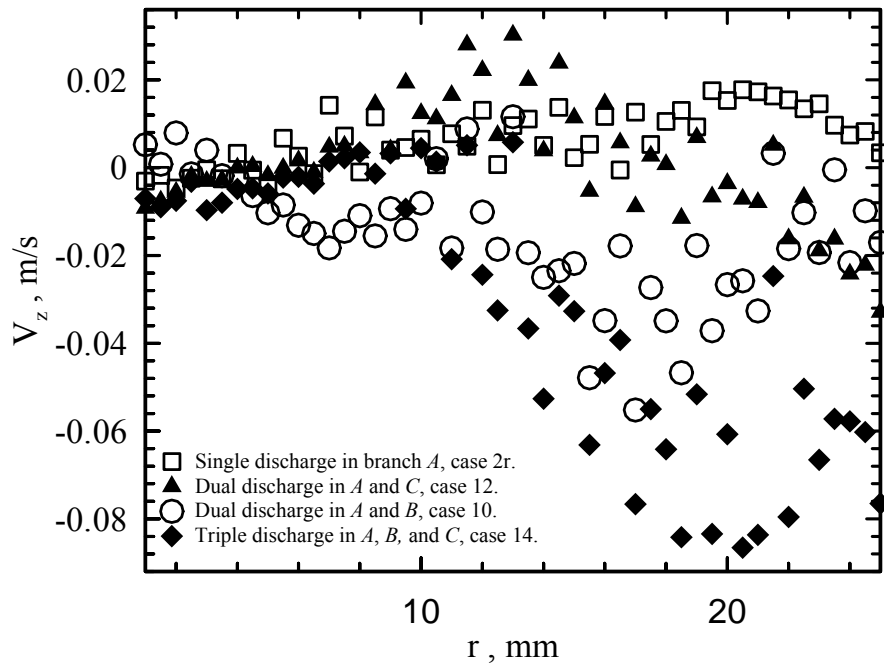
Figure 5.55 Average vertical velocity change along r in plane 5 for different flow configurations at (a) High Froude number in branch *A*, and (b) Medium Froude number in branch *A*.

(a) High Froude number in branch *A*, plane 6.
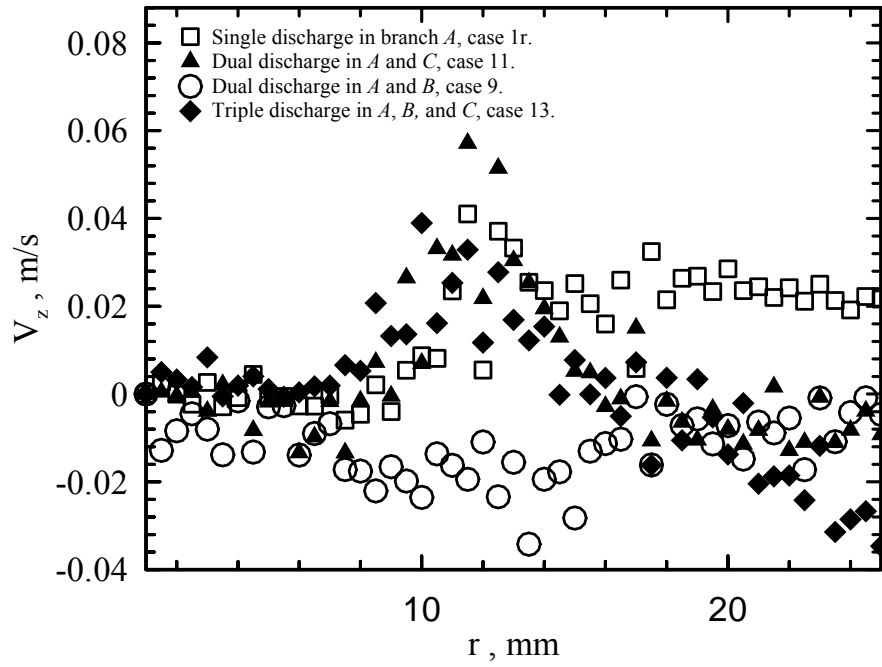
(b) Medium Froude number in branch *A*, plane 6.
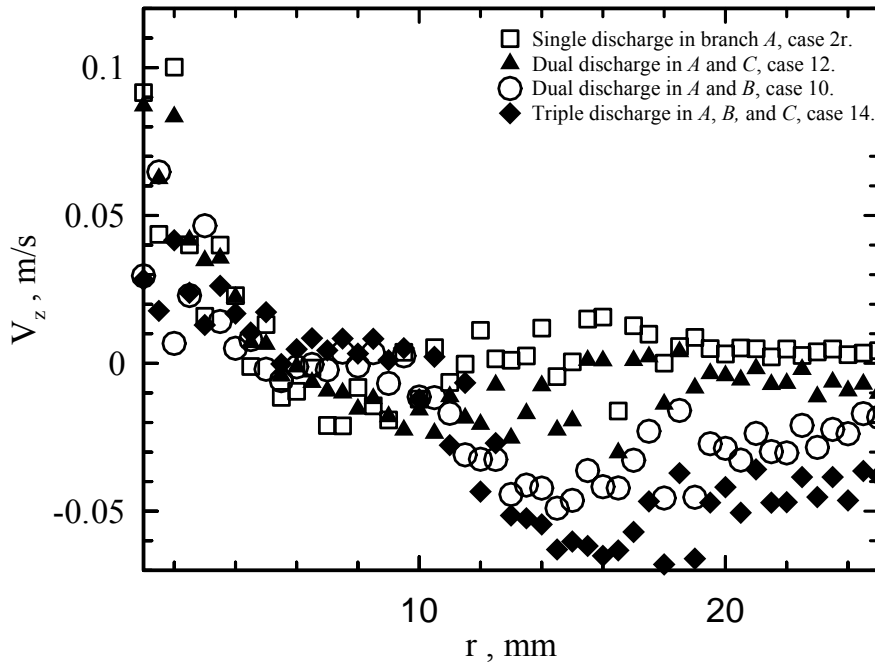
Figure 5.56 Average vertical velocity change along r in plane 6 for different flow configurations at (a) High Froude number in branch *A*, and (b) Medium Froude number in branch *A*.

(a) High Froude number in branch *A*, plane 7.
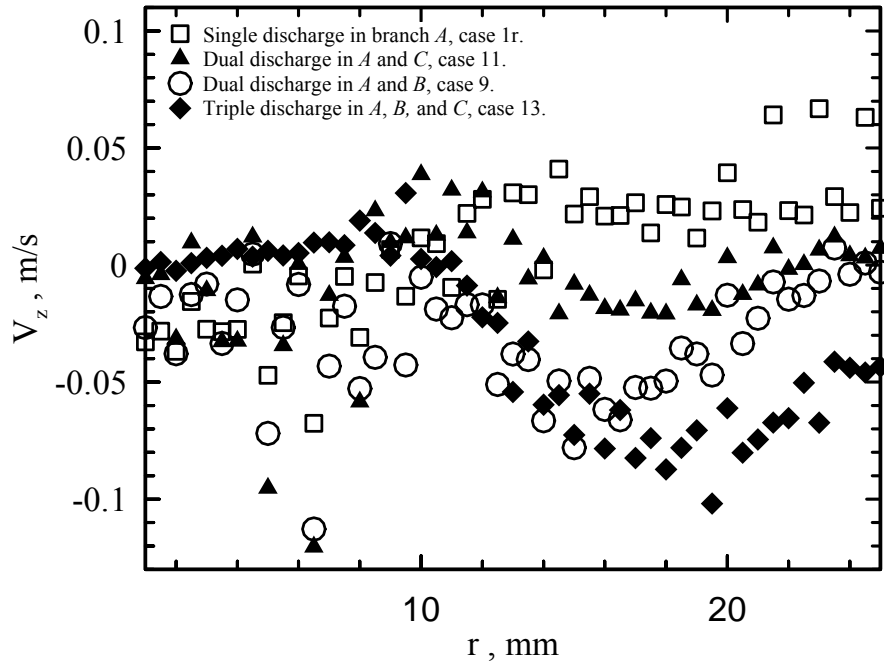
(b) Medium Froude number in branch *A*, plane 7.
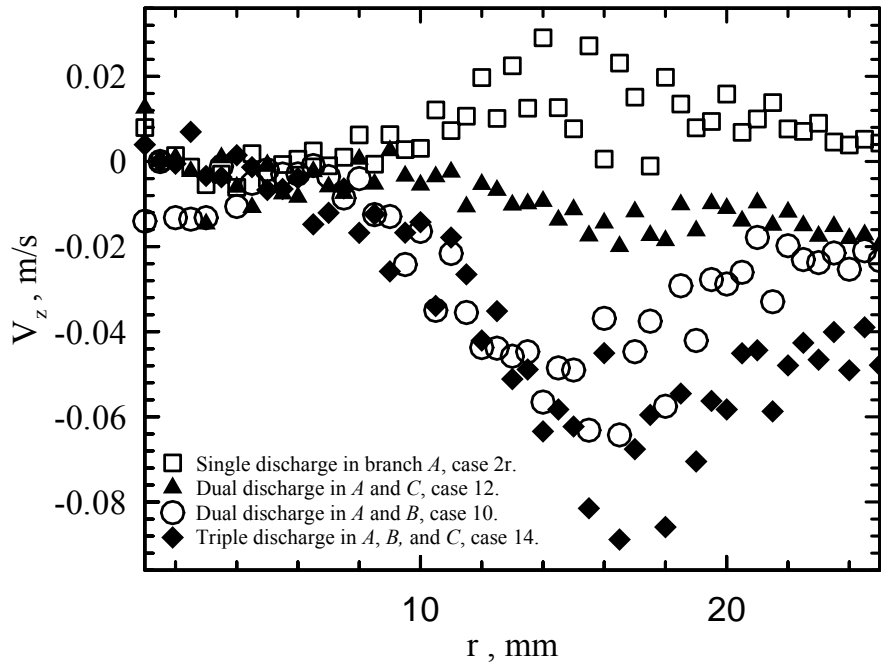
Figure 5.57 Average vertical velocity change along r in plane 7 for different flow configurations at (a) High Froude number in branch *A*, and (b) Medium Froude number in branch *A*.

(a) High Froude number in branch *A*, plane 8.
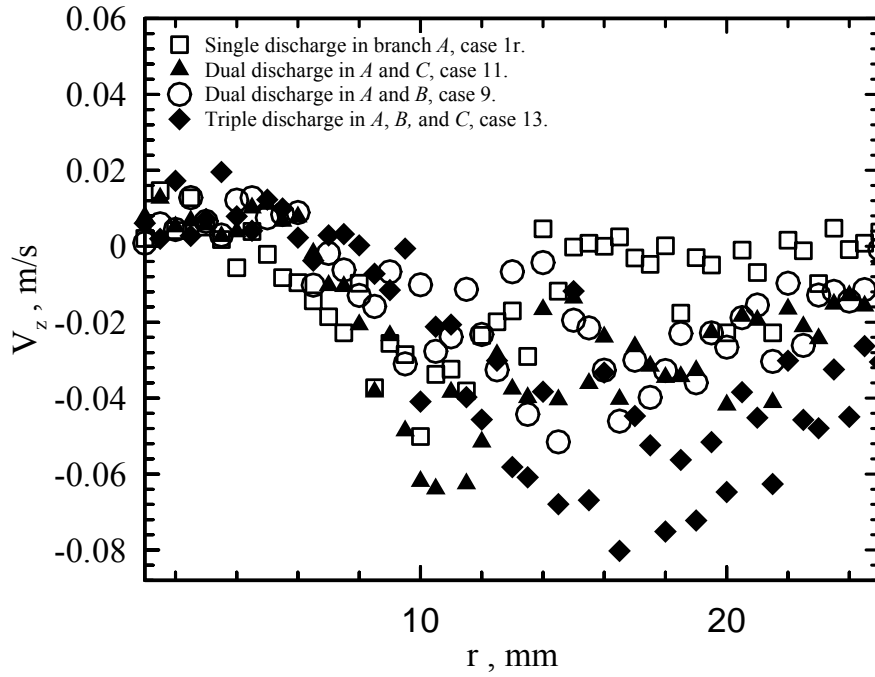
(b) Medium Froude number in branch *A*, plane 8.
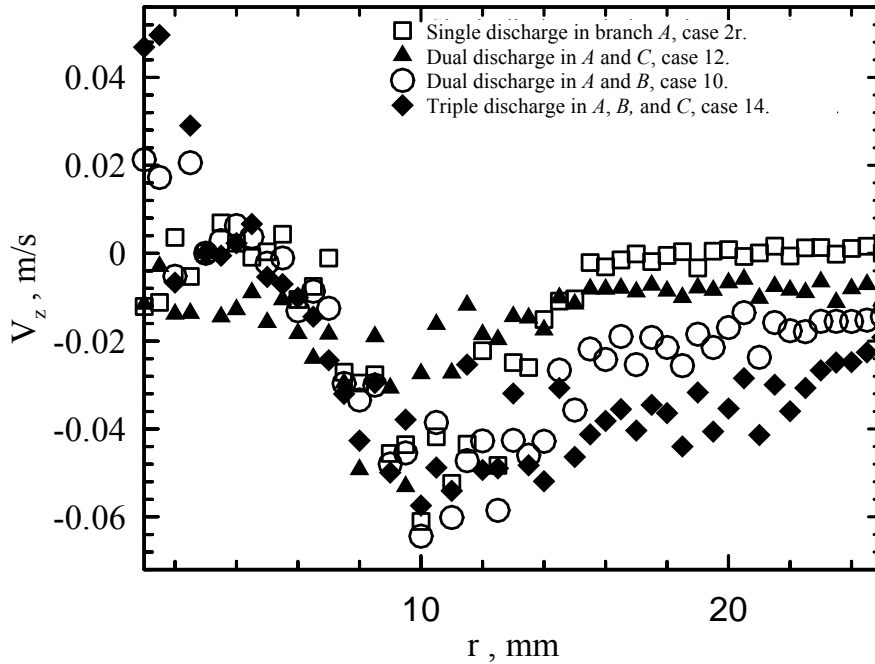
Figure 5.58 Average vertical velocity change along r in plane 8 for different flow configurations at (a) High Froude number in branch *A*, and (b) Medium Froude number in branch *A*.

Chapter 6

A Hybrid Model to Predict the OGE

with Surface Tension Effects

One of the main elements of the analytical approach of OGE is to consider that a dip forms in the heavier liquid surface, followed by a catastrophic collapse of the surface equilibrium – resulting in gas entrainment. It is well known from experimental studies, (e. g. Ahmad and Hassan, 2006), that the dip forms prior to gas entrainment. It is believed that the dip forms in part due to surface tension and not from centrifugal forces, which are associated with vortex flows. There are no reports for the size, shape, or effects of flow conditions on the dip at the present time. In this chapter a hybrid theoretical analysis will be presented to determine the effects of surface tension on the dip formation assumption. The resultsl will be compared with the generated experimental data to quantify the effects of surface tension on the critical height at the onset of gas entrainment. A single discharge installed at the bottom of a circular pipe will be considered, based on the scaling relationships from a typical CANDU header-feeder system. Reasoning for the inclusion of surface tension effects will become clear from the dimensional analysis. A single feeder bank of a CANDU header will be used as a prototype, since its geometry has many salient features that could be common to other systems.

6.1 Dimensional Analysis

The relevant geometric parameters are shown in Figure 6.1. The header has a circular cross-section of diameter D with a single downward discharge of diameter d, located circumferentially at $\beta = 180°$; for convenience this is labeled branch C. The effects of additional discharges, and additional feeder banks, are not considered so all separating distances between branches (L_1 to L_4) and feeder banks (L_5 & L_6) are not included in this analysis. The two fluid phases are represented in Figure 6.1 as gas and liquid but each has a set of independent variables that is relevant to the problem. Considering first the gas phase as ideal, the pressure and temperature are satisfied by the density (ρ_G) from the ideal gas law and the dynamic viscosity is (μ_G). The liquid density (ρ_L), dynamic viscosity (μ_L) and the surface tension (σ) are relevant at the interface between the gas and liquid. For stratified flows the gravitational acceleration (g) is an important parameter. Craya (1949) suggested that it should be incorporated with the density ratio to address buoyancy as $g(\rho_L - \rho_G)/\rho_L$. The single phase liquid mass flow rate in branch C is $\dot{m}_C$. With the required independent geometrical and fluid properties established, some comments about the phenomena are needed to establish the dependant variables. The flow through branch C is single phase prior to OGE. Onset of gas entrainment occurs when the branch flow is no longer a single phase liquid, but a mixture of the gas and liquid phases. The onset of entrainment has been characterized previously by the vertical distance, or height H, between the branch inlet and the gas-liquid interface. Zuber (1980) discussed previously that with the gas-liquid interface above the branch centerline, initially liquid only flow in the branch, a critical value of H will exist at which the gas phase will entrain into the branch at H_{OGE}. The critical height

is expected to be a function of the independent parameters discussed above, which include the single phase liquid properties, mass flow rate, and geometry. For onset of gas entrainment in branch C, the functional relationship is expected to be:

$$H_{OGE,C} = f\left(d,\ D,\ \beta_C,\ \frac{g\Delta\rho}{\rho_L},\ \mu_L,\ \rho_L,\ \sigma,\ \dot{m}_C\right).$$ (6-1)

Reduction of Variables: Pi Theorem

In the simplest case of a single discharging branch, there are at most five dimensionless groups – using three basic dimensions of mass, length, and time. A dimensional analysis was performed using the branch diameter, single phase liquid density, and liquid mass flow rate as repeating variables. The resulting relationship for the critical height ($H_{OGE,C}$) was found to be,

$$\frac{H_{OGE,C}}{d} = f\left(\frac{D}{d},\ \beta_C,\ Fr_C,\ \mathrm{Re}_C,\ We_C\right).$$ (6-2)

Where,

$$Fr_C = \frac{\dot{m}_C^2}{gd^5\rho_L(\rho_L - \rho_G)},$$ (6-3)

$$\mathrm{Re}_C = \frac{\dot{m}_C}{\mu_L d},$$ (6-4)

and

$$We_C = \frac{\dot{m}_C^2}{\sigma \cdot d^3 \rho_L}.$$ (6-5)

The discharge Froude number (Fr_C) is the ratio of inertial to gravitational forces, the discharge Reynolds (Re_C) number is the ratio of inertial to viscous forces, and the Weber (We_C) number is a ratio of inertial to surface tension forces.

Consider now a typical CANDU header which operates with heavy-water (D_2O) nominally at temperatures and pressures in the range of 300ºC and 10 MPa (Banerjee and Nieman, 1982). The physical fluid properties of heavy-water are strikingly similar to those of light-water (H_2O) at standard conditions. During a LOCA, the pressure within the header will decrease causing the heavy-water to vaporize. At 300ºC the saturation pressure is approximately 8.6 MPa and the saturated liquid and vapour properties are listed in Table 6-1. The saturation properties are used here as an estimate, to determine the properties of the vapour phase.

Table 6-1 Saturation properties of Heavy-water at 300ºC and 8.6 MPa.

	Saturated Liquid	Saturated Vapor
Density (kg/m^3)	784.87	52.64
Viscosity (N.s/m^2)	9.36E-05	1.97E-05
Surface Tension (N/m)	1.39E-02	

Using the saturation properties, the variation of the idealized liquid Froude, Reynolds, and Weber numbers were evaluated, using $d = 50.8$ mm, and presented in Figure 6-2. The gravitational force is shown to be dominant when compared to the viscous (Reynolds) and surface tension (Weber) forces, as demonstrated by the Froude number. The Froude number is commonly used in free-surface flows, particularly in geophysical flows, such as rivers and oceans. The Weber number shows that surface tension effects are relevant at low values of v_C. What is interesting to note from this

190

figure is that with the Froude and Weber numbers below one, at particular values of v_C, the inertia forces become smaller than the gravitational and surface tension forces. This implies that the gravitational and surface tension forces will begin to compete with each other. In this case, a new dimensionless group emerges at these low values of liquid velocity, v_C, the Bond (*Bo*) number, which is a ratio of gravitational to surface tension forces. This concept will be further demonstrated in the theoretical analysis below.

6.2 Point-Sink Analysis

Figure 6.3 shows the geometry that will be simulated as the point sink model. Here, only the bottom branch *C* is used in the analysis. Also, the flow exiting from this branch is liquid only. The liquid level starts from the highest point inside the circular domain called *S*, and then begins to descend. At a certain instant, a dip will appear in the gas-liquid interface – due to the vortex-free flow field. By descending the liquid level further, the dip size will increase. The surface will then suddenly collapse, causing both the gas and liquid phases to flow into the branch, as the liquid height above the branch is further decreased.

The flow field is considered steady, incompressible, inviscid, and irrotational. These assumptions are the characteristic of potential flow and are governed by forces of inertia and gravity. The potential flow assumption allows Bernoulli's equation to be applied between two points within the flow field. Bernoulli's equation will be applied on the interface between the points *a* and *b*. Consider first the heavier fluid side which results in,

$$P_{a,L} + \frac{1}{2}\rho_L v_{a,L}^2 + \rho_L gH = P_{b,L} + \frac{1}{2}\rho_L v_{b,L}^2 + \rho_L gh . \qquad (6\text{-}6)$$

Considering $v_{a,L} \ll v_{b,L}$, Eq. (6-6) becomes

$$P_{a,L} + \rho_L gH = P_{b,L} + \frac{1}{2}\rho_L v_{b,L}^2 + \rho_L gh . \qquad (6\text{-}7)$$

By applying Bernoulli's equation on the lighter fluid side, which is considered as stagnant, results in,

$$P_{a,G} + \rho_G gH = P_{b,G} + \rho_G gh . \qquad (6\text{-}8)$$

The Kelvin-Laplace equation is now introduced to consider the effects of surface tension. The general equation is defined by White (1991) as follows,

$$P_L(x,y,\eta) = P_G - \sigma\left(\frac{1}{R_x} + \frac{1}{R_y}\right) , \qquad (6\text{-}9)$$

where the pressure on the liquid side is P_L and the pressure on the gas side is P_G. The co-ordinates x and y are defined in a plane parallel to the gas-liquid interface with η describing the height of the interface above the x-y plane, and generally $\eta = \eta(x,y)$. The surface tension coefficient is σ, and the radii of curvature in x and y directions are R_x and R_y, respectively. The shape of the dip is assumed to be represented by a segment of a sphere, which simplifies the general Kelvin-Laplace equation to have $R_x = R_y = ROC$. Applying this assumption to the general equation at point a results in,

$$P_{aG} = P_{aL} + \left(\frac{2\sigma}{ROC_a}\right) . \qquad (6\text{-}10)$$

Similarly, by applying the Kelvin-Laplace equation at point b results in,

$$P_{bG} = P_{bL} + \left(\frac{2\sigma}{ROC_b}\right) . \qquad (6\text{-}11)$$

The radius of curvature at point a (ROC_a) is very large, since at this location the gas-liquid interface is considered to be flat, therefore $P_{aG} \approx P_{aL}$. From Eqs. (6-7), (6-8), (6-10), and (6-11), the critical height (H) at the onset of gas entrainment can now be found to be,

$$\frac{H_{OGE}}{d} = \frac{h}{d} + \frac{v_b^2 \rho_L}{2gd(\rho_L - \rho_G)} - \frac{2\sigma}{ROC_b gd(\rho_L - \rho_G)} \ . \qquad (6\text{-}12)$$

The last term on the right is a ratio of surface tension to gravitational forces, which is a modified form of the dimensionless group commonly known as the Bond number. The dip radius of curvature figures prominently in Eq. (6-12) and is the only variable if fluid properties remain constant. To find the velocity at point b, the branch C is assumed to be a point sink with volumetric flow rate Q_C. The surface area S of the flow field is a hemisphere intersected by a cylinder, and the branch is located at the center of this flow field. The velocity at any point on the surface S of the flow field is,

$$v_r = \frac{\partial \Phi}{\partial r} = \frac{Q_C}{S\big|_r} \ . \qquad (6\text{-}13)$$

Where Φ is the potential function, r is the radius of the flow field in general, and S in general is given by

$$S = 2\pi r^2 - 4r \int_0^r \arctan \frac{1}{\sqrt{\frac{4R^2}{r^2 - z^2} - 1}} dz \ . \qquad (6\text{-}14)$$

The surface area of the flow field at point b is given by,

$$S\big|_{r=h} = 2\pi h^2 - 4h \int_0^h \arctan \frac{1}{\sqrt{\dfrac{4R^2}{h^2 - z^2} - 1}} dz \; . \tag{6-15}$$

The criterion used to predict the onset of gas entrainment is the equality between the acceleration of the liquid above the branch, and the acceleration of gravity, g, at point b, is derived from Taylor (1950). The principle (for onset of gas entrainment in a vertical plane) is given as,

$$a_b = -g \; . \tag{6-16}$$

This states that if the acceleration at point b is equal, or exceeds, the gravitational acceleration then the surface will become unstable, causing the onset of gas entrainment. Using Eqs. (6-13) and (6-16) to define the condition for the onset of gas entrainment yields,

$$\frac{\partial \Phi}{\partial r}\bigg|_{r=h} \cdot \frac{\partial^2 \Phi}{\partial r^2}\bigg|_{r=h} = -g \; . \tag{6-17}$$

To find $\dfrac{\partial \Phi}{\partial r}$, Eq. (6-15) is substituted in Eq. (6-13) which results in,

$$\frac{\partial \Phi}{\partial r}\bigg|_b = \frac{Q_c}{S\big|_{r=h}} = \frac{Q_C}{2\pi h^2 - 4h \int_0^h \arctan \dfrac{1}{\sqrt{\dfrac{4R^2}{h^2 - z^2} - 1}} dz} \; . \tag{6-18}$$

The derivative of $\dfrac{\partial \Phi}{\partial r}$ with respect to r, at point b with $r = h$ yields,

$$\frac{\partial^2 \Phi}{\partial r^2}\bigg|_b = -Q_C \left(\frac{4\pi h - 4I_1 - 4hI_2}{\left(2\pi h^2 - 4hI_1\right)^2} \right) \; . \tag{6-19}$$

194

Where,

$$I_1 = \int_0^h \arctan \frac{1}{\left(z^* - 1\right)^{1/2}} dz \; , \tag{6-20}$$

$$I_2 = \int_0^h \frac{4R^2 r}{\left(z^* - 1\right)^{1.5}\left(h^2 - z^2\right)^2 \left(1 + \frac{1}{z^* - 1}\right)} dz \; , \tag{6-21}$$

and,

$$z^* = \frac{4R^2}{h^2 - z^2} \; . \tag{6-22}$$

If we use the definition of Fr_C to be,

$$Fr_C = \frac{v_C}{\sqrt{gd \frac{\Delta\rho}{\rho}}} \; , \tag{6-23}$$

and using the average velocity instead of the mass flow rate. The volumetric flow rate (Q_C) can then be defined as,

$$Q_C = Fr_C \sqrt{gd \frac{\Delta\rho}{\rho}} \left(\frac{\pi}{4} d^2\right) . \tag{6-24}$$

In summary, Eqs. (6-12) and (6-17) form a system of two equations with three unknowns. The unknowns are the critical height H, the height of the dip above the branch inlet h, and the radius of curvature ROC of the dip at point b. Without a third equation the system is ill-posed. To find the radius of curvature of the surface dip analytically, considering the effects of surface tension as the main cause in a potential

195

flow analysis, posed a very serious challenge. The experimentally obtained values for the radius of curvature were therefore used to provide a reasonable alternative.

6.3 Two-Dimensional Finite-Branch Analysis

In this analysis, a two-dimensional finite branch model is considered with a single slot installed on the bottom of a semi-circular section, as shown in Figure 6.4, with a branch discharge velocity V_C. Two fluid phases are present, where, the lighter fluid is considered stationary, and the heavier fluid is considered to be incompressible, homogeneous, and irrotational. These assumptions are characteristic of potential flow and are governed by forces of inertia and gravity. The potential flow assumption allows Bernoulli's equation to be applied between two points within the flow field. Bernoulli's equation will be applied on the interface between the points *a* and *b*. Re-introducing Eqs. (6-6), (6-7), and (6-8), from above, the Kelvin-Laplace equation, Eq. (6-9), is now introduced to consider the effects of surface tension in the 2-D model. Therefore, the general equation, Eq. (6-9), defined by White (1991) becomes,

$$P_L(y,\eta) = P_G - \sigma\left(\frac{1}{R_y}\right).$$
(6-25)

The co-ordinate y is defined as a horizontal line parallel to the gas-liquid interface with η describing the height of the interface above the y line, and generally $\eta = \eta(y)$. The radius of curvature in the y direction is R_y. The shape of the dip is assumed to be represented by a segment of a cylinder, which simplifies the general Kelvin-Laplace equation to have $R_y = ROC$. Applying this assumption to the general equation at point *a* results in,

$$P_{aG} = P_{aL} + \left(\frac{\sigma}{ROC_a} \right).$$
(6-26)

Similarly, by applying the Kelvin-Laplace equation at point b results in,

$$P_{bG} = P_{bL} + \left(\frac{\sigma}{ROC_b} \right).$$
(6-27)

Again the radius of curvature at point a (ROC_a) is very large since at this location the gas-liquid interface is considered to be flat, therefore $P_{aG} \approx P_{aL}$. From Eqs. (6-7), (6-8), (6-26), and (6-27), the critical height (H) at the onset of gas entrainment can now be found to be,

$$\frac{H_{OGE}}{d} = \frac{h}{d} + \frac{v_b^2 \rho_L}{2gd(\rho_L - \rho_G)} - \frac{\sigma}{ROC_b gd(\rho_L - \rho_G)}.$$
(6-28)

To find the velocity at point b, the two-dimensional flow field will be solved by applying the continuity equation, in cylindrical coordinates, to the heavier fluid, we obtain,

$$\frac{1}{r} \frac{\partial}{\partial r} \left(r \frac{\partial \Phi}{\partial r} \right) + \frac{1}{r^2} \frac{\partial^2 \Phi}{\partial \theta^2} = 0.$$
(6-29)

Assuming a separable solution exists such that,

$$\Phi(r,\theta) = Y(r)Z(\theta),$$
(6-30)

and the solution is finite at $r = 0$, the general solution will be,

$$\Phi(r,\theta) = \alpha_0 + \sum_{n=1}^{n=\infty} r^n(\alpha_n \cos(n\theta) + \beta_n \sin(n\theta)) \ . \tag{6-31}$$

The form of this general solution is defined as the Neumann problem by having,

$$\frac{\partial \Phi}{\partial r}\bigg|_{r=R} = f(\theta) = V_r \ , \tag{6-32}$$

along the circumference, where $r = R$. The partial derivative of Φ with respect to r along the circumference is,

$$\frac{\partial \Phi}{\partial r}(R,\theta) = \sum_{n=1}^{n=\infty}[(nR^{n-1})(\alpha_n \cos(n\theta) + \beta_n \sin(n\theta))] \ . \tag{6-33}$$

If $f(\theta)$ is also represented as a Fourier series, as indicated by Smith (1967),

$$\frac{\partial \Phi}{\partial r} = f(\theta) = V_r = \frac{a_0}{2} + \sum_{n=1}^{n=\infty}[a_n \cos(n\theta) + b_n \sin(n\theta)] \ , \tag{6-34}$$

and by comparing these two equations, Eqs. (6-33) and (6-34), a necessary condition that must be satisfied to yield a solution is,

$$\pi a_0 = \int_0^{2\pi} f(\theta)d\theta = 0 \ , \tag{6-35}$$

Multiplying Eq. (6-35) by R results in balancing the inlet and outlet flow rates through the boundary. On the inlet side, opposite to the slot, the area is divided into several imaginary branches with equivalent size as the discharge branch. The objective is to define the radial velocity component, V_{ri}, in the direction of the domain center and along the semi-circular inlet, from the free stream velocity V_∞. From Figure 6.5, the free stream velocity is defined by,

$$V_\infty = v_C \cdot \frac{(2\delta \cdot R)}{H} . \tag{6-36}$$

The number of branches along the imaginary boundary is determined by the height of the heavier fluid in the domain by H. From Figure 6.5, a balance of the flow across the imaginary domain for a single imaginary branch gives,

$$V_\infty \cdot dz = V_i \cdot 2\delta \cdot R . \tag{6-37}$$

The solution of Φ can now be found and given by Smith (1967) as,

$$\Phi(r,\theta) = \frac{\alpha_0 \cdot R}{\pi} - \frac{R}{2\pi} \cdot \int_0^{2\pi} V_r \log\left\{ \frac{(R^2 - 2Rr\cos(\theta - \theta') + r^2)}{R^2} \right\} d\theta' , \tag{6-38}$$

with the following boundary conditions at $r = R$,

(i) $\quad \dfrac{3\pi}{2} - \delta < \theta < \dfrac{3\pi}{2} + \delta$, $\dfrac{\partial \Phi}{\partial r} = v_C$,

(ii) $\quad \dfrac{3\pi}{2} - (2n+2)\delta < \theta < \dfrac{3\pi}{2} - (2n)\delta$, $V_{r_{i_n}} = V_\infty \cos(\dfrac{3\pi}{2} - (2n+1)\delta)$, $n = 0,1,2$, (6-39)

(iii) $\quad \dfrac{3\pi}{2} + \delta < \theta < \dfrac{\pi}{2}$, $V_r = 0$.

Each partial derivative in Eq. (6-17) can be evaluated using the definitions of Φ, r, and θ from the above equations.

The values of all integrations in Eqs. (6-17) and (6-38) are calculated using numerical integration techniques. To validate the 2-D finite branch analysis model, a comparison was made between the experimental work of Ahmad and Hassan (2006), carried out for a circular hole and the present 2-D finite branch analysis model.

6.4 Radius of Curvature of the Air-Water Interface Dip at OGE

6.4.1 Radius of Curvature Measurements

Measurements were achieved by first filling the two-phase reservoir Figure 3.3 (by opening the two-phase reservoir inlet valve) so that the air-water interface was well above (high enough to not have the dip at the air-water interface) branch *C*. Branches *A* and *B* were not active. The reservoir was then pressurized to 206 kPa and the discharge flow rate through the test section was set using the flow meter to a certain constant value (a constant Froude number). The air-water interface was then slowly decreased (by reducing the inlet flow) until a steady dip was formed in the interface. The dip is formed without gas entrainment occurring. This means that for a certain Foude number or flow rate, there is one OGE height and one dip shape with a certain radius of curvature (*ROC*). This experiment was repeated for the rest of Froude numbers. Images of the dip were then taken using a HiSense MkII CCD camera, with 1344 x 1024 pixel resolution. A random sample of the images was then used to measure the size and shape of the dip, the sample size was typically on the order of 20 images. This was found to be sufficient to describe the relatively stable dip formation. A sample image is shown in Figure 6.6, with the dip formation prominently displayed above discharge branch *C.* The measurement of the dip shape and size were achieved by importing the image into the Digi-XY software. Using this software, the spatial resolution could be easily established, and points of the dip profile could be extracted manually. For each image, an average of 20 to 30 unique points were selected to describe the surface profile. The process was repeated for a total of seven discharge Froude numbers ranging from approximately 1 to 30. A sample of the

extracted points for three different Froude numbers is presented in Figure 6.7. This figure quickly provides an estimate of the size and shape of the dip as the Froude number is varied. As can be seen from the figure, as the Froude number increases, the data scatter also seems to increase. From the visual observations, as the Froude number increases the interface and dip become increasingly unstable as the critical height is approached. It was observed that at low Froude numbers the interface, and dip, were relatively stable – resulting in less scatter.

6.4.2 Radius of Curvature Correlations

To include the experimental data in the theoretical modeling, a data reduction method was developed so that the radius of curvature could be presented as a function of the Froude number. The objective was to first to fit the data to a polynomial equation for each Froude number tested. With seven Froude numbers, seven different polynomials were produced. To coincide with the original assumption that the surface was formed as a portion of a sphere, a second order polynomial was chosen. The polynomial is of the form, $z = C_1 y^2 + C_2 y + C_3$ where C's are the curve fitting constants. A sample of the second order polynomial curve fit is shown in Figure 6.8 for $Fr = 6.92$. In order to adapt this function to the theoretical model, the lowest point of the dip should be found, this is point b from Figure 6.3. The lowest point can be found by searching for the location where the slope of the curve is zero. This implies that for the polynomial with $z = f(y)$,

$$\left. \frac{dz}{dy} \right|_b = 0 \; . \tag{6-40}$$

The radius of curvature (ROC) of a function of the form $z = f(y)$ can then be found from,

$$ROC = \frac{\left(1+\left(\dfrac{dz}{dy}\right)^2\right)^{3/2}}{\left|\dfrac{d^2z}{dy^2}\right|} \; , \tag{6-41}$$

and since dz/dy = 0 at point b, the *ROC* can be found to be,

$$ROC_b = \left(\left|\frac{d^2z}{dy^2}\right|\right)^{-1} = \frac{1}{2C_1} \; . \tag{6-42}$$

With a second order polynomial used as the fitting function, using Eq. (6-42) simply reduces to a function of the fitting coefficient C_1. For each of the seven Froude numbers tested, the dip radius of curvature was found by this method. The resulting values are shown in Figure 6.9. A second relationship is now required to describe *ROC* = *f(Fr)* to complement the theoretical model. A data fit was used to establish this functional relationship. A second order polynomial fit was chosen as a suitable data fitting function. The polynomial equation that results from this fit is,

$$ROC = 10^{-3}\left(0.03 \times Fr^2 - 0.3 \times Fr + 24.5\right). \tag{6-43}$$

This polynomial is the first estimate of the dip radius of curvature, in meters, for a single downward discharge on a curved surface.

6.5 Summary and Concluding Remarks

A computer code, using Maple ver.11, was written to solve the system of the three equations (Eqs. 6-22, 6-27, and 6-43) for the critical height as a function of the Froude number. The critical height was calculated with and without surface tension effects. The

results of the analysis are presented in Figure 6.10 and are compared with the experimental work of Ahmad and Hassan (2006). The dimensions and fluid used in the theoretical analysis are similar to their experimental work. It can be seen that without surface tension effects, the model over predicts the critical height. On the other hand the surface tension parameter, the Bond number, serves to reduce the predicted critical height. The critical height result shows an excellent agreement with the experiments using the hybrid model. The predicted critical height deviates from the experimental at low Froude numbers if the surface tension is neglected. It was hypothesized that this was due to the surface tension effects based on the observations of the phenomena. By including the Kelvin-Laplace equation into Bernouilli's equation, on either fluid side, the surface tension effects were included. The character of the new term, the modified Bond number, had a reducing effect on the critical height. The three-dimensional point sink approach, with surface tension effects, is a reasonable approach to modeling the onset of gas entrainment in a single downward discharge.

Figure 6.11 shows the effect of surface tension on the critical height. From the figure, it can be seen that the critical height decreases with the inclusion of surface tension in the model. There are two heights of the water surface at the point of OGE, H, which refers to the free air-water interface surface height. Its maximum value is limited by the test section geometry, at a maximum physical height of $H \leq 2D$. The height h, which refers to the dip bottom height and its minimum value, is limited by the physical edge of the bottom branch at $h \geq (R - R\cos\delta)$. These two limits were achieved in the present 2-D finite branch model. The analytical model could not be solved for a Froude number greater than $Fr = 30$ or lower than $Fr = 0.88$, due to the physical limits. The

disagreement between the experimental data and the 2-D analytical model is also expected, since the 2-D flow field is different from the experiment, which is 3-D. Even though there is similarity with the 3-D experimental results in the definition of the Froude number, the flow rate and velocity distribution inside the flow field are not the same, hence the disagreement with the experimental data and present 2-D model.
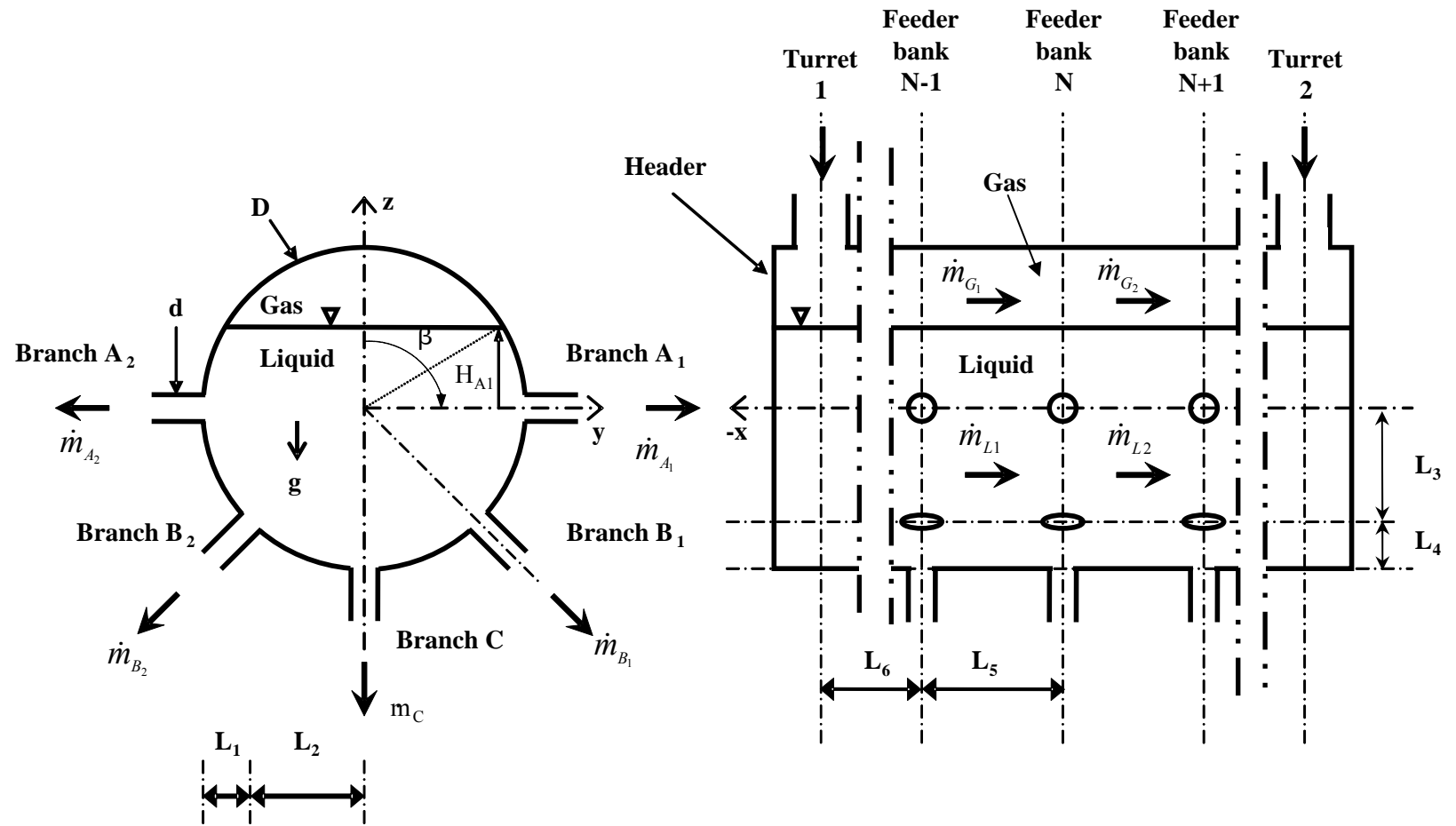
Figure 6.1 A typical header with three feeder banks.
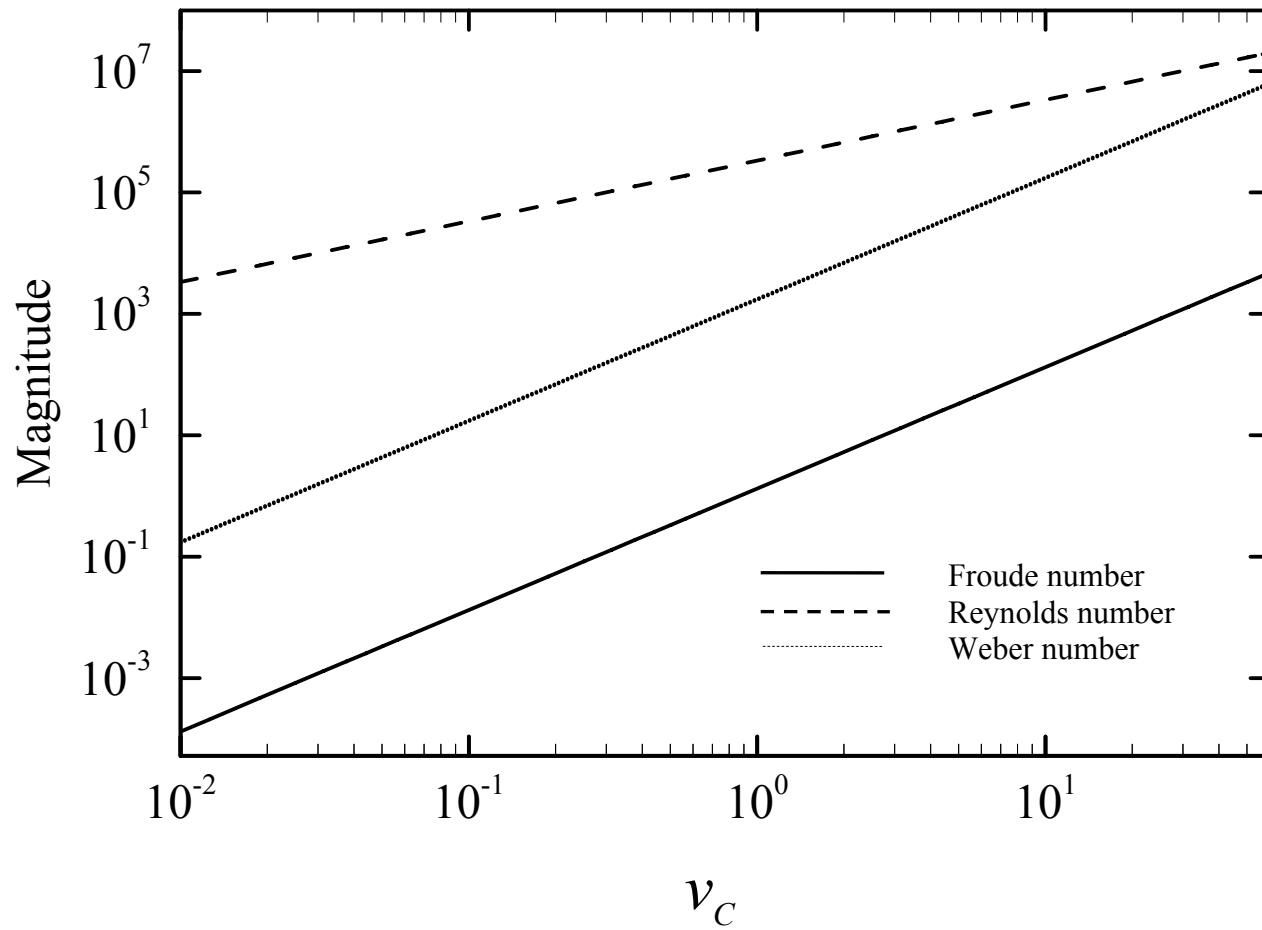
Figure 6.2 Estimated dimensionless numbers of liquid flow in a feeder branch.
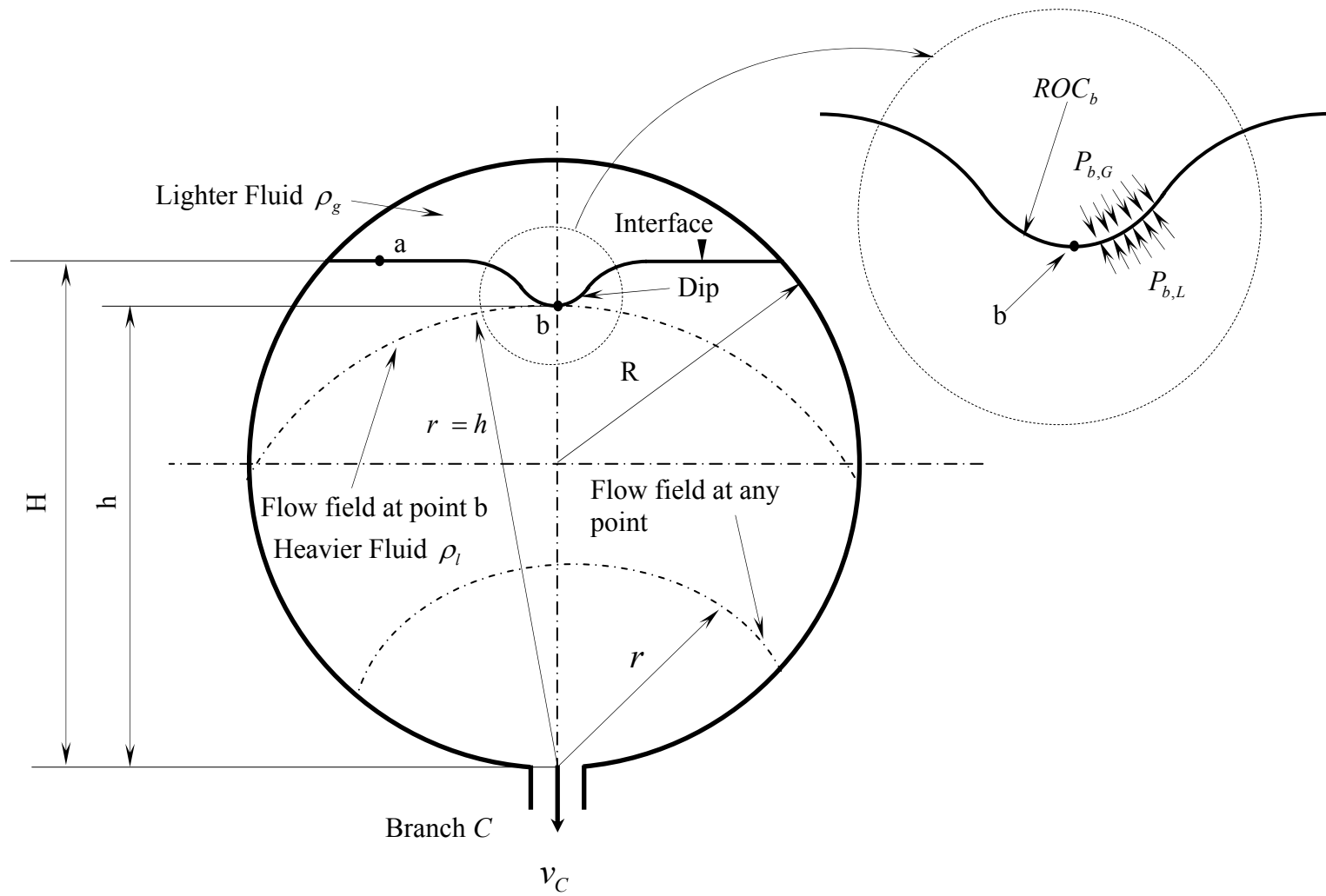
Figure 6.3 Geometry used in Point-Sink analysis.

Figure 6.4 Configuration for finite branch analysis.
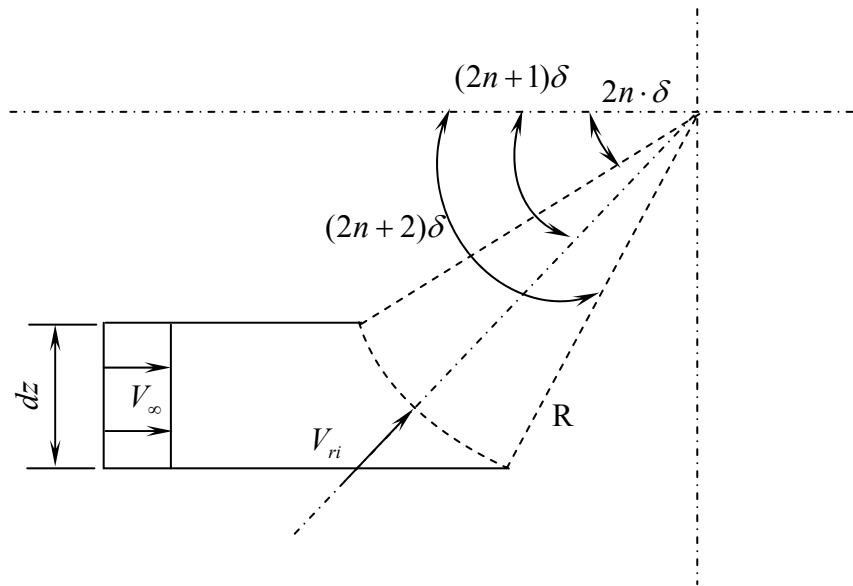
Figure 6.5 A Balance of the flow across one of the imaginary branches.
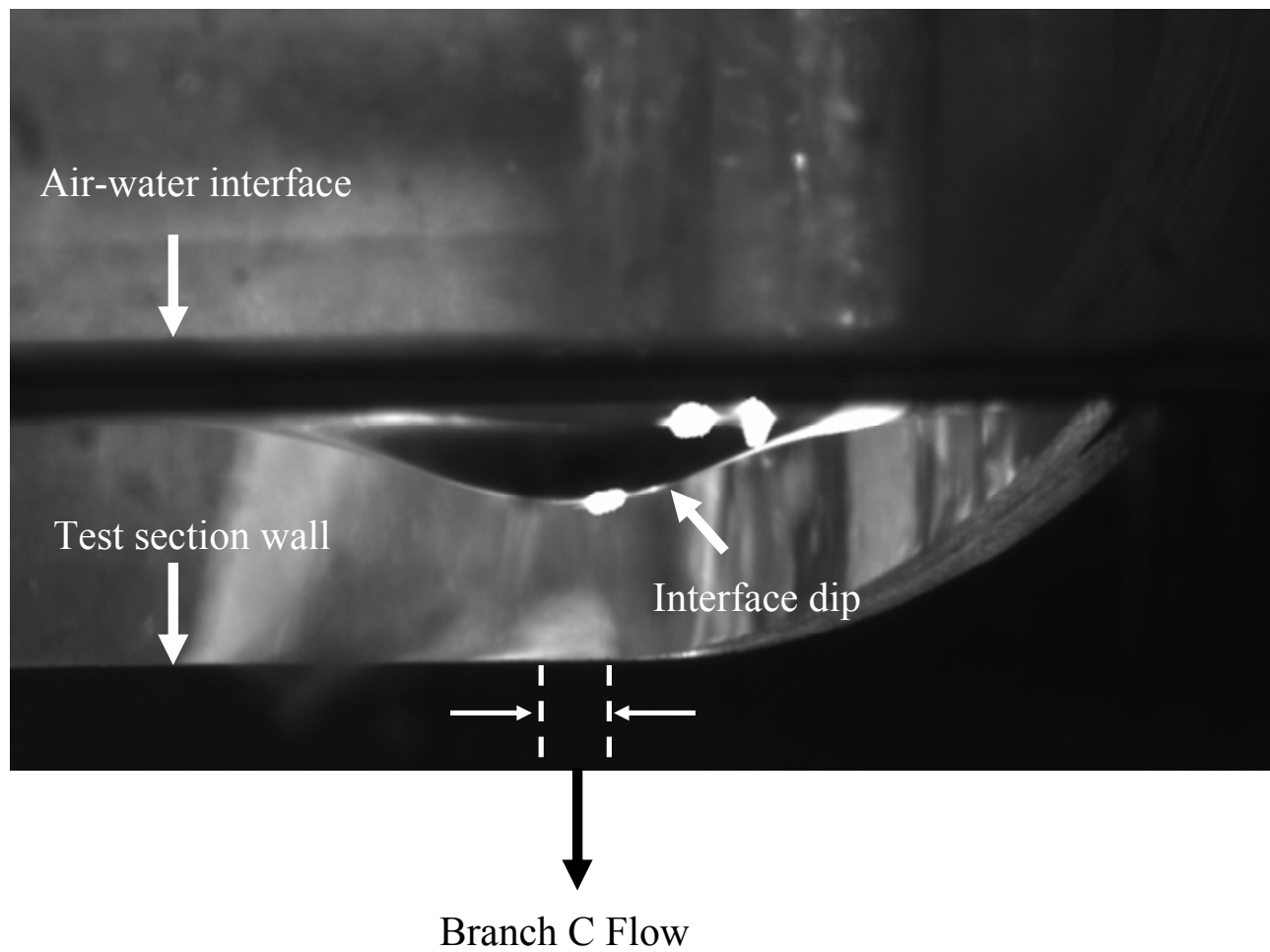
Figure 6.6 Image of dip formed prior to the onset of gas entrainment.
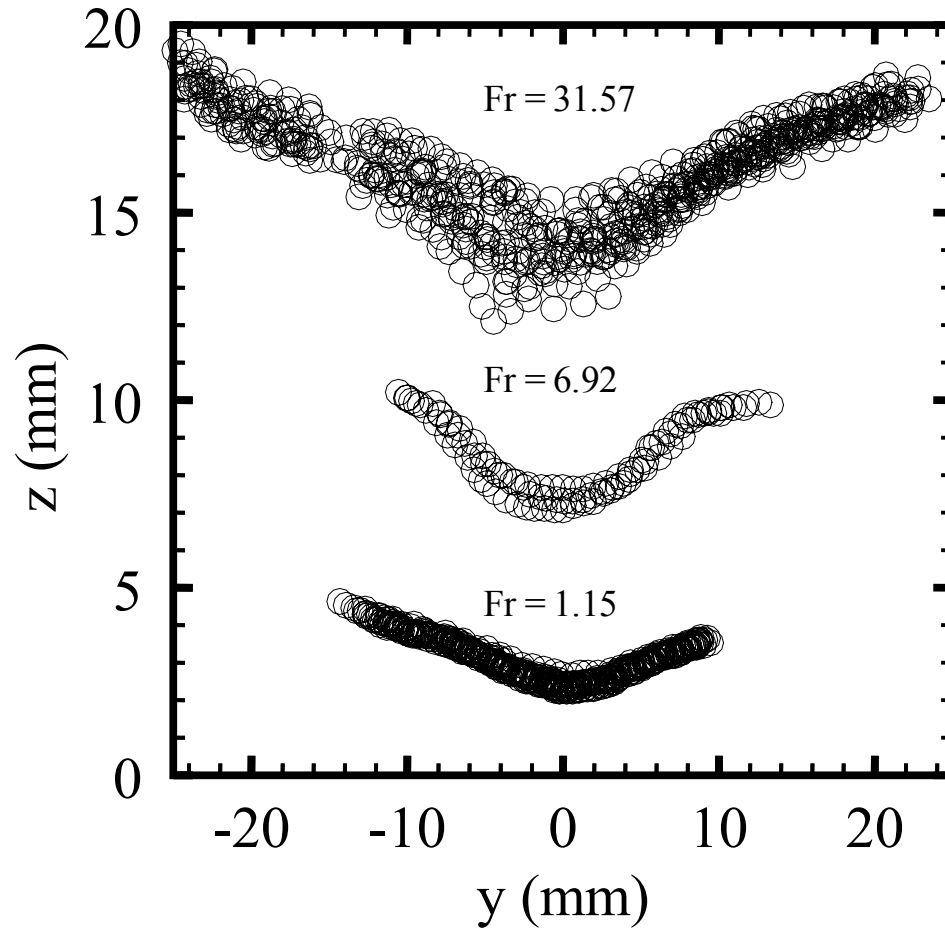
Figure 6.7 The dip shape at three Froude numbers.
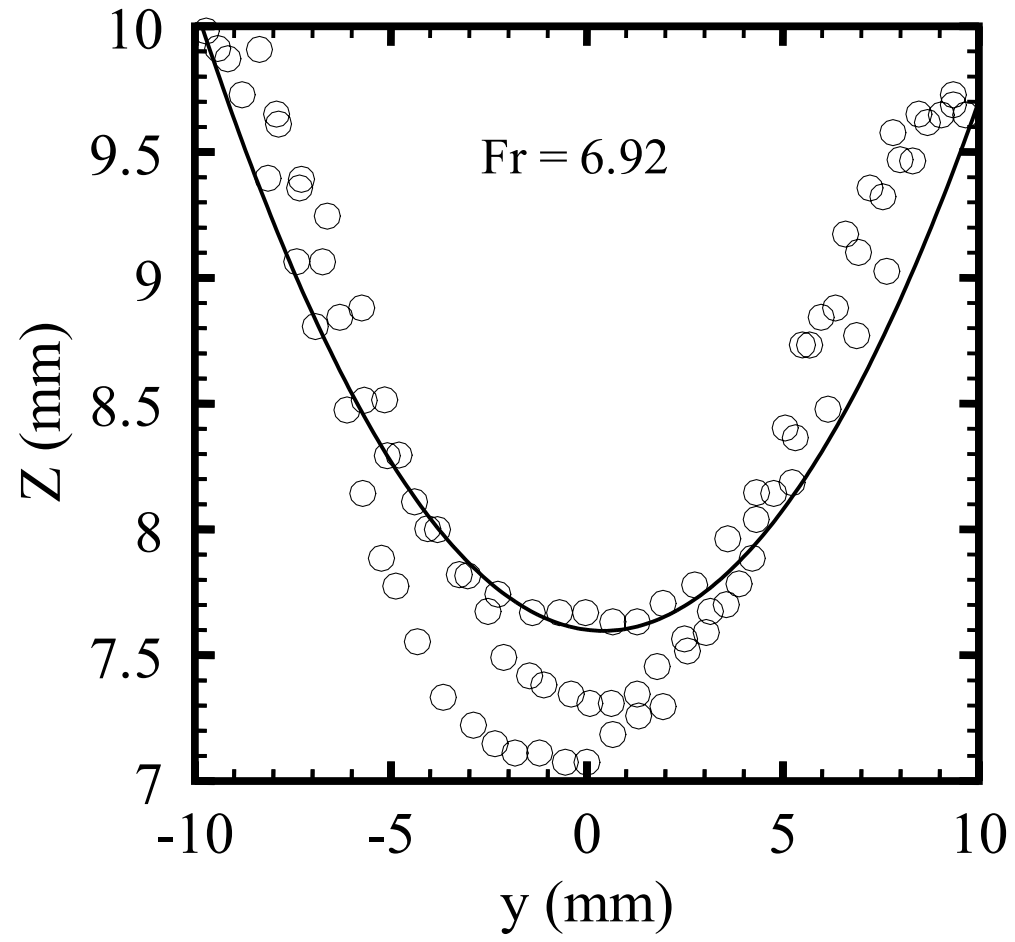
Figure 6.8 Example of curve fitting the dip shape.
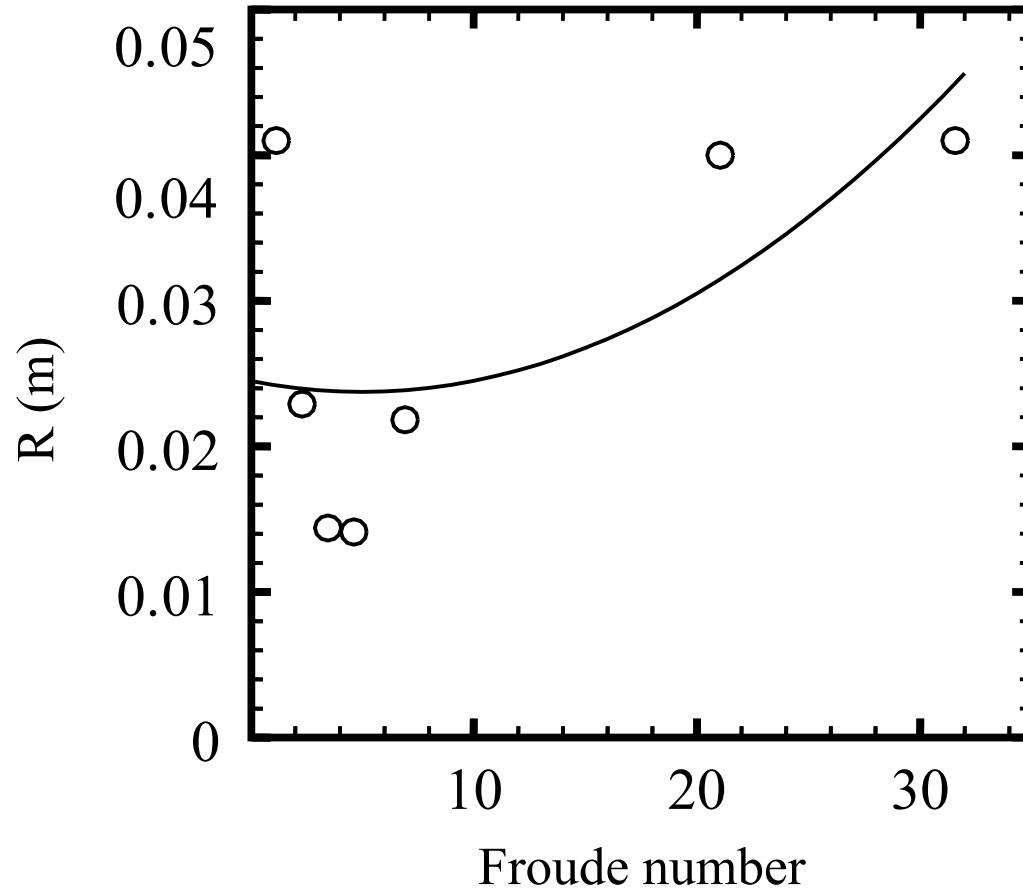
Figure 6.9 The dip radius of curvature as a function of the discharge Froude number.
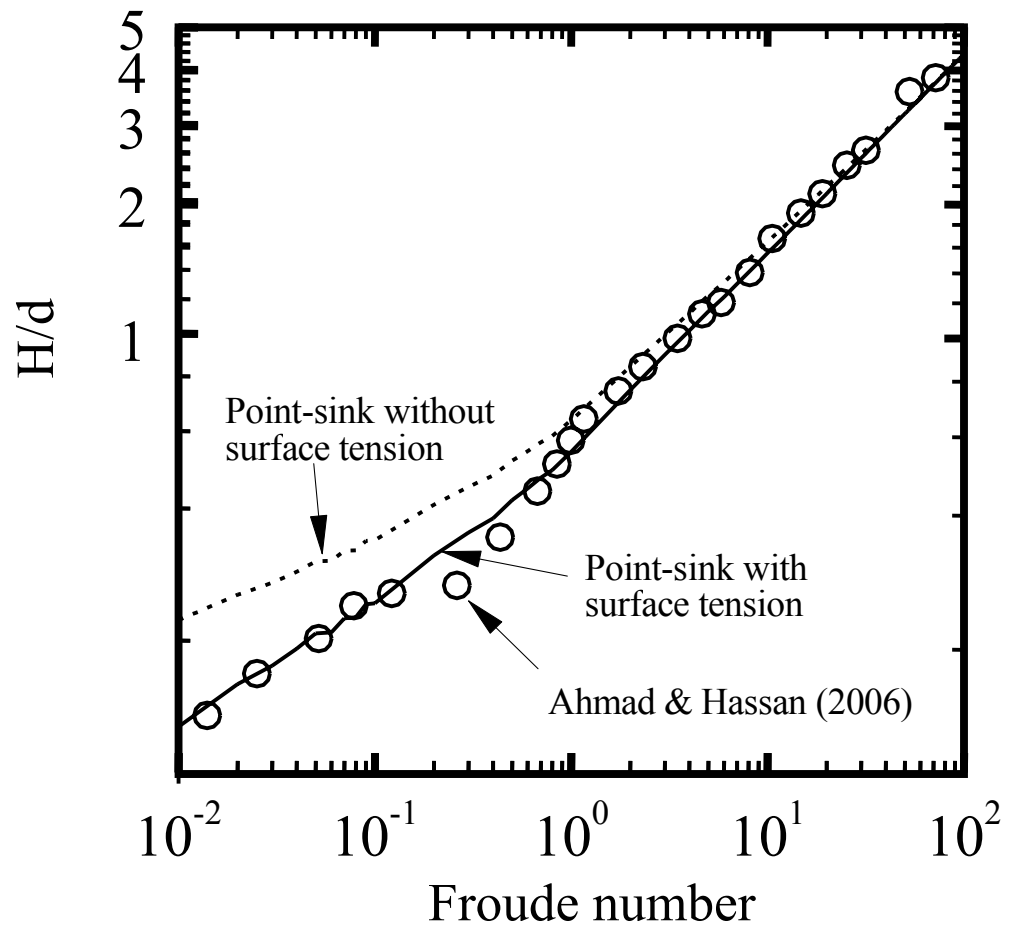
Figure 6.10 Predicted values of the critical height with and without surface tension.
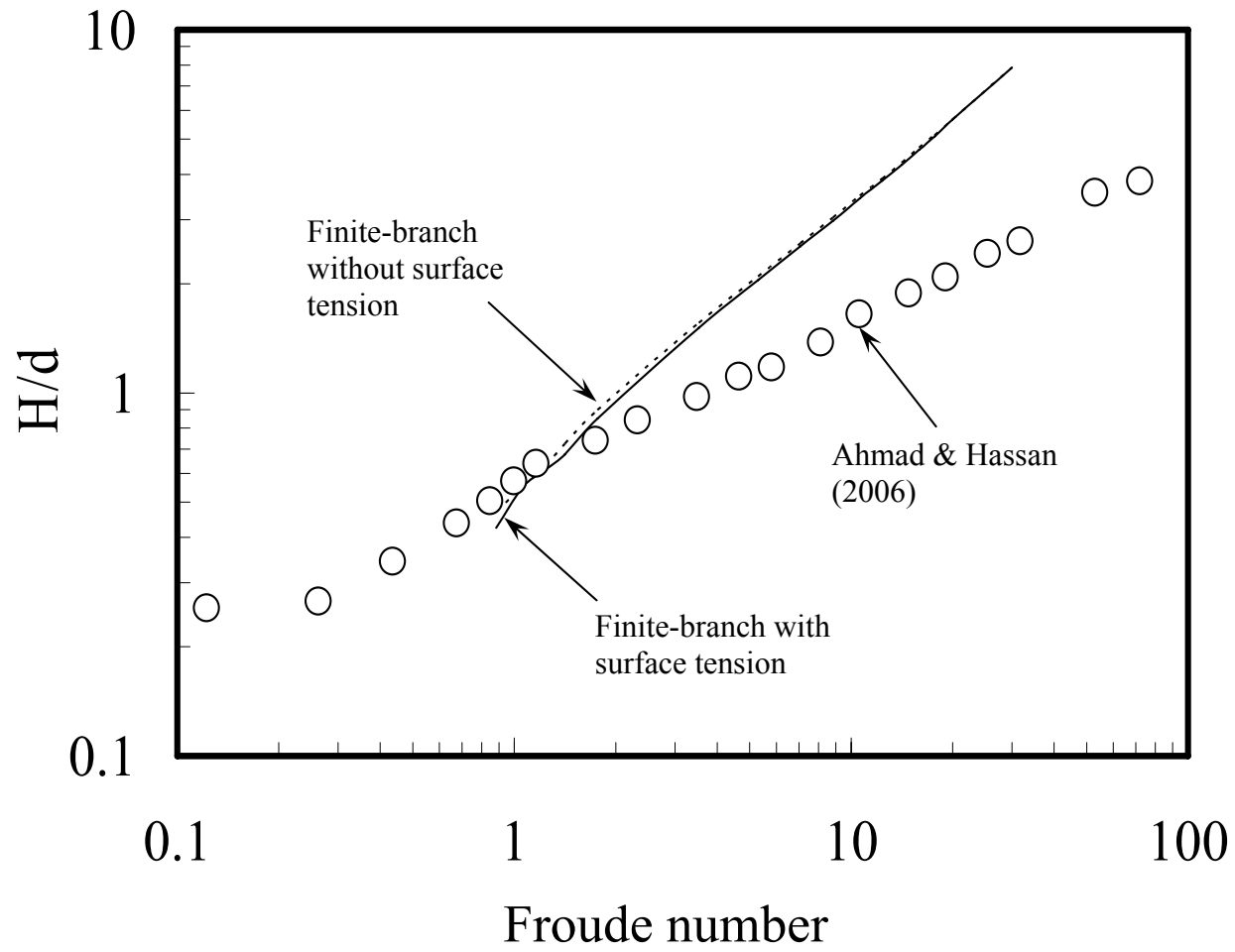
Figure 6.11 Predicted values of the critical height with and without surface tension with 2-D finite branch modeling.

Chapter 7

Dual and Triple Discharge Modeling

7.1 Point-Sink Analysis (Dual and Triple Discharges)

Figure 7.1 shows the geometry (with a main pipe diameter of 50.8 mm and three branches of diameter 6.35 mm, with scale 1/8 of the typical CANDU header-feeder system) used in the point sink model. The flow field is considered steady, incompressible, inviscid, with negligible surface tension, and irrotational. This potential flow assumption allows Bernoulli's equation to be applied between two points within the two-phase flow field. The analysis will be developed for the case of OGE at the primary branch A while there is a liquid flow in the secondary branches B and C. Bernoulli's equation is applied on the interface between the points a and b, Figure 7.1. Considering first the heavier fluid side which results in,

$$P_{a,L} + \frac{1}{2}\rho_L v_{a,L}^2 + \rho_L gH = P_{b,L} + \frac{1}{2}\rho_L v_{b,L}^2 + \rho_L gh \ . \tag{7-1}$$

Since $v_{a,L} \ll v_{b,L}$, and point a is located at $x = \infty$, Eq. (7-1) becomes

$$P_{a,L} + \rho_L gH = P_{b,L} + \frac{1}{2}\rho_L v_{b,L}^2 + \rho_L gh \ . \tag{7-2}$$

By applying Bernoulli's equation on the lighter fluid side, which is considered as stagnant, it gives,

$$P_{a,G} + \rho_G gH = P_{b,G} + \rho_G gh \ . \tag{7-3}$$

From Eqs. (7-2) and (7-3), the critical height (H) at the onset of gas entrainment can now be written in a dimensionless form, as,

$$\frac{H_{OGE}}{d} = \frac{h}{d} + \frac{v_b^2 \rho_L}{2gd(\rho_L - \rho_G)} \ . \tag{7-4}$$

The potential function for a triple discharge flow (three points sinks) is defined as

$$\Phi = \Phi_A + \Phi_B + \Phi_C \ . \tag{7-5}$$

To find the velocity at point b, which is directed toward the primary branch A, the partial derivative of the total potential function, Φ, with respect to the variable radius r_A could be written as

$$v_b = \frac{\partial \Phi}{\partial r_A}\bigg|_{r_A = h_A} = \frac{\partial \Phi_A}{\partial r_A} + \frac{\partial \Phi_B}{\partial r_A} + \frac{\partial \Phi_C}{\partial r_A} = \frac{\partial \Phi_A}{\partial r_A} + \frac{\partial \Phi_B}{\partial r_B}\frac{\partial r_B}{\partial r_A} + \frac{\partial \Phi_C}{\partial r_C}\frac{\partial r_C}{\partial r_A} \ . \tag{7-6}$$

Where the value of $\dfrac{\partial \Phi_A}{\partial r_A}$ is the redial velocity if there is only a point-sink flow at branch A, with a volumetric flow rate of Q_A, and can be obtained from the following equation:

$$\frac{\partial \Phi_A}{\partial r_A} = \frac{Q_A}{S\big|_{r_A = h_A}} \ . \tag{7-7}$$

Where S is the surface area of the flow field, which is a part of a sphere intersected by a cylinder, and the branch is located at the center of this flow field. S is given by

$$\left.S\right|_{r_A=h_A} = 2\pi h_A^2 - 4h_A \int_0^{h_A} \arctan \frac{1}{\sqrt{\dfrac{4R^2}{h_A^2 - r_A^2} - 1}} dr_A \quad. \tag{7-8}$$

Following the same concept, the values of $\dfrac{\partial \Phi_B}{\partial r_B}$ and $\dfrac{\partial \Phi_C}{\partial r_C}$ can be obtained as follows

$$\frac{\partial \Phi_B}{\partial r_B} = \frac{Q_B}{\left.S\right|_{r_B=h_B}} \quad, \tag{7-9}$$

and

$$\frac{\partial \Phi_C}{\partial r_C} = \frac{Q_C}{\left.S\right|_{r_C=h_C}} \quad. \tag{7-10}$$

Where Q_B, and Q_C are the volumetric flow rates at branches B and C, and

$$r_B = \left(r_A^2 + z_{BA}^2 + y_{BA}^2 + 2 \cdot \frac{r_A}{R} \left(z_{BA} \cdot \left(R^2 - \left(\frac{r_A}{2}\right)^2 \right)^{0.5} - y_{BA} \cdot \left(\frac{r_A}{2}\right) \right) \right)^{0.5} \quad. \tag{7-11}$$

and

$$r_C = \left(r_A^2 + z_{CA}^2 + y_{CA}^2 + 2 \cdot \frac{r_A}{R} \left(z_{CA} \cdot \left(R^2 - \left(\frac{r_A}{2}\right)^2 \right)^{0.5} - y_{CA} \cdot \left(\frac{r_A}{2}\right) \right) \right)^{0.5} \quad. \tag{7-12}$$

The criterion used to predict the onset of gas entrainment is the equality between the acceleration vertical component of the liquid at the dip nose, and the acceleration of gravity, g, Taylor (1950). At point b, the principle (for the onset of gas entrainment happening along an inclined line) is given as,

$$a_b \cdot \cos(\theta_A) = -g \quad. \tag{7-13}$$

Where

$$a_b = \frac{\partial}{\partial t} v_b = \frac{\partial}{\partial t}\left(\frac{\partial \Phi}{\partial r_A}\right) = \frac{\partial}{\partial r_A}\left(\frac{\partial \Phi}{\partial r_A}\right) \cdot \frac{\partial r_A}{\partial t} = \frac{\partial^2 \Phi}{\partial r_A^2} \cdot \frac{\partial r_A}{\partial t} = \frac{\partial^2 \Phi}{\partial r_A^2} \cdot v_b = \frac{\partial^2 \Phi}{\partial r_A^2} \cdot \frac{\partial \Phi}{\partial r_A} . \qquad (7\text{-}14)$$

Equation (7-13) states that, if the acceleration vertical component at point b is equal, or exceeds, the gravitational acceleration, then the surface will become unstable, leading potentially to the onset of gas entrainment. Using Eqs. (7-13) and (7-14) to define the condition for the onset of gas entrainment yields,

$$\left.\frac{\partial \Phi}{\partial r_A}\right|_{r_A=h_A} \cdot \left.\frac{\partial^2 \Phi}{\partial r_A^2}\right|_{r_A=h_A} \cdot \cos(\theta_A) = -g . \qquad (7\text{-}15)$$

Where $\dfrac{\partial \Phi}{\partial r_A}$, can be obtained by substituting with Eqs. (7-7), (7-8), (7-9), (7-10), partial derivative of r_B in Eq. (7-11) with respect to r_A, and partial derivative of r_C in Eq. (7-12) with respect to r_A, in Eq. (7-6). Also $\left.\dfrac{\partial^2 \Phi}{\partial r_A^2}\right|_{r_A=h_A}$ can be obtained from the following equation:

$$\left.\frac{\partial^2 \Phi}{\partial r_A^2}\right|_{r_A=h_A} = \frac{\partial^2 \Phi_A}{\partial r_A^2} + \frac{\partial \Phi_B}{\partial r_B}\frac{\partial^2 r_B}{\partial r_A^2} + \left(\frac{\partial r_B}{\partial r_A}\right)^2 \frac{\partial^2 \Phi_B}{\partial r_B^2} + \frac{\partial \Phi_C}{\partial r_C}\frac{\partial^2 r_C}{\partial r_A^2} + \left(\frac{\partial r_C}{\partial r_A}\right)^2 \frac{\partial^2 \Phi_C}{\partial r_C^2} . \qquad (7\text{-}16)$$

In summary, Eq. (7-15) is a function of Q_A, Q_B, Q_C and h_A. This Eq. is solved by trial and error until the OGE condition was achieved. Then the values of h_A and v_b are used in Eq. (7-4) to obtain the OGE critical height H_{OGE}. A Maple software 11 computer code was developed to do the mathematical calculations. This analytical model is developed for the case of triple discharge and it could also be used for dual discharge by inserting the

volume flow rate for the blocked branch as zero. Also, this analytical model can be used with different branch orientations. In summary this model is modified to study the following cases stated in table 7-1:

- 1A- OGE at the primary branch *A*, with a liquid flow in branch *B*.

- 2A- OGE at the primary branch *A*, with a liquid flow in branch *C*.

- 3A- OGE at the primary branch *B*, with a liquid flow in branch *C*.

- 4A- OGE at the primary branch *B*, with a liquid flow in branch *A*.

- 5A- OGE at the primary branch *C*, with a liquid flow in branch *B*.

- 6A- OGE at the primary branch *A*, with a liquid flows in branches *B* and *C*.

- 7A- OGE at branches *B* and *C* simultaneously (dual discharge).

7.2 Results and Discussion

7.2.1 Dual Discharge

Two methods are used to validate the analytical model. First by comparing the flow field velocity components, measured by using the stereoscopic PIV technique with those obtained from the analytical model. The second method, by comparing the OGE height obtained from the experimental results of Ahmad and Hassan (2006) with the predicted OGE height. To do so (the second method of validation), the definition of the Froude number is modified to include the volumetric flow rates through the branches as follows:

$$Fr = \frac{4Q}{\pi \sqrt{gd^5(\rho_L - \rho_G)/\rho_L}} \; . \tag{7-17}$$

In the first validation method, the flow field velocity which was measured by using stereoscopic PIV (case 1 in chapter 3) are used. The acceptable error value ranged from 25 % to 15 %, at a control volume radius ranging from 15 mm to 25 mm. The experimental results in this range only (r = - 15 mm to r = - 25 mm) will be used to validate the analytical model. Figures 7.2(a) to 7.2.f compare the velocity obtained by the analytical model and the PIV measurements. In all figures, the tangential velocity is zero as calculated by the analytical model and its value fluctuates around zero for PIV tangential velocity. The analytical model predicted the velocity of vertical component in planes number 2, 3, and 4 very well and in planes number 1, 5, and 6 with an acceptable value of deviation. This deviation is due to the absence of the air water interface and the bottom wall of the test section in the analytical model. The analytical model predicted the radial component velocity in planes number 3 and 4 very well and in planes number 1, 2, 5, and 6 with an acceptable value of deviation. This deviation is again because the analytical model does not consider the air water interface or the bottom wall of the test section. Branch A

For the second validation method, a few comparisons between the OGE height obtained by the analytical model and those obtained experimentally by Ahmad and Hassan (2006) will be presented. The analytical flow field will be presented here for some of the compared cases. Figure 7.3 shows the predicted velocity flow field and vertical acceleration contours for dual discharge in branches A and B and single onset at branch A. The discharge Froude number at branch A is 30, the discharge Froude number at branch B is 50, and the OGE critical height is 1.7 cm, measured from branch A centre ($H_{OGE}/d = 2.7$). There are two conditions, which should be satisfied to achieve the OGE

height. The first condition is that the vertical acceleration at the onset location should be equal to -9.81 m/s^2. The second necessary condition is the applicability of the Bernoulli equation between any location at the air-water interface and the location of onset. Figure 7.3 shows that there are two vertical acceleration contour lines having a value of -9.81 m/s^2. These lines are located in a zone higher than the active branches (A, B). Hence the analytical model searches for a point located on these contour lines and achieves the second condition. It was found that the highest point on the vertical acceleration contour line with a value of -9.81 m/s^2 represents the OGE point, located at the lowest point on the OGE dip. Also, it can be concluded from this figure that there is no OGE in branch B and the OGE will happen in branch A first. This is because the distance between the air-water interface and the highest point (which is located at vertical acceleration contour line for branch B with the value of -9.81 m/s^2) is higher than the distance between the air-water interface and the highest point (located at vertical acceleration contour line for branch A with the value of -9.81 m/s^2).

Figure 7.4 shows the flow field streamlines and the vertical acceleration contours for dual discharge with a single onset at branch A (case 1A). This figure shows the interaction zone between the two branches. By looking at this zone and the vertical acceleration contour lines for branch B, an important conclusion can be made: the vertical acceleration contour line (with a value of -9.81 m/s^2 for branch B) is located in this zone. If the OGE in branch A is already achieved, the air-water free surface will be extended towards the entrance of branch A. So that, the distance between the air-water interface and the highest point (which is located at vertical acceleration counter line for branch B with the value of -9.81 m/s^2) is not large any more, and the OGE in branch B can be

obtained from the air core which extended inside branch A (which has already two-phase flow). In other words, the OGE will happen in branch A, then it will develop to have two-phase flow inside this branch, following the OGE will happen in branch B and the air core will extend from branch A to branch B.

Figures 7.5 and 7.6 show comparisons between predicted OGE critical height at the primary branch A and the experimental results for different values of Fr_B at the secondary branch B (case 1A). As the Fr_B increases, the OGE critical height in branch A, increases too. The existence of the secondary branch B enables the OGE phenomenon by pulling more liquid toward the primary branch A. As predicted, the analytical results are slightly over predicting the experimental results, since the model assumes the flow field is inviscid, and the surface tension is neglected. The surface tension force resists the gas-pull through the air-water interface. This surface tension dependence is more significant at low Froude number, where the surface tension forces become predominant. The deviation percentage in predicting the OGE height was 15 % for Fr_A greater than 10, and it is consistent with the deviation percentage in predicting the OGE height in dual discharge by (Ahmed, 2006) analytical work.

Figures 7.7 and 7.8 show the comparison between the predicted OGE critical height at the primary branch A and experimental results for different values of Fr_C at the secondary branch C (case 2A). Again as the Fr_C increases, the OGE critical height in branch A increases. This is due to the existence of the secondary branch C which pulls more liquid toward the primary branch A, thus allowing the OGE phenomena to occur.

Figures 7.9. and 7.10. compare the effects of Fr_B and Fr_C in branches B and C on the OGE critical height in the primary branch A. It can be stated that the effect of

increasing Fr_B in branch B on increasing the OGE critical height in the primary branch A is greater than the effect of increasing Fr_C in branch C on increasing OGE critical height in the primary branch A. This is obvious because of the distance between branches A and B is shorter than the distance between branches A and C.

After validating the analytical model in dual discharge with the available experimental data, the model was used to investigate the OGE phenomena more thoroughly. Figure 7.11 shows the comparison between the predicted OGE critical heights at the primary branch B at different values of Fr_C at the secondary branch C (case 3A). At small values of Fr_B, the OGE critical height changes significantly with the change of Fr_C. At higher values of Fr_B, the OGE critical height does not change significantly with the change of Fr_C. Also in this curve, when the Fr_C is increased, the OGE critical height in branch B increases. Hence, the presence of the secondary branch C pulls more liquid toward the primary branch B.

Figure 7.12 shows the comparison between the predicted OGE critical heights at the primary branch B for different values of Fr_A at the secondary branch A (case 4A). In this case, the effect of the existence of the secondary branch A will not be included in the analytical model until the air-water interface liquid height reaches the centre of the secondary branch A (H_{OGE}/d = 2.82). After this, branch A begins to resist the OGE phenomenon in branch B by taking some of the liquid field from branch B. The net effect of this resistance is to decrease the OGE height in primary branch B when the Fr_A was increased in the secondary branch A. Similarly in figure 7.13, when the value of Fr_B increases in the secondary branch B, the OGE critical height in the primary branch C also

increases. This means that the secondary branch *B* attracts more liquid toward the primary branch *C,* thus enabling the OGE phenomena.

7.2.2 Triple Discharge

Figures 7.14 and 7.15 show the flow field velocity, streamlines and vertical acceleration contours for triple discharge and single onset at branch *A* (case 6A). The discharge Froude number at branch *A* is 30, the discharge Froude numbers at branches *B,* and *C* are the same and equal to 34.4, and the OGE critical height is 1.8 cm measured from branch *A* centre (*H*/*d* = 2.8). There are three vertical acceleration contour lines, which have a value of -9.81 m/s^2 (at which the unbalance of the air-water interface or OGE could happen) for each of the active branches (*A*, *B*, *C*). The highest point on the highest vertical acceleration contour line with a value of -9.81 m/s^2 represents the OGE in the highest branch *A*. By looking at the interaction zone between, the two branches *A* and *B* and the interaction zone between the two branches *B* and *C*, it can be concluded that the OGE in branch *B* can be created from the two-phase flow in branch *A* (when existing) or the two-phase flow in branch *C* (when existing). Also the OGE in branch *C,* can be created from the two-phase flow in branch *A* (when existing). This means that in the modeling of two-phase flow process, future works should investigate the probability of having OGE in one branch from the other two branches and not only from the air-water free surface.

To validate the analytical modeling in the case of triple discharge, comparisons with experimental results were carried out, in Figure 7.16 and 7.17, to show the effect of increasing *Fr*$_B$ in branch *B* and *Fr*$_C$ in branch *C,* at the same time with equal values, on the OGE critical height in the primary branch *A* (triple discharge). The two Figures show

the model's accuracy in predicting the critical height. Also, the two Figures show that the secondary branch or branches accelerate the OGE phenomenon. The study was, thus, extended to predict the OGE in two branches simultaneously.

7.2.3 Simultaneous OGE in Branches *B* and *C*

Figure 7.18 is a schematic sketch for the OGE criterion at branches *B* and *C* simultaneously (case 7A). In this case the analytical model was solved twice. First, by changing the two Froude numbers in the branches *B* and *C* until the OGE in branch *B* obtained the assumed air-water level. Secondly, by checking if for the same two Froude numbers in branches *B* and *C*, as well as the same air-water level, will the OGE phenomenon occur at branch *C* or not. If this condition is achieved, the two Froude numbers in the branches *B* and *C* and the air-water level will present a point on the curve in Figure 7.20. Figure 7.19 shows the flow field velocity and vertical acceleration contours for dual discharge and dual onset in branches *B* and *C,* simultaneously. The discharge Froude number at branch *B* is 5, the discharge Froude number at branch *C* is 35, and the OGE critical height is 1.8 cm, measured from branch C centre (*H/d* = 2.8). If we follow the vertical acceleration contour lines which have a value of -9.81 m/s^2, we will find that there are two contour lines of this value for each of the active branches (*B*, *C*). To have simultaneous OGE at the two branches *B*, and *C*, the highest points on the two contour lines (at which the acceleration is equal to -9.81 m/s^2) should be close to the air-water interface and the Bernoulli equation must be applicable between any point on the air-water interface and these two points. Figure 7.20 shows a simple regime map for three zones that can exist during dual discharge. The line in this Figure, represents the OGE in branches *B* and *C,* simultaneously, and the corresponding critical height. The

zone under this line represents the probability of OGE in branch B and the improbability of OGE in branch C. The zone over this line represents the probability of OGE in branch C and the improbability of OGE in branch B.

7.3 Summary and Concluding Remarks

An analytical model has been developed to predict the OGE critical height during dual and triple discharge from a stratified two-phase region through any two branches mounted on a curved surface. The predicted critical height was found to be in a good agreement with the available experimental data. The percentage of the deviation of the experimental data from the point sink model prediction is about 15% at $Fr_A > 10$. Based on this model, it was found that the effect of increasing the Froude number in the secondary branch on the prediction of the OGE critical height in the primary branch does not always have the same effect, the value or the same trend. In some cases, in dual discharge, the flow in the secondary branch accelerates the OGE phenomena to occur in the primary branch (effect of branch B on A, C on A, B on C, and C on B) and in other cases, the flow in the secondary branch resists the OGE phenomena to occur in the primary branch (effect of A on B). The velocities and acceleration flow field (in vertical planes) obtained by the analytical modeling explained the interaction between the branches (OGE in the lower branch developing from the higher branch and not from the air-water interface), and the simultaneous OGE in two branches. Finally, the comparison between the velocity field (in horizontal planes) obtained by the analytical modelling and those obtained experimentally using stereoscopic PIV showed that the analytical model can present the actual flow field with an acceptable error.
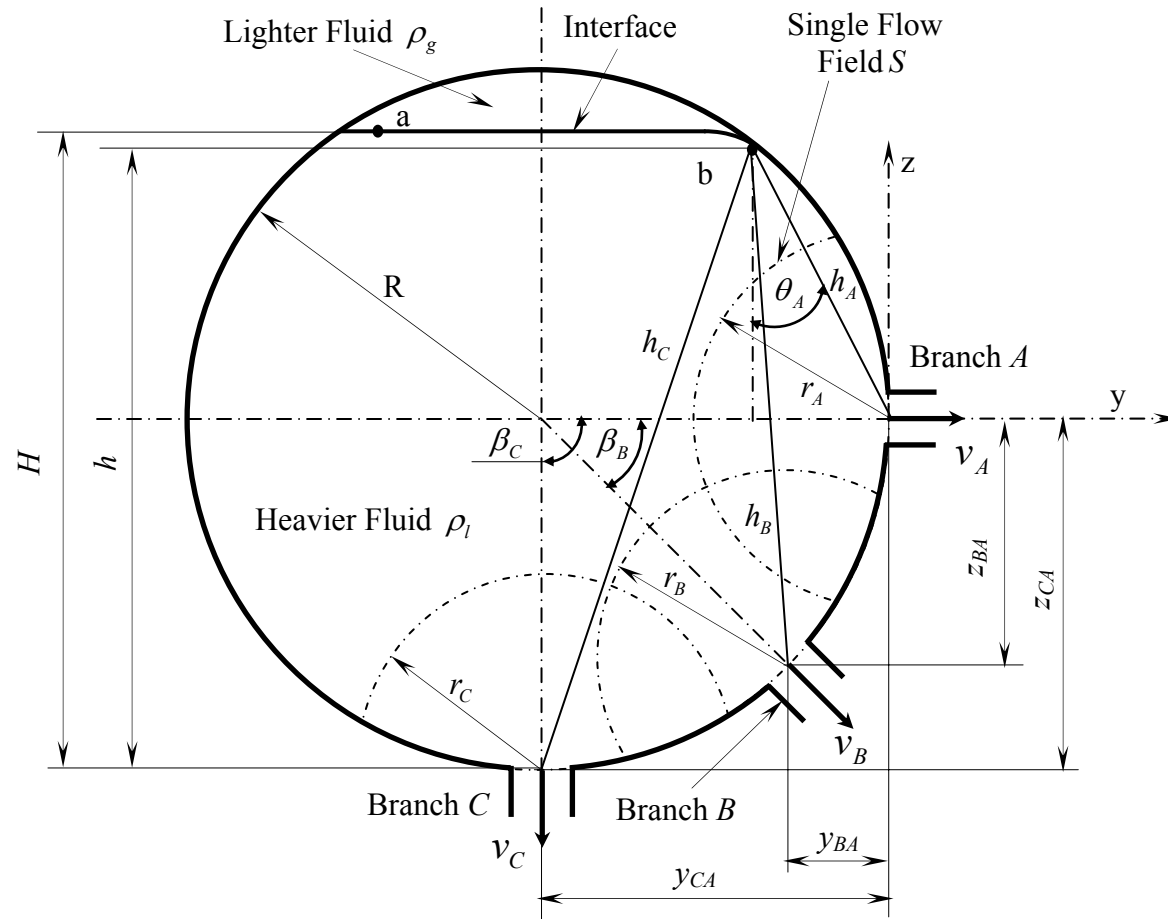
Figure 7.1 The geometry that was simulated as the point sink model.

Table 7-1 Analytical test matrix.

Specifications / Case no.	Branch A	Branch B	Branch C	OGE is happening at branch or branches	Case name	Case figures
Case 1A	Active	Active	Not active	A	Dual discharge single onset	7.3., 7.4., 7.5., and 7.6.
Case 2A	Active	Not active	Active	A	Dual discharge single onset	7.7., and 7.8.
Case 3A	Not active	Active	Active	B	Dual discharge single onset	7.11.
Case 4A	Active	Active	Not active	B	Dual discharge single onset	7.12.
Case 5A	Not active	Active	Active	C	Dual discharge single onset	7.13.
Case 6A	Not active	Active	Active	B, C	Dual discharge dual onset	7.18., 7.19., and 7.20.
Case 7A	Active	Active	Active	A	Triple discharge single onset	7.14., 7.15., 7.16., and 7.17.
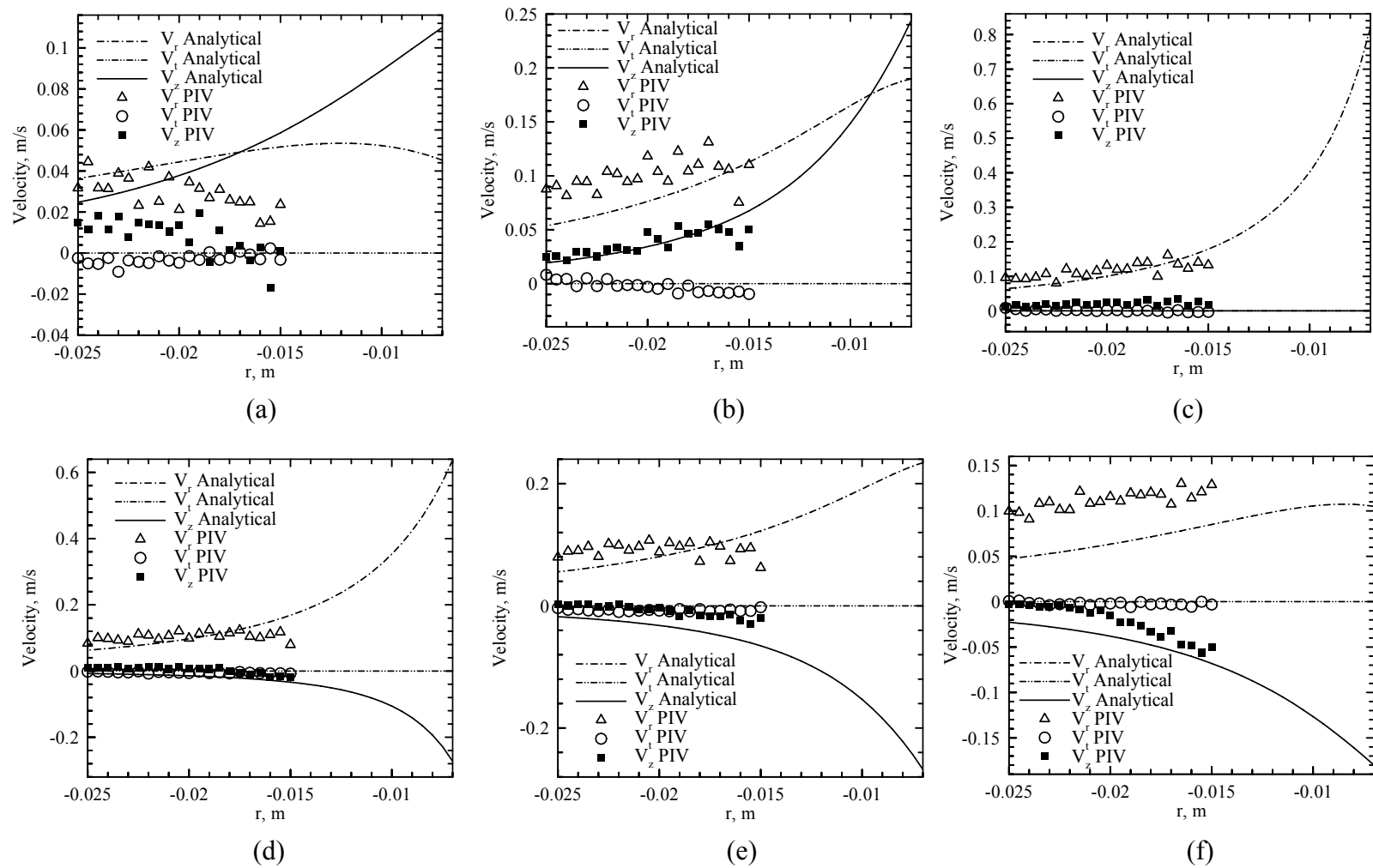
Figure 7.2 Comparison between analytical flow field velocities and experimental PIV results for single discharge side branch (Fr_A = 32) at 6 different investigated planes (8, 16, 25, 28, 33, and 37 mm from bottom branch C).
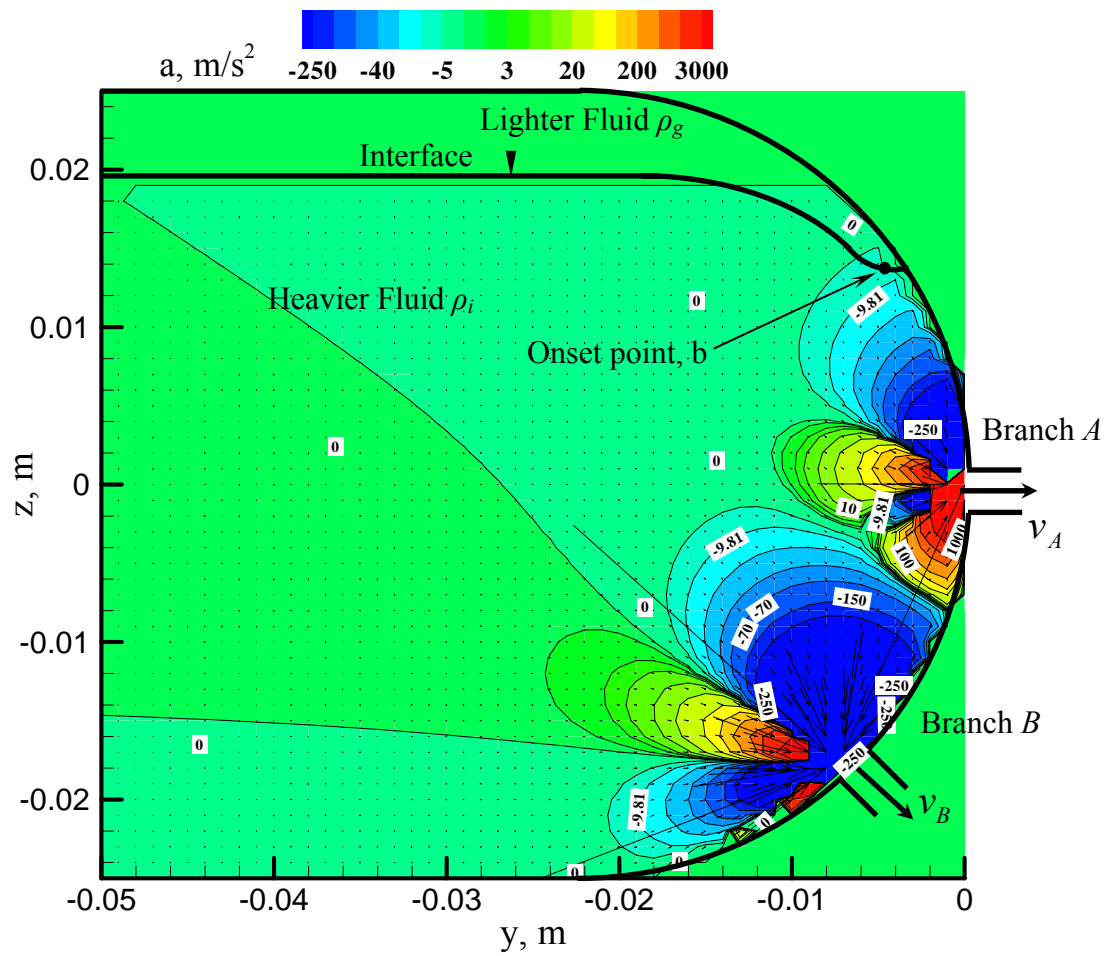
Figure 7.3 Flow field velocity and vertical acceleration contours for dual discharge and single onset at branch *A*.
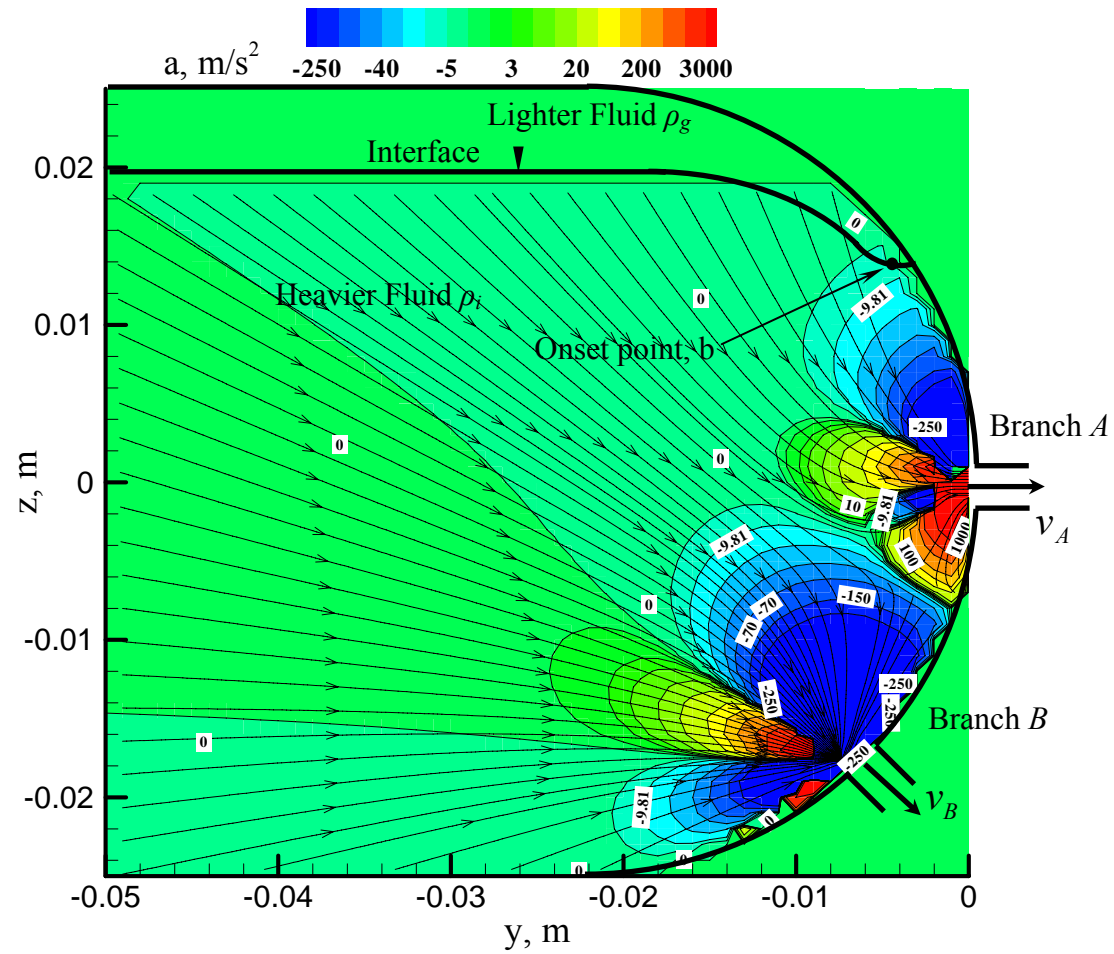
Figure 7.4 Flow field stream lines and vertical acceleration contours for dual discharge and single onset at branch *A*.
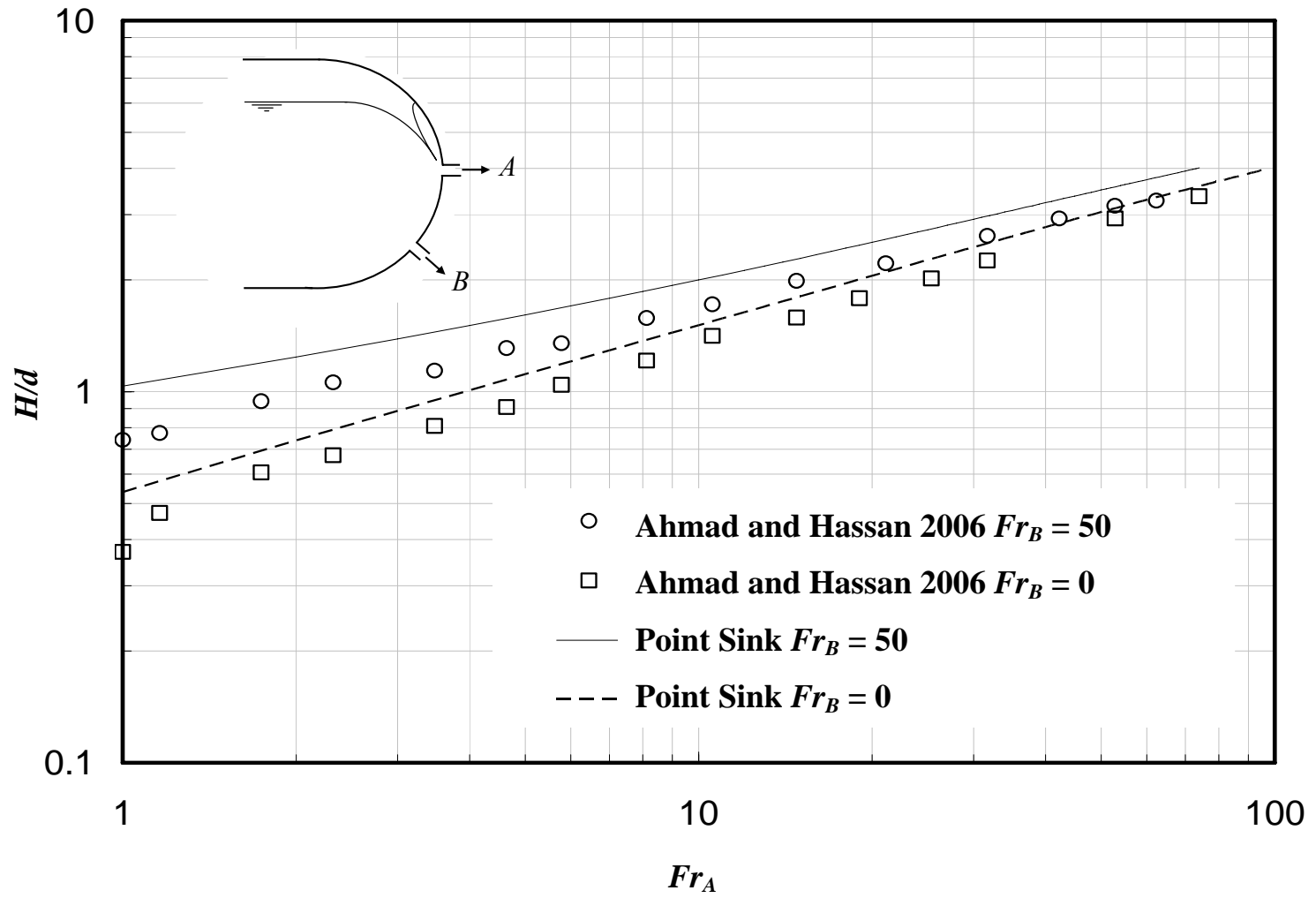
Figure 7.5 Comparisons between predicted and experimental results at different values of Fr_B.
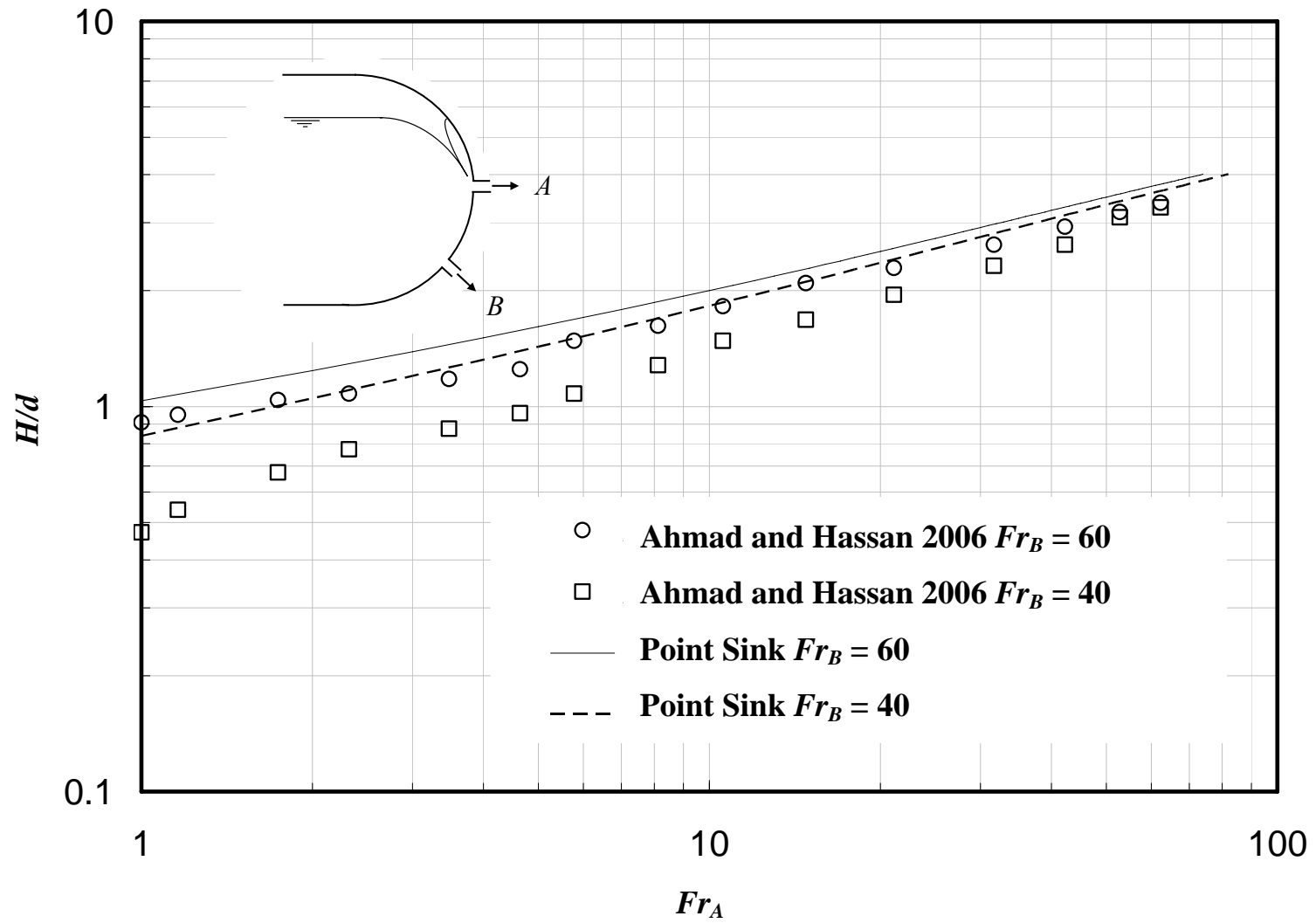
Figure 7.6 Comparisons between predicted and experimental results at different values of Fr_B.
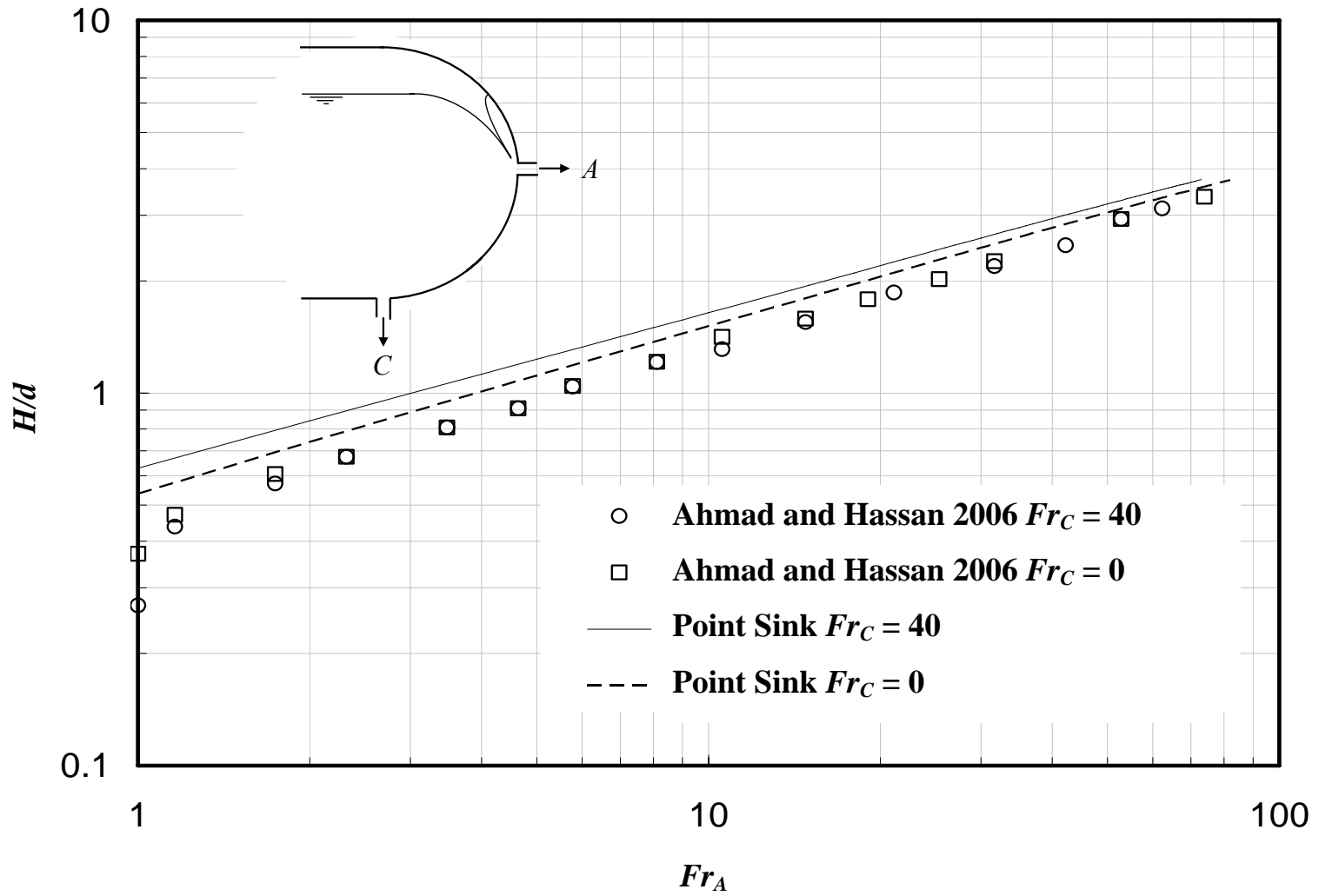
Figure 7.7 Comparisons between predicted and experimental results at different values of Fr_C.
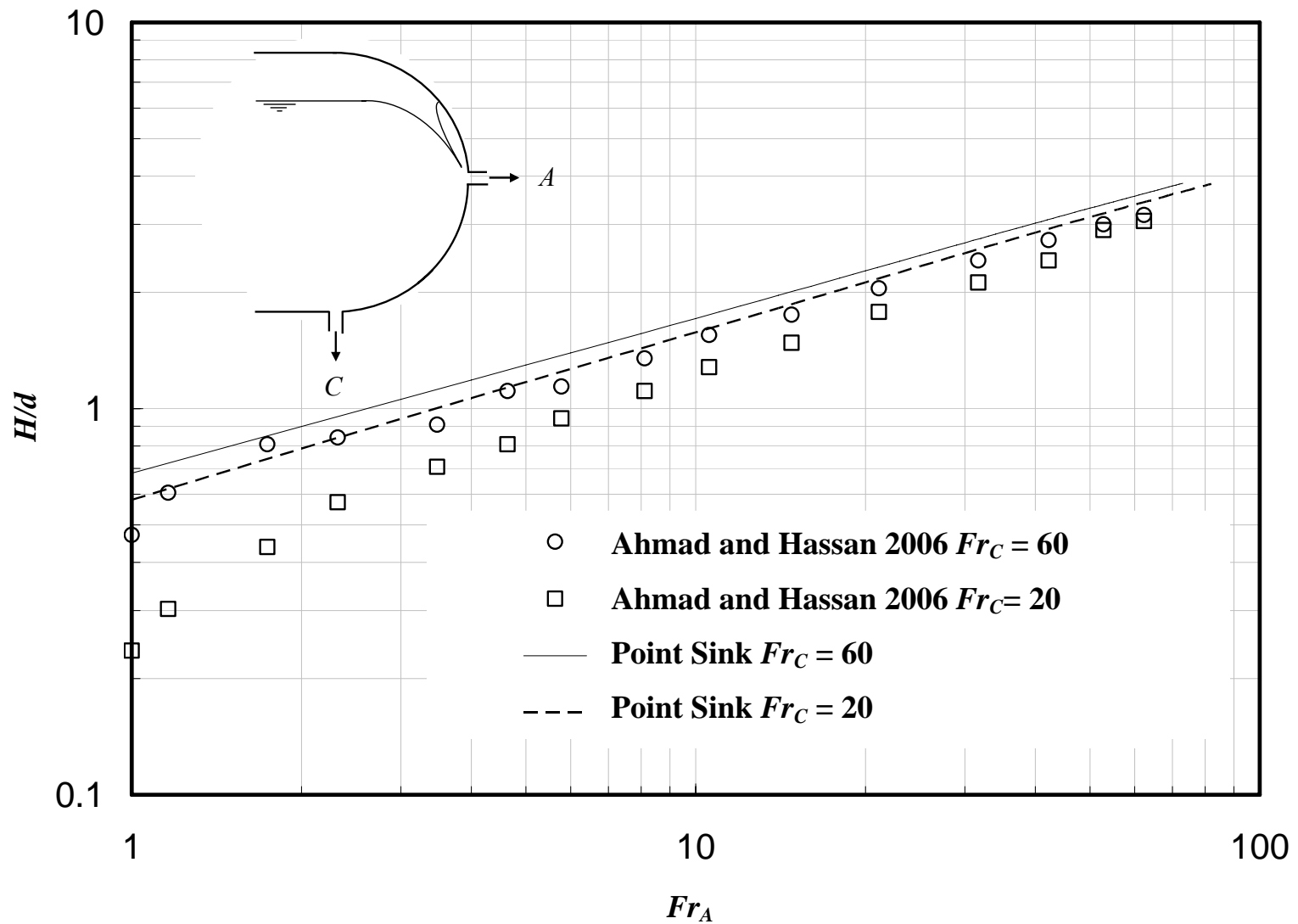
Figure 7.8 Comparisons between predicted and experimental results at different values of Fr_C.
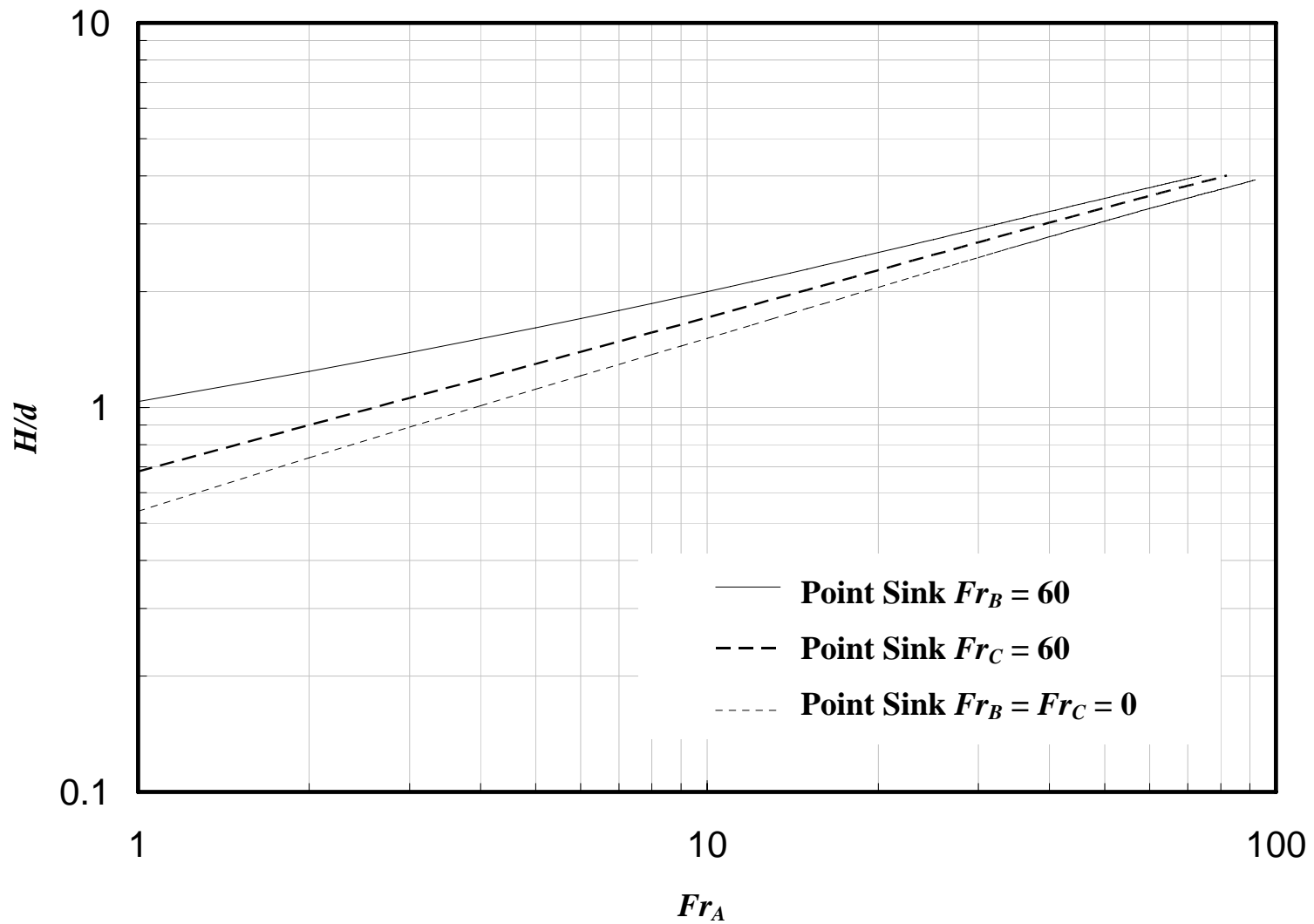
Figure 7.9 The effect of the secondary discharge at branch *C* or at branch *B* on the OGE critical height at branch *A*.
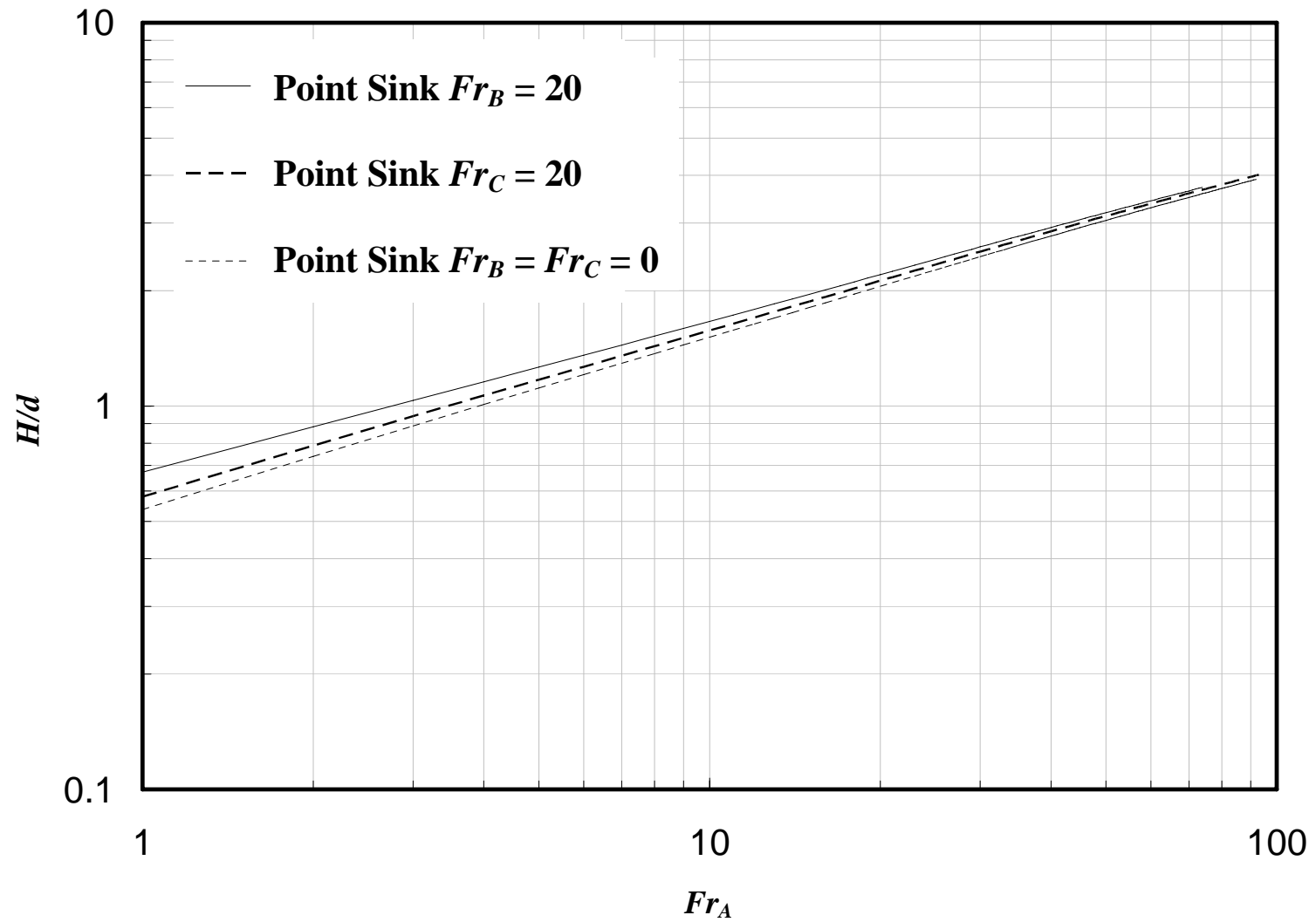
Figure 7.10 The effect of the secondary discharge at branch *C* or at branch *B* on the OGE critical height at branch *A*.
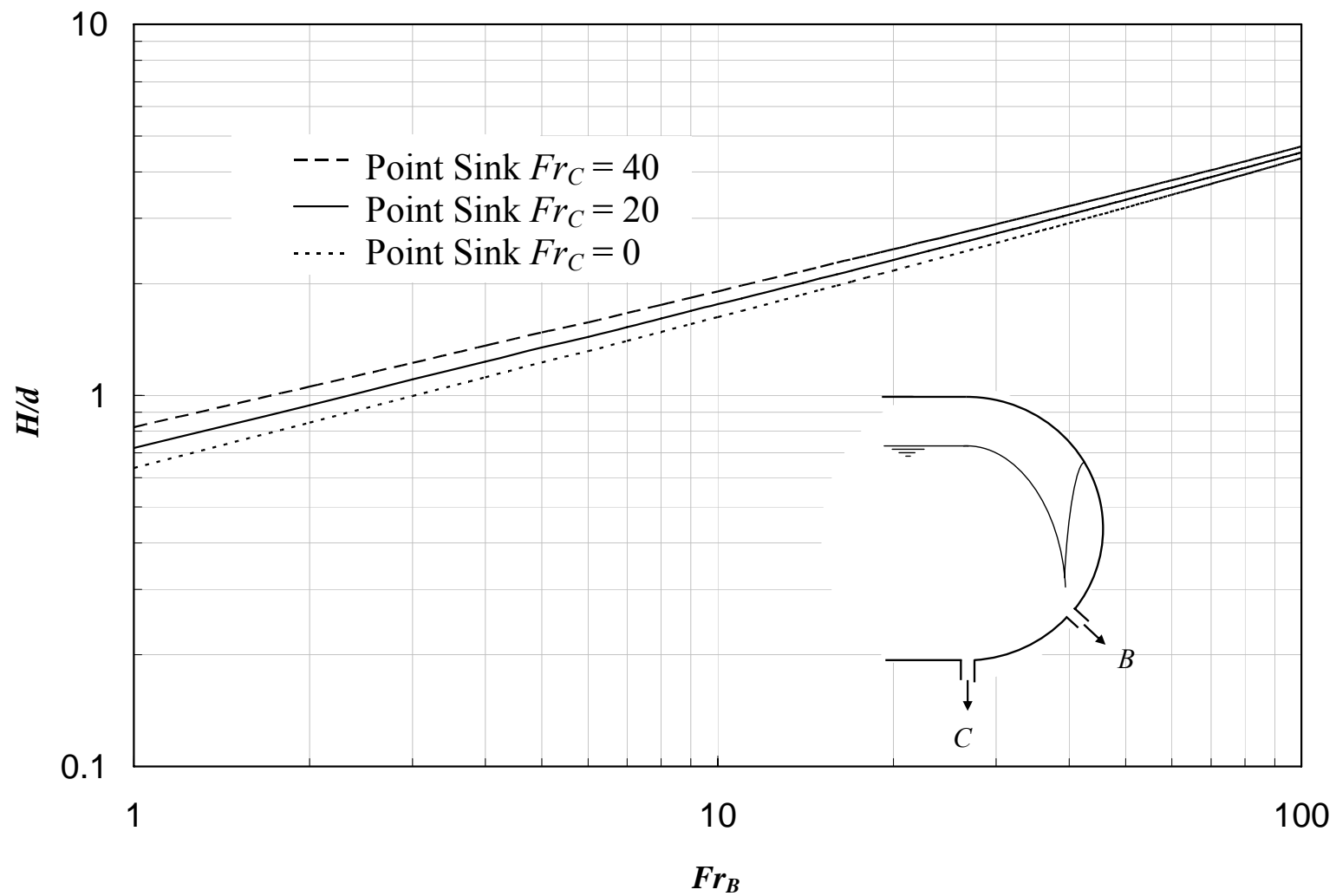
Figure 7.11 The effect of increasing the secondary discharge at branch C on the OGE critical height at branch B.
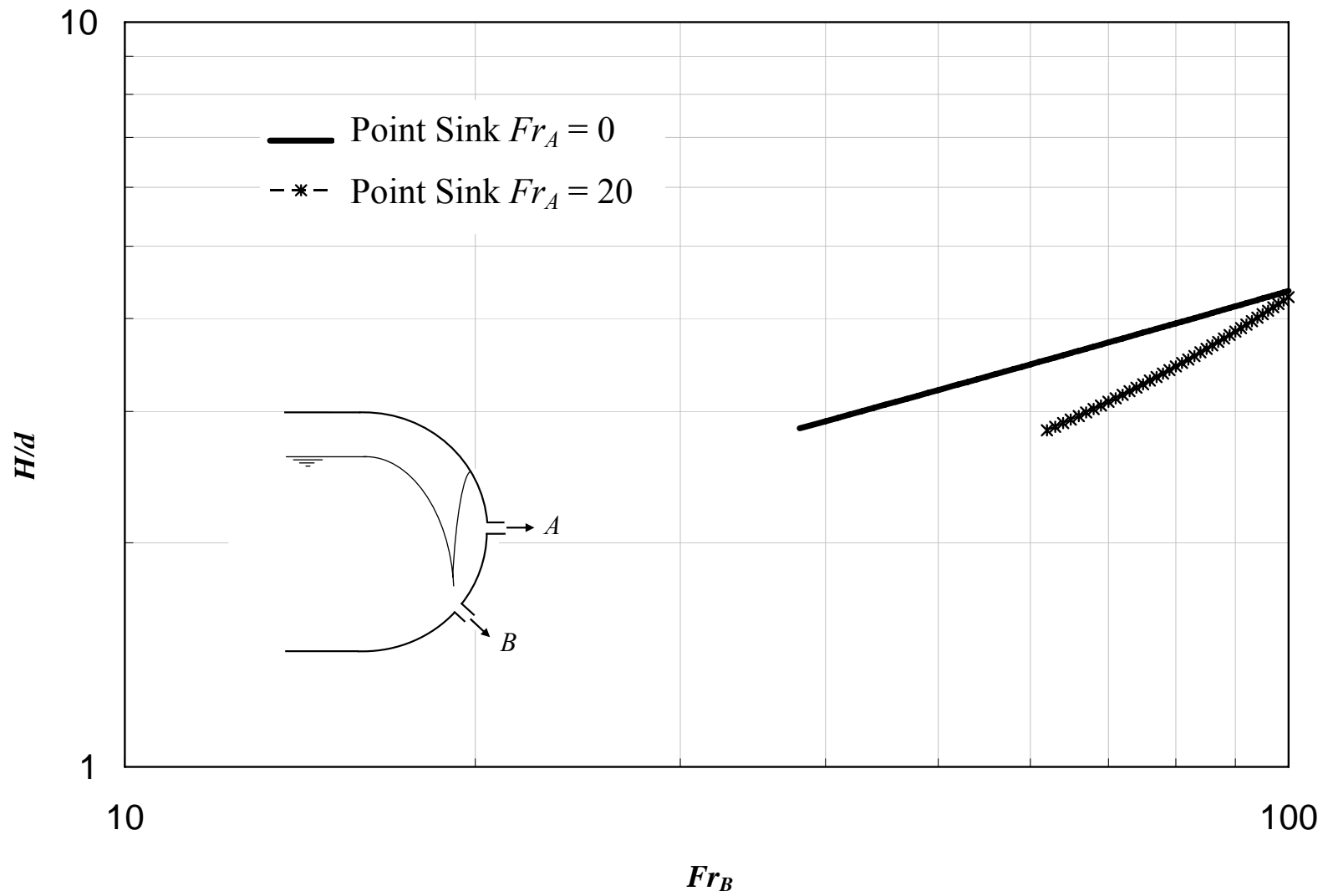
Figure 7.12 The effect of increasing the secondary discharge at branch A on the OGE critical height at branch B.
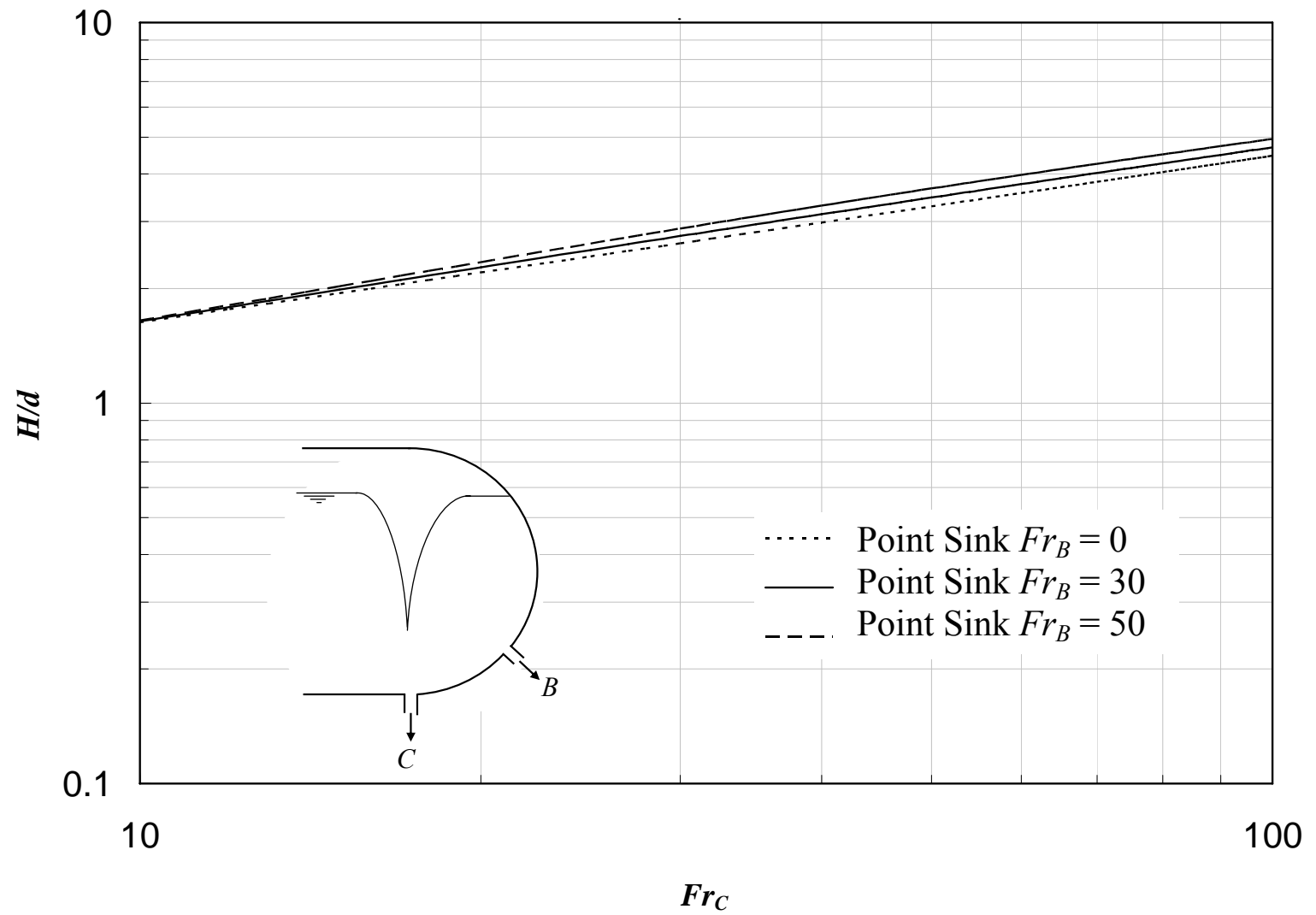
Figure 7.13 The effect of increasing the secondary discharge at branch *B* on the OGE critical height at branch *C*.
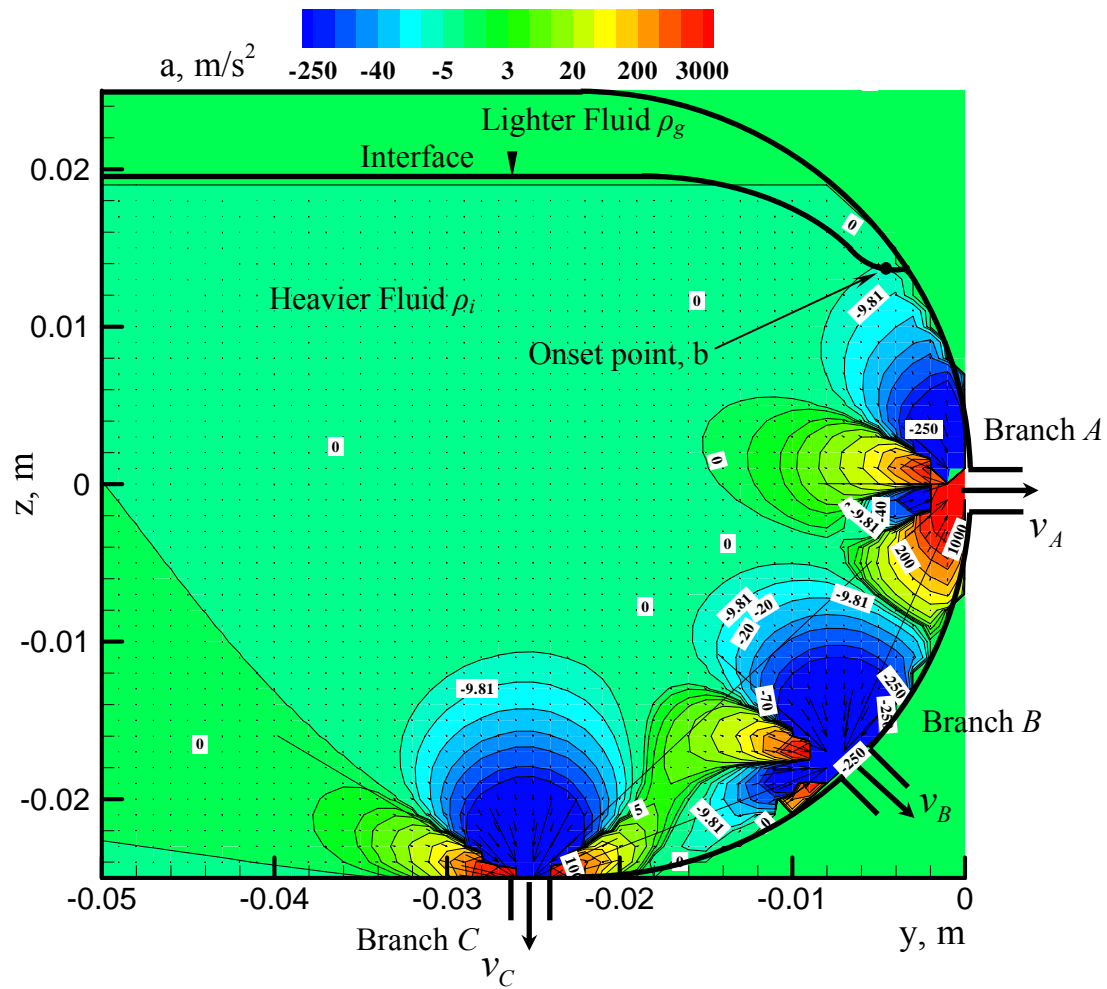
Figure 7.14 Flow field velocity and vertical acceleration contours for triple discharge and single onset at branch *A*.
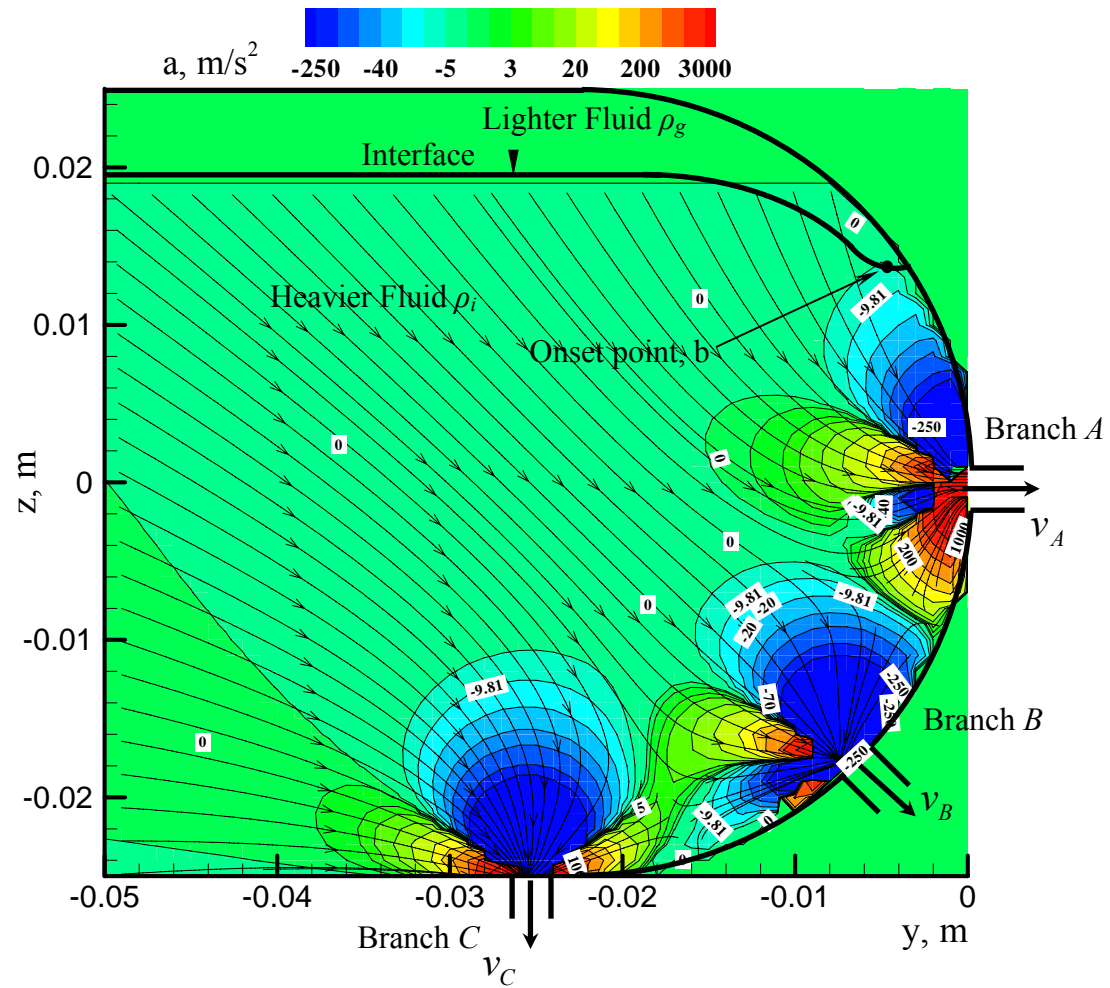
Figure 7.15 Flow field streamlines and vertical acceleration contours for dual discharge and single onset at branch A.
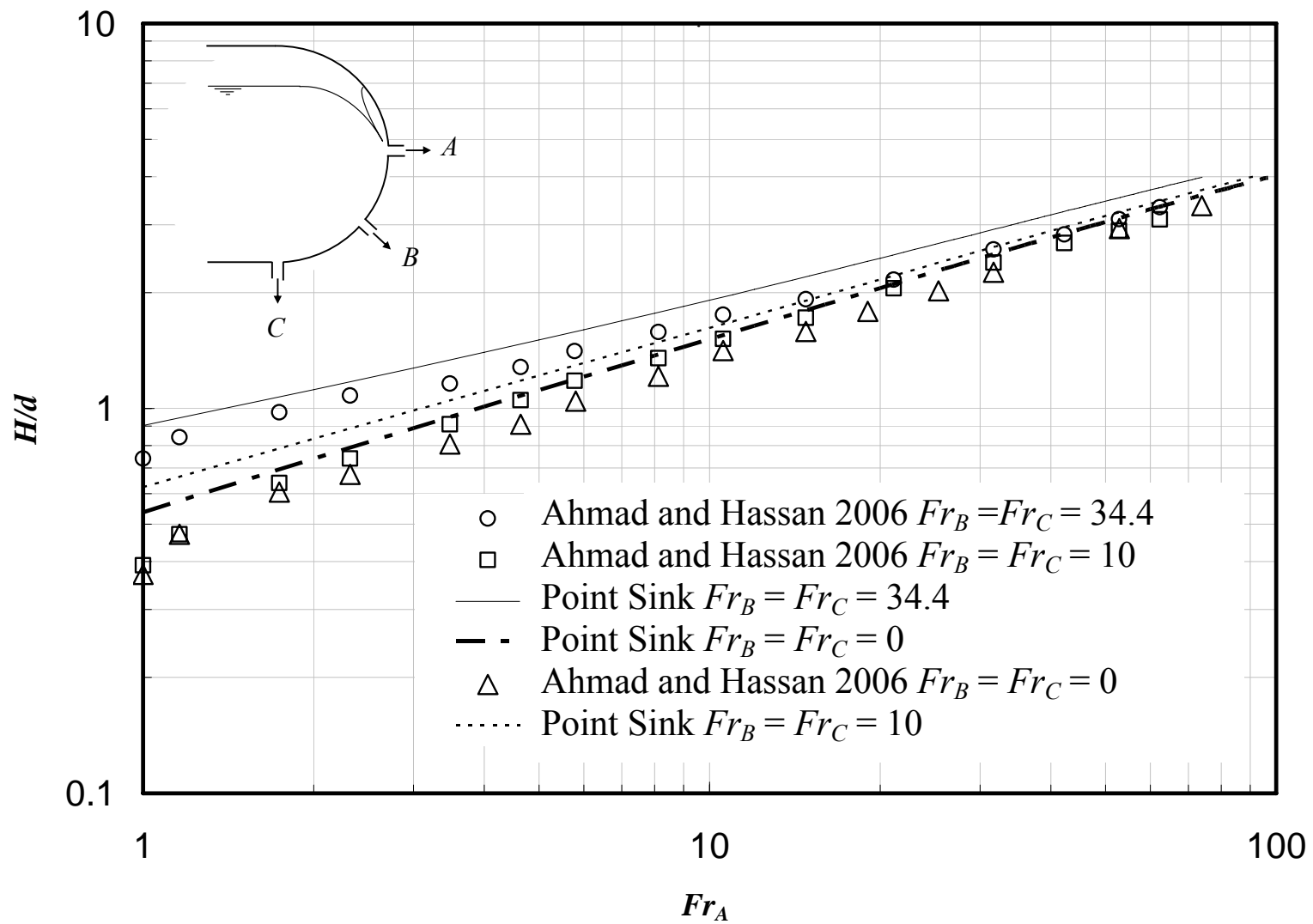
Figure 7.16 Comparisons between predicted and experimental results at different values of Fr_C and Fr_B.
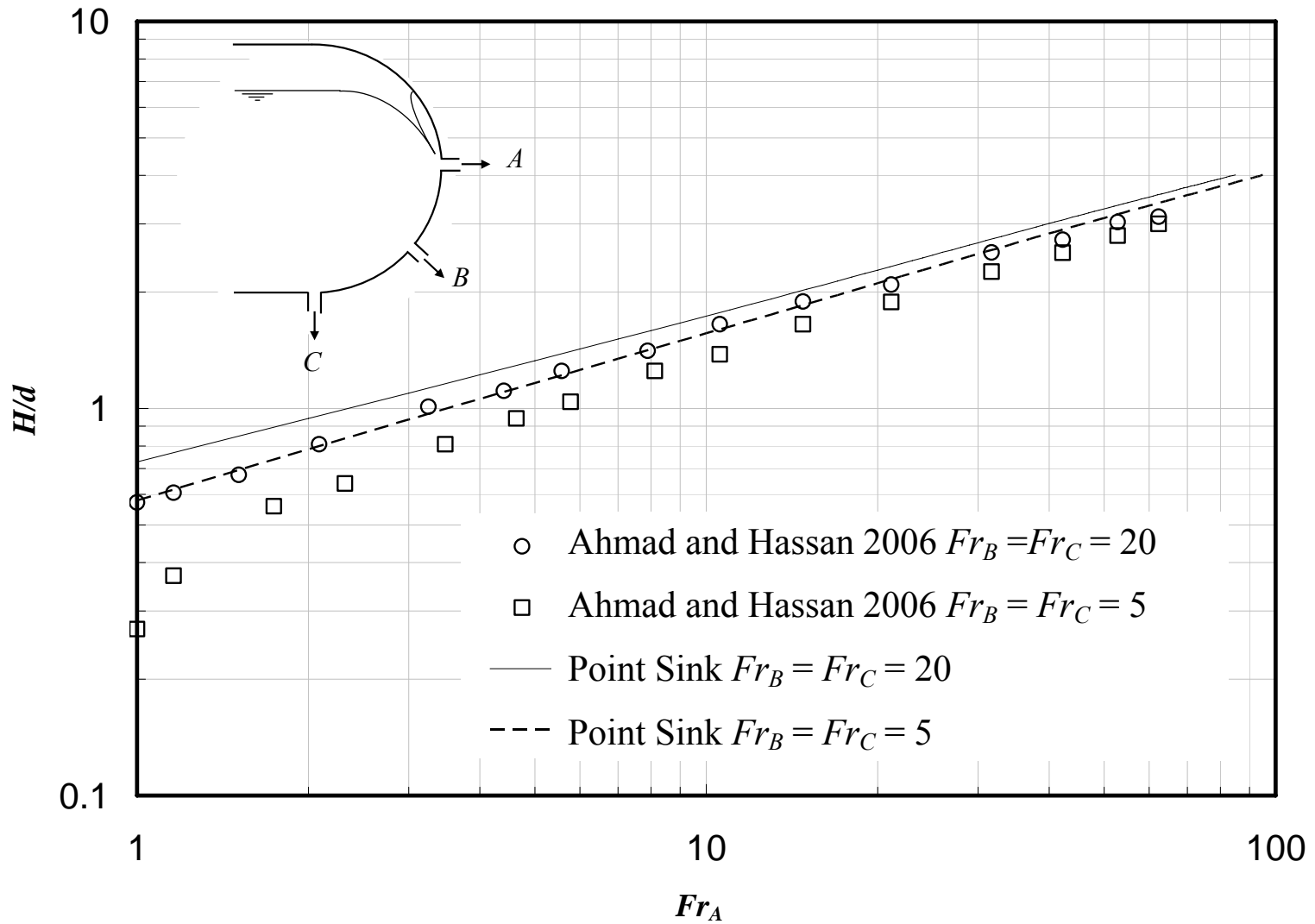
Figure 7.17 Comparisons between predicted and experimental results at different values of Fr_C and Fr_B.
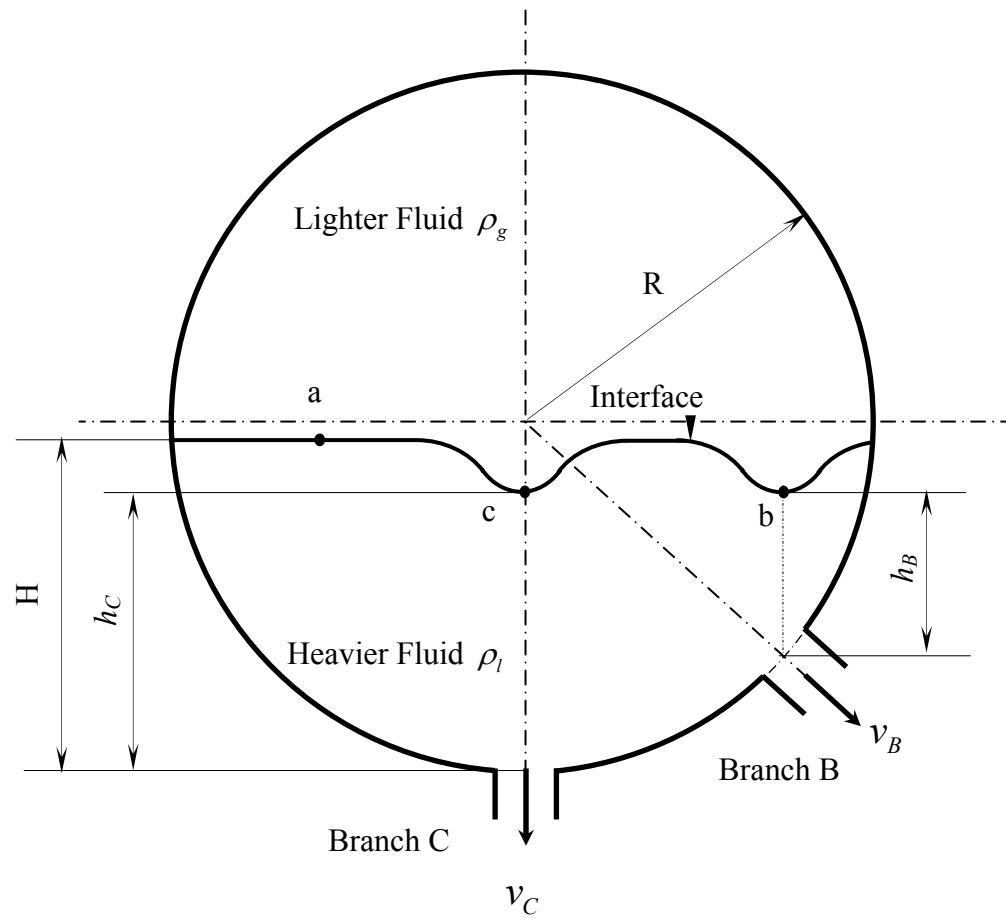
Figure 7.18 Schematic sketch for the OGE criterion at branches *B* and *C* simultaneously.
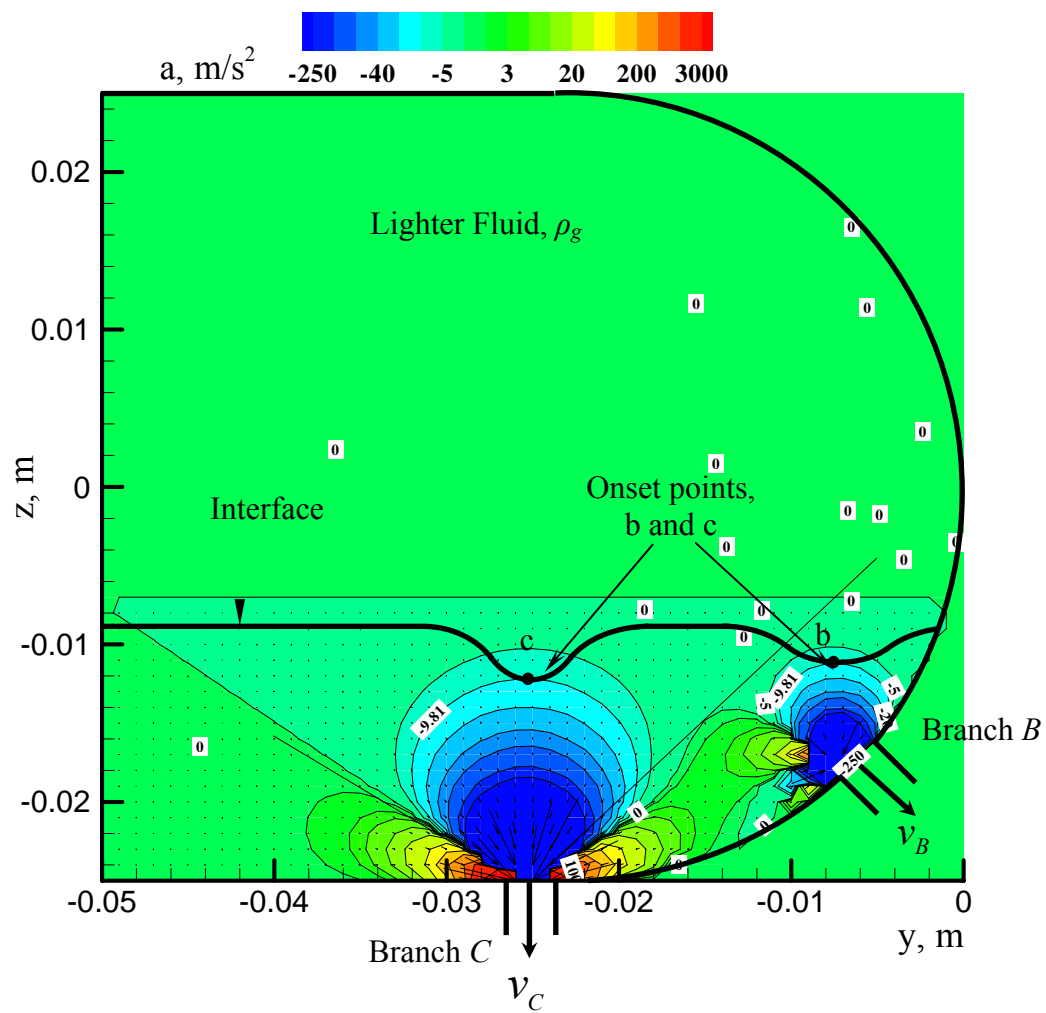
Figure 7.19 Flow field velocity and vertical acceleration contours for dual discharge and dual onset in branches *B* and *C*.
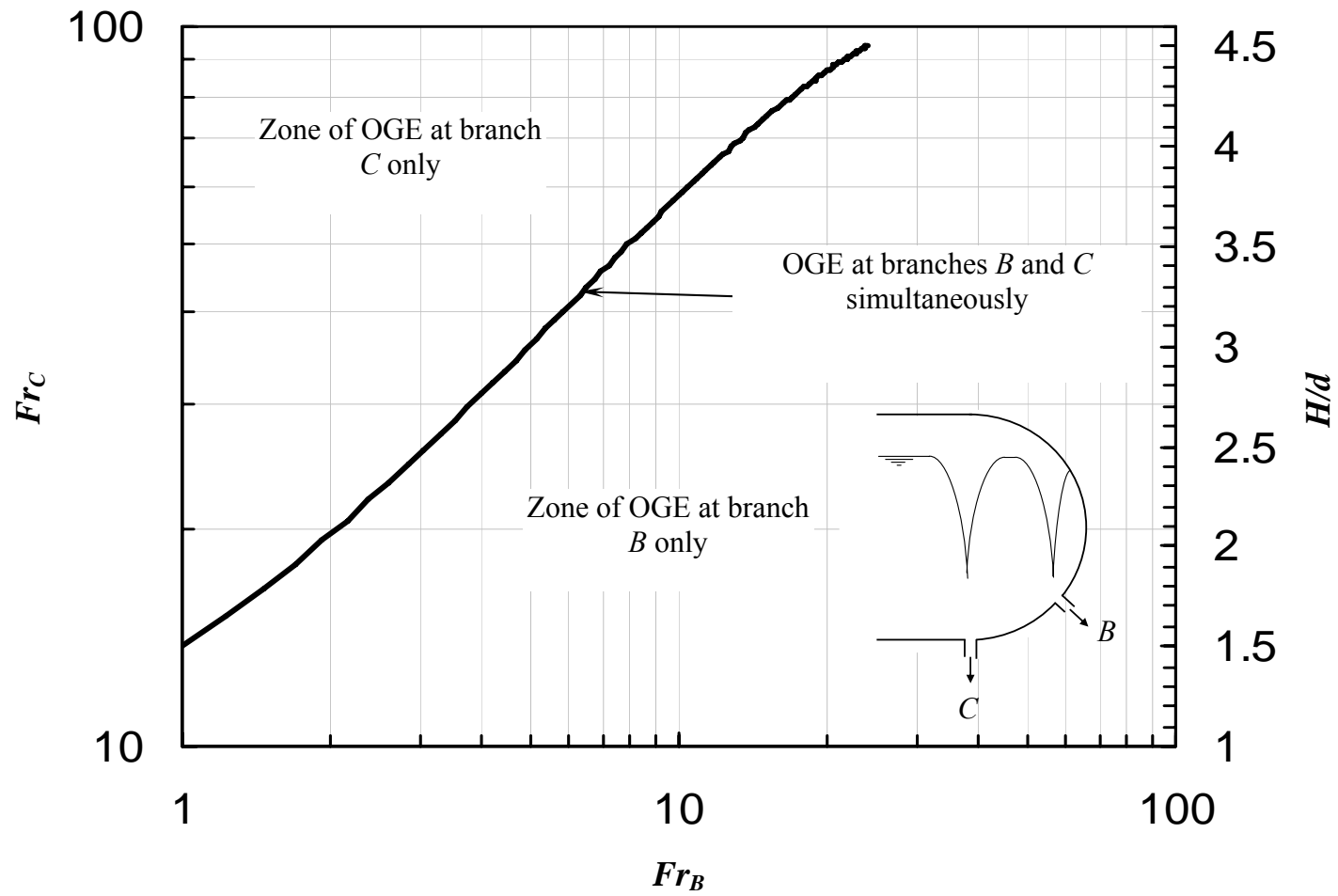
Figure 7.20 OGE critical height at which OGE phenomena are achieved at branches *B* and *C* simultaneously.

Chapter 8

Conclusions and Future Directions

8.1 Conclusions

Extensive experimental data are reported on the flow structure at the onset of entrainment from a large stratified region through header-channel junctions. Three groups of data were generated by using a stereoscopic PIV technique, each group corresponds to a particular branch configuration. The first group contains the data for a single discharge flow, at three values of Froude number (31.69, 10.56, and 3.48) and at different branch orientations, of 0, 45 and 90 degrees from the horizontal. The velocity vector field, and the vorticity field at the onset of gas entrainment were generated. The flow fields verified the existence of vortices with horizontal axes. These vortical structures are responsible for the negative and positive vertical velocities observed within the same planes, in addition to the branch overflow. The PIV technique was successful in determining the two-phase flow field, yet a high degree of error was found in the region close to the branch inlet. The number of image planes used, the resolution of the image planes, and consequently the number of vectors used to calculate the flow rate contributed to the PIV error. However, the measured PIV data provided a full description of the flow field in the onset flow domain. The generated data was used in developing semi-empirical correlations for the onset of gas entrainment, and in the validation of the developed analytical models.

The second and third groups contain the experimental data for dual and triple discharges, respectively. Dimensions of the branches and orientation were selected to be in direct proportion to the CANDU header-feeder system. Six data sets were collected in the second and third groups covering the dual discharge cases *A* and *B*, and *A* and *C* and triple discharge cases *A*, *B*, and *C* with two different Froude numbers in branch *A* at different investigated planes. The velocity vector field, the vorticity field, and the average flow field velocities along the radius *r*, were generated. Comparisons between single, dual and triple discharge cases, according to average velocities in the same planes, and for two different Froude numbers in branch *A*, were investigated. The flow field showed similar trends as the point sink-model developed in the second part of the thesis, however satellite vortices created above the bottom branch were observed. The PIV results quantified well the effects of the secondary branch(s) on the flow field at the onset of entrainment in the upper branch, for different operating conditions.

To the best of knowledge of the author, there is no information currently exists (experimentally or analytically) on the flow field structure at branch-header junctions, and so the information is completely lacking in the literature. It is the first time such data is reported. A hybrid model, based on the generated experimental data and the potential flow theory, for the onset of gas entrainment in a single downward discharge was developed. The branch was modeled as a point-sink and Kelvin-Laplace's equation was used to incorporate surface tension effects. The predicted critical height demonstrated good agreement with experimental data and the three-dimensional points-sink model, while poor agreement was found with the two-dimensional finite-branch approach. The inclusion of surface tension improved the model's ability to predict the critical height,

particularly at discharge Froude numbers below one. The theoretical analysis was extended to predict the critical height at the onset of gas entrainment (OGE) during dual and triple discharges from a stratified two-phase region through discharge branches mounted on a curved wall. A point-sink model was developed to predict the critical height and to map the velocities and acceleration flow fields during OGE. The model was validated with present and available experimental data in literature. The theoretically predicted critical height was found to be a function of mass flow rate through the branches, and the position of the secondary branch (maintaining liquid phase flow only) with respect to the primary branch position (at which OGE occurs) and the angle between the branches. The effects of these variables on the predicted OGE height were investigated in detail. A simultaneous OGE in two branches, B and C, was investigated for the first time. The acceleration flow field demonstrated the correct OGE modeling assumptions, when and where the gravitational acceleration, the beginning of onset, is achieved.

The present analysis applies to any two immiscible fluids with the term "gas entrainment" referring to the appearance of the lighter fluid through the upper branch. The present work will provide, in the short and long terms, a benchmark data for two-phase modeling and validation that would ultimately lead to the proper design of two-phase headers with multiple branches.

8.2 Future Directions

The future work could be classified into three directions: improving the PIV measurements, performing additional experiments to investigate the flow field from the onset of gas entrainment to the onset of liquid entrainment in a branch, and extending the

251

present two-dimensional analysis to the three dimensional domains; following are the details. The recommended improvements to the PIV measurements can be summarized as: 1- The position of the two cameras can be changed to look at the flow field from below. In this case, the curved air-water interface which could distort the field of view will be avoided, and the air cone effects will be diminished during investigation at the lower planes. 2- The test section could be extended on the two sides to eliminate, or at least reduce the wake effect, and to be closer to the header-feeder prototype. 3- The test section could be manufactured with different sizes to investigate the scaling effects. A smaller calibration target could be used to capture the turbulent intensity inside the flow field in order to obtain more details about the flow characteristic. 4- The investigated planes could be captured by PIV within three stages. Each stage should have its own temporal calibration. This will reduce the out of plane vectors and improve the dynamic range within the investigated part of the plane.

Experiments should be continued to investigate the flow structure at two-phase discharge from one or more branches, i.e., from the onset of gas entrainment at the upper branch to the onset of liquid entrainment at the lower branch(s), under the conditions of equal hydraulic resistance for the branches and equal pressure drop across the branches. Developing empirical relations or models for the generated flow details is highly desirable. Finally, the theoretical analysis could be extended to improve the numerical predictions at low Froude number conditions. A three-dimensional finite branch model could be adapted, since it is more sensitive to the branch size and the flow field boundary. Two-phase modeling between two onsets of entrainment at a branch should be initiated;

to the best knowledge of the author, only few attempts are reported in literature, and extensive work is needed in this area of modeling.

References

Adrian, R.J, "Twenty Years of Particle Image Velocimetry", Experiments in Fluids, 39, 159-169, 2005.

Ahmad, T., Hassan, I., "Experimental Investigation on the Onset of Gas Entrainment from a Stratified Two-Phase Region through Multiple Branches Mounted on a Curved Surface", Journal of Fluids Engineering, ASME, v128, pp. 726 − 733, 2006.

Ahmed, M., Hassan, I., Esmail, N., "Modeling the Onset of Gas Entrainment through a Finite-Side Branch", Journal of Fluids Engineering, ASME, v125, pp. 902-909, 2003.

Ahmed, M., Hassan, I.G., Esmail, N., "The Onset of Gas Pull-through During Dual Discharge from a Stratified Two-Phase Region: Theoretical Analysis", Journal Physics of Fluids, v16, pp. 3385-3392, 2004.

Ahmed, M., "Theoretical Analysis of the Onset of Gas Entrainment from a Stratified Two-Phase Region through Two Side-Oriented Branches Mounted on a Vertical Wall" Journal of Fluids Engineering, ASME, v128, pp. 131-141, 2006.

Ahmed, M., "Influence of Wall Inclination Angles on the Onset of Gas Entrainment During Single and Dual Discharges from a Reservoir" Journal of Fluids Engineering, ASME, v 130, pp. 1-16, 2008.

Andaleeb, A.F., Hassan, I., Saleh, W., Ahmad, T., "Modeling the Onset of Gas Entrainment From a Stratified Two-Phase Region Through Branches on a Curved Surface", Journal of Fluids Engineering, ASME, v128, pp. 717 – 725, 2006.

Banerjee, S., Nieman, Re., "Fundamental Studies on Heavy Water Reactor Thermal Hydraulics" Heat Transfer in Nuclear Reactor Safety, pp. 49-86, 1982.

Bowden, R.C., Hassan, I.G., "Flow Field Characterization at the Onset of Gas Entrainment in a Single Downward Discharge using Particle Image Velocimetry", Journal of Fluids Engineering, ASME, v129, pp. 1565 – 1576, 2007.

Bowden, R.C., Hassan, I.G., "Incipience of Liquid Entrainment from a Stratified Gas-Liquid Region in Multiple Discharging Branches", Journal of Fluids Engineering, ASME, v130, pp. 011301-1 – 011301-10, 2008.

Flow Manager Software and Introduction to PIV Instrumentation, 2000.

Graftieaux L., Michard M., and Grosjean N., "Combining PIV, POD and Vortex Identification Algorithms for the Study of Unsteady Turbulent Swirling Flows", Measurements Science and Technology, v12, pp. 1422-1429, 2001.

Hassan, I.G., Soliman, H.M., Sims, G.E., Kowalski, J.E., "Experimental Investigation of the Two-phase Discharge from a Stratified Region through Two Side Branches Oriented Vertically", Experimental Thermal and Fluid Science, v13, pp. 117-128, 1996a.

Hassan, I.G., Soliman, H.M., Sims, G.E., Kowalski, J.E., "Discharge from a Smooth Stratified Two-Phase Region through Two Horizontal Side Branches Located in the Same Vertical Plane", International Journal of Multiphase Flow, v 22, , pp. 1123-1142, 1996b.

Hassan, I.G., Soliman, H.M., Sims, G.E. Kowalski, J.E., "Single and Multiple Discharge from a Stratified Two-Phase Region through Small Branches", Nuclear Engineering and Design, v176, pp. 233-245, 1997.

Hassan, I.G., Soliman, H.M., Sims, G.E., Kowalski, J.E., "Two-Phase Flow from a Stratified Region through a Small Side Branch", Journal of Fluids Engineering, v120, pp. 605 – 612, 1998.

Hassan, Y.A., Ortiz-Villafuerte, J., Schmidl, W.D., "Three-Dimensional Measurements of Single Bubble Dynamics in a Small Diameter Pipe using Stereoscopic Particle Image Velocimetry", International Journal of Multiphase Flow, v27, pp. 817-842, 2001.

Honkanen, M., Saarenrinne, P., "Turbulent Bubbly Flow Measurements in a Mixing Vessel with PIV", 11th International Symposium Application of Laser Techniques to Fluid Mechanics Lisbon, Portugal, July 8 -11, 2002.

Kowalski, J.E. and Krishnan, V.S., "Two-Phase Flow Distribution in a Large Manifold", AIChE Annual Meeting, New York, USA, November 15-20, 1987.

Maciaszek, T., Micaelli, J.C., "CATHARE Phase Separation Modeling for Small Breaks in Horizontal Pipes with Stratified Flow", Nuclear Engineering and Design, v124, pp. 247-256, 1990.

Maier, M.R., Soliman, H.M., Sims, G.E., "Onsets of Entrainment During Dual Discharge from a Stratified Two-Phase Region through Horizontal Branches with Centerlines Falling in an Inclined Plane: Part 1 – Analysis of Liquid Entrainment", International Journal of Multiphase Flow, v 27, pp. 1011-1028, 2001.

Maier, M.R., Soliman, H.M., Sims, G.E., "Onsets of Entrainment During Dual Discharge from a Stratified Two-Phase Region through Horizontal Branches with Centerlines Falling in an Inclined Plane: Part 2 – Experiments on Gas and Liquid Entrainment", International Journal of Multiphase Flow, v27, pp. 1029-1049, 2001.

Majumdar, P., Lele, H. G., and Gupta, S. K., "Modeling the Effect of Vapour Pull through and Entrainment in the Simulationof Stratified Header in Pressurized Heavy Water Reactors", 7th International Conference on Nuclear Engineering, Tokyo, Japan, April 19, 1999.

Michard, J., Graftieux, L., Lollini, N., and Grosjean, N., "Identification of Vortical Structures by a Non Local Criterion: Application to PIV Measurements and DNS-LES Results of Turbulent Rotating Flows" 11th Symposium Turbulent Shear Flows, Grenoble, France, pp. 278 -290, 1997.

Noguchi, T., Yukimoto, S., Kimura, R., Niino, H., "Structure and Instability of a Sink Vortex", Proceedings of PSFVIP-4, Chamonix, France, June 3-5, 2003.

Parrott, S. D., Soliman, H. M., Sims, G. E., and Krishnan, V.S., "Experiments on the Onset of Gas Pull-through During Dual Discharge from a Reservoir", International Journal of Multiphase Flow, v17, pp. 119-129, 1991.

Prasad, A.K., "Stereoscopic Particle Image Velocimetry", Experiments in Fluids, v29, pp. 103-116, 2000.

Raffel, M., Willert, C., Kompenhans, J., "Particle Image Velocimetry: A Practical Guide", 3rd Edition, Springer-Verlag, New York, USA, 1998.

Reimann, J., Khan, M.,"Flow through a Small Break at the Bottom of a Large Pipe with Stratified Flow", Nuclear Science and Engineering, v88, pp. 297-310, 1984.

Schrock, V.E., Revankar, S.T., Mannheimer, R., Wang, C.H., and Jia, D., "Steam-Water Critical Flow through Small Pipes from Stratified Upstream Regions", In Proceedings of the 8th International Heat Transfer Conference, v5, San Francisco, CA, pp. 2307-2311, 1986.

Singh, P.K., "Scale Model Experiments and Numerical Study on a Steel Teeming Process", M.Sc. Thesis, University of Kentucky, Kentucky, USA, 2004.

Smith, M. G., "Introduction to the Theory of Partial Differential Equations", London, Princeton, New Jersey, Van Nostrand, pp. 74-77, 1967.

Smoglie, C., Reimann, J., "Two-phase Flow through Small Branches in a Horizontal Pipe with Stratified Flow", International Journal of Multiphase Flow, v12, pp. 609-625, 1986.

Smoglie, C., Reimann, J., and Muller, U., "Two-Phase Flow through Small breaks in a Horizontal Pipe with Stratified Flow", Nuclear Engineering and Design, v 99, pp. 117-130, 1987.

Taylor, G.I., "The Instability of Liquid Surfaces when Accelerated in a Direction Perpendicular to the Planes", Proceedings of the Royal Society of London. Series A, Mathematical and Physical Sciences, v201, Issue 1065, pp. 192-196, 1950.

White, F.M., "Viscous Fluid Flow", McGraw-Hill, New York, USA, 1991.

Willert, C.E., Gharib, M., "Digital Particle Image Velocimetry", Experiments in Fluids, v10, pp. 181-193, 1991.

Yonomoto, T., Tasaka, K., "New Theoretical Model for Two-Phase Flow Discharged from Stratified Two-Phase Region through Small Break", Journal of Nuclear Science and Technology, v 25, pp. 441-455, 1988.

Yonomoto, T., Tasaka, K., "Liquid and Gas Entrainment to a Small Break Hole from a Stratified Two-Phase Region", International Journal of Multiphase Flow, v17, pp. 745-765, 1991.

Zhang, Z., Hugo, R.J., "Stereo Particle Image Velocimetry Applied to a Vortex Pipe Flow", Experiments in Fluids, v40,pp. 333 – 346, 2006.

Zuber, N., "Problems in Modeling of Small Break LOCA", Nuclear Regulatory Commission Report, NUREG-0724, 1980.

Appendix A

Flow Fields Structure from PIV Experimental Data

The data shown in the following tables are the three velocity components measured by PIV technique for the points located at vertical planes passing through the three branches centers (x = 0.0 mm). The point's height is measured from the bottom branch entrance in all cases (z direction). The z axis passes through the branch center where OGE occurs – either branch A, B, or C. The y coordinate is always measured from the z axis in all cases.
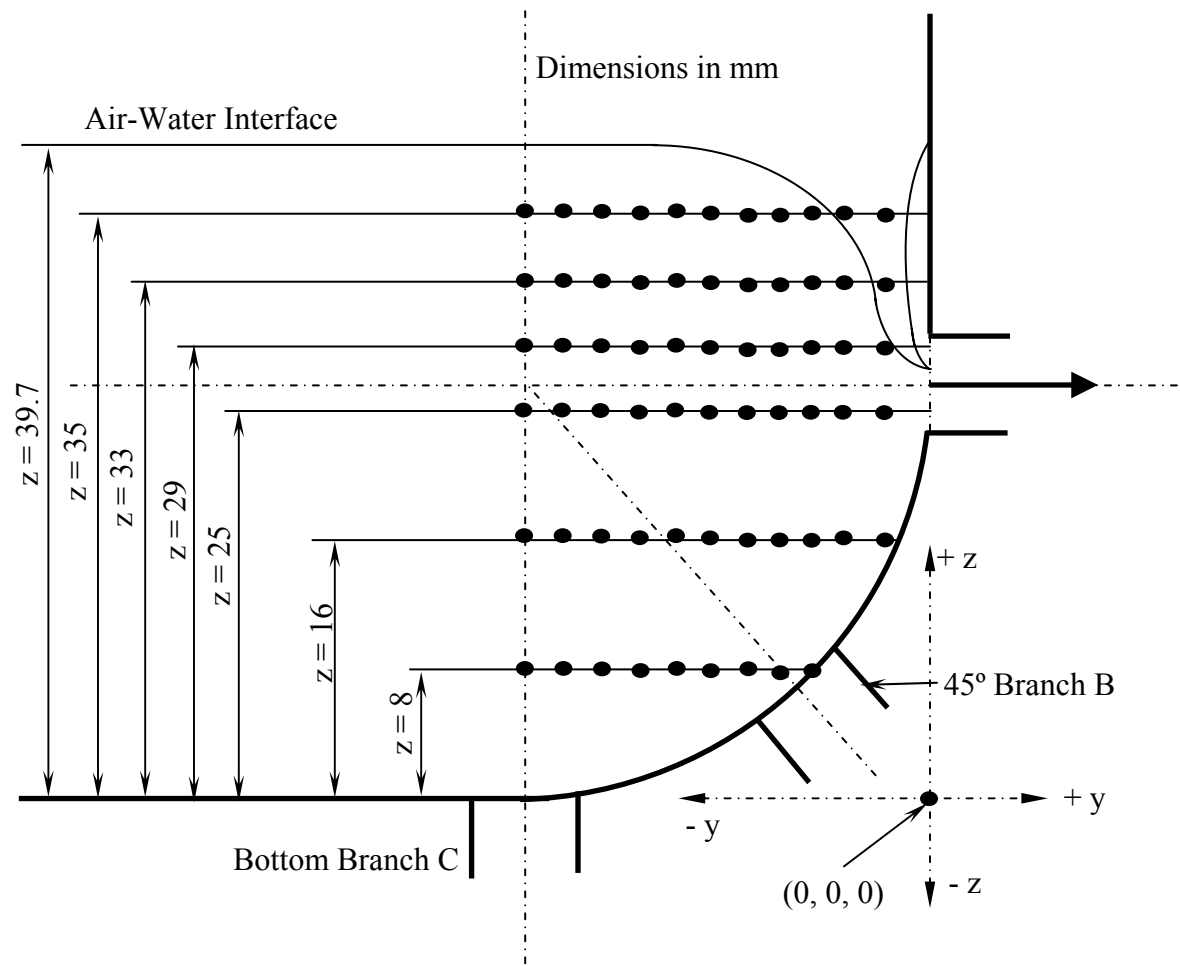
Figure A.1 Sketch for the locations of the data shown in the next table (case 1).

A.1 Single Discharge

A.1.1 Side Branch, *A*

Table A-1 Single discharge in side branch, *A*, Fr_A =31.69 and H_{OGE} = 39.7 mm (case 1).

y, mm	x = 0.0 mm, z = 8.0 mm			x = 0.0 mm, z = 16.0 mm			x = 0.0 mm, z = 25.0 mm		
	U, m/s	V, m/s	W, m/s	U, m/s	V, m/s	W, m/s	U, m/s	V, m/s	W, m/s
-24.9	0.001	0.045	0.031	0.004	0.102	0.035	-0.009	0.102	0.023
-23.7	0.002	0.050	0.038	0.005	0.110	0.040	-0.009	0.111	0.025
-22.4	0.002	0.054	0.044	0.006	0.120	0.047	-0.010	0.121	0.028
-21.2	0.003	0.059	0.048	0.007	0.130	0.055	-0.010	0.134	0.032
-19.9	0.005	0.063	0.051	0.008	0.143	0.065	-0.010	0.148	0.036
-18.6	0.007	0.064	0.049	0.010	0.157	0.077	-0.010	0.165	0.041
-17.4	0.007	0.062	0.042	0.011	0.171	0.090	-0.010	0.184	0.046
-16.1	0.007	0.055	0.032	0.013	0.180	0.098	-0.009	0.201	0.053
-14.9	0.005	0.039	0.016	0.014	0.173	0.093	-0.008	0.207	0.058
-13.6	0.003	0.020	-0.001	0.013	0.143	0.073	-0.006	0.191	0.061
-12.3	0.002	0.005	-0.017	0.007	0.093	0.044	-0.003	0.151	0.059
-11.1	0.002	-0.001	-0.027	0.002	0.045	0.021	0.001	0.101	0.055
-9.8	0.002	-0.001	-0.035	-0.001	0.015	0.007	0.002	0.064	0.052
-8.6	0.002	0.000	-0.041	0.000	0.004	0.003	0.001	0.044	0.051
-7.3	0.002	0.001	-0.043	-0.001	0.002	0.001	0.000	0.034	0.049
-6.0	0.000	0.000	0.000	-0.001	0.002	0.000	0.001	0.024	0.039
-4.8	0.000	0.000	0.000	0.000	0.001	-0.001	0.001	0.013	0.023
-3.5	0.000	0.000	0.000	0.000	0.001	-0.001	0.000	0.004	0.010
-2.3	0.000	0.000	0.000	0.000	0.000	0.000	-0.001	-0.001	0.004
-1.0	0.000	0.000	0.000	0.000	0.000	0.000	-0.001	-0.002	0.003

y, mm	x = 0.0 mm, z = 29.0 mm			x = 0.0 mm, z = 33.0 mm			x = 0.0 mm, z = 35.0 mm		
	U, m/s	V, m/s	W, m/s	U, m/s	V, m/s	W, m/s	U, m/s	V, m/s	W, m/s
-24.9	0.008	0.102	0.011	0.008	0.096	0.008	0.005	0.115	0.001
-23.7	0.008	0.110	0.011	0.009	0.100	0.008	0.006	0.123	-0.001
-22.4	0.009	0.119	0.011	0.010	0.104	0.007	0.006	0.132	-0.004
-21.2	0.010	0.128	0.011	0.010	0.107	0.007	0.008	0.142	-0.009
-19.9	0.011	0.137	0.011	0.011	0.111	0.005	0.010	0.154	-0.016
-18.6	0.011	0.146	0.009	0.010	0.115	0.003	0.013	0.167	-0.023
-17.4	0.011	0.151	0.011	0.010	0.118	0.000	0.015	0.179	-0.028
-16.1	0.013	0.157	0.013	0.012	0.118	-0.002	0.014	0.189	-0.035
-14.9	0.014	0.159	0.016	0.013	0.115	-0.005	0.010	0.195	-0.045
-13.6	0.013	0.161	0.019	0.015	0.109	-0.004	0.007	0.195	-0.062
-12.3	0.012	0.153	0.026	0.012	0.102	-0.003	0.007	0.182	-0.073
-11.1	0.015	0.132	0.032	0.012	0.091	0.001	0.015	0.158	-0.088
-9.8	0.017	0.103	0.038	0.011	0.082	0.000	0.023	0.127	-0.097
-8.6	0.017	0.080	0.039	0.017	0.075	0.001	0.020	0.102	-0.101
-7.3	0.012	0.069	0.032	0.023	0.071	-0.005	0.011	0.076	-0.085
-6.0	0.012	0.059	0.001	0.026	0.068	-0.026	0.001	0.051	-0.059
-4.8	0.007	0.037	-0.027	0.025	0.056	-0.040	0.002	0.026	-0.029
-3.5	0.001	0.011	-0.048	0.017	0.035	-0.035	-0.001	0.008	-0.007
-2.3	-0.007	-0.013	-0.057	0.009	0.014	-0.015	-0.005	-0.002	0.007
-1.0	-0.004	-0.018	-0.048	0.005	0.004	0.000	-0.004	-0.005	0.015

Table A-2 Single discharge in side branch, A, Fr_A =31.69 and H_{OGE} = 39.7 mm (case 1r).

y, mm	x = 0.0 mm, z = 4.0 mm			x = 0.0 mm, z = 8.0 mm			x = 0.0 mm, z = 12.0 mm		
	U, m/s	V, m/s	W, m/s	U, m/s	V, m/s	W, m/s	U, m/s	V, m/s	W, m/s
-25.9	0.008	0.020	0.014	0.019	0.036	0.022	-0.012	0.075	0.048
-24.7	0.006	0.017	0.012	0.015	0.043	0.026	-0.013	0.082	0.061
-23.5	0.003	0.013	0.008	0.010	0.044	0.031	-0.012	0.084	0.076
-22.3	0.001	0.013	0.006	0.008	0.045	0.036	-0.006	0.086	0.082
-21.1	0.001	0.015	0.003	0.009	0.046	0.045	-0.003	0.087	0.087
-19.9	0.001	0.016	0.000	0.005	0.050	0.044	0.003	0.088	0.094
-18.7	0.001	0.015	-0.003	0.001	0.050	0.046	0.006	0.078	0.090
-17.5	0.002	0.011	-0.005	-0.002	0.043	0.037	0.008	0.068	0.080
-16.3	0.001	0.005	-0.003	-0.002	0.029	0.022	0.008	0.066	0.085
-15.1	0.000	0.001	-0.001	-0.002	0.016	0.008	0.010	0.074	0.111
-13.8	0.000	0.000	0.001	-0.001	0.011	0.007	0.017	0.079	0.134
-12.6	0.000	0.000	0.001	-0.001	0.010	0.007	0.014	0.068	0.093
-11.4	0.000	0.000	0.000	0.000	0.006	0.004	0.012	0.053	0.038
-10.2	0.000	0.000	0.000	0.000	0.002	-0.001	0.005	0.038	0.000
-9.0	0.000	0.000	0.000	-0.001	0.001	-0.003	0.003	0.022	0.002
-7.8	0.000	0.000	0.000	0.000	0.000	0.000	0.001	0.008	0.008
-6.6	0.000	0.000	0.000	0.000	0.000	0.000	0.001	0.003	0.005
-5.4	0.000	0.000	0.000	0.000	0.000	0.000	0.001	0.003	0.002
-4.2	0.000	0.000	0.000	0.000	0.000	0.000	0.000	0.000	0.000
-3.0	0.000	0.000	0.000	0.000	0.000	0.000	0.000	0.000	0.000
-1.8	0.000	0.000	0.000	0.000	0.000	0.000	0.000	0.000	0.000

y, mm	x = 0.0 mm, z = 16.0 mm			x = 0.0 mm, z = 20.0 mm			x = 0.0 mm, z = 24.0 mm		
	U, m/s	V, m/s	W, m/s	U, m/s	V, m/s	W, m/s	U, m/s	V, m/s	W, m/s
-25.9	0.012	0.084	0.042	-0.001	0.102	0.038	-0.007	0.109	0.027
-24.7	0.013	0.088	0.052	0.002	0.108	0.046	-0.004	0.118	0.029
-23.5	0.013	0.090	0.066	0.005	0.114	0.053	-0.004	0.129	0.032
-22.3	0.010	0.092	0.070	0.010	0.123	0.058	-0.006	0.140	0.040
-21.1	0.003	0.096	0.073	0.012	0.135	0.059	-0.008	0.153	0.049
-19.9	-0.006	0.102	0.083	0.012	0.144	0.057	-0.007	0.164	0.050
-18.7	-0.017	0.106	0.098	0.009	0.150	0.053	0.001	0.178	0.052
-17.5	-0.024	0.113	0.117	0.009	0.152	0.060	0.012	0.198	0.065
-16.3	-0.028	0.116	0.129	0.009	0.153	0.082	0.021	0.219	0.079
-15.1	-0.027	0.119	0.146	0.011	0.152	0.124	0.024	0.229	0.081
-13.8	-0.026	0.117	0.166	0.013	0.144	0.156	0.019	0.222	0.080
-12.6	-0.022	0.111	0.184	0.012	0.121	0.153	0.004	0.197	0.078
-11.4	-0.016	0.096	0.178	0.011	0.092	0.109	-0.009	0.150	0.067
-10.2	-0.009	0.077	0.125	0.010	0.060	0.044	-0.015	0.091	0.022
-9.0	-0.010	0.058	0.073	0.009	0.039	-0.001	-0.014	0.046	-0.004
-7.8	-0.009	0.035	0.027	0.005	0.022	-0.014	-0.011	0.025	-0.009
-6.6	-0.010	0.020	0.013	0.001	0.015	-0.005	-0.008	0.019	0.006
-5.4	-0.002	0.012	-0.002	0.000	0.008	0.000	-0.002	0.013	0.005
-4.2	0.001	0.014	0.001	-0.002	0.005	0.004	0.000	0.007	0.000
-3.0	0.002	0.009	0.002	-0.004	0.002	0.011	0.002	0.003	-0.007
-1.8	0.000	0.000	0.000	-0.002	0.003	0.022	0.006	0.004	-0.003

y, mm	x = 0.0 mm, z = 28.0 mm			x = 0.0 mm, z = 32.0 mm			x = 0.0 mm, z = 36.0 mm		
	U, m/s	V, m/s	W, m/s	U, m/s	V, m/s	W, m/s	U, m/s	V, m/s	W, m/s
-25.9	-0.005	0.111	0.021	-0.004	0.116	-0.008	-0.014	0.115	-0.009
-24.7	-0.007	0.119	0.024	-0.005	0.121	-0.014	-0.014	0.124	-0.006
-23.5	-0.010	0.128	0.028	-0.007	0.129	-0.013	-0.014	0.130	-0.003
-22.3	-0.012	0.140	0.035	-0.012	0.141	-0.004	-0.018	0.138	-0.005
-21.1	-0.016	0.155	0.044	-0.020	0.155	0.012	-0.026	0.149	-0.020
-19.9	-0.018	0.173	0.058	-0.029	0.171	0.019	-0.031	0.159	-0.034
-18.7	-0.019	0.188	0.068	-0.039	0.192	0.017	-0.031	0.170	-0.036
-17.5	-0.029	0.200	0.070	-0.049	0.222	0.020	-0.033	0.178	-0.028
-16.3	-0.045	0.212	0.080	-0.058	0.245	0.025	-0.037	0.188	-0.041
-15.1	-0.054	0.226	0.109	-0.064	0.264	0.037	-0.043	0.195	-0.081
-13.8	-0.055	0.225	0.119	-0.071	0.270	0.011	-0.052	0.202	-0.136
-12.6	-0.051	0.204	0.100	-0.079	0.265	-0.033	-0.067	0.196	-0.182
-11.4	-0.046	0.158	0.065	-0.097	0.230	-0.074	-0.076	0.180	-0.185
-10.2	-0.028	0.111	0.031	-0.116	0.160	-0.067	-0.079	0.140	-0.146
-9.0	-0.004	0.070	0.007	-0.112	0.097	-0.055	-0.074	0.101	-0.103
-7.8	0.009	0.038	-0.009	-0.078	0.057	-0.035	-0.057	0.069	-0.061
-6.6	0.006	0.017	-0.004	-0.037	0.045	-0.014	-0.027	0.054	0.006
-5.4	-0.002	0.005	0.000	-0.014	0.035	0.012	0.003	0.036	0.050
-4.2	-0.009	0.004	-0.009	-0.006	0.027	0.014	0.031	0.026	0.048
-3.0	-0.030	0.007	-0.041	0.003	0.032	0.012	0.046	0.021	-0.011
-1.8	-0.070	0.020	-0.098	0.011	0.045	0.006	0.054	0.019	-0.028

Table A-3 Single discharge in side branch, *A, Fr_A* =10.56 and *H_OGE* = 34.4 mm (case 2).

y, mm	x = 0.0 mm, z = 8.0 mm			x = 0.0 mm, z = 16.0 mm			x = 0.0 mm, z = 25.0 mm		
	U, m/s	V, m/s	W, m/s	U, m/s	V, m/s	W, m/s	U, m/s	V, m/s	W, m/s
-25.4	0.003	0.018	0.007	0.050	0.357	0.133	0.000	0.044	0.009
-24.2	0.004	0.019	0.009	0.059	0.379	0.151	0.000	0.048	0.011
-22.9	0.005	0.021	0.012	0.068	0.405	0.171	0.001	0.052	0.012
-21.6	0.005	0.021	0.013	0.077	0.433	0.192	0.001	0.056	0.014
-20.3	0.006	0.021	0.014	0.089	0.461	0.216	0.002	0.062	0.015
-19.1	0.006	0.022	0.015	0.102	0.492	0.246	0.002	0.068	0.017
-17.8	0.006	0.023	0.016	0.116	0.523	0.278	0.003	0.076	0.020
-16.5	0.005	0.020	0.014	0.130	0.543	0.308	0.004	0.086	0.024
-15.3	0.003	0.014	0.009	0.142	0.527	0.319	0.006	0.098	0.029
-14.0	0.001	0.006	0.005	0.122	0.432	0.267	0.009	0.111	0.035
-12.7	0.001	0.003	0.001	0.074	0.276	0.160	0.011	0.121	0.038
-11.5	0.001	0.002	0.000	0.021	0.119	0.055	0.010	0.117	0.036
-10.2	0.001	0.002	-0.002	0.002	0.032	0.008	0.009	0.088	0.025
-8.9	0.000	0.001	-0.002	-0.001	0.005	0.001	0.006	0.051	0.013
-7.6	0.000	0.000	0.000	-0.001	0.001	-0.002	0.005	0.024	0.006
-6.4	0.000	0.000	0.000	-0.003	-0.002	0.001	0.003	0.013	0.004
-5.1	0.000	0.000	0.000	-0.001	-0.004	0.003	0.001	0.007	0.003
-3.8	0.000	0.000	0.000	-0.001	-0.003	0.003	0.000	0.002	0.001
-2.6	0.000	0.000	0.000	0.000	-0.002	0.003	0.000	0.001	0.000
-1.3	0.000	0.000	0.000	0.000	0.000	0.000	0.001	0.000	0.000

y, mm	x = 0.0 mm, z = 28.0 mm			x = 0.0 mm, z = 32.0 mm		
	U, m/s	V, m/s	W, m/s	U, m/s	V, m/s	W, m/s
-25.4	0.003	0.045	0.008	0.001	0.043	0.002
-24.2	0.003	0.049	0.009	0.001	0.046	0.002
-22.9	0.003	0.053	0.010	0.001	0.049	0.003
-21.6	0.004	0.058	0.011	0.001	0.052	0.003
-20.3	0.004	0.064	0.011	0.002	0.056	0.003
-19.1	0.005	0.072	0.011	0.002	0.060	0.002
-17.8	0.006	0.079	0.012	0.002	0.065	0.002
-16.5	0.007	0.087	0.014	0.003	0.070	0.002
-15.3	0.007	0.094	0.019	0.004	0.075	0.001
-14.0	0.007	0.103	0.026	0.005	0.081	-0.001
-12.7	0.010	0.105	0.025	0.006	0.088	-0.005
-11.5	0.009	0.097	0.019	0.008	0.094	-0.010
-10.2	0.008	0.076	0.004	0.009	0.103	-0.018
-8.9	0.004	0.054	-0.002	0.012	0.114	-0.034
-7.6	0.004	0.039	-0.003	0.017	0.128	-0.058
-6.4	0.003	0.028	0.001	0.018	0.134	-0.109
-5.1	0.002	0.016	0.002	0.020	0.108	-0.142
-3.8	0.000	0.006	0.000	0.015	0.060	-0.130
-2.6	0.000	0.001	0.000	0.012	0.019	-0.075
-1.3	-0.001	0.000	0.000	0.003	0.003	-0.028

Table A-4 Single discharge in side branch, A, Fr_A = 10.56 and H_{OGE} = 34.4 mm (case 2r).

y, mm	x = 0.0 mm, z = 4.0 mm			x = 0.0 mm, z = 8.0 mm			x = 0.0 mm, z = 12.0 mm		
	U, m/s	V, m/s	W, m/s	U, m/s	V, m/s	W, m/s	U, m/s	V, m/s	W, m/s
-25.7	0.004	0.016	0.010	0.002	0.022	0.013	-0.001	0.022	0.009
-24.4	0.004	0.012	0.008	0.001	0.024	0.012	-0.001	0.023	0.011
-23.2	0.002	0.006	0.005	0.000	0.023	0.008	-0.002	0.024	0.013
-22.0	0.002	-0.003	0.004	-0.001	0.022	0.003	-0.002	0.025	0.014
-20.8	0.003	-0.010	0.004	0.001	0.019	0.004	-0.001	0.025	0.013
-19.6	0.004	-0.016	0.002	0.002	0.017	0.011	-0.002	0.024	0.010
-18.4	0.002	-0.017	-0.003	0.001	0.013	0.017	-0.002	0.024	0.012
-17.1	-0.002	-0.014	-0.007	-0.001	0.010	0.017	-0.003	0.023	0.015
-15.9	-0.003	-0.009	-0.007	-0.001	0.006	0.012	-0.002	0.020	0.017
-14.7	-0.002	-0.004	-0.004	0.000	0.003	0.007	-0.002	0.016	0.017
-13.5	0.000	-0.002	-0.001	0.000	0.001	0.003	0.002	0.010	0.017
-12.3	0.000	0.000	0.000	0.000	0.000	0.002	0.008	-0.003	0.019
-11.1	0.000	0.000	0.000	0.001	-0.001	0.000	0.008	-0.015	0.013
-9.8	0.000	0.000	0.000	0.000	0.000	0.000	0.002	-0.018	0.004
-8.6	0.000	0.000	0.000	0.000	0.000	0.000	-0.003	-0.012	-0.004
-7.4	0.000	0.000	0.000	0.000	0.000	0.000	-0.002	-0.005	-0.004
-6.2	0.000	0.000	0.000	0.000	0.000	0.000	0.000	-0.002	0.001
-5.0	0.000	0.000	0.000	0.000	0.000	0.000	0.000	-0.001	0.002
-3.7	0.000	0.000	0.000	0.000	0.000	0.000	0.000	0.000	0.000
-2.5	0.000	0.000	0.000	0.000	0.000	0.000	0.000	0.000	0.000
-1.3	0.000	0.000	0.000	0.000	0.000	0.000	0.000	0.000	0.000

y, mm	x = 0.0 mm, z = 16.0 mm			x = 0.0 mm, z = 20.0 mm			x = 0.0 mm, z = 24.0 mm		
	U, m/s	V, m/s	W, m/s	U, m/s	V, m/s	W, m/s	U, m/s	V, m/s	W, m/s
-25.7	-0.004	0.042	0.028	0.000	0.047	0.019	0.002	0.052	0.012
-24.4	-0.004	0.043	0.031	0.000	0.049	0.021	0.002	0.056	0.009
-23.2	-0.005	0.043	0.031	-0.001	0.052	0.025	0.002	0.059	0.012
-22.0	-0.006	0.043	0.030	-0.002	0.056	0.030	0.002	0.063	0.022
-20.8	-0.008	0.045	0.031	-0.003	0.060	0.036	0.000	0.068	0.036
-19.6	-0.009	0.047	0.035	-0.003	0.065	0.042	0.000	0.076	0.048
-18.4	-0.010	0.050	0.040	-0.002	0.071	0.047	0.002	0.084	0.058
-17.1	-0.008	0.049	0.043	-0.001	0.075	0.050	0.003	0.095	0.063
-15.9	-0.006	0.043	0.045	0.001	0.074	0.054	0.003	0.107	0.071
-14.7	-0.002	0.033	0.043	0.004	0.067	0.059	0.004	0.117	0.080
-13.5	-0.001	0.022	0.035	0.004	0.055	0.060	0.007	0.118	0.082
-12.3	0.001	0.009	0.020	0.002	0.041	0.052	0.011	0.115	0.071
-11.1	0.001	-0.004	0.004	0.002	0.028	0.038	0.018	0.104	0.056
-9.8	0.003	-0.014	-0.011	0.006	0.019	0.026	0.020	0.080	0.040
-8.6	0.003	-0.012	-0.016	0.008	0.012	0.017	0.017	0.040	0.026
-7.4	0.003	-0.008	-0.010	0.004	0.006	0.008	0.009	0.007	0.015
-6.2	0.002	-0.005	-0.001	-0.003	0.002	0.000	0.005	-0.006	0.011
-5.0	0.000	-0.004	0.002	-0.008	0.000	-0.007	0.004	-0.003	0.009
-3.7	0.000	-0.001	0.001	-0.006	0.001	-0.009	0.006	0.000	0.004
-2.5	0.000	0.000	0.000	-0.002	0.000	-0.010	0.005	-0.003	0.011
-1.3	0.000	0.000	0.000	0.003	0.000	-0.009	-0.004	-0.002	0.021

268

y, mm	x = 0.0 mm, z = 28.0 mm			x = 0.0 mm, z = 32.0 mm		
	U, m/s	V, m/s	W, m/s	U, m/s	V, m/s	W, m/s
-25.7	-0.005	0.046	0.003	-0.003	0.044	0.000
-24.4	-0.006	0.051	0.004	-0.004	0.048	0.000
-23.2	-0.006	0.057	0.001	-0.005	0.052	0.000
-22.0	-0.007	0.062	0.002	-0.005	0.057	-0.001
-20.8	-0.005	0.070	0.009	-0.007	0.063	-0.002
-19.6	-0.005	0.079	0.017	-0.007	0.069	-0.001
-18.4	-0.007	0.090	0.022	-0.009	0.077	0.002
-17.1	-0.011	0.103	0.025	-0.010	0.086	0.007
-15.9	-0.013	0.117	0.030	-0.014	0.095	0.005
-14.7	-0.017	0.133	0.035	-0.020	0.101	-0.014
-13.5	-0.024	0.146	0.042	-0.029	0.101	-0.052
-12.3	-0.034	0.157	0.050	-0.036	0.097	-0.097
-11.1	-0.045	0.162	0.053	-0.042	0.094	-0.142
-9.8	-0.054	0.142	0.032	-0.042	0.087	-0.159
-8.6	-0.048	0.096	-0.006	-0.040	0.070	-0.141
-7.4	-0.031	0.042	-0.029	-0.029	0.041	-0.088
-6.2	-0.011	0.008	-0.026	-0.016	0.015	-0.041
-5.0	-0.002	-0.002	-0.008	-0.006	0.001	-0.015
-3.7	-0.014	0.000	0.023	-0.002	-0.002	-0.008
-2.5	-0.054	-0.002	0.110	-0.001	0.000	-0.011
-1.3	-0.121	0.002	0.275	-0.004	0.002	-0.020

Table A-5 Single discharge in side branch, A, $Fr_A = 3.48$ and $H_{OGE} = 30.5$ mm (case 3).

y, mm	x = 0.0 mm, z = 8.0 mm			x = 0.0 mm, z = 16.0 mm		
	U, m/s	V, m/s	W, m/s	U, m/s	V, m/s	W, m/s
-25.2	0.000	0.005	0.001	0.001	0.014	0.004
-23.9	0.000	0.006	0.002	0.001	0.015	0.005
-22.6	0.000	0.006	0.002	0.001	0.016	0.006
-21.3	0.000	0.006	0.002	0.002	0.018	0.007
-20.0	0.000	0.005	0.002	0.002	0.019	0.008
-18.6	0.000	0.005	0.002	0.003	0.020	0.010
-17.3	0.000	0.004	0.002	0.003	0.022	0.011
-16.0	0.000	0.004	0.002	0.004	0.023	0.013
-14.7	0.000	0.002	0.001	0.003	0.022	0.012
-13.4	0.000	0.001	0.000	0.002	0.017	0.009
-12.1	0.000	0.000	0.000	0.001	0.010	0.004
-10.8	0.000	0.000	-0.001	0.000	0.004	0.000
-9.5	0.000	0.000	-0.001	0.000	0.001	0.000
-8.2	0.000	0.000	0.000	0.000	0.000	0.000
-6.8	0.000	0.000	0.000	0.000	0.000	0.000
-5.5	0.000	0.000	0.000	0.000	0.000	0.000
-4.2	0.000	0.000	0.000	0.000	0.000	0.000
-2.9	0.000	0.000	0.000	0.000	0.000	0.000
-1.6	0.000	0.000	0.000	0.000	0.000	0.000
-0.3	0.000	0.000	0.000	0.000	0.000	0.000

y, mm	x = 0.0 mm, z = 25.0 mm			x = 0.0 mm, z = 28.0 mm		
	U, m/s	V, m/s	W, m/s	U, m/s	V, m/s	W, m/s
-25.2	0.000	0.015	0.002	0.003	0.018	0.007
-23.9	0.000	0.016	0.003	0.004	0.019	0.009
-22.6	0.000	0.018	0.003	0.005	0.021	0.012
-21.3	0.001	0.019	0.004	0.005	0.021	0.013
-20.0	0.001	0.021	0.004	0.006	0.021	0.014
-18.6	0.001	0.023	0.005	0.006	0.022	0.015
-17.3	0.001	0.026	0.006	0.006	0.023	0.016
-16.0	0.001	0.029	0.008	0.005	0.020	0.014
-14.7	0.002	0.033	0.009	0.003	0.014	0.009
-13.4	0.002	0.038	0.012	0.001	0.006	0.005
-12.1	0.003	0.044	0.015	0.001	0.003	0.001
-10.8	0.003	0.050	0.018	0.001	0.002	0.000
-9.5	0.004	0.054	0.019	0.001	0.002	-0.002
-8.2	0.004	0.051	0.016	0.000	0.001	-0.002
-6.8	0.003	0.040	0.010	0.000	0.001	-0.002
-5.5	0.002	0.025	0.004	0.000	0.001	-0.001
-4.2	0.001	0.010	0.001	0.001	0.001	-0.001
-2.9	0.000	0.003	0.000	0.001	0.000	-0.001
-1.6	0.000	0.000	0.000	0.000	0.000	-0.001
-0.3	0.000	0.000	0.000	0.000	0.001	0.000

A.1.2 Inclined Branch, *B*

Table A-6 Single discharge in inclined branch, *B*,
$Fr_B = 31.69$ and $H_{OGE} = 24.7$ mm (case 4).

y, mm	x = 0.0 mm, z = 2.0 mm			x = 0.0 mm, z = 11.0 mm			x = 0.0 mm, z = 22.0 mm		
	U, m/s	V, m/s	W, m/s	U, m/s	V, m/s	W, m/s	U, m/s	V, m/s	W, m/s
-17.9	0.013	0.025	-0.040	-0.015	0.170	-0.004	-0.015	0.170	-0.004
-16.6	0.005	0.008	-0.016	-0.015	0.186	-0.014	-0.015	0.186	-0.014
-15.3	0.001	0.001	-0.004	-0.017	0.203	-0.020	-0.017	0.203	-0.020
-14.1	0.000	0.000	-0.002	-0.020	0.224	-0.024	-0.020	0.224	-0.024
-12.8	-0.001	0.000	-0.002	-0.023	0.251	-0.029	-0.023	0.251	-0.029
-11.5	-0.001	0.001	-0.002	-0.025	0.276	-0.036	-0.025	0.276	-0.036
-10.2	-0.002	0.000	-0.005	-0.022	0.280	-0.043	-0.022	0.280	-0.043
-8.9	-0.003	0.000	-0.012	-0.019	0.248	-0.041	-0.019	0.248	-0.041
-7.6	0.000	0.000	0.000	-0.014	0.184	-0.031	-0.014	0.184	-0.031
-6.3	0.000	0.000	0.000	-0.008	0.113	-0.017	-0.008	0.113	-0.017
-5.0	0.000	0.000	0.000	-0.003	0.060	-0.007	-0.003	0.060	-0.007
-3.7	0.000	0.000	0.000	0.001	0.032	-0.004	0.001	0.032	-0.004
-2.5	0.000	0.000	0.000	0.005	0.018	-0.005	0.005	0.018	-0.005
-1.2	0.000	0.000	0.000	0.006	0.011	-0.007	0.006	0.011	-0.007
0.1	0.000	0.000	0.000	0.005	0.006	-0.007	0.005	0.006	-0.007
1.4	0.000	0.000	0.000	0.003	0.002	-0.005	0.003	0.002	-0.005
2.7	0.000	0.000	0.000	0.002	-0.003	-0.004	0.002	-0.003	-0.004
4.0	0.000	0.000	0.000	0.000	0.000	0.000	0.002	-0.003	-0.006
5.3	0.000	0.000	0.000	0.000	0.000	0.000	-0.001	-0.001	-0.011
6.6	0.000	0.000	0.000	0.000	0.000	0.000	-0.001	0.001	-0.012

Table A-7 Single discharge in inclined branch, B,
$Fr_B = 10.56$ and $H_{OGE} = 18.5$ mm (case 5).

y, mm	x = 0.0 mm, z = 2.0 mm			x = 0.0 mm, z = 8.0 mm			x = 0.0 mm, z = 14.0 mm		
	U, m/s	V, m/s	W, m/s	U, m/s	V, m/s	W, m/s	U, m/s	V, m/s	W, m/s
-17.8	0.010	0.045	0.013	-0.004	0.095	0.004	0.011	0.076	-0.010
-16.5	0.007	0.027	0.009	-0.005	0.107	0.009	0.012	0.082	-0.014
-15.2	0.003	0.011	0.004	-0.005	0.123	0.014	0.013	0.089	-0.019
-13.9	0.000	0.003	0.001	-0.006	0.143	0.017	0.015	0.096	-0.024
-12.6	0.000	0.001	0.001	-0.006	0.162	0.022	0.018	0.104	-0.029
-11.3	0.001	0.001	0.002	-0.007	0.174	0.029	0.023	0.114	-0.036
-10.0	0.001	0.002	0.003	-0.008	0.169	0.038	0.027	0.125	-0.047
-8.7	0.000	0.000	0.000	-0.009	0.148	0.045	0.032	0.137	-0.062
-7.4	0.000	0.000	0.000	-0.008	0.117	0.048	0.037	0.148	-0.081
-6.1	0.000	0.000	0.000	-0.005	0.079	0.039	0.044	0.158	-0.106
-4.7	0.000	0.000	0.000	-0.001	0.040	0.023	0.053	0.166	-0.138
-3.4	0.000	0.000	0.000	0.001	0.012	0.007	0.064	0.167	-0.176
-2.1	0.000	0.000	0.000	0.000	0.002	0.001	0.074	0.154	-0.214
-0.8	0.000	0.000	0.000	-0.001	0.002	-0.001	0.077	0.115	-0.250
0.5	0.000	0.000	0.000	0.000	0.000	0.000	0.072	0.065	-0.275
1.8	0.000	0.000	0.000	0.000	0.000	0.000	0.062	0.021	-0.267
3.1	0.000	0.000	0.000	0.000	0.000	0.000	0.045	0.000	-0.204
4.4	0.000	0.000	0.000	0.000	0.000	0.000	0.025	-0.004	-0.110

Table A-8 Single discharge in inclined branch, B,
$Fr_B = 3.48$ and $H_{OGE} = 14.5$ mm (case 6).

y, mm	x = 0.0 mm, z = 3.0 mm			x = 0.0 mm, z = 7.0 mm			x = 0.0 mm, z = 12.0 mm		
	U, m/s	V, m/s	W, m/s	U, m/s	V, m/s	W, m/s	U, m/s	V, m/s	W, m/s
-17.1	0.002	0.008	0.001	0.002	0.040	0.002	0.000	0.036	-0.004
-15.8	0.001	0.005	0.001	0.002	0.046	0.004	0.000	0.040	-0.004
-14.5	0.001	0.004	0.001	0.002	0.053	0.007	0.000	0.044	-0.005
-13.2	0.001	0.004	0.001	0.002	0.060	0.009	0.000	0.049	-0.006
-11.9	0.001	0.004	0.001	0.002	0.069	0.012	0.000	0.055	-0.007
-10.6	0.000	0.003	0.001	0.002	0.076	0.014	0.000	0.061	-0.010
-9.3	0.000	0.002	0.000	0.000	0.077	0.017	-0.001	0.066	-0.012
-8.0	0.000	0.001	0.000	-0.001	0.067	0.018	-0.002	0.071	-0.015
-6.7	0.000	0.000	0.000	-0.002	0.043	0.014	-0.002	0.074	-0.019
-5.4	0.000	0.000	0.000	-0.001	0.019	0.007	-0.004	0.075	-0.024
-4.1	0.000	0.000	0.000	0.000	0.003	0.001	-0.006	0.069	-0.029
-2.8	0.000	0.000	0.000	0.000	0.000	-0.002	-0.005	0.052	-0.029
-1.5	0.000	0.000	0.000	0.000	0.000	-0.002	-0.004	0.029	-0.021
-0.2	0.000	0.000	0.000	0.000	0.001	-0.002	-0.002	0.011	-0.010
1.1	0.000	0.000	0.000	0.000	0.000	0.000	-0.001	0.002	-0.002
2.4	0.000	0.000	0.000	0.000	0.000	0.000	0.000	0.000	0.000

A.1.3 Bottom Branch, *C*

Table A-9 Single discharge in bottom branch, *C*,
Fr_C = 31.69 and H_{OGE} = 22.7 mm (case 7).

y, mm	x = 0.0 mm, z = 2.0 mm			x = 0.0 mm, z = 10.0 mm			x = 0.0 mm, z = 18.0 mm		
	U, m/s	V, m/s	W, m/s	U, m/s	V, m/s	W, m/s	U, m/s	V, m/s	W, m/s
-13.8	0.009	0.027	0.007	0.006	0.146	-0.018	-0.008	0.059	0.004
-12.6	0.009	0.024	0.005	0.005	0.130	-0.015	-0.010	0.054	0.008
-11.4	0.010	0.024	0.006	0.004	0.109	-0.007	-0.010	0.046	0.009
-10.2	0.010	0.022	0.007	0.005	0.086	-0.001	-0.012	0.037	0.008
-8.9	0.011	0.021	0.006	0.006	0.063	0.001	-0.015	0.032	0.009
-7.7	0.011	0.019	0.006	0.007	0.043	-0.002	-0.018	0.028	0.009
-6.5	0.013	0.020	0.003	0.006	0.029	-0.004	-0.020	0.024	0.007
-5.2	0.015	0.020	0.001	0.003	0.020	-0.005	-0.026	0.017	-0.002
-4.0	0.016	0.017	-0.001	-0.003	0.015	-0.005	-0.037	0.008	-0.022
-2.8	0.013	0.012	0.005	-0.011	0.011	-0.003	-0.051	-0.004	-0.051
-1.6	0.009	0.005	0.017	-0.019	0.006	-0.003	-0.059	-0.019	-0.076
-0.3	0.008	-0.002	0.030	-0.024	-0.004	-0.007	-0.055	-0.031	-0.082
0.9	0.013	-0.008	0.037	-0.023	-0.014	-0.011	-0.041	-0.038	-0.070
2.1	0.020	-0.012	0.043	-0.015	-0.024	-0.012	-0.022	-0.042	-0.051
3.4	0.025	-0.016	0.053	-0.003	-0.034	-0.008	-0.004	-0.044	-0.035
4.6	0.025	-0.016	0.067	0.007	-0.042	0.000	0.010	-0.043	-0.025
5.8	0.024	-0.013	0.081	0.013	-0.046	0.010	0.018	-0.039	-0.019
7.0	0.023	-0.008	0.089	0.015	-0.044	0.019	0.022	-0.031	-0.015
8.3	0.022	-0.002	0.093	0.015	-0.037	0.022	0.023	-0.023	-0.010
9.5	0.021	0.004	0.091	0.014	-0.028	0.020	0.022	-0.014	-0.006
10.7	0.000	0.000	0.000	0.012	-0.019	0.018	0.018	-0.006	-0.003
11.9	0.000	0.000	0.000	0.009	-0.009	0.018	0.016	0.001	0.001
13.2	0.000	0.000	0.000	0.007	0.000	0.017	0.014	0.006	0.006
14.4	0.000	0.000	0.000	0.006	0.006	0.010	0.012	0.011	0.006
15.6	0.000	0.000	0.000	0.004	0.009	0.002	0.009	0.013	0.002
16.9	0.000	0.000	0.000	0.002	0.010	-0.002	0.006	0.013	-0.001
18.1	0.000	0.000	0.000	0.000	0.010	-0.003	0.001	0.010	0.002
19.3	0.000	0.000	0.000	-0.001	0.007	-0.003	-0.004	0.008	0.004
20.5	0.000	0.000	0.000	-0.002	0.006	-0.008	-0.007	0.006	0.004
21.8	0.000	0.000	0.000	0.000	0.000	0.000	-0.006	0.003	0.001
23.0	0.000	0.000	0.000	0.000	0.000	0.000	-0.001	0.001	0.003
24.2	0.000	0.000	0.000	0.000	0.000	0.000	0.005	0.011	0.009

Table A-10 Single discharge in bottom branch, C,
$Fr_C = 10.56$ and $H_{OGE} = 13$ mm (case 8).

y, mm	x = 0 mm, z = 2 mm			x = 0 mm, z = 6 mm			x = 0 mm, z = 10 mm		
	U, m/s	V, m/s	W, m/s	U, m/s	V, m/s	W, m/s	U, m/s	V, m/s	W, m/s
-5.0	0.023	0.038	0.036	0.033	0.098	0.048	-0.011	0.022	-0.004
-3.8	0.010	0.016	0.017	0.032	0.087	0.053	-0.014	0.015	-0.008
-2.5	0.004	0.007	0.010	0.028	0.073	0.050	-0.014	0.010	-0.008
-1.3	0.003	0.003	0.012	0.026	0.059	0.043	-0.015	0.006	-0.006
0.0	0.005	0.001	0.016	0.028	0.046	0.038	-0.017	0.003	-0.004
1.2	0.008	0.000	0.022	0.033	0.031	0.038	-0.018	0.002	-0.002
2.5	0.011	0.000	0.029	0.039	0.014	0.040	-0.018	0.004	0.000
3.7	0.013	0.001	0.034	0.044	-0.002	0.041	-0.017	0.008	0.003
5.0	0.014	0.003	0.035	0.047	-0.012	0.041	-0.016	0.012	0.004
6.2	0.014	0.004	0.033	0.047	-0.015	0.037	-0.014	0.016	0.003
7.4	0.015	0.005	0.034	0.043	-0.012	0.030	-0.011	0.019	0.001
8.7	0.012	0.006	0.032	0.040	-0.007	0.024	-0.008	0.021	-0.001
9.9	0.000	0.000	0.000	0.038	-0.003	0.021	-0.004	0.021	-0.003
11.2	0.000	0.000	0.000	0.038	0.001	0.022	-0.001	0.017	-0.005
12.4	0.000	0.000	0.000	0.038	0.004	0.024	0.002	0.012	-0.006
13.7	0.000	0.000	0.000	0.034	0.010	0.025	0.003	0.006	-0.007
14.9	0.000	0.000	0.000	0.026	0.015	0.020	0.005	0.000	-0.008
16.2	0.000	0.000	0.000	0.014	0.017	0.010	0.006	-0.001	-0.007
17.4	0.000	0.000	0.000	0.000	0.000	0.000	0.006	0.000	-0.005
18.6	0.000	0.000	0.000	0.000	0.000	0.000	0.003	0.000	-0.001
19.9	0.000	0.000	0.000	0.000	0.000	0.000	0.001	-0.001	0.000

A.2 Dual Discharge

A.2.1 Dual *A* and *B*

Table A- 11 Dual discharge in branches *A* and *B*. $Fr_A = 31.69$, $Fr_B = 34.4$, and OGE in branch *A*, $H_{OGE} = 41.02$ mm (case 9).

y, mm	x = 0.0 mm, z = 4.0 mm			x = 0.0 mm, z = 8.0 mm			x = 0.0 mm, z = 12.0 mm		
	U, m/s	V, m/s	W, m/s	U, m/s	V, m/s	W, m/s	U, m/s	V, m/s	W, m/s
-25.9	-0.026	0.202	0.025	-0.049	0.116	0.132	-0.034	0.177	-0.018
-24.7	-0.022	0.204	-0.016	-0.048	0.121	0.146	-0.018	0.171	0.011
-23.5	-0.024	0.214	-0.113	-0.029	0.109	0.109	0.015	0.162	0.024
-22.3	-0.031	0.224	-0.231	0.010	0.088	0.078	0.033	0.137	0.031
-21.1	-0.043	0.249	-0.319	0.021	0.066	0.005	0.038	0.112	0.014
-19.9	-0.065	0.275	-0.346	0.008	0.054	-0.056	0.022	0.089	-0.003
-18.7	-0.087	0.273	-0.299	-0.014	0.048	-0.099	0.005	0.065	-0.011
-17.5	-0.090	0.238	-0.220	-0.020	0.042	-0.094	-0.009	0.037	-0.031
-16.3	-0.063	0.153	-0.149	-0.014	0.044	-0.080	-0.009	0.016	-0.042
-15.1	-0.031	0.079	-0.082	-0.009	0.047	-0.077	-0.008	0.012	-0.064
-13.8	-0.011	0.030	-0.030	-0.002	0.051	-0.070	0.003	0.023	-0.059
-12.6	-0.006	0.012	0.002	-0.001	0.048	-0.055	-0.001	0.048	-0.074
-11.4	0.000	0.000	0.000	-0.004	0.042	-0.039	-0.008	0.069	-0.084
-10.2	0.000	0.000	0.000	-0.008	0.031	-0.026	-0.018	0.071	-0.093
-9.0	0.000	0.000	0.000	-0.011	0.020	-0.019	-0.014	0.046	-0.070
-7.8	0.000	0.000	0.000	0.000	0.000	0.000	-0.006	0.020	-0.039
-6.6	0.000	0.000	0.000	0.000	0.000	0.000	-0.002	0.007	-0.012
-5.4	0.000	0.000	0.000	0.000	0.000	0.000	-0.002	0.007	-0.002
-4.2	0.000	0.000	0.000	0.000	0.000	0.000	0.000	0.000	0.000
-3.0	0.000	0.000	0.000	0.000	0.000	0.000	0.000	0.000	0.000
-1.8	0.000	0.000	0.000	0.000	0.000	0.000	0.000	0.000	0.000

y, mm	x = 0.0 mm, z = 16.0 mm			x = 0.0 mm, z = 20.0 mm			x = 0.0 mm, z = 24.0 mm		
	U, m/s	V, m/s	W, m/s	U, m/s	V, m/s	W, m/s	U, m/s	V, m/s	W, m/s
-25.9	-0.024	0.177	0.110	0.023	0.076	0.057	-0.026	0.207	-0.016
-24.7	-0.033	0.157	0.099	0.031	0.059	0.067	-0.006	0.208	-0.032
-23.5	-0.066	0.140	0.091	0.035	0.053	0.075	-0.002	0.198	-0.038
-22.3	-0.092	0.127	0.114	0.034	0.067	0.053	-0.025	0.180	-0.038
-21.1	-0.106	0.124	0.144	0.032	0.079	0.015	-0.038	0.169	-0.023
-19.9	-0.111	0.122	0.151	0.022	0.078	-0.013	-0.041	0.167	-0.034
-18.7	-0.118	0.113	0.090	0.013	0.065	-0.021	-0.028	0.178	-0.046
-17.5	-0.108	0.081	-0.001	0.003	0.047	-0.024	-0.016	0.186	-0.049
-16.3	-0.089	0.036	-0.093	-0.002	0.025	-0.026	-0.011	0.180	-0.055
-15.1	-0.059	-0.002	-0.125	-0.004	0.009	-0.019	-0.002	0.147	-0.093
-13.8	-0.039	-0.020	-0.114	-0.006	0.008	-0.005	0.008	0.110	-0.130
-12.6	-0.027	-0.007	-0.094	-0.006	0.016	0.008	0.014	0.079	-0.129
-11.4	-0.019	0.019	-0.062	-0.004	0.027	0.011	0.016	0.054	-0.090
-10.2	-0.014	0.048	-0.049	-0.001	0.031	0.009	0.022	0.032	-0.063
-9.0	-0.010	0.060	-0.038	-0.001	0.031	0.005	0.023	0.018	-0.046
-7.8	-0.006	0.045	-0.033	-0.001	0.022	0.001	0.017	0.017	-0.022
-6.6	-0.004	0.028	-0.019	-0.001	0.016	0.000	0.006	0.020	0.001
-5.4	-0.004	0.018	-0.008	0.000	0.008	0.000	0.003	0.017	0.006
-4.2	-0.002	0.020	-0.006	0.001	0.004	-0.004	0.003	0.009	0.000
-3.0	0.000	0.012	-0.011	0.001	0.001	0.003	0.005	0.004	-0.013
-1.8	0.000	0.000	0.000	0.002	0.001	0.014	0.004	0.001	-0.023

y, mm	x = 0.0 mm, z = 28.0 mm			x = 0.0 mm, z = 32.0 mm			x = 0.0 mm, z = 36.0 mm		
	U, m/s	V, m/s	W, m/s	U, m/s	V, m/s	W, m/s	U, m/s	V, m/s	W, m/s
-25.9	-0.022	0.200	-0.031	-0.004	0.187	-0.058	-0.031	0.168	-0.051
-24.7	-0.025	0.216	-0.030	0.013	0.200	-0.080	-0.042	0.179	-0.076
-23.5	-0.029	0.234	-0.036	0.012	0.216	-0.110	-0.041	0.193	-0.082
-22.3	-0.028	0.258	-0.043	-0.004	0.234	-0.119	-0.037	0.200	-0.078
-21.1	-0.035	0.280	-0.057	-0.030	0.251	-0.124	-0.030	0.211	-0.073
-19.9	-0.041	0.297	-0.054	-0.044	0.265	-0.098	-0.043	0.226	-0.095
-18.7	-0.041	0.313	-0.049	-0.061	0.263	-0.055	-0.056	0.239	-0.116
-17.5	-0.033	0.337	-0.049	-0.093	0.256	0.018	-0.065	0.235	-0.127
-16.3	-0.020	0.360	-0.042	-0.122	0.248	0.069	-0.074	0.221	-0.095
-15.1	-0.020	0.369	-0.029	-0.135	0.235	0.082	-0.088	0.215	-0.078
-13.8	-0.023	0.338	0.001	-0.125	0.213	0.057	-0.106	0.224	-0.101
-12.6	-0.005	0.285	0.032	-0.120	0.177	0.017	-0.115	0.234	-0.139
-11.4	0.030	0.224	0.028	-0.104	0.143	-0.048	-0.113	0.220	-0.149
-10.2	0.065	0.168	-0.029	-0.072	0.102	-0.080	-0.100	0.166	-0.111
-9.0	0.066	0.107	-0.070	-0.034	0.070	-0.047	-0.073	0.107	-0.081
-7.8	0.046	0.051	-0.062	-0.005	0.047	0.006	-0.041	0.065	-0.031
-6.6	0.019	0.016	-0.018	0.004	0.040	0.033	-0.002	0.055	0.031
-5.4	0.004	0.005	0.004	0.007	0.034	0.023	0.026	0.043	0.068
-4.2	-0.003	0.003	0.002	0.001	0.025	0.009	0.048	0.032	0.091
-3.0	-0.032	0.007	-0.030	0.001	0.019	0.002	0.057	0.023	0.101
-1.8	-0.093	0.033	-0.080	0.003	0.012	0.003	0.062	0.019	0.123

Table A-12 Dual discharge in branches *A* and *B*. Fr_A = 10.56, Fr_B = 34.4, and OGE in branch *A*, H_{OGE} = 35.24 mm (case 10).

y, mm	x = 0.0 mm, z = 4.0 mm			x = 0.0 mm, z = 8.0 mm			x = 0.0 mm, z = 12.0 mm		
	U, m/s	V, m/s	W, m/s	U, m/s	V, m/s	W, m/s	U, m/s	V, m/s	W, m/s
-25.7	-0.065	0.233	0.116	0.026	0.164	0.024	-0.027	0.232	-0.027
-24.4	-0.050	0.226	0.134	0.017	0.170	0.034	-0.042	0.261	-0.013
-23.2	-0.019	0.196	0.127	0.027	0.174	0.006	-0.048	0.273	-0.018
-22.0	0.002	0.093	0.099	0.055	0.179	-0.042	-0.045	0.270	-0.047
-20.8	0.033	-0.096	0.065	0.089	0.174	-0.060	-0.040	0.242	-0.073
-19.6	0.091	-0.277	0.007	0.100	0.132	-0.051	-0.039	0.191	-0.071
-18.4	0.164	-0.419	-0.073	0.089	0.069	-0.029	-0.033	0.115	-0.037
-17.1	0.176	-0.423	-0.155	0.058	0.016	-0.022	-0.027	0.045	-0.010
-15.9	0.139	-0.352	-0.156	0.026	-0.004	-0.022	-0.015	0.008	-0.001
-14.7	0.083	-0.190	-0.113	0.010	-0.018	-0.045	-0.003	-0.006	-0.011
-13.5	0.048	-0.073	-0.062	0.010	-0.041	-0.086	0.015	-0.017	0.002
-12.3	0.000	0.000	0.000	0.013	-0.051	-0.111	0.038	-0.043	0.014
-11.1	0.000	0.000	0.000	0.010	-0.036	-0.082	0.035	-0.061	0.021
-9.8	0.000	0.000	0.000	0.004	-0.011	-0.033	0.022	-0.060	0.008
-8.6	0.000	0.000	0.000	0.001	-0.001	-0.005	0.002	-0.036	0.003
-7.4	0.000	0.000	0.000	0.000	0.000	0.000	0.000	-0.013	0.001
-6.2	0.000	0.000	0.000	0.000	0.000	0.000	0.000	-0.003	0.001
-5.0	0.000	0.000	0.000	0.000	0.000	0.000	0.000	-0.002	0.001
-3.7	0.000	0.000	0.000	0.000	0.000	0.000	0.000	0.000	0.000
-2.5	0.000	0.000	0.000	0.000	0.000	0.000	0.000	0.000	0.000
-1.3	0.000	0.000	0.000	0.000	0.000	0.000	0.000	0.000	0.000

y, mm	x = 0.0 mm, z = 16.0 mm			x = 0.0 mm, z = 20.0 mm			x = 0.0 mm, z = 24.0 mm		
	U, m/s	V, m/s	W, m/s	U, m/s	V, m/s	W, m/s	U, m/s	V, m/s	W, m/s
-25.7	-0.052	0.238	-0.017	-0.053	0.190	-0.053	-0.021	0.134	-0.069
-24.4	-0.046	0.241	-0.029	-0.046	0.204	-0.038	-0.023	0.137	-0.079
-23.2	-0.023	0.246	-0.040	-0.035	0.214	-0.038	-0.023	0.143	-0.088
-22.0	0.009	0.252	-0.046	-0.026	0.216	-0.048	-0.024	0.150	-0.100
-20.8	0.031	0.241	-0.047	-0.025	0.217	-0.073	-0.023	0.156	-0.106
-19.6	0.031	0.205	-0.047	-0.037	0.218	-0.093	-0.022	0.161	-0.113
-18.4	0.016	0.148	-0.029	-0.043	0.217	-0.131	-0.021	0.165	-0.120
-17.1	0.004	0.090	-0.016	-0.046	0.208	-0.150	-0.021	0.167	-0.127
-15.9	0.001	0.039	0.000	-0.042	0.181	-0.148	-0.019	0.166	-0.125
-14.7	0.005	0.015	-0.015	-0.033	0.138	-0.118	-0.022	0.162	-0.109
-13.5	0.004	0.000	-0.018	-0.018	0.092	-0.087	-0.024	0.154	-0.080
-12.3	0.007	-0.014	-0.027	-0.004	0.056	-0.066	-0.024	0.145	-0.044
-11.1	0.018	-0.034	-0.030	0.003	0.037	-0.055	-0.023	0.130	-0.010
-9.8	0.024	-0.044	-0.036	0.009	0.025	-0.043	-0.020	0.103	0.010
-8.6	0.024	-0.032	-0.040	0.011	0.011	-0.038	-0.012	0.057	0.013
-7.4	0.013	-0.021	-0.028	0.008	-0.001	-0.033	-0.004	0.015	0.002
-6.2	0.007	-0.012	-0.008	0.002	-0.006	-0.026	-0.001	-0.006	-0.005
-5.0	0.001	-0.011	0.004	0.001	-0.003	-0.014	-0.001	-0.006	-0.006
-3.7	-0.001	-0.004	0.004	0.000	0.000	-0.009	0.003	-0.002	-0.013
-2.5	0.000	0.000	0.000	-0.001	0.000	0.002	0.005	0.000	-0.019
-1.3	0.000	0.000	0.000	-0.006	0.000	0.016	0.001	0.001	-0.023

y, mm	x = 0.0 mm, z = 28.0 mm			x = 0.0 mm, z = 32.0 mm		
	U, m/s	V, m/s	W, m/s	U, m/s	V, m/s	W, m/s
-25.7	-0.011	0.146	-0.035	-0.014	0.123	-0.016
-24.4	-0.012	0.150	-0.040	-0.016	0.127	-0.018
-23.2	-0.017	0.155	-0.050	-0.016	0.129	-0.023
-22.0	-0.024	0.159	-0.066	-0.017	0.131	-0.033
-20.8	-0.031	0.161	-0.078	-0.020	0.135	-0.043
-19.6	-0.032	0.163	-0.082	-0.024	0.144	-0.046
-18.4	-0.030	0.171	-0.074	-0.027	0.155	-0.047
-17.1	-0.026	0.187	-0.062	-0.029	0.165	-0.047
-15.9	-0.030	0.201	-0.063	-0.032	0.175	-0.051
-14.7	-0.034	0.210	-0.065	-0.036	0.184	-0.060
-13.5	-0.040	0.212	-0.054	-0.040	0.195	-0.076
-12.3	-0.047	0.212	-0.026	-0.048	0.205	-0.103
-11.1	-0.056	0.195	0.003	-0.058	0.205	-0.126
-9.8	-0.051	0.148	0.023	-0.068	0.178	-0.142
-8.6	-0.031	0.082	0.028	-0.066	0.117	-0.129
-7.4	-0.009	0.028	0.016	-0.044	0.049	-0.083
-6.2	0.001	0.002	0.002	-0.017	0.004	-0.035
-5.0	0.001	-0.003	-0.001	-0.001	-0.007	-0.006
-3.7	-0.008	-0.001	0.020	0.003	-0.005	-0.002
-2.5	-0.025	-0.001	0.055	0.004	0.000	0.011
-1.3	-0.046	0.003	0.089	0.007	0.001	0.016

A.2.2 Dual *A* and *C*

Table A-13 Dual discharge in branches *A* and *C*. $Fr_A = 31.69$, $Fr_C = 34.4$, and OGE in branch *A*, $H_{OGE} = 39.75$ mm (case 11).

y, mm	x = 0.0 mm, z = 4.0 mm			x = 0.0 mm, z = 8.0 mm			x = 0.0 mm, z = 12.0 mm		
	U, m/s	V, m/s	W, m/s	U, m/s	V, m/s	W, m/s	U, m/s	V, m/s	W, m/s
-25.9	-0.042	-0.085	-0.084	0.112	-0.163	-0.087	-0.027	0.030	-0.070
-24.7	-0.048	-0.079	-0.064	0.114	-0.191	-0.076	-0.052	0.025	-0.035
-23.5	-0.036	-0.037	-0.061	0.067	-0.184	-0.077	-0.057	0.025	-0.030
-22.3	-0.049	0.063	0.002	0.014	-0.166	-0.056	-0.047	0.034	-0.049
-21.1	-0.041	0.196	0.045	-0.035	-0.151	-0.059	-0.035	0.034	-0.040
-19.9	-0.033	0.263	0.067	-0.050	-0.141	-0.077	-0.024	0.025	-0.004
-18.7	-0.009	0.253	0.025	-0.044	-0.104	-0.107	-0.016	0.014	0.032
-17.5	-0.006	0.195	0.030	-0.027	-0.050	-0.101	-0.007	0.011	0.049
-16.3	-0.008	0.099	0.035	-0.014	0.000	-0.076	-0.006	0.024	0.055
-15.1	-0.006	0.033	0.022	-0.002	0.034	-0.033	-0.005	0.039	0.069
-13.8	0.002	0.003	0.017	0.002	0.051	-0.002	-0.003	0.051	0.087
-12.6	0.006	0.005	0.019	0.003	0.048	0.015	0.006	0.062	0.106
-11.4	0.000	0.000	0.000	0.001	0.033	0.014	0.005	0.073	0.093
-10.2	0.000	0.000	0.000	0.000	0.017	0.008	0.006	0.071	0.071
-9.0	0.000	0.000	0.000	0.002	0.009	0.011	0.001	0.045	0.032
-7.8	0.000	0.000	0.000	0.000	0.000	0.000	0.003	0.018	0.015
-6.6	0.000	0.000	0.000	0.000	0.000	0.000	0.000	0.006	0.000
-5.4	0.000	0.000	0.000	0.000	0.000	0.000	0.000	0.007	0.000
-4.2	0.000	0.000	0.000	0.000	0.000	0.000	0.000	0.000	0.000
-3.0	0.000	0.000	0.000	0.000	0.000	0.000	0.000	0.000	0.000
-1.8	0.000	0.000	0.000	0.000	0.000	0.000	0.000	0.000	0.000

y, mm	x = 0.0 mm, z = 16.0 mm			x = 0.0 mm, z = 20.0 mm			x = 0.0 mm, z = 24.0 mm		
	U, m/s	V, m/s	W, m/s	U, m/s	V, m/s	W, m/s	U, m/s	V, m/s	W, m/s
-25.9	-0.055	0.037	-0.054	-0.033	0.058	-0.094	-0.011	0.117	-0.061
-24.7	-0.049	0.032	-0.031	-0.025	0.055	-0.078	-0.009	0.127	-0.065
-23.5	-0.043	0.042	-0.029	-0.015	0.064	-0.073	-0.010	0.136	-0.064
-22.3	-0.037	0.058	-0.041	0.000	0.084	-0.063	-0.018	0.145	-0.060
-21.1	-0.032	0.074	-0.058	0.016	0.103	-0.051	-0.029	0.160	-0.038
-19.9	-0.029	0.084	-0.068	0.029	0.108	-0.014	-0.029	0.180	-0.030
-18.7	-0.023	0.089	-0.051	0.043	0.109	0.055	-0.021	0.205	-0.036
-17.5	-0.024	0.090	-0.022	0.051	0.109	0.125	-0.012	0.224	-0.054
-16.3	-0.029	0.090	0.000	0.048	0.111	0.159	-0.014	0.231	-0.056
-15.1	-0.035	0.091	0.026	0.035	0.103	0.151	-0.022	0.233	-0.028
-13.8	-0.039	0.093	0.061	0.018	0.092	0.129	-0.027	0.232	0.023
-12.6	-0.043	0.091	0.106	0.012	0.076	0.107	-0.029	0.220	0.052
-11.4	-0.046	0.081	0.141	0.008	0.061	0.064	-0.024	0.183	0.036
-10.2	-0.035	0.072	0.121	0.005	0.044	0.018	-0.021	0.129	-0.015
-9.0	-0.024	0.065	0.072	-0.001	0.032	-0.011	-0.011	0.078	-0.056
-7.8	-0.010	0.049	0.013	-0.003	0.021	-0.014	-0.004	0.044	-0.056
-6.6	-0.008	0.034	0.003	-0.003	0.015	-0.009	0.002	0.028	-0.034
-5.4	-0.003	0.022	-0.002	-0.001	0.008	-0.003	0.001	0.017	-0.006
-4.2	-0.001	0.022	-0.001	0.001	0.005	-0.002	0.001	0.008	0.002
-3.0	-0.002	0.014	-0.001	0.002	0.001	-0.002	0.000	0.004	0.001
-1.8	0.000	0.000	0.000	0.003	0.001	0.003	0.001	0.002	-0.005

y, mm	x = 0.0 mm, z = 28.0 mm			x = 0.0 mm, z = 32.0 mm			x = 0.0 mm, z = 36.0 mm		
	U, m/s	V, m/s	W, m/s	U, m/s	V, m/s	W, m/s	U, m/s	V, m/s	W, m/s
-25.9	-0.004	0.132	-0.037	-0.028	0.138	-0.012	-0.014	0.119	-0.028
-24.7	-0.007	0.140	-0.039	-0.026	0.146	-0.026	-0.017	0.127	-0.024
-23.5	-0.007	0.152	-0.037	-0.025	0.158	-0.041	-0.022	0.136	-0.024
-22.3	-0.015	0.164	-0.039	-0.025	0.167	-0.049	-0.030	0.141	-0.038
-21.1	-0.020	0.178	-0.043	-0.028	0.175	-0.054	-0.037	0.145	-0.062
-19.9	-0.018	0.193	-0.030	-0.032	0.187	-0.055	-0.031	0.156	-0.058
-18.7	-0.014	0.217	-0.025	-0.038	0.212	-0.071	-0.023	0.169	-0.055
-17.5	-0.010	0.250	-0.034	-0.054	0.238	-0.083	-0.018	0.179	-0.057
-16.3	-0.008	0.286	-0.067	-0.067	0.255	-0.101	-0.023	0.183	-0.057
-15.1	0.001	0.320	-0.065	-0.075	0.258	-0.109	-0.028	0.183	-0.049
-13.8	0.002	0.343	-0.019	-0.075	0.259	-0.133	-0.042	0.176	-0.038
-12.6	-0.017	0.353	0.056	-0.072	0.239	-0.189	-0.060	0.161	-0.041
-11.4	-0.059	0.317	0.141	-0.087	0.201	-0.186	-0.073	0.142	-0.044
-10.2	-0.082	0.231	0.198	-0.101	0.142	-0.140	-0.076	0.110	-0.045
-9.0	-0.065	0.128	0.166	-0.099	0.098	-0.054	-0.067	0.088	-0.060
-7.8	-0.021	0.054	0.078	-0.065	0.066	-0.018	-0.042	0.055	-0.039
-6.6	0.010	0.023	0.012	-0.025	0.047	0.007	-0.001	0.038	0.008
-5.4	0.013	0.007	0.016	-0.004	0.035	0.017	0.025	0.016	0.048
-4.2	0.004	0.003	0.011	-0.006	0.025	0.013	0.035	0.012	0.064
-3.0	-0.032	0.007	0.007	-0.016	0.032	0.011	0.039	0.009	0.068
-1.8	-0.087	0.041	-0.017	-0.030	0.046	0.024	0.056	0.008	0.112

Table A- 14 Dual discharge in branches *A* and C. Fr_A = 10.56, Fr_C = 34.4, and OGE in branch *A*, H_{OGE} = 34.16 mm (case 12).

y, mm	x = 0.0 mm, z = 4.0 mm			x = 0.0 mm, z = 8.0 mm			x = 0.0 mm, z = 12.0 mm		
	U, m/s	V, m/s	W, m/s	U, m/s	V, m/s	W, m/s	U, m/s	V, m/s	W, m/s
-25.7	-0.106	-0.258	0.081	-0.075	-0.095	-0.179	-0.039	-0.049	-0.277
-24.4	-0.066	-0.224	0.046	-0.050	-0.137	-0.131	-0.027	-0.061	-0.251
-23.2	-0.039	-0.164	0.022	-0.037	-0.156	-0.132	-0.021	-0.068	-0.226
-22.0	0.005	-0.155	0.058	-0.036	-0.154	-0.156	-0.022	-0.069	-0.200
-20.8	0.063	-0.244	0.085	-0.025	-0.142	-0.166	-0.022	-0.063	-0.165
-19.6	0.077	-0.356	0.041	-0.007	-0.118	-0.144	-0.017	-0.052	-0.131
-18.4	0.041	-0.466	-0.063	0.007	-0.090	-0.102	-0.010	-0.041	-0.096
-17.1	0.006	-0.454	-0.109	0.008	-0.065	-0.070	-0.007	-0.030	-0.075
-15.9	0.015	-0.357	-0.045	0.002	-0.045	-0.057	-0.004	-0.022	-0.057
-14.7	0.021	-0.178	0.018	-0.004	-0.037	-0.057	0.004	-0.017	-0.043
-13.5	0.009	-0.062	0.014	-0.006	-0.037	-0.055	0.031	-0.021	0.006
-12.3	0.000	0.000	0.000	-0.006	-0.034	-0.045	0.094	-0.044	0.112
-11.1	0.000	0.000	0.000	-0.003	-0.020	-0.028	0.129	-0.066	0.191
-9.8	0.000	0.000	0.000	-0.002	-0.006	-0.010	0.108	-0.072	0.170
-8.6	0.000	0.000	0.000	-0.001	0.000	-0.001	0.046	-0.048	0.083
-7.4	0.000	0.000	0.000	0.000	0.000	0.000	0.008	-0.024	0.017
-6.2	0.000	0.000	0.000	0.000	0.000	0.000	0.001	-0.010	0.000
-5.0	0.000	0.000	0.000	0.000	0.000	0.000	0.001	-0.008	-0.001
-3.7	0.000	0.000	0.000	0.000	0.000	0.000	0.000	0.000	0.000
-2.5	0.000	0.000	0.000	0.000	0.000	0.000	0.000	0.000	0.000

y, mm	x = 0.0 mm, z = 16.0 mm			x = 0.0 mm, z = 20.0 mm			x = 0.0 mm, z = 24.0 mm		
	U, m/s	V, m/s	W, m/s	U, m/s	V, m/s	W, m/s	U, m/s	V, m/s	W, m/s
-25.7	-0.013	-0.009	-0.148	-0.015	0.047	-0.092	-0.002	0.041	-0.050
-24.4	-0.017	-0.025	-0.136	-0.009	0.046	-0.083	-0.002	0.040	-0.042
-23.2	-0.021	-0.032	-0.133	-0.010	0.047	-0.075	-0.003	0.039	-0.039
-22.0	-0.024	-0.031	-0.130	-0.011	0.049	-0.061	-0.001	0.040	-0.037
-20.8	-0.022	-0.029	-0.125	-0.013	0.050	-0.045	0.000	0.042	-0.039
-19.6	-0.018	-0.027	-0.115	-0.012	0.055	-0.036	0.002	0.046	-0.037
-18.4	-0.013	-0.024	-0.103	-0.011	0.061	-0.031	0.005	0.049	-0.037
-17.1	-0.011	-0.019	-0.085	-0.010	0.068	-0.019	0.009	0.055	-0.036
-15.9	-0.009	-0.014	-0.066	-0.008	0.074	-0.002	0.011	0.064	-0.033
-14.7	-0.007	-0.009	-0.046	-0.007	0.078	0.015	0.010	0.075	-0.025
-13.5	-0.005	-0.004	-0.031	-0.007	0.073	0.029	0.007	0.089	-0.017
-12.3	-0.004	-0.004	-0.022	-0.004	0.060	0.039	0.006	0.104	-0.005
-11.1	-0.003	-0.012	-0.014	-0.003	0.047	0.049	0.006	0.114	0.013
-9.8	-0.002	-0.022	-0.007	-0.002	0.035	0.052	0.004	0.102	0.027
-8.6	-0.003	-0.019	0.004	-0.001	0.021	0.041	0.001	0.064	0.021
-7.4	-0.004	-0.013	0.006	0.000	0.008	0.021	-0.002	0.020	0.001
-6.2	-0.003	-0.006	0.005	-0.002	0.001	0.005	-0.002	-0.004	-0.014
-5.0	-0.001	-0.005	0.001	-0.003	0.000	0.000	-0.003	-0.006	-0.016
-3.7	0.000	-0.002	0.001	-0.002	0.000	-0.003	0.000	-0.002	-0.020
-2.5	0.000	0.000	0.000	0.003	0.000	-0.007	0.000	-0.002	-0.007

y, mm	x = 0.0 mm, z = 28.0 mm			x = 0.0 mm, z = 32.0 mm		
	U, m/s	V, m/s	W, m/s	U, m/s	V, m/s	W, m/s
-25.7	-0.010	0.055	-0.037	-0.006	0.061	-0.016
-24.4	-0.010	0.057	-0.034	-0.006	0.064	-0.015
-23.2	-0.011	0.061	-0.031	-0.006	0.067	-0.015
-22.0	-0.012	0.067	-0.028	-0.007	0.071	-0.014
-20.8	-0.012	0.075	-0.022	-0.008	0.076	-0.014
-19.6	-0.011	0.085	-0.012	-0.008	0.082	-0.013
-18.4	-0.007	0.095	-0.001	-0.007	0.090	-0.014
-17.1	-0.004	0.107	0.006	-0.006	0.100	-0.015
-15.9	-0.002	0.121	0.011	-0.008	0.111	-0.016
-14.7	-0.003	0.136	0.001	-0.015	0.124	-0.017
-13.5	-0.005	0.152	-0.021	-0.031	0.142	-0.019
-12.3	-0.004	0.168	-0.047	-0.045	0.157	-0.013
-11.1	-0.002	0.168	-0.058	-0.058	0.164	-0.015
-9.8	-0.002	0.134	-0.050	-0.072	0.143	-0.041
-8.6	-0.002	0.074	-0.027	-0.076	0.096	-0.081
-7.4	-0.001	0.023	-0.006	-0.055	0.041	-0.087
-6.2	0.001	-0.001	0.001	-0.023	0.003	-0.055
-5.0	0.001	-0.003	0.000	-0.003	-0.007	-0.019
-3.7	-0.011	0.000	0.026	0.001	-0.005	0.001
-2.5	-0.053	0.001	0.111	0.003	-0.002	0.005

A.3 Triple Discharge *A*, *B* and *C*

Table A- 15 Triple discharge in branches *A*, *B* and C. $Fr_A = 31.69$, $Fr_C = 34.4$ $Fr_B = 34.4$, and OGE in branch *A*, $H_{OGE} = 39.75$ mm (case 13).

y, mm	x = 0.0 mm, z = 4.0 mm			x = 0.0 mm, z = 8.0 mm			x = 0.0 mm, z = 12.0 mm		
	U, m/s	V, m/s	W, m/s	U, m/s	V, m/s	W, m/s	U, m/s	V, m/s	W, m/s
-25.9	0.031	-0.068	0.140	0.017	0.134	-0.072	-0.024	0.113	0.071
-24.7	0.008	-0.105	0.035	-0.025	0.115	-0.137	-0.040	0.111	0.060
-23.5	-0.013	-0.075	-0.042	-0.071	0.093	-0.194	-0.046	0.100	0.042
-22.3	0.002	0.020	-0.163	-0.124	0.103	-0.246	-0.050	0.096	0.063
-21.1	-0.006	0.175	-0.311	-0.137	0.150	-0.200	-0.047	0.092	0.106
-19.9	-0.050	0.344	-0.463	-0.130	0.208	-0.125	-0.039	0.086	0.152
-18.7	-0.118	0.463	-0.574	-0.120	0.259	-0.126	-0.021	0.076	0.155
-17.5	-0.151	0.505	-0.644	-0.118	0.263	-0.212	-0.005	0.068	0.117
-16.3	-0.147	0.436	-0.592	-0.076	0.213	-0.241	0.001	0.054	0.073
-15.1	-0.120	0.319	-0.451	-0.021	0.143	-0.195	0.001	0.040	0.027
-13.8	-0.075	0.185	-0.274	0.017	0.091	-0.113	0.009	0.031	0.004
-12.6	-0.038	0.087	-0.150	0.014	0.076	-0.051	0.013	0.035	-0.012
-11.4	0.000	0.000	0.000	0.002	0.074	-0.008	0.008	0.054	-0.012
-10.2	0.000	0.000	0.000	-0.003	0.067	0.017	-0.002	0.061	-0.011
-9.0	0.000	0.000	0.000	-0.004	0.051	0.016	-0.005	0.046	-0.012
-7.8	0.000	0.000	0.000	0.000	0.000	0.000	-0.003	0.020	-0.008
-6.6	0.000	0.000	0.000	0.000	0.000	0.000	0.000	0.006	-0.005
-5.4	0.000	0.000	0.000	0.000	0.000	0.000	0.000	0.006	0.000
-4.2	0.000	0.000	0.000	0.000	0.000	0.000	0.000	0.000	0.000
-3.0	0.000	0.000	0.000	0.000	0.000	0.000	0.000	0.000	0.000
-1.8	0.000	0.000	0.000	0.000	0.000	0.000	0.000	0.000	0.000

y, mm	x = 0.0 mm, z = 16.0 mm			x = 0.0 mm, z = 20.0 mm			x = 0.0 mm, z = 24.0 mm		
	U, m/s	V, m/s	W, m/s	U, m/s	V, m/s	W, m/s	U, m/s	V, m/s	W, m/s
-25.9	-0.066	0.137	-0.222	-0.028	0.083	-0.069	-0.026	0.111	-0.090
-24.7	-0.087	0.115	-0.183	-0.021	0.087	-0.065	-0.037	0.097	-0.091
-23.5	-0.107	0.107	-0.144	-0.011	0.074	-0.080	-0.029	0.075	-0.079
-22.3	-0.108	0.108	-0.117	-0.007	0.052	-0.104	-0.011	0.060	-0.051
-21.1	-0.097	0.111	-0.102	-0.001	0.029	-0.112	0.007	0.056	-0.035
-19.9	-0.087	0.098	-0.101	0.007	0.017	-0.088	0.010	0.063	-0.027
-18.7	-0.085	0.082	-0.096	0.015	0.022	-0.039	-0.001	0.064	-0.030
-17.5	-0.085	0.065	-0.089	0.017	0.033	-0.001	-0.019	0.051	-0.034
-16.3	-0.089	0.054	-0.099	0.011	0.036	0.014	-0.027	0.030	-0.019
-15.1	-0.071	0.038	-0.078	0.010	0.023	0.013	-0.024	0.016	-0.003
-13.8	-0.048	0.020	-0.057	0.012	0.008	0.019	-0.013	0.017	0.012
-12.6	-0.020	0.011	-0.019	0.016	0.007	0.030	0.006	0.020	0.044
-11.4	-0.008	0.011	-0.008	0.013	0.015	0.034	0.023	0.025	0.088
-10.2	-0.001	0.024	0.007	0.004	0.022	0.021	0.029	0.029	0.102
-9.0	0.003	0.035	0.011	-0.002	0.023	0.009	0.022	0.030	0.080
-7.8	0.003	0.034	0.002	-0.004	0.018	0.000	0.011	0.024	0.045
-6.6	0.002	0.023	-0.010	-0.002	0.014	-0.001	0.004	0.016	0.019
-5.4	0.000	0.013	-0.011	-0.001	0.008	-0.002	0.001	0.010	0.004
-4.2	0.000	0.012	-0.006	0.000	0.004	-0.001	0.000	0.005	0.001
-3.0	0.000	0.006	0.000	0.000	0.001	-0.003	0.000	0.002	0.005
-1.8	0.000	0.000	0.000	0.002	0.002	-0.001	-0.001	0.000	0.004

y, mm	x = 0.0 mm, z = 28.0 mm			x = 0.0 mm, z = 32.0 mm			x = 0.0 mm, z = 36.0 mm		
	U, m/s	V, m/s	W, m/s	U, m/s	V, m/s	W, m/s	U, m/s	V, m/s	W, m/s
-25.9	-0.014	0.201	-0.060	-0.032	0.199	-0.111	-0.028	0.161	-0.027
-24.7	-0.027	0.214	-0.061	-0.048	0.200	-0.124	-0.054	0.162	-0.049
-23.5	-0.037	0.223	-0.081	-0.063	0.205	-0.123	-0.062	0.173	-0.066
-22.3	-0.039	0.227	-0.119	-0.075	0.210	-0.125	-0.062	0.172	-0.111
-21.1	-0.030	0.235	-0.145	-0.070	0.217	-0.133	-0.049	0.175	-0.153
-19.9	-0.033	0.238	-0.178	-0.053	0.227	-0.146	-0.063	0.198	-0.230
-18.7	-0.041	0.240	-0.175	-0.044	0.249	-0.168	-0.098	0.228	-0.268
-17.5	-0.057	0.235	-0.160	-0.049	0.272	-0.179	-0.132	0.234	-0.293
-16.3	-0.062	0.225	-0.130	-0.067	0.288	-0.172	-0.149	0.232	-0.317
-15.1	-0.047	0.215	-0.082	-0.087	0.278	-0.174	-0.132	0.224	-0.363
-13.8	-0.023	0.192	-0.031	-0.119	0.243	-0.170	-0.110	0.238	-0.399
-12.6	-0.006	0.151	0.021	-0.144	0.193	-0.147	-0.083	0.226	-0.397
-11.4	0.005	0.090	0.036	-0.143	0.144	-0.080	-0.063	0.198	-0.356
-10.2	0.006	0.036	0.038	-0.112	0.088	-0.002	-0.044	0.145	-0.299
-9.0	0.006	0.006	0.023	-0.065	0.043	0.032	-0.034	0.100	-0.230
-7.8	-0.003	0.000	0.013	-0.030	0.021	0.036	-0.027	0.076	-0.150
-6.6	-0.005	0.003	0.004	-0.008	0.021	0.015	-0.021	0.063	-0.072
-5.4	-0.003	0.004	0.004	-0.002	0.021	0.007	-0.010	0.053	-0.012
-4.2	0.000	0.002	0.003	0.002	0.013	0.004	-0.008	0.037	0.001
-3.0	0.007	0.000	-0.001	0.001	0.014	0.010	-0.008	0.028	0.027
-1.8	0.002	-0.001	-0.004	-0.007	0.025	0.018	-0.004	0.019	0.054

Table A-16 Triple discharge in branches *A, B* and C. Fr_A = 10.56, Fr_C = 34.4, Fr_B = 34.4, and OGE in branch *A*, H_{OGE} = 36.75 mm (case 14).

y, mm	x = 0.0 mm, z = 4.0 mm			x = 0.0 mm, z = 8.0 mm			x = 0.0 mm, z = 12.0 mm		
	U, m/s	V, m/s	W, m/s	U, m/s	V, m/s	W, m/s	U, m/s	V, m/s	W, m/s
-25.7	-0.026	-0.136	0.075	0.063	0.125	-0.243	-0.088	0.231	-0.355
-24.4	-0.023	-0.080	0.084	0.062	0.132	-0.231	-0.082	0.260	-0.388
-23.2	-0.018	-0.008	0.129	0.043	0.135	-0.212	-0.081	0.284	-0.400
-22.0	-0.008	-0.029	0.134	0.027	0.150	-0.187	-0.088	0.301	-0.392
-20.8	0.028	-0.181	0.153	0.019	0.166	-0.118	-0.083	0.288	-0.357
-19.6	0.079	-0.388	0.158	0.002	0.156	-0.049	-0.059	0.253	-0.293
-18.4	0.140	-0.566	0.150	-0.019	0.111	-0.009	-0.030	0.173	-0.198
-17.1	0.138	-0.611	0.035	-0.026	0.053	-0.008	-0.010	0.096	-0.102
-15.9	0.101	-0.537	-0.065	-0.022	0.014	-0.022	-0.002	0.032	-0.043
-14.7	0.047	-0.328	-0.111	-0.016	-0.011	-0.047	0.003	0.001	-0.035
-13.5	0.026	-0.132	-0.051	-0.018	-0.038	-0.073	0.015	-0.022	-0.035
-12.3	0.000	0.000	0.000	-0.017	-0.054	-0.083	0.041	-0.055	-0.014
-11.1	0.000	0.000	0.000	-0.011	-0.044	-0.062	0.046	-0.078	0.011
-9.8	0.000	0.000	0.000	-0.004	-0.020	-0.029	0.036	-0.077	0.021
-8.6	0.000	0.000	0.000	0.000	-0.005	-0.008	0.014	-0.047	0.017
-7.4	0.000	0.000	0.000	0.000	0.000	0.000	0.006	-0.017	0.009
-6.2	0.000	0.000	0.000	0.000	0.000	0.000	0.003	-0.004	0.005
-5.0	0.000	0.000	0.000	0.000	0.000	0.000	0.001	-0.004	0.003
-3.7	0.000	0.000	0.000	0.000	0.000	0.000	0.000	0.000	0.000
-2.5	0.000	0.000	0.000	0.000	0.000	0.000	0.000	0.000	0.000
-1.3	0.000	0.000	0.000	0.000	0.000	0.000	0.000	0.000	0.000

y, mm	x = 0.0 mm, z = 16.0 mm			x = 0.0 mm, z = 20.0 mm			x = 0.0 mm, z = 24.0 mm		
	U, m/s	V, m/s	W, m/s	U, m/s	V, m/s	W, m/s	U, m/s	V, m/s	W, m/s
-25.7	-0.043	0.223	-0.236	-0.041	0.153	-0.182	-0.010	0.187	-0.103
-24.4	-0.038	0.226	-0.217	-0.054	0.155	-0.195	-0.008	0.192	-0.105
-23.2	-0.031	0.229	-0.174	-0.063	0.171	-0.220	-0.005	0.195	-0.113
-22.0	-0.030	0.224	-0.126	-0.072	0.199	-0.223	-0.005	0.202	-0.131
-20.8	-0.035	0.217	-0.104	-0.076	0.211	-0.220	-0.008	0.208	-0.150
-19.6	-0.042	0.203	-0.095	-0.083	0.206	-0.204	-0.011	0.214	-0.157
-18.4	-0.041	0.161	-0.117	-0.074	0.191	-0.193	-0.014	0.218	-0.150
-17.1	-0.028	0.094	-0.118	-0.059	0.178	-0.163	-0.011	0.221	-0.134
-15.9	-0.013	0.026	-0.106	-0.045	0.171	-0.146	-0.007	0.220	-0.128
-14.7	-0.001	-0.003	-0.056	-0.044	0.155	-0.141	-0.004	0.211	-0.127
-13.5	0.000	-0.008	-0.014	-0.041	0.126	-0.132	-0.004	0.192	-0.118
-12.3	0.006	-0.012	0.001	-0.032	0.087	-0.109	-0.007	0.170	-0.098
-11.1	0.006	-0.030	0.007	-0.021	0.058	-0.077	-0.012	0.146	-0.069
-9.8	0.005	-0.048	-0.004	-0.012	0.040	-0.049	-0.019	0.107	-0.045
-8.6	0.001	-0.039	-0.008	-0.005	0.024	-0.022	-0.020	0.051	-0.032
-7.4	0.000	-0.028	-0.012	-0.002	0.009	-0.004	-0.016	0.003	-0.025
-6.2	0.001	-0.015	-0.005	-0.004	0.001	-0.007	-0.007	-0.018	-0.016
-5.0	0.000	-0.012	0.002	-0.006	0.001	-0.011	-0.002	-0.013	-0.006
-3.7	0.000	-0.005	0.005	-0.006	0.001	-0.010	0.001	-0.005	-0.004
-2.5	0.000	0.000	0.000	-0.013	0.001	-0.015	0.003	-0.001	-0.003
-1.3	0.000	0.000	0.000	-0.028	0.001	-0.021	-0.006	0.000	0.002

y, mm	x = 0.0 mm, z = 28.0 mm			x = 0.0 mm, z = 32.0 mm		
	U, m/s	V, m/s	W, m/s	U, m/s	V, m/s	W, m/s
-25.7	-0.022	0.147	-0.083	-0.010	0.117	-0.052
-24.4	-0.025	0.147	-0.079	-0.012	0.117	-0.053
-23.2	-0.026	0.150	-0.075	-0.012	0.118	-0.059
-22.0	-0.027	0.153	-0.089	-0.010	0.118	-0.071
-20.8	-0.024	0.157	-0.109	-0.007	0.121	-0.081
-19.6	-0.023	0.161	-0.131	-0.011	0.126	-0.088
-18.4	-0.025	0.164	-0.140	-0.020	0.133	-0.078
-17.1	-0.025	0.171	-0.134	-0.029	0.141	-0.069
-15.9	-0.023	0.179	-0.118	-0.034	0.147	-0.068
-14.7	-0.030	0.186	-0.100	-0.043	0.156	-0.080
-13.5	-0.050	0.193	-0.081	-0.055	0.165	-0.079
-12.3	-0.076	0.198	-0.054	-0.076	0.180	-0.077
-11.1	-0.089	0.195	-0.018	-0.102	0.195	-0.083
-9.8	-0.081	0.152	0.015	-0.128	0.193	-0.113
-8.6	-0.047	0.084	0.033	-0.132	0.146	-0.131
-7.4	-0.014	0.022	0.027	-0.092	0.067	-0.091
-6.2	0.001	-0.002	0.013	-0.042	0.000	-0.034
-5.0	0.001	-0.003	0.004	-0.008	-0.021	0.007
-3.7	-0.005	-0.001	0.011	-0.006	-0.013	0.012
-2.5	-0.028	0.000	0.050	-0.011	-0.001	0.032
-1.3	-0.046	0.000	0.085	-0.012	0.000	0.073